Etude du controle global de l'interférometre central de VIRGO

Luca Matone

ORSAY
n° d'ordre :

LAL 99-57
Octobre 1999

UNIVERSITÉ DE PARIS-SUD
Centre d'Orsay

THÈSE

présentée
pour obtenir

Le GRADE de DOCTEUR EN SCIENCES PHYSIQUES
de L'UNIVERSITÉ PARIS XI ORSAY

par

Luca MATONE

Étude du Contrôle Global de l'Interféromètre Central de VIRGO

Soutenue le 29 Octobre 1999 devant la Commission d'examen

MM.	A.	BRILLET	
	M.	DAVIER	
	G.	GIORDANO	
	F.	LE DIBERDER	Rapporteur
	F.	RICHARD	Président
	D.	SHOEMAKER	Rapporteur

A mio padre e a mia madre,
e a Christina

Contents

Introduction **xi**

I **1**

1 Gravitational Waves **3**
1.1 Einstein's Equations . . . 3
1.2 Weak Field Approximation . . . 4
1.2.1 Wave Equation . . . 5
1.2.2 Geodesic Deviation . . . 6
1.2.3 Generation of Gravitational Waves . . . 7
1.3 Sources . . . 9
1.3.1 Impulsive Sources . . . 9
1.3.2 Coalescing Compact Binaries . . . 10
1.3.3 Spinning Neutron Stars . . . 11
1.3.4 Stochastic Background . . . 12

2 Interferometric Detectors **13**
2.1 The Interferometric Principle:
The Michelson Interferometer . . . 13
2.1.1 The Frequency Response . . . 17
2.1.2 The Angular Response . . . 19
2.2 Noise Sources . . . 19
2.2.1 The Signal-to-Noise Ratio . . . 20
2.2.2 Phase Noise . . . 21
2.2.3 Displacement Noise . . . 22
2.3 Detector Design Improvements . . . 24
2.3.1 The Suspension System . . . 24
2.3.2 The Michelson Interferometer with Fabry-Perot Arms . . . 25
2.3.3 The Recycled Michelson with Fabry-Perot Arms . . . 28
2.4 The Frontal Modulation Scheme . . . 29

3 The Optical Resonator:
Response and Control **33**
3.1 Propagation Modes of a Laser Beam . . . 33
3.2 Geometrical Properties of Optical Resonators . . . 35
3.2.1 Resonator Stability . . . 36
3.2.2 Cavity Modes . . . 36
3.2.3 Resonance Condition . . . 37
3.3 Optical response of a Fabry-Perot . . . 38
3.3.1 The Longitudinal Response . . . 38
3.3.2 The Angular Response . . . 43

3.4 Longitudinal Locking: The Pound-Drever Method . . . 47
3.5 Automatic Alignment . . . 49
3.5.1 The Anderson Technique . . . 49
3.5.2 The Ward Technique . . . 49
3.5.3 The Quadrant Photodiode . . . 50

4 The VIRGO Project **53**
4.1 The Optical Configuration . . . 53
4.2 The Beam Source . . . 54
4.2.1 The Laser System . . . 54
4.2.2 The Input Bench . . . 54
4.2.3 The Input Mode-Cleaner . . . 56
4.2.4 Laser Source Requirements . . . 56
4.3 The Detection Bench . . . 57
4.3.1 The Output Mode-Cleaner . . . 57
4.3.2 The Photodiodes . . . 58
4.4 The Superattenuator . . . 58
4.4.1 The Mechanical Filter . . . 59
4.4.2 The Pre-Isolator stage . . . 59
4.4.3 The Marionetta and Reference Mass/Mirror System . . . 62
4.5 The Vacuum System . . . 63
4.6 Foreseen Sensitivity of VIRGO . . . 64
4.7 Online/Offline Activities . . . 64
4.8 Global Control . . . 67
4.8.1 Specifications . . . 67
4.8.2 RIOT . . . 68

II **71**

5 The Central Area Interferometer **73**
5.1 The Longitudinal Control . . . 73
5.2 Optical Configuration . . . 75
5.3 The Sensitivity Curve for the CITF . . . 76
5.4 Mirror Motion Specifications . . . 79
5.5 Mirror Displacement Noises . . . 79
5.5.1 Thermal Noise . . . 80
5.5.2 Seismic Excitation and Transfer Functions . . . 80
5.5.3 Mirror Motion Estimates . . . 84
5.6 The Longitudinal Response and Ratio of Signals . . . 84
5.7 The Angular Response . . . 88
5.7.1 Case 1: Symmetric CITF . . . 88
5.7.2 Case 2: Mode-Matched CITF . . . 90
5.7.3 Case 3: The Actual CITF Configuration . . . 91
5.8 The Asymmetry Matrix . . . 91
5.9 The Reconstruction Procedure . . . 94
5.10 Angular Control . . . 100
5.10.1 The Control System . . . 100
5.10.2 Autoalignment: Open and Closed Loop . . . 105
5.11 Conclusion . . . 109

6 The Mode-Cleaner Prototype **113**
6.1 Why a Suspended Mode-Cleaner? . . . 113
6.1.1 Beam Jitter and Optical Defects . . . 114
6.1.2 Frequency and Power Fluctuation Filtering . . . 116
6.2 The VIRGO Mode-Cleaner . . . 116
6.3 The Mode-Cleaner Prototype . . . 116
6.3.1 Local Controls . . . 117
6.4 Cavity Control Elements and Models . . . 118
6.4.1 The Control System . . . 119
6.5 Performance of Control . . . 127
6.5.1 The Open-Loop Transfer Function . . . 129
6.5.2 The Closed-Loop Transfer Function . . . 129
6.6 The Acquisition of Lock Problem . . . 132
6.6.1 The Control System Time Response . . . 132
6.6.2 The Error Signal . . . 136
6.7 The Acquisition of Lock: $\mathcal{F} = 100$ . . . 136
6.7.1 Example: t = 140 s . . . 139
6.7.2 Example: t = 825 s . . . 143
6.8 Acquisition of Lock: $\mathcal{F} = 1600$ . . . 143
6.9 Conclusion . . . 149

7 The Ringing Effect **151**
7.1 The Ringing Effect Model . . . 152
7.2 Measurement Fits . . . 154
7.3 Measuring the Finesse: An Alternative Method . . . 156
7.4 The Properties of the Effect . . . 156
7.4.1 The Relative Velocity Estimate . . . 158
7.5 Conclusion . . . 158

8 Lock Acquisition Strategy **165**
8.1 Acquisition Time Estimate . . . 165
8.2 The VIRGO Fabry-Perot Model . . . 166
8.2.1 Mirror Dynamics and Control . . . 166
8.2.2 The Optical Response and The Linear Control System . . . 167
8.2.3 Lock Acquisition Strategy . . . 167
8.2.4 The Analysis Procedure . . . 170
8.2.5 The Acting Procedure . . . 171
8.3 The CITF Locking Strategy . . . 174
8.3.1 The Model for the CITF . . . 174
8.3.2 Lock Acquisition Strategy . . . 175
8.3.3 Results . . . 181
8.4 Conclusion . . . 181

Conclusion **185**

A Control Systems **187**
A.1 The Stability Criteria . . . 188
A.2 Design Specifications . . . 189
A.3 Amplitude and Phase Margin . . . 189

Remerciements **195**

List of Figures

1.1 The effect of the passage of a gravitational wave on a ring of particles. 6
1.2 Waveform examples for core collapse[8] 10
1.3 Waveform for a coalescing compact binary. 11

2.1 The suspended Michelson Interferometer. 14
2.2 The Michelson Interferometer: notations for the electromagnetic fields. 14
2.3 A simple pendulum: notations. 15
2.4 The plot of abs($\Delta\phi/h$) as a function of the radiation frequency for a Michelson interferometer 18
2.5 Angle notations for impinging gravitational wave radiation. 19
2.6 The plot of $F_+^2(\theta,\phi) + F_\times^2(\theta,\phi)$ as a function of the angles θ and ϕ. 20
2.7 The pendulum mode contribution to thermal noise. 24
2.8 The Michelson Interferometer with Fabry-Perot arms. 25
2.9 The plot of abs($\phi_{R2} - \phi_{R1}$)/h for a Michelson interferometer with Fabry-Perot arms. 27
2.10 The Recycled Michelson Interferometer with Fabry-Perot arms. 28
2.11 The Michelson interferometer in the frontal modulation scheme. 29

3.1 The laser beam profile. 34
3.2 The optical resonator and its optical axis. 36
3.3 The resonator mode. 37
3.4 The Fabry-Perot: notations. 38
3.5 The Fabry-Perot stored power. 39
3.6 The Fabry-Perot transmitted power. 40
3.7 The Fabry-Perot reflected power. 41
3.8 The optical axis as a function of mirror tilts. 44
3.9 The beam and cavity reference systems S and S'. 45
3.10 Misaligned Fabry-Perot: notations. 46
3.11 The Pound-Drever error signal as a function of the cavity length (modulo λ). . . . 48
3.12 The quadrant photodiode. 50

4.1 The optical configuration of VIRGO 55
4.2 The output mode-cleaner. 58
4.3 The configuration of the 16 photodiodes on the detection bench. 58
4.4 The superattenuator. 60
4.5 The mechanical filter: perspective view. 61
4.6 The mechanical filter: side view. 61
4.7 The calculated transfer function of the pre-isolator stage with a chain of five mechanical filters. 62
4.8 The vacuum system. 63
4.9 The foreseen VIRGO sensitivity curve. 65
4.10 The RIOT crate. 69

5.1 The CITF interferometer. 74

5.2 The foreseen CITF sensitivity curve, expressed in $m/\sqrt{Hz}$ units, for different values of the quality factor Q. 77
5.3 The foreseen CITF sensitivity curve, expressed in $rad/\sqrt{Hz}$ units, for different values of the quality factor Q. 78
5.4 Conventions for the mirror's six degrees of freedom. 79
5.5 The calculated free mirror motion estimates due to seismic and thermal excitation. 81
5.6 The calculated free mirror motion estimates due to seismic and thermal excitation. 82
5.7 The calculated free mirror motion estimates due to seismic and thermal excitation. 83
5.8 The CITF seen as a Fabry-Perot cavity. 85
5.9 The ratio of $\mid \Psi_1 \mid^2$ with $\mid \Psi_5 \mid^2$ as a function of the phase $k\Delta l$ and for different values of l_r. 86
5.10 The ratio of the demodulated component d_1^{ph} with d_1^{dc} as a function of the phase $k\Delta l$ and for different values of l_r. 87
5.11 The quadrant photodiode configuration for the CITF. 92
5.12 The demodulated signals from Ψ_7 as a function of ϕ_{00} and for two values of θ_1. . . 93
5.13 Distribution of the difference between the true angle $\theta_0^{\rm true}$ and the reconstructed angle $\theta_0^{\rm recon}$. 96
5.14 Distribution of the difference between the true angle $\theta_1^{\rm true}$ and the reconstructed angle $\theta_1^{\rm recon}$. 97
5.15 Distribution of the difference between the true angle $\theta_2^{\rm true}$ and the reconstructed angle $\theta_2^{\rm recon}$. 98
5.16 The χ^2 distribution for the angular reconstruction procedure. 99
5.17 Block diagram for the mirror angular control. 100
5.18 The estimated torque for the mirror angular control from the reference mass. . . . 101
5.19 The estimated torque for the mirror angular control from the steering filter of the superattenuator. 102
5.20 The B transfer function relating the torque applied from the steering filter to the mirror tilt θ_x. 103
5.21 The open loop transfer function G for the mirror angular control. 104
5.22 The angle reconstruction as a function of the real angular value. 105
5.23 The angle reconstruction as a function of the real angular value and with the angular cuts shown. 106
5.24 The DC power fluctuations as the mirrors move in free motion. 107
5.25 The angular density spectrum in open/closed loop. 108
5.26 The angular displacement running RMS value. 109
5.27 The angular RMS values in closed loop and the dark fringe DC power fluctuations expressed in percent. 110

6.1 The mode-cleaner optical configuration. 113
6.2 The mode-cleaner seen as a Fabry-Perot cavity. 115
6.3 Sketch of the mode-cleaner prototype MC30. 117
6.4 The mode-cleaner MC30 block diagram. 120
6.5 The MC30 mirror suspension system and the magnet-coil system for the longitudinal control of the cavity. 121
6.6 The MC30 amplitude spectral density of the length fluctuations. 122
6.7 The MC30 running RMS of the mirror displacement amplitude spectral density. . . 123
6.8 The MC30 measured and simulated mechanical transfer function $M(s)$. 124
6.9 The calculated MC30 transmitted power and error signal. 125
6.10 The MC30 measured and simulated coil driver transfer function. 126
6.11 The corrector $G(s)$ used for the control, in the p state, of MC30[24] 128
6.12 The block diagram for the longitudinal control of MC30. 129
6.13 The open-loop transfer function for the MC30. 130
6.14 The closed-loop transfer function for the MC30. 131
6.15 The seismic noise attenuation factor for the MC30. 132

6.16 The amplitude of the MC30 closed-loop transfer function $\mid \mathcal{C}(s) \mid$ and its approximations. 134
6.17 The step response of a harmonic oscillator as a function of $\omega\, t$ and for different values of δ. 136
6.18 The step response of the closed-loop transfer function $\mathcal{C}(s)$. 137
6.19 The MC30 model used for the acquisition of lock simulation. 137
6.20 First example of lock acquisition from the simulation run of MC30 with $\mathcal{F} = 100$. . 138
6.21 First example of lock acquisition from the simulation run of MC30 with $\mathcal{F} = 100$. . 140
6.22 First example of lock acquisition from the simulation run of MC30 with $\mathcal{F} = 100$: a close-up in the region around the kick. 141
6.23 First example of lock acquisition from the simulation run of MC30 with $\mathcal{F} = 100$: a close-up in the region around the kick. 142
6.24 A close-up of the acquisition of lock region. Right: the cavity length L(t) as a function of time; center: the corresponding error signal d_2^{ph} as a function of length L; left: the corresponding DC transmitted power d_7^{dc} as a function of cavity length L. 144
6.25 The time evolution of the error signal d_2^{ph} and the transmitted DC power d_7^{dc} as the loop is closed at t= 825 s. 145
6.26 Second example of lock acquisition from the simulation run of MC30 with $\mathcal{F} = 100$. 146
6.27 A close-up in the region around the acquisition of lock. Right: the cavity length L(t) as a function of time; center: the corresponding error signal d_2^{ph} as a function of length L; left: the corresponding DC transmitted power d_7^{dc} as a function of cavity length L. 147
6.28 The calculated MC30 transmitted DC power and the error signal for the two polarization states. 148

7.1 The observed *ringing effect* on the transmitted DC power of the MC30 prototype. 151
7.2 The model used for the study of the MC30 ringing effect. 152
7.3 The calculated Fabry-Perot transmitted power as a function of cavity length ΔL as the resonance is swept at different velocities. 153
7.4 The observed ringing effect for the MC30 prototype: measurements and eye fits. . 154
7.5 The observed ringing effect for the MC30 prototype: measurements and eye fits. . 155
7.6 The calculated stored power as a function of time, with a fixed expansion rate, for different finesse values. 157
7.7 The simulated stored power of a Fabry-Perot expanding at a constant rate and the plot of the n-th derivative zero as a function of time. 159
7.8 Fit results for the mirror relative velocity reconstruction. 160
7.9 Fit results for the mirror relative velocity reconstruction. 161
7.10 Fit results for the mirror relative velocity reconstruction. 162
7.11 Fit results for the mirror relative velocity reconstruction. 163
7.12 Fit results for the mirror relative velocity reconstruction. 164

8.1 The model used for the Fabry-Perot non-linear locking scheme. 167
8.2 The simulated displacement amplitude spectral density for each mirror. 168
8.3 The simulated transmitted DC power and the Pound-Drever error signal for the VIRGO Fabry-Perot cavity. 169
8.4 The effect of the application of a single pulse to a mirror. 171
8.5 A short simulation run shows the effect of the algorithm with pulses sent to mirror M_1. 172
8.6 The train of pulses used by the non-linear locking algorithm and the resulting transmitted DC power. 173
8.7 The CITF seen as a Fabry-Perot cavity. 175
8.8 The velocities $v_{\Delta l}$ and v_{l_r} and the time distribution Δt for the CITF mirrors in free motion, as the system enters dark fringe and maximum recycling. 176
8.9 The error for the reconstruction of $v_{\Delta l}$. 178

8.10 The error for the reconstruction of $v_{\Delta l}$. 179
8.11 The error for the reconstruction of $v_{\Delta l}$ with the use of 16 bit ADCs. 180
8.12 Results from a simulation run: the plot, as a function of time, of the pulses sent to M_1, Δl and $v_{\Delta l}$. 182
8.13 Results from a simulation run: the plot, as a function of time, of the pulses sent to M_0, l_r and v_{l_r}. 183
8.14 Results from a simulation run: d_1^{dc} and d_7^{dc} as a function of time. 184

A.1 The pendulum system and its block diagram representation. 187
A.2 The block diagram of a closed-loop system. 188

List of Tables

5.1 The mirror optical characteristics for the CITF. 75
5.2 The characteristics of the laser beam. 76
5.3 The asymmetry matrix for a CITF. 91
5.4 The asymmetry matrix for a CITF configuration. 92
5.5 The asymmetry matrix for the CITF with two quadrant photodiodes monitoring each beam. 95

6.1 The prototype MC30 configuration is shown with respect to the VIRGO MC144. . 118
6.2 The poles and zeros (in rad/s) for the closed-loop transfer function $\mathcal{C}(s)$. 133

7.1 The precision of eq.(7.5) as a function of finesse, using simulation outputs instead of measurements. 156
7.2 Fit results for the mirror relative velocity reconstruction. 160

Introduction

According to Einstein's General Theory of Relativity, the acceleration of bodies creates a perturbation of the space-time metric that propagates through the universe at the speed of light. This perturbation is referred to as Gravitational Wave.

To date, this phenomenon lacks direct experimental evidence. However, Russel Hulse and Joseph Taylor were awarded the Nobel Prize in 1993 for having indirectly proven their existence[1]. Their work was based on the discovery of the binary system PSR 1913+16 and on the measurements performed by Taylor and his colleagues on the system's inward spiraling. By observing the orbital period of the system, the authors were able to estimate the energy emitted as gravitational radiation and to calculate the velocity of the inward spiral. This result was found to be in agreement with measurements within 1%.

The detection of gravitational waves is one of the most interesting problems the scientific community faces today. The possibility of such detection will open the way to a completely new astronomy that would give us a key to a better understanding of the universe. Many countries are collaborating in this challenge: Italy and France with the VIRGO project, the United States with LIGO, Japan with TAMA, and Great Britain and Germany with the GEO project.

The goal of this thesis is to make a small contribution to this search in the context of the VIRGO project, a gravitational wave antenna in the process of being built in Cascina, Italy. Before launching the final configuration of a recycled Michelson interferometer with Fabry-Perot arms, VIRGO will first operate in a test configuration, known as the Central Area Interferometer (CITF). The subject of this thesis consists of a numerical study for the global control of this interferometer. In particular, the problems of autoalignment and acquisition of lock will be addressed.

The manuscript is divided in two parts. The first is an introduction to the theory of gravitational waves and to interferometer-based detectors. The second describes the CITF, focusing on its optical response to angular and longitudinal mirror motions, thus allowing the study of signals useful for the longitudinal and angular mirror control. Based on this study, the CITF autoalignment is investigated. The problem of lock acquisition is then addressed by first examining the mode-cleaner prototype (MC30), which allowed the comparison of simulation with experiment. Finally, an algorithm for guiding the CITF into linear regime is given.

Ch.(1) introduces the reader to Einstein's field equations and their linearized form in the weak field approximation. It will be shown how gravitational waves are generated, what their properties are and what effects are induced by their passage. An order of magnitude of these effects is then given for different types of sources.

The following three chapters address the problem of detection by interferometry. In Ch.(2), the principle of the simple suspended Michelson interferometer is introduced. Its coupling to gravitational wave radiation, as well as its frequency and angular response are first discussed. Then, as the weak signals expected will be bathed by many Gaussian and non-Gaussian noises, the different noise contributions will be outlined and the concept of *signal-to-noise ratio* (SNR) is introduced. Finally, it will be shown how the detector design can be modified so as to improve the SNR due to *shot-noise*, *thermal noise* and *seismic noise*.

Ch.(3) illustrates the *Fabry-Perot* resonator, a common optical configuration which will be often referred to in this thesis. The fundamental concepts of resonator stability, resonance condition, laser beam propagation modes, and cavity modes are here presented. Its optical response to

longitudinal and angular mirror displacements serves as ground work for the response of more complicated optical systems. The chapter closes by presenting three well-known methods for cavity control: the *Pound-Drever*[44] technique for the longitudinal control and the *Anderson*[45] and *Ward*[46] techniques for angular control.

The VIRGO project is presented in Ch.(4). The optical configuration, as well as the laser system, the detection bench, the suspension system, and the vacuum system are here described. The foreseen sensitivity curve is shown as well. Finally, the chapter focuses on the *Global Control* system, in charge of supervising the phases of *lock acquisition*, *linear locking* and *autoalignment*.

The last four chapters center on VIRGO's first stage of testing, the CITF, and the main contributions of this thesis towards the understanding of the optical response of this interferometer to mirror movements and towards lock acquisition.

Ch.(5) describes the CITF, by presenting the expected mirror displacements in free motion, its sensitivity and the mirror control requirements. The chapter then presents the study carried out to understand the optical response of the CITF to longitudinal and angular motions of the mirrors. This response will be taken into account in the strategies of lock acquisition, locking and alignment. In particular, a quadrant photodiode configuration is presented and simulated in order to reconstruct the angular motions of the mirrors once the CITF is locked. The performance of a control system for the autoalignment of the CITF is then given. Also in this chapter, it will be shown how the ratio of photodiode signals can be used to detect and lock the dark fringe regardless of the recycling power buildup. This ratio of signals will be used by the lock acquisition algorithm (described in c.(8)) to guide the CITF from a non-linear state to the locked state.

The process of lock acquisition by a linear control system is described in ch.(6) by considering the mode-cleaner prototype in Orsay. First, the general purpose of mode-cleaning is given, then the prototype configuration is presented. Measurements performed on the prototype made it possible to tune the simulation of the interferometer, focusing on the acquisition of lock by a linear feedback. A rotation of the laser beam polarization state allowed a change in the finesse of MC30 from $\mathcal{F} \simeq 100$ to about $\mathcal{F} \simeq 1600$, thus allowing a comparison of the process for the two states.

Before applying a lock acquisition strategy to the CITF, ch.(7) discusses an interesting phenomenon observed on the MC30 in high finesse: the ringing effect. Its properties and behavior are studied and simulated. By fitting measurements with simulation output, an estimate of the finesse is given as well as an estimate on the relative velocity of mirrors as the optical resonance is crossed. The chapter closes by describing an empirical formula for the reconstruction of the relative mirror velocity.

Ch.(8) returns to the lock acquisition problem addressed in ch.(6), this time suggesting a strategy to guide the CITF into lock. The model used will be described and the simulation results will close the chapter.

Finally, Appendix A addresses basic notions of control systems, such as stability criteria and design specifications, necessary for an understanding of the work presented in this thesis.

Part I

Chapter 1

Gravitational Waves

One of the consequences of General Relativity is the concept of Gravitational Wave, a time-dependent perturbation of the metric, indirectly proven to exist by the experimental results of R.A. Hulse and J.H. Taylor[1]. To date, the direct observation of such phenomena has not been achieved.

This chapter briefly describes, after having outlined the Einstein field equations and their linearized form, the properties of gravitational waves within the weak field approximation. An outline of the generation mechanism and the possible astronomical sources will close the chapter.

Most of the arguments here presented originate from references [2, 3, 4, 5, 6]. The reader is addressed to references [2, 3, 4] for an introduction to the subject and to references [5, 6] for an in-depth treatment.

1.1 Einstein's Equations

The Einstein field equations relating the curvature of space with energy density are

$$R_{\mu\nu} - \frac{1}{2} g_{\mu\nu} R = \frac{8\pi G}{c^4} T_{\mu\nu} \tag{1.1}$$

where

- $g_{\mu\nu}$ is the metric tensor through which the invariant

$$ds^2 \;=\; g_{\alpha\beta}\, dx^\alpha dx^\beta \tag{1.2}$$

  is defined;

- $R_{\mu\nu}$ is the *Ricci* tensor, defined as the contraction of the *Riemann* tensor $R^\alpha{}_{\beta\mu\nu}$:

$$R_{\mu\nu} \equiv g^{\sigma\beta}\, g_{\alpha\sigma} R^\alpha{}_{\beta\mu\nu} \tag{1.3}$$

  where

$$R^\alpha{}_{\beta\mu\nu} \equiv \Gamma^\alpha{}_{\beta\nu,\mu} - \Gamma^\alpha{}_{\beta\mu,\nu} + \Gamma^\alpha{}_{\sigma\mu}\Gamma^\sigma{}_{\beta\nu} - \Gamma^\alpha{}_{\sigma\nu}\Gamma^\sigma{}_{\beta\mu} \tag{1.4}$$

  and $\Gamma^\alpha{}_{\mu\nu}$ is the *affine connection* whose relation to the metric tensor $g_{\mu\nu}$ is[1]

$$\Gamma^\alpha{}_{\mu\nu} = \frac{1}{2} g^{\alpha\beta} (g_{\beta\mu,\nu} + g_{\beta\nu,\mu} - g_{\mu\nu,\beta}) \tag{1.5}$$

[1] The notation in use for the partial derivative of an arbitrary tensor V^α is

$$V^\alpha{}_{,\beta} \equiv \frac{\partial V^\alpha}{\partial x^\beta}$$

while the *covariant derivative* of the same tensor V^α is defined as

$$V^\alpha{}_{;\beta} \equiv V^\alpha{}_{,\beta} + V^\mu \Gamma^\alpha{}_{\mu\beta}$$

- R is the *scalar curvature*, the contraction of the *Ricci* tensor:

$$R \equiv g^{\mu\nu} R_{\mu\nu} \tag{1.6}$$

- $T_{\mu\nu}$ is the *stress-energy* tensor describing, in an arbitrary reference system, the energy-momentum densities and fluxes;
- c is the speed of light;
- G is the gravitational constant.

Due to the symmetry of the *Ricci* $R_{\mu\nu}$ tensor and the $g_{\mu\nu}$ metric tensor, the gravitational field is described by ten non-linear differential equations of the second order in $g_{\mu\nu}$. These equations

1. lead, in the classical limit, to the Newtonian laws of gravitation

$$\nabla^2 \phi(x,y,z) \;=\; 4\,\pi\,G\,\rho(x,y,z) \tag{1.7}$$

   where $\phi(x,y,z)$ is the gravitational classical field and $\rho(x,y,z)$ is the mass density;

2. are covariant, i.e. independent from the choice of the reference system;
3. conserve energy and momentum, i.e.

$$T_{\mu\nu;\nu} = 0 \tag{1.8}$$

Two observations can be made from the equations' non-linearity. Unlike the electromagnetic case, solutions of eq.(1.1) do not obey the superposition principle, i.e., the linear combination of solutions is not, in general, a solution. Furthermore, the matter and momentum distributions determine the metric tensor just as the metric tensor determines the matter and momentum distributions. For this reason, these distributions cannot be assigned arbitrarily.

1.2 Weak Field Approximation

One possible solution for the metric tensor $g_{\mu\nu}$ in vacuum, i.e. $T_{\mu\nu} = 0$, is the Minkowski tensor

$$\eta_{\mu\nu} \equiv \begin{pmatrix} 1 & 0 & 0 & 0 \\ 0 & -1 & 0 & 0 \\ 0 & 0 & -1 & 0 \\ 0 & 0 & 0 & -1 \end{pmatrix} \tag{1.9}$$

In a weak gravitational field described by a metric of the form

$$g_{\mu\nu} = \eta_{\mu\nu} + h_{\mu\nu} \quad \text{with} \quad |\, h_{\mu\nu} \,| \ll 1 \tag{1.10}$$

eq.(1.1) simplifies and its solution can be treated as a perturbation of the Minkowski metric.

It can be shown that by making the substitution of eq.(1.10) in eq.(1.1), making the change of variable

$$\overline{h}_{\mu\nu} \equiv h_{\mu\nu} - \frac{1}{2}\eta_{\mu\nu} h \tag{1.11}$$

where h is the contraction of $h_{\mu\nu}$, and dropping all second order terms in $h_{\mu\nu}$, eq.(1.1) reduces to

$$\left[\overline{h}_{\mu\nu,\sigma}{}^{\sigma} + \eta_{\mu\nu}\, \overline{h}_{\sigma\gamma}{}^{,\sigma\gamma} - \overline{h}_{\mu\sigma,\nu}{}^{\sigma} - \overline{h}_{\nu\sigma,\mu}{}^{\sigma} \right] \;=\; -\frac{16\,\pi\,G}{c^4}\, T_{\mu\nu} \tag{1.12}$$

It is possible to find a reference system such that

$$\overline{h}_{\mu\nu,\nu} = 0 \tag{1.13}$$

Such a transformation, known as the *Lorentz gauge*, simplifies eq.(1.12), reducing the ten degrees of freedom of $\overline{h}_{\mu\nu}$ to six. Eq.(1.12) becomes

$$\Box \overline{h}_{\mu\nu} \;=\; -\,\frac{16\,\pi\,G}{c^{\,4}}\,T_{\mu\nu} \tag{1.14}$$

where $\Box$ is the d'Alambertian operator defined as

$$\Box \equiv \eta^{\mu\nu}\,\frac{\partial^2}{\partial x^{\mu}\,\partial x^{\nu}} \tag{1.15}$$

Eq.(1.14) is thus the weak-field approximation of eq.(1.1).

1.2.1 Wave Equation

In the absence of matter, eq.(1.14) reduces to the *propagation equation*

$$\Box \overline{h}_{\mu\nu} \;=\; 0 \tag{1.16}$$

One possible solution for the metric perturbation $\overline{h}_{\mu\nu}$, often referred to as *gravitational wave*, is a monochromatic plane wave propagating in the z-direction at the speed of light

$$\overline{h}_{\mu\nu} \;=\; A_{\mu\nu}\,e^{\,i\,\omega\,(\,t\,-\,z\,/\,c)} \tag{1.17}$$

The *Lorentz gauge* requires that

$$A_{\mu 0} \;=\; A_{\mu 3} \tag{1.18}$$

The six degrees of freedom are now reduced to two by applying a second gauge, known as *traceless and transverse* (TT), requiring that

$$\begin{aligned} A_{m0} \;&=\; 0 \\ A^{\alpha}{}_{\alpha} \;&=\; 0 \end{aligned} \tag{1.19}$$

By defining the non-null components of $A_{\mu\nu}$ as

$$\begin{aligned} h_{\times} \equiv A_{12} &= \;\; A_{21} \\ h_{+} \equiv -A_{11} &= A_{22} \end{aligned} \tag{1.20}$$

eq.(1.17) can be rewritten in the form

$$\overline{h}^{\,TT}_{\mu\nu} \;=\; \Big[\,h_{+}\,e_{+} \;+\; h_{\times}\,e_{\times}\,\Big]\,e^{\,i\,\omega\,(\,t\,-\,z\,/\,c\,)} \tag{1.21}$$

where

$$e_{+} \equiv \begin{pmatrix} 0 & 0 & 0 & 0 \\ 0 & 1 & 0 & 0 \\ 0 & 0 & -1 & 0 \\ 0 & 0 & 0 & 0 \end{pmatrix} \qquad\qquad e_{\times} \equiv \begin{pmatrix} 0 & 0 & 0 & 0 \\ 0 & 0 & 1 & 0 \\ 0 & 1 & 0 & 0 \\ 0 & 0 & 0 & 0 \end{pmatrix} \tag{1.22}$$

denote the two polarization states. A diagram, shown in fig.(1.1), shows the effect of these states on a ring of particles placed on a plane perpendicular to the direction of the incoming wave.

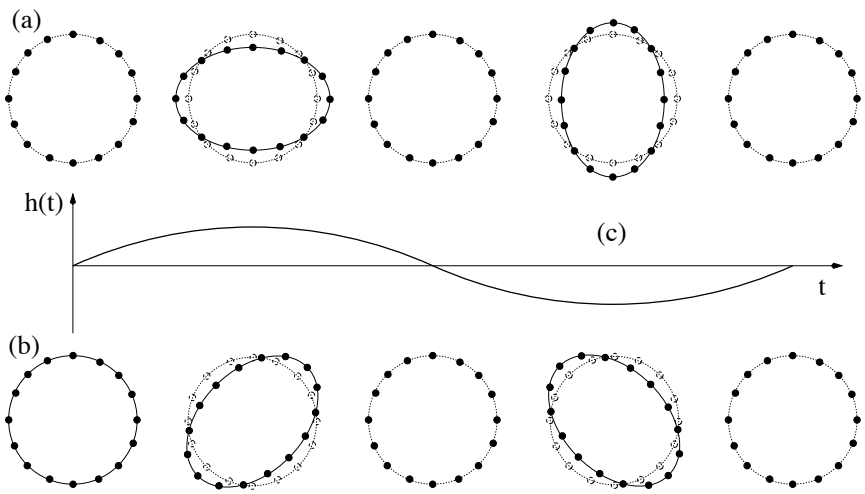

Figure 1.1: The effect of the passage of a gravitational wave on a ring of particles distributed on a plane perpendicular to the incoming radiation. (a) shows the perturbation on the ring as a function of time due to the $h_+ \neq 0$ component only, (b) the perturbation due to the $h_\times \neq 0$ component only and (c) the overall contribution h(t).

1.2.2 Geodesic Deviation

Let's describe the effect of a gravitational wave on a physical system by recalling that a *geodesic* describes the motion of a free falling particle under the influence of a gravitational field in the context of General Relativity. The equation of motion can be written as

$$\frac{du^\mu}{ds} + \Gamma^\mu_{\nu\lambda}\, u^\nu\, u^\lambda = 0 \tag{1.23}$$

where x^μ is the particle trajectory and $u^\mu \equiv dx^\mu/ds$ is the quadri-velocity.

Let's consider a pair of nearby free falling particles, following the paths $x^\mu(s)$ and $x^\mu(s)+\delta x^\mu(s)$. The *geodesic* equations for the two particles can be written as

$$\begin{aligned} 0 &= \frac{d^2 x^\mu}{ds^2} + \Gamma^\mu_{\nu\lambda}(x)\,\frac{dx^\nu}{ds}\,\frac{dx^\lambda}{ds} \\ 0 &= \frac{d^2}{ds^2}(x^\mu + \delta x^\mu) + \Gamma^\mu_{\nu\lambda}(x+\delta x)\,\frac{d}{ds}(x^\mu+\delta x^\mu)\,\frac{d}{ds}(x^\mu+\delta x^\mu) \end{aligned} \tag{1.24}$$

It can be shown that by taking the difference between these two expressions and dropping all second order terms in δx^μ, the *geodesic deviation* between the two particles follows the equation

$$\frac{D^2}{ds^2}\delta x^\lambda + R^\lambda_{\nu\mu\rho}\,\frac{dx^\nu}{ds}\,\frac{dx^\rho}{ds}\,\delta x^\mu = 0 \tag{1.25}$$

where

$$\frac{D}{ds}\delta x^\mu \equiv \frac{d}{ds}\delta x^\mu + \Gamma^\mu_{\nu\lambda}\, u^\lambda\, \delta x^\nu \tag{1.26}$$

is the *covariant derivative* along $x^\mu(s)$.

In the weak field approximation and using the TT gauge, the curvature tensor $R_{\alpha\gamma\beta\lambda}$ can be written as

$$R_{\alpha 0\beta 0} = R_{0\alpha 0\beta} = -R_{\alpha 00\beta} = -R_{0\alpha\beta 0} = -\frac{1}{2}\,\ddot{h}^{TT}_{\alpha\beta} \tag{1.27}$$

where $h^{TT}_{\alpha\beta}$ describes the evolution of the gravitational wave in the TT gauge and a dot the time derivative. Eq.(1.25) can then be approximated as

$$\frac{d^2}{dt^2}\delta x_\alpha(t) = R_{\alpha 0 \beta 0}\ \delta x^\beta(0) = -\frac{1}{2}\ \ddot{h}^{TT}_{\alpha\beta}(t)\ \delta x^\beta(0) \tag{1.28}$$

By integrating twice with respect to time, we obtain

$$\delta x_\alpha(t) = \delta x^\beta(0)\ [\delta_{\alpha\beta} + \frac{1}{2} h^{TT}_{\alpha\beta}(t)] \tag{1.29}$$

which leads to

$$\Delta x_\alpha(t)\ =\ \frac{1}{2}\, h^{TT}_{\alpha\beta}(t)\ \delta x^\beta(0) \tag{1.30}$$

where

$$\Delta x_\alpha(t)\ \equiv\ \delta x_\alpha(t)\ -\ \delta x_\alpha(0) \tag{1.31}$$

By assuming an incoming plane wave in the z-direction, as expressed in eq.(1.21), the induced change, shown in eq.(1.30), due only to the "+" component, can be written as

$$\begin{aligned} \Delta x_1(t) &= +\frac{1}{2}\left[\ h^{TT}_{+}\ e^{i\,\omega\,(\,t\,-\,z\,/\,c)}\ \right]\ \delta x^1(0) \\ \Delta x_2(t) &= -\frac{1}{2}\left[\ h^{TT}_{+}\ e^{i\,\omega\,(\,t\,-\,z\,/\,c)}\ \right]\ \delta x^2(0) \end{aligned} \tag{1.32}$$

In this case, the induced displacement is proportional to the gravitational wave amplitude and to the distance between the two particles.

1.2.3 Generation of Gravitational Waves

We have seen how a plane wave can be a solution for eq.(1.16). Let's see now what kind of sources can produce such a dynamical metric perturbation. Let's solve eq.(1.14) in an approximate way by assuming that

1. there is a sinusoidal time dependence of the *stress-energy* tensor $T_{\mu\nu}$ of the form

$$T_{\mu\nu}\ =\ S_{\mu\nu}\,(x^\alpha)\,e^{-i\,\Omega\,t} \tag{1.33}$$

   where Ω is the oscillation frequency for the source;

2. the typical velocities, in a sphere of radius ϵ, are much less than the speed of light

$$\frac{\varepsilon\Omega}{2\pi} \ll c \tag{1.34}$$

These assumptions can be justified in the following way:

- through the use of the Fourier analysis, an arbitrary function can always be rewritten as a sum of different sinusoidal contributions. Furthermore, many gravitational wave sources like binary systems and pulsars do have a periodic or quasi-periodic component;
- the second assumption facilitates calculations and is probably satisfied by most gravitational wave sources, with the exception of the strongest sources.

With these assumptions, a possible solution for eq.(1.14) can be written as

$$\overline{h}_{\mu\nu} = B_{\mu\nu}(x^\beta)e^{-i\Omega t} \tag{1.35}$$

and by substituting this solution back into eq.(1.14) we obtain

$$\left(\nabla^2 + \frac{\Omega^2}{c^2}\right)B_{\mu\nu} = -\frac{16\pi G}{c^4}S_{\mu\nu} \tag{1.36}$$

Let's distinguish two cases:

i. for the region of space outside the sphere of radius ε, eq.(1.36) reduces to

$$(\nabla^2 + \frac{\Omega^2}{c^2})B_{\mu\nu} = 0 \tag{1.37}$$

and a possible solution can be a spherical wave propagating from the origin $r = 0$:

$$B_{\mu\nu} = \frac{A_{\mu\nu}}{r} e^{i\Omega r/c} \tag{1.38}$$

where $A_{\mu\nu}$ is a constant to be determined. The gravitational wave can then be written as

$$\overline{h}_{\mu\nu} = \frac{A_{\mu\nu}}{r} e^{i\Omega(r/c-t)} \tag{1.39}$$

Notice how the amplitude of a gravitational wave decreases as the inverse of the distance.

ii. by defining

$$J_{\mu\nu} \equiv \int S_{\mu\nu} d^3x \tag{1.40}$$

it is possible to demonstrate that the relationship between the distribution of matter within the sphere of radius ε and the amplitude of the gravitational wave can be described as

$$\overline{h}_{\mu\nu} = \frac{4G}{c^4} \frac{1}{r} J_{\mu\nu} e^{i\Omega(r/c-t)} \tag{1.41}$$

Making use of the source's *quadrupole moment* tensor, defined as

$$I^{lm} \equiv \int T^{00} x^l x^m d^3x = D^{lm} e^{-i\Omega t} \tag{1.42}$$

and the property

$$\frac{d^2}{dt^2} \int T^{00} x^l x^m d^3x = 2 \int T^{lm} d^3x \tag{1.43}$$

the gravitational wave amplitude can be re-written as

$$\overline{h}_{jk} = -\frac{2G}{c^4} \frac{\Omega^2}{r} D_{jk} e^{i\Omega(r/c-t)} \tag{1.44}$$

where the *slow-motion* approximation has been used.

The TT gauge can be chosen so that the propagation is in the z-direction and eq.(1.44) transforms into

$$\begin{aligned} \overline{h}^{TT}_{zi} &= 0 \\ \overline{h}^{TT}_{xx} &= -\overline{h}^{TT}_{xy} = -\frac{G}{c^4} \frac{e^{i\Omega r}}{r} \Omega^2 (\mathcal{I}_{xx} - \mathcal{I}_{yy}) \\ \overline{h}^{TT}_{xy} &= -2\frac{G}{c^4} \frac{e^{i\Omega r}}{r} \Omega^2 \mathcal{I}_{xy} \end{aligned} \tag{1.45}$$

where

$$\mathcal{I}_{jk} = I_{jk} - \frac{1}{3}\delta_{jk} I^l_l \tag{1.46}$$

is the *reduced quadrupole moment* tensor.

Notice how the amplitude has the same time dependence as the *energy-stress* tensor. In addition, observe that the metric perturbation is generated by asymmetric motion. This can be seen from eq.(1.46). If the motion had spherical symmetry, the tensor $\mathcal{I}_{jk}$ would be proportional to δ_{jk}. However, the only tensor proportional to δ_{jk} and with null trace is the zero tensor.

1.3 Sources

Gravitational wave emission causes an energy loss by the source that can be written analytically as

$$\langle \frac{dE}{dt} \rangle = -\frac{G}{5c^5} \langle \dddot{\mathcal{I}}_{ij} \dddot{\mathcal{I}}^{ij} \rangle \tag{1.47}$$

where dE/dt is the energy variation and the mean is taken over the typical period of the source. The formula in eq.(1.47) is known as the *radiation reaction formula*. The coefficient $G/5c^5 = 5.5\ 10^{-54} m^{-2}\ kg^{-1}\ s^3$ is so low that astronomical objects are the only possible sources that we can detect.

From eq.(1.45) and eq.(1.47), it is possible to show that, for an order-of-magnitude estimate,

$$\begin{aligned} \mathcal{I} &\sim \epsilon\, M\, R^2 \\ h_+ &\sim h_\times \sim \epsilon \left(\frac{R_s}{R}\right) \left(\frac{R_s}{r}\right) \\ \Delta E &\sim \epsilon^2 \left(\frac{R_s}{R}\right)^2 \left(\frac{V}{c}\right)^6 \end{aligned} \tag{1.48}$$

where R and V are, respectively, the typical size and velocity of the source, M is its mass, $R_s \equiv 2GM/c^2$ is the *Schwarzschild radius* and ϵ is the dimensionless measure of the source asymmetry.

From the estimates in eq.(1.48), it is possible to determine the conditions for strong emission of gravitational waves :

i. the source must be extremely dense with its radius R comparable to the Schwarzschild radius R_s;

ii. the source must have a velocity V that approaches the speed of light;

iii. the source motion must be asymmetric.

As shown in eq.(1.48), the amplitude decreases as the inverse of the distance: an increase of one order of magnitude in the detector sensitivity leads to an increase of the event rate by a factor of a thousand for a uniform spatial distribution of sources.

Only astronomical objects can radiate enough energy to be detected. These anticipated gravitational wave sources can be classified into three types, depending on the radiation temporal behaviour. These are impulsive sources, such as supernovae explosions, quasi-periodic and periodic sources, such as coalescing compact binaries and spinning neutron stars, and stochastic sources.

1.3.1 Impulsive Sources

One of the most interesting and spectacular gravitational wave sources is the *supernovae explosion*. The construction of gravitational wave detectors was first motivated by the detection of such explosions. The basic process is known. Once a massive star finishes its nuclear fuel, the central core begins to collapse as the star fails to support itself from its own gravity. This results in a violent expulsion of the star's outer layer caused by the shock wave bounce, which can be 5-10 times as massive as the central core. While the electromagnetic signal is dominated by the ejected mantle, the gravitational wave signal is dominated by the dynamics of the collapsing core.

An order of magnitude estimate for the gravitational wave amplitude from a supernovae explosion can be obtained from eq.(1.48). The expected supernovae event rate of $1/(30 \div 40)$yr/galaxy [7] forces us to look out of the galaxy in order to bring the event rate up to several per year. Monitoring of the Virgo cluster, a distance of 20Mpc away from us, containing about 2500 galaxies, would increase the supernova rate to a few events per year.

Now, assuming a core mass equal to 1.4 solar masses in the Virgo cluster, collapsing to a size ten times its Schwarzschild radius, and with a value of $\varepsilon = 10^{-3}$, would lead to an amplitude value

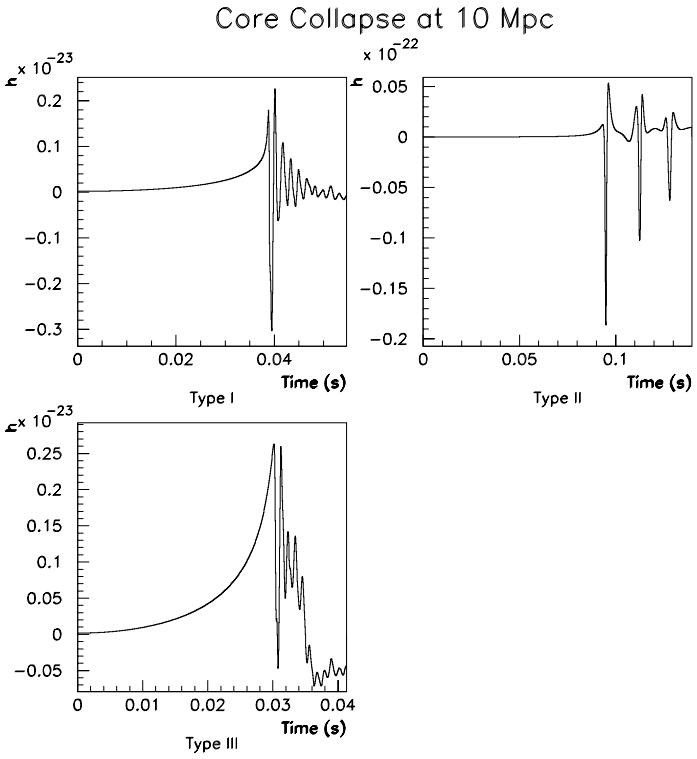

Figure 1.2: Waveform examples for core collapse[8]

of about $10^{-24} \div 10^{-23}$. Fig.(1.2) shows the results of a numerical simulation conducted in 1997 by Zwerger & Müller[8] presenting three typical waveforms we could expect.

The value of ε is uncertain. In the case of a symmetrical collapse, $\varepsilon = 0$ and no gravitational waves would be emitted. However, there are two reasons to assume a non-spherical collapse. To begin with, all stellar cores probably rotate and rotation would prevent a symmetrical collapse [7]. In addition, the presence of a companion star orbiting around the collapsing one would also generate an asymmetry[3].

Since most of the energy released in the explosion originates from gravitational binding energy, the expected wave frequency is of the order of kHz, the natural dynamical frequency of the source. Therefore, gravitational wave detectors need to be sensitive to amplitudes of the order of $10^{-24} \div 10^{-23}$ in the kHz region if a rate of several events per year is desired.

1.3.2 Coalescing Compact Binaries

The best understood gravitational wave source is the coalescing of compact binaries consisting of neutron stars (NS) and/or black holes (BH). The famous PSR 1913+16 is an example of a NS/NS binary. Its orbital period is about 8 hours, emitting gravitational wave radiation at double its orbital frequency, about 10^{-4}Hz. This frequency region is too low for ground detectors. However, due to its emission, the system loses energy and its frequency dependence increases as the stars spiral in toward each other. In about 10^8 years, the emitted signal would be observable by ground detectors. By using eq.(1.47), the time derivative of the orbital period can be calculated. The result agrees with the observed time derivative to within a percent[1].

It is possible to estimate the gravitational waveform. By assuming a circular binary orbit, neglecting the change in the eccentricity, and treating the stars as point particles (a good approximation for compact objects), it can be shown that the radiation is emitted at double its angular frequency.

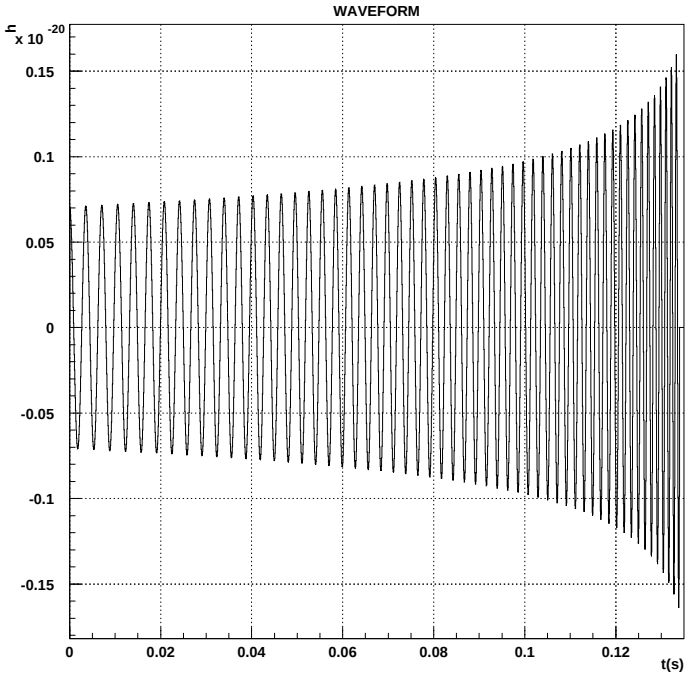

Figure 1.3: Waveform for a coalescing compact binary.

In addition, it can be shown that gravitational wave radiation is *linearly polarized* and weakly emitted in the orbital plane. Maximum emission, instead, is in the orthogonal direction to the orbital plane with *circular polarization*. This causes the emitted radiation to be *elliptically polarized* for an arbitrary direction.

Assuming masses of the order of 1.4 solar masses at a distance of 10Mpc in the 100Hz frequency range, leads to $h \sim 10^{-22} \div 10^{-21}$. Fig.(1.3) shows the expected waveform amplitude for the coalescence of such a compact binary. It is worth noting that the signal to noise ratio for such a signal can be improved by time integrating for sufficiently long periods once the waveform is known.

Even though the mechanism behind the coalescence of compact binaries is well understood, the event rate is not clear. Estimates range from $1/(10^5$ yr)[9] to $1/(10^6$yr)[10] per galaxy. In order to have a sufficiently high rate of several/yr, we may have to monitor as far as 400Mpc.

1.3.3 Spinning Neutron Stars

Another possible source of gravitational waves are rotating neutron stars, believed to be the remnants of supernovae explosions. These sources are believed to radiate gravitational waves only if there is a deviation from the symmetry around its rotational axis. Such asymmetries must be present due to an off-axis magnetic field, but their degree is unclear.

The asymmetries may come from irregularities on the crust, or from the stars' internal magnetic field. The amplitude estimate can be written as[3]

$$h_+ \sim h_\times \sim \epsilon f^2 (GMR^2/2c^4) \tag{1.49}$$

where f is the gravitational wave frequency. For a NS of radius $R = 10\ R_s$, we can write[3]

$$h_{ij}^{TT} \sim 10^{-21}\, \epsilon \left(\frac{f}{100Hz} \right)^2 \left(\frac{10kpc}{r} \right) \tag{1.50}$$

From radio astronomy we could infer the location and period of the pulsar. Gravitational wave detection would then lead to an estimate of ε.

1.3.4 Stochastic Background

This consists of a gravitational wave background noise due to, for example, a large number of distant gravitational wave sources whose signals overlap. Other contributions may come from ancient supernovae explosions, pregalactic massive stars and collapses to black holes that now would be observed as stochastic background. Also, cosmological processes such as cosmic string oscillations and inflation may contribute significantly to this background radiation.

Chapter 2

Interferometric Detectors

The aim of interferometric detectors is to observe the effect of a gravitational wave passage. The goal is to monitor the induced length change between two points as expressed in eq.(1.30) or, in simpler notation,

$$\Delta L = \frac{1}{2} h L \tag{2.1}$$

where L is the distance between them and ΔL is the induced change. Such detection is indeed ambitious: assuming $h \sim 10^{-21}$ and the monitoring of a length of the order of $L \sim 100$ m, the estimated displacement is of the order of 10^{-19}m.

In this chapter, a general overview of the Michelson interferometer, at the heart of the interferometric principle, is presented. The DC detection mechanism is outlined as well as its frequency and angular response to impinging gravitational wave radiation.

However, the gravitational wave signals to be observed will be bathed in Gaussian and non-Gaussian noise. For this reason, this chapter will list the main noise sources expected, outlining their statistical properties. It will then be shown how the implementation of Fabry-Perot arms and the presence of a recycling mirror can improve the signal-to-noise ratio (SNR) due to shot-noise.

The drawback of the DC detection scheme is its sensitivity to power fluctuations and to 1/f electronic noise, both strong at low frequencies. The last section presents the frontal modulation scheme, allowing the shift of detection to radio frequencies (RF).

2.1 The Interferometric Principle: The Michelson Interferometer

The Michelson interferometer with suspended mirrors, as shown in fig.(2.1) and fig.(2.2), is at the heart of interferometric gravitational wave detectors. It consists of three mirrors, placed in a "L"-shaped configuration: the beam splitter M_{BS} at the vertex and the two end mirrors, M_1 and M_2, a distance l_1 and l_2 away from M_{BS}. A laser source injects a beam into this system of mirrors, which is then divided in two by M_{BS}. Each beam propagates along its arm and is sent back to the beam splitter where the two beams interfere. A photodiode, placed at the interferometer output, converts photons to a signal in current.

There is a dual purpose to the mirror suspensions. As it will be shown, the suspension isolates the mirrors from seismic noise. Furthermore, the mirrors form a *free falling* reference system, behaving as free masses in the frequency range above the pendulum resonance. This can be easily seen by writing the equation of motion for a simple pendulum. Fig.(2.3) shows such a mechanical system, where $x(t)$ indicates the mass position, $x_0(t)$ the suspension point, m the mirror mass, l the suspension length and $F(t)$ any force acting on the mass. In the small angle approximation and no dissipation of energy, the equation of motion is

$$F(t) - m\,\omega_0^2\,[\,x(t) - x_0(t)\,] = m\,\ddot{x}(t) \tag{2.2}$$

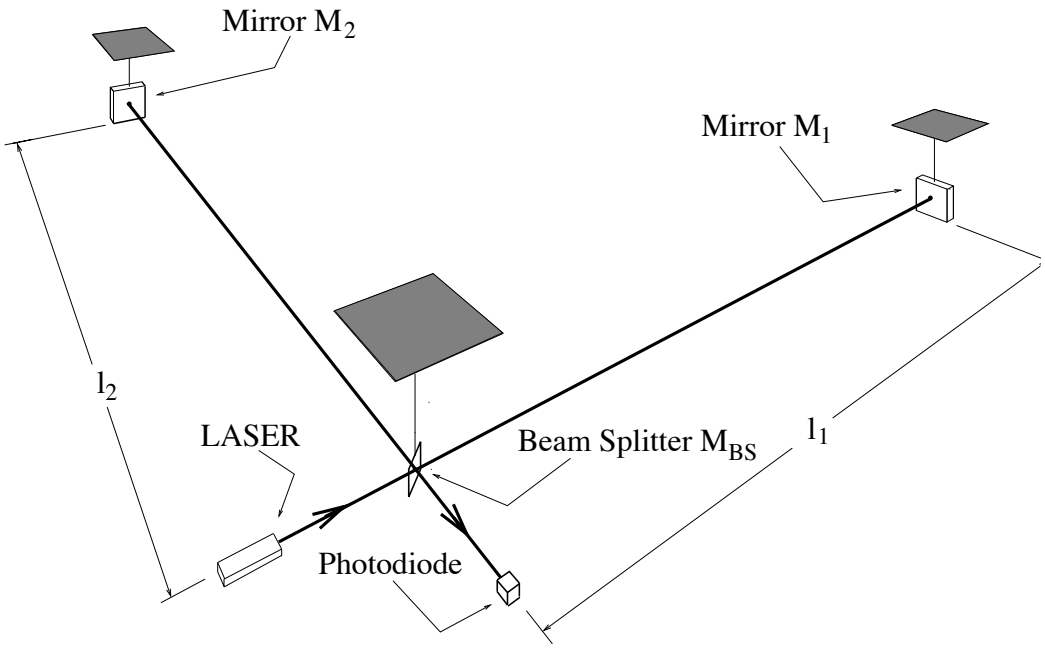

Figure 2.1: The suspended Michelson Interferometer.

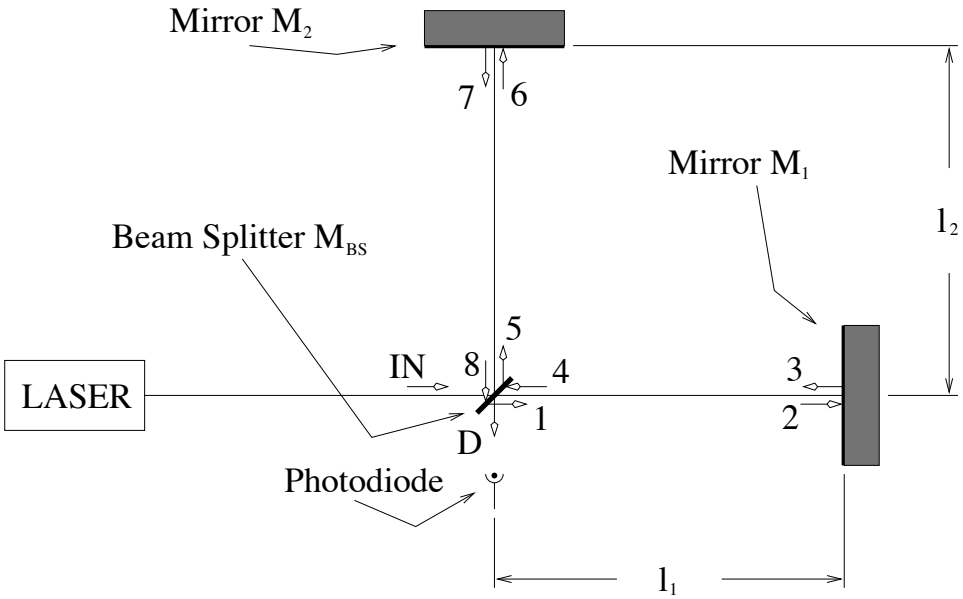

Figure 2.2: The Michelson Interferometer: notations for the electromagnetic fields.

where the time derivative is indicated by a dot and $\omega_0^2 \equiv g/l$. By Laplace transforming[1] eq.(2.2), the equation of motion expressed in the frequency domain becomes

$$x(s) = \frac{F(s)/m + \omega_0^2\, x_0(s)}{s^2 + \omega_0^2} \tag{2.3}$$

The advantage of the transformation is the introduction of the *transfer function* concept. This consists of the ratio between two polynomials in s relating an input function, such as the force $F(s)$ or the point $x_0(s)$, to an output one, in this case $x(s)$.

Assuming a fixed suspension point $x_0(s) = 0$, the transfer function $g(s)$ relating the position $x(s)$ to the force $F(s)$ is

$$g(s) \;\equiv\; \frac{x(s)}{F(s)} = \frac{1/m}{s^2 + \omega_0^2} \tag{2.4}$$

In the limit $|s| >> \omega_0$, $g(s)$ reduces to

$$g(s) \;\simeq\; \frac{1/m}{s^2} \tag{2.5}$$

corresponding to the equation of motion of a free mass. It is for this reason that for frequencies above the pendulum frequency the passage of a gravitational wave freely perturbs the system.

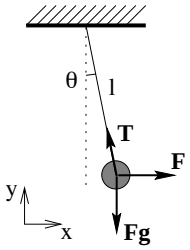

Figure 2.3: A simple pendulum: notations.

By writing the electromagnetic fields inside the optical system shown in fig.(2.2), it is possible to show how the interferometer couples to the incoming gravitational wave radiation. We will assume, unless otherwise stated, that the electromagnetic field Ψ propagates instantaneously and that it is approximated by plane waves.

The convention in use is

i. the unknown electromagnetic field at point 2, a distance l from the known field at point 1, is described as $\Psi_2 = e^{-ikl}\,\Psi_1$;

ii. the transmitted field through a mirror of transmission amplitude t is $\Psi_t = t\,\Psi_{in}$;

iii. the reflected field from a mirror of amplitude reflectivity r is $\Psi_r = i\,r\,\Psi_{in}$;

where $k = 2\pi/\lambda$, λ is the light wavelength, $r^2 + t^2 + p^2 = 1$ (p^2 is the mirror power loss) and i is the imaginary unit.

The electromagnetic fields shown in fig.(2.2) can be written as

$$\begin{aligned}
\Psi_1 &= t_{BS}\,\Psi_{in} & \Psi_5 &= i\,r_{BS}\,\Psi_{in} \\
\Psi_2 &= \exp(-i\,k\,l_1)\,\Psi_1 & \Psi_6 &= \exp(-i\,k\,l_2)\,\Psi_5 \\
\Psi_3 &= i\,r_1\,\Psi_2 & \Psi_7 &= i\,r_2\,\Psi_6 \\
\Psi_4 &= \exp(-i\,k\,l_1)\,\Psi_3 & \Psi_8 &= \exp(-i\,k\,l_2)\,\Psi_7
\end{aligned} \tag{2.6}$$

[1] defined as $F(s) \equiv \mathcal{L}[f(t)] \equiv \int_0^\infty f(t)\,e^{-s\,t}\,dt$ and $f(t) = \mathcal{L}^{-1}[F(s)] = \frac{1}{2\pi i}\int_{\sigma_0 - i\infty}^{\sigma_0 + i\infty} F(s)\,e^{s\,t}\,ds$ where f(t) is an arbitrary function of time and $s \equiv \sigma + i\omega$

where r_j and t_j are the amplitude reflectivity and transmittivity of the j-th mirror. The field seen by the photodiode is then

$$\Psi_D = i\, r_{BS}\, \Psi_4 + t_{BS}\, \Psi_8 \tag{2.7}$$

whose square modulus is

$$\begin{aligned} |\,\Psi_D\,|^2 &= |\,\Psi_{in}\,|^2\, r_{BS}^2\, t_{BS}^2\, [\, r_1^2 + r_2^2 + 2\, r_1\, r_2 \cos\phi_{mic}\,] \\ &= |\,\Psi_{in}\,|^2\, r_{BS}^2\, t_{BS}^2\, (\, r_1^2 + r_2^2\,)\, [\, 1 + C\, \cos\, \phi_{mic}\,] \end{aligned} \tag{2.8}$$

where $\phi_{mic} \equiv 2\, k\, \delta l$, $\delta l \equiv l_2 - l_1$ and C is the contrast, defined as

$$C \equiv \frac{|\,\Psi_D\,|^2_{max} - |\,\Psi_D\,|^2_{min}}{|\,\Psi_D\,|^2_{max} + |\,\Psi_D\,|^2_{min}} = \frac{2\, r_1\, r_2}{r_1^2 + r_2^2} \qquad \Rightarrow \qquad 1 - C = \frac{(\, r_1 - r_2\,)^2}{(\, r_1^2 + r_2^2\,)} \tag{2.9}$$

In the case of a non-ideal interferometer, the contrast indicates not only the degree of asymmetry in the reflectivities of the two arms, but also any optical defects of the mirrors. For an ideal interferometer with equal reflectivities, i.e. $r_1 = r_2$, the contrast is C = 1. Eq.(2.8) can be simplified by assuming a symmetric beam splitter ($r_{BS} = t_{BS} = \sqrt{1/2}$) and considering mirror reflectivities close to unity ($r_1 \simeq r_2 \simeq 1$). In this case

$$|\,\Psi_D\,|^2 = \frac{|\,\Psi_{in}\,|^2}{2}\, [\, 1 + C\, \cos\phi_{mic}\,] \tag{2.10}$$

Any change in the lengths l_1 and l_2 causes a change in the photodiode's output current. Destructive interference is possible when $\phi_{mic} = (2n+1)\pi$ or

$$\delta l = \frac{\lambda}{4}\,(\, 2\, n + 1\,) \qquad\qquad \text{n} = 0,\, 1,\, 2,\, 3,\, ... \tag{2.11}$$

where n is an integer, corresponding to a power

$$|\,\Psi_D\,|^2 = \frac{|\,\Psi_{in}\,|^2}{2}\, [\, 1 - C\,] \tag{2.12}$$

In the case of an ideal interferometer with $C = 1$, no power leaks out to the detector, reflecting all back to the laser source.

Let's study the effect on the power seen by the photodiode caused by a small length perturbation due to the passage of a gravitational wave. The "+" component h_+ of a gravitational wave irradiating in the direction perpendicular to the plane of the detector induces the following arm length change

$$\begin{aligned} l_1' &= l_1 + \frac{1}{2}\, h_+\, l_1 \\ l_2' &= l_2 - \frac{1}{2}\, h_+\, l_2 \end{aligned} \tag{2.13}$$

whose difference is

$$\delta l = l_2' - l_1' = (\, l_2 - l_1\,) - \frac{1}{2}\, h_+\, (\, l_1 + l_2\,) \tag{2.14}$$

The phase ϕ_{mic} can then be expressed as a sum of an offset term ϕ_{off} with a perturbation term ϕ_{gw}

$$\phi_{mic} = \phi_{off} + \phi_{gw} \tag{2.15}$$

where

$$\begin{aligned} \phi_{off} &= 2\,k\,(l_2 - l_1) \\ \phi_{gw} &= -k\,h_+\,(l_1 + l_2) \end{aligned} \tag{2.16}$$

The power seen by the photodiode is then

$$|\,\Psi_D\,|^2 = \frac{|\,\Psi_{in}\,|^2}{2}\,[1 + C\,\cos(\phi_{off} + \phi_{gw})] \tag{2.17}$$

Therefore, the induced phase change ϕ_{gw} results proportional to the strain h_+ and to the arm lengths being monitored. In order to amplify this phase change, the use of the longest arms possible is desired. Sec.(2.2.2) will determine ϕ_{off} by maximizing the signal-to-noise ratio due to shot-noise.

2.1.1 The Frequency Response

The frequency response of the detector to gravitational radiation is strictly connected to the laser light travel time within the arms. If, for example, the period of a gravitational wave is equal to the round trip time of light, a null effect would result on the photodiode output current.

By dropping the assumption of infinite light speed, it is possible to estimate the frequency response of such a detector. Once again let the radiation come in the z direction, perpendicular to the x-y plane of the arms. Due to the light speed invariance from the reference system along the x-arm we find

$$\begin{aligned} ds^2 = 0 &= g_{\mu\,\nu}\,dx^{\mu}\,dx^{\nu} \\ &= [\,\eta_{\mu\,\nu} + h^{TT}_{\mu\,\nu}(t)\,]\,dx^{\mu}\,dx^{\nu} \\ &= -c^2\,dt^2 + [\,1 + h_+(t)\,]\,dx^2 \end{aligned}$$

Assuming that

$$h_+(t) = h\,e^{i\,\omega\,t} \tag{2.18}$$

where $\omega = 2\,\pi\,f$ is the angular frequency of the gravitational wave and h is the gravitational wave amplitude, the time travel to the x-arm end mirror is

$$\tau^x = \int_0^{\tau^x} dt = \frac{1}{c}\int_0^{l_0} \sqrt{1 + h_+\left(\frac{x}{c}\right)}\,dx \tag{2.19}$$

which, with $h_+(x/c) \ll 1$, can be approximated as

$$\tau^x \simeq \int_0^{l_0} [\,1 + \frac{1}{2}\,h_+\left(\frac{x}{c}\right)]\,dx = \frac{l_0}{c} + \frac{1}{2\,c}\int_0^{l_0} h_+\left(\frac{x}{c}\right)dx \tag{2.20}$$

Substituting eq.(2.18), we obtain

$$\tau^x = \frac{l_0}{c} + \frac{1}{2\,c}\int_0^{l_0} h\,e^{i\,\omega\,x\,/\,c}\,dx = \frac{l_0}{c} + \frac{h}{2\,i\,\omega}\,[\,e^{i\,\omega\,l_0\,/\,c} - 1\,] \tag{2.21}$$

and the round trip time is

$$\tau_0^x = \frac{2\,l_0}{c} + \frac{h}{2\,i\,\omega}\,[\,e^{i\,\omega\,l_0\,/\,c} + 1\,]\,[\,e^{i\,\omega\,l_0\,/\,c} - 1\,] \tag{2.22}$$

The same calculation can be done on the y-arm

$$\tau_0^y = \frac{2\,l_0}{c} - \frac{h}{2\,i\,\omega}\,[\,e^{i\,\omega\,l_0\,/\,c} + 1\,]\,[\,e^{i\,\omega\,l_0\,/\,c} - 1\,] \tag{2.23}$$

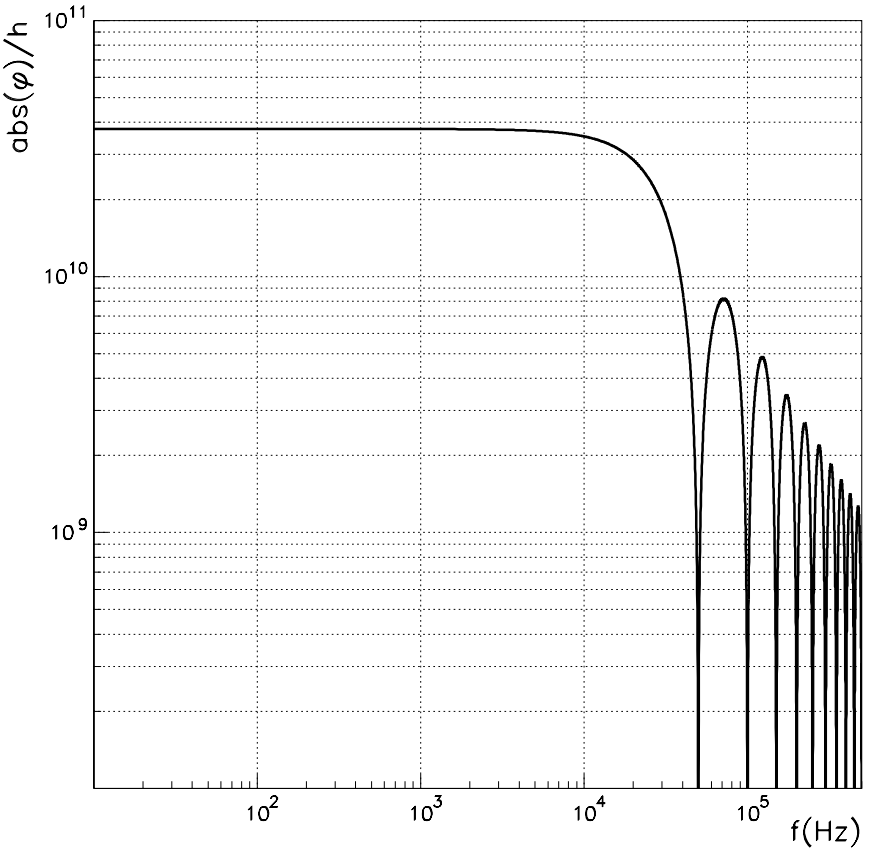

Figure 2.4: The plot of abs($\Delta\phi/h$) as a function of the radiation frequency for a Michelson interferometer with $l_0 = 3$ km and $\lambda = 1\,\mu$m. For frequencies multiple of $c\,/\,2\,l_0 = 50$ kHz, the interferometer is blind.

Notice that τ_0^x differs from τ_0^y by one sign change due to the quadrupolar nature of gravitational wave radiation. The time difference $\Delta\tau_0$ is then

$$\begin{aligned} \Delta\tau_0 &\equiv \tau_0^x - \tau_0^y = \frac{h}{i\,\omega}\,[\,e^{\,2\,i\,\omega\,l_0\,/\,c} - 1\,] \\ &= h\;\tau_0\;e^{\,i\,\omega\,l_0\,/\,c}\;\frac{sin(\,\omega\,l_0\,/\,c)}{\omega\,l_0\,/\,c} \end{aligned} \tag{2.24}$$

where $\tau_0 = 2\,l_0\,/\,c$. The phase of the output beam will be

$$\Delta\phi = \frac{2\,\pi\,c}{\lambda}\,\Delta\tau_0 \tag{2.25}$$

and its modulus is plotted, in logarithmic scale, in fig.(2.4). This figure puts into evidence two effects: a 1/f decay and the presence of frequencies under which no phase change is generated. Once a gravitational wave irradiates the detector at a frequency greater than $1/\tau_0$, the detector fails to respond optimally: within one round trip of light, the metric changes by more than one cycle. The worst case is when the frequency is a multiple of $1/\tau_0$: in this case, the gravitational wave passage has no total effect on the detector and no signal is detected.

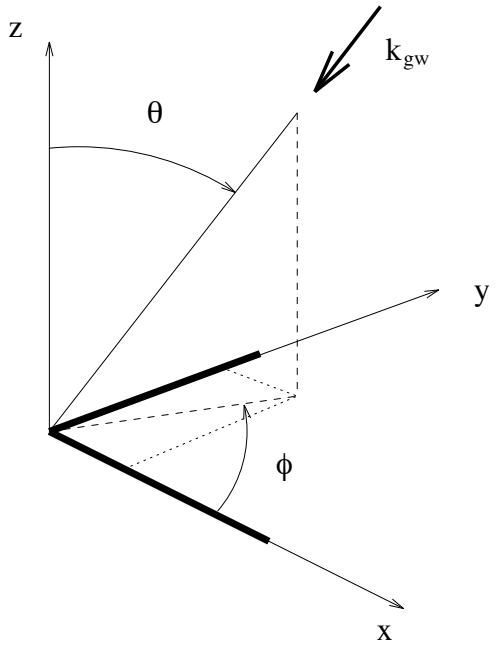

Figure 2.5: Angle notations for impinging gravitational wave radiation. The interferometer arms lie on the x and y axis.

2.1.2 The Angular Response

Let the interferometer arms lie on the $x-y$ plane and let a gravitational wave radiate in the direction θ and ϕ as shown in fig.(2.5). It can be shown[11] that the induced change Δl in the arm lengths is

$$\frac{\Delta l}{l} = F_+(\theta,\phi)\; h_+(t) + F_\times(\theta,\phi)\; h_\times(t) \tag{2.26}$$

where $h_+(t)$ and $h_\times(t)$ are the gravitational wave amplitudes in the two polarization states, whereas F_+ and $F_\times$, defined as

$$\begin{aligned} F_+ &= \frac{1}{2}(1+\cos^2\theta)\;\cos 2\phi \\ F_\times &= \cos\theta\;\sin 2\phi \end{aligned} \tag{2.27}$$

describe the antenna angular response to the radiation. Fig.(2.6) shows the plot of $F_+^2(\theta,\phi) + F_\times^2(\theta,\phi)$ as a function of the angles θ and ϕ. As can be seen in the figure, the maximum response is found along the z-axis, whereas a null response is found along the bisector of the $x-y$ axis. In the latter case, the arm length changes are the same for the two arms, resulting in a null global effect.

2.2 Noise Sources

Due to the weak gravitational wave effect, the output signal will necessarily have a non-negligible noise contribution. It is necessary, therefore, to comprehend the main sources of noise and to statistically quantify the random processes involved.

The sources can be classified as either *displacement* or *phase* noise sources. Displacement noise comes from the effective motion of the mirrors, mainly caused by

- the seismic excitation of the ground;

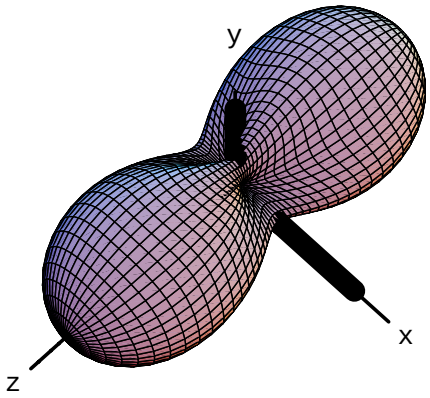

Figure 2.6: The plot of $F_+^2(\theta,\phi) + F_\times^2(\theta,\phi)$ as a function of the angles θ and ϕ. The x and y axis denote the interferometer's arms.

- the stochastic gravitational field, generated by mass density fluctuations, which couples directly to the mirrors;
- the thermal excitation of the suspension wires and optical elements;
- the radiation pressure fluctuations.

Phase noise, instead, is generated by

- the fluctuation of the index of refraction in the arm tubes;
- the amplitude and frequency fluctuation of the incoming laser beam;
- the shot-noise, the quantum mechanical limit to the counting of photons.

Once the many noise contributions are brought under control, the interferometer sensitivity will be determined by three noise sources: the photon *shot-noise*, *thermal noise* and *seismic noise*.

Before discussing these sources, the concept of *signal-to-noise ratio* (SNR), a quantitative description of the detector's sensitivity, is presented.

2.2.1 The Signal-to-Noise Ratio

The output time series $s(t)$ can be written as a sum of a deterministic signal $h(t)$, whose form could be predetermined, i.e. a gravitational wave, and a random noise contribution $n(t)$:

$$s(t) = h(t) + n(t) \tag{2.28}$$

It is often convenient to describe the deterministic signal through the *Fourier Transform Equations*

$$\begin{aligned} \tilde{h}(f) &= \mathcal{F}[h(t)] = \int_{-\infty}^{\infty} h(t)\, e^{2\pi i f t} dt \\ h(t) &= \mathcal{F}^{-1}[\tilde{h}(f)] = \int_{-\infty}^{\infty} \tilde{h}(f)\, e^{-2\pi i f t} df \end{aligned} \tag{2.29}$$

where $\mathcal{F}$ denotes the linear transformation. Such operation allows a study of the frequency components of $h(t)$.

On the other hand, the statistical properties of a random process $n(t)$ can be better characterized through the *one-sided power spectrum density* defined as

$$P_n(f) \equiv 2\, \mathcal{F}[\mathrm{corr}_{n,n}(\mathrm{t})] \qquad 0 \le f < \infty \tag{2.30}$$

where $\mathrm{corr}_{n,n}(\mathrm{t})$ is the *autocorrelation function* of $n(t)$

$$\mathrm{corr}_{n,n}(\tau) \equiv \lim_{T\to\infty} \frac{1}{T} \int_{-T/2}^{T/2} n(t)\, n(t+\tau) dt \tag{2.31}$$

The usual representation is the *one-sided amplitude spectral density*

$$\tilde{h}_n(f) \equiv \sqrt{P_n(f)} \tag{2.32}$$

where $\tilde{h}_n(f)$ is expressed in units of $1/\sqrt{Hz}$ if $n(t)$ is adimensional. The root mean square value (RMS) of $n(t)$, in the frequency band $f_1 \leq f \leq f_2$, is then

$$n_{rms} = \sqrt{\int_{f_1}^{f_2} P_n(f) df} \tag{2.33}$$

It is necessary to put the deterministic signal $\tilde{h}(f)$, expressed in units of $1/Hz$, in relation with its counterpart $\tilde{h}_n(f)$, expressed in units of $1/\sqrt{Hz}$. This is possible once the frequency band in question is known. Precisely, assuming a known waveform $h(t)$ impinging on the detector with a known noise spectrum, it is possible to show[11] that the power signal-to-noise ratio is

$$\left(\frac{S}{N}\right)^2 = \int_0^\infty \frac{4\,|\tilde{h}(f)|^2}{P_n(f)} df \tag{2.34}$$

An order-of-magnitude estimate is possible. Assuming an incoming radiation of one cycle, lasting for $\tau = 1ms$ and with a bandwidth of the order of $\Delta f \sim 1/\tau$ and with known amplitude h_0, the amplitude SNR can be estimated to be

$$\frac{S}{N} \sim \frac{h_0}{\sqrt{P_n(\Delta f)\Delta f}} \sim \frac{h_0}{\tilde{h}_n(\Delta f)}\sqrt{\tau} \tag{2.35}$$

If the signal-to-noise ratio for a known periodic signal (frequency f_0 and amplitude h_0) is in question, the bandwidth Δf is determined by the observation time $T \sim 1/\Delta f$ and

$$\frac{S}{N} \sim \frac{h_0}{\sqrt{P_n(f_0)\Delta f}} \sim \frac{h_0}{\tilde{h}_n(f_0)}\sqrt{T} \tag{2.36}$$

The estimate in eq.(2.36) shows an important property of time integration: for a periodic signal, the SNR can be improved, in principle, by a factor of $\sqrt{r}$ if the integration time is increased by a factor r.

2.2.2 Phase Noise

The fundamental limit to interferometer sensitivity is set by the photon *shot-noise* and by the *radiation pressure noise*, both caused by the inevitable fluctuations in the number of photons in the laser beam. The number N of photons detected follows the Poissonian statistics with fluctuations that go like $\sqrt{N}$.

Let's rewrite eq.(2.10) in the form

$$P \;=\; \frac{P_0}{2}\,[\,1 \,+\, C\,\cos\,\phi\,] \tag{2.37}$$

where P is the power seen by the photodetector and P_0 is the incoming laser power. The RMS power fluctuation can then be written as

$$\delta P_{shot} = \sqrt{\frac{P_0}{2}\,\frac{\hbar\,\omega}{\eta\,\Delta t}}\,\sqrt{1 \,+\, C\,\cos\phi} \tag{2.38}$$

where $\hbar$ is the reduced Plank constant, ω is the light angular frequency, Δt is the observation time interval and η is the photodiode quantum efficiency.

The presence of a gravitational wave perturbs the power P, to first order approximation, as

$$P(\phi + \delta\phi_{gw}) \simeq P(\phi) + \frac{dP}{d\phi}\,\delta\phi_{gw} = P(\phi) + \delta P_{gw} \tag{2.39}$$

where δP_{gw} denotes the induced power change and $\delta\phi_{gw}$ the phase perturbation.

By taking the ratio between δP_{gw} and δP_{shot}, the SNR is found to be

$$\left|\frac{S}{N}\right| = \left|\frac{\delta P_{gw}}{\delta P_{shot}}\right| = \sqrt{\frac{P_0}{2}\,\frac{\eta\,\Delta t}{\hbar\,\omega}}\;\frac{C\,\sin\phi}{\sqrt{1 + C\,\cos\phi}}\,\delta\phi_{gw} \tag{2.40}$$

We would like to see under what conditions the SNR is maximal. Let's first neglect any contrast defect ($C = 1$) and treat an ideal interferometer. In this case, the SNR is maximal in condition of dark fringe, i.e. $\cos\phi = -1$, corresponding to a minimum detectable dephasing of

$$\delta\phi_{shot} = \sqrt{\frac{\hbar\,\omega}{\eta\,P_0\,\Delta t}} \tag{2.41}$$

On the other hand, considering an interferometer with $C < 1$, the SNR is maximum at

$$\cos\phi = -1 + \sqrt{2\,(1 - C)} \tag{2.42}$$

or, in other words, slightly detuned from destructive interference.

Eq.(2.41) can be rewritten as a spectral density

$$\delta\tilde{\phi}_{shot} = \sqrt{\frac{\hbar\,\omega}{\eta\,P_0}} \qquad [1/\sqrt{Hz}] \tag{2.43}$$

resulting in the equivalent amplitude shot-noise spectral density limit of

$$\tilde{h}_{shot} = \frac{1}{2\,k\,l_0}\sqrt{\frac{\hbar\omega}{\eta\,P_0}} \qquad [1/\sqrt{Hz}] \tag{2.44}$$

This limit can only be lowered by increasing the product $l_0\sqrt{P_0}$. Assuming a laser power of $P_0 = 20$ W with interferometer arms of length $l_0 = 3000$ m and $\eta = 1$, the shot-noise limit is

$$\tilde{h}_{shot} \sim 10^{-21} \qquad [1/\sqrt{Hz}] \tag{2.45}$$

This sensitivity needs to be improved by at least two orders of magnitude if any supernovae events are to be detected in the kHz region.

2.2.3 Displacement Noise

At the very low end of the frequency spectrum, the sensitivity of the detector is limited by seismic activity. Measurements conducted around the world have shown that ground movement is isotropic, exhibiting a $1/f^2$ behavior above $1\,Hz$. In particular, for the VIRGO site in Cascina (Pisa, Italy), measurements[23] have shown that the displacement spectral density can be described by the empirical formula

$$\tilde{x}_{seism}(f) \sim \frac{a}{f^2}\,\frac{f^2 + f_0^2}{f^2 + f_1^2} \qquad [m/\sqrt{Hz}] \tag{2.46}$$

where $f_0 \sim 0.1\,Hz$, $f_1 \sim 0.5\,Hz$ and the amplitude a varies from a pessimistic value of 10^{-6} to an optimistic one of 10^{-7}.

Particular attention is necessary when considering the differential movement of two points on the ground. Depending on the frequency range of observation, the motion of the two points may be correlated. Assuming seismic vibrations that propagate in the ground at a speed $v_s \sim 500\, m/s$ with wavelength λ_s, the motion of the points is correlated if

$$l_0 << \lambda_s \tag{2.47}$$

where l_0 is the distance between the two points. In other words, for frequencies f such that

$$f << \frac{v_s}{l_0} \tag{2.48}$$

the motion of the two points may be considered as correlated. For points a distance $l_0 = 3$ km apart, the motion is correlated for $f << 0.17$ Hz.

Therefore, by assuming uncorrelated ground vibrations, the noise amplitude contributions of each mass can be quadratically summed. The equivalent amplitude spectral density, above f_1, can then be written in the form

$$\tilde{h}_{seism}(f) = \frac{2\sqrt{2}}{l_0}\, \tilde{x}_{seism}(f) \sim \frac{10^{-9}}{f^2} \qquad [1/\sqrt{Hz}] \tag{2.49}$$

and an attenuation of more than ten orders of magnitude is necessary in order to detect any events at 10Hz. One way to decrease the limit is to increase the length l_0 being monitored regardless of the optical configuration. This is true for any displacement source.

Another important source of displacement noise is thermal, arising from any motion induced by a macroscopic system being in thermal equilibrium with its environment. For the mechanical system in question, it is important to identify the normal modes and to assign an energy $E = \frac{1}{2} k\, T$ to each mode, where k is Boltzman's constant and T is the temperature of the system.

The normal modes can be classified in two: the suspension modes and the internal vibrational modes. These modes couple to the interferometer in different ways. The internal vibrational modes treat the mirror as an elastic body with an unmoving center of mass. The suspension modes treat the mirror as a solid body and consist of pendulum, violin and vertical modes.

The thermal noise present in any macroscopic system with dissipation can be found using the *fluctuation-dissipation theorem*. By considering a simple resonator, with resonant frequency $f_0 = \omega_0/2\pi$, temperature T, mass m, quality factor Q and using the internal damping model[20], the power spectral density displacement can be expressed as

$$|\, \tilde{x}_{therm}(\omega)\, |^2 = \frac{4\, k\, T}{m\, Q\, \omega}\, \frac{\omega_0^2}{(\omega_0^2 - \omega^2)^2 + \omega_0^4 / Q^2} \qquad [m^2/Hz] \tag{2.50}$$

The frequency dependence of the noise spectrum can then be classified in the following way:

$$|\, \tilde{x}_{therm}(\omega)\, | = \sqrt{\frac{4\, k\, T}{m}} \begin{cases} 1 / (\omega_0 \sqrt{Q\, \omega}) & \text{for } \omega << \omega_0 \\ \sqrt{Q} / \omega_0^{3/2} & \text{for } \omega = \omega_0 \\ \omega_0 / (\omega^{5/2} \sqrt{Q}) & \text{for } \omega >> \omega_0 \end{cases} \tag{2.51}$$

Let's first consider the pendulum mode. Its resonance frequency f_0 is below the detection band of the detector, and the resulting spectral density displacement is inversely proportional to $f^{5/2}\sqrt{Q\, m}$. A large mirror mass m is therefore desired, as well as a high quality factor Q. The motion due to this mode becomes negligible at high frequencies but plays a central role in the low to intermediate frequencies. Fig(2.7) shows the pendulum contribution to thermal noise in the case of a mirror mass m = 40 Kg, quality factor Q = 100, mode of energy $4\, k\, T = 1.66 \times 10^{-20} J$ and a resonance frequency $f_0 = 0.6$ Hz. In this case, the equivalent amplitude spectral density is

$$\tilde{h}_{ther} \sim 10^{-19} \qquad [1/\sqrt{Hz}] \ @\ 10 \text{ Hz} \tag{2.52}$$

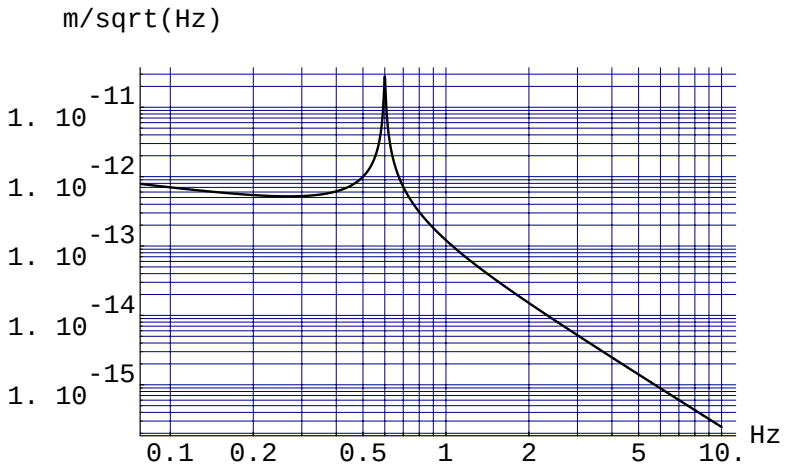

Figure 2.7: The pendulum mode contribution to thermal noise: the amplitude spectral density of the mass displacement as a function of frequency. The parameters used are: quality factor Q = 100, mode of energy $4\,k\,T = 1.66 \times 10^{-20} J$, mass m = 40 Kg and resonance frequency $f_0 = 0.6$ Hz.

In order to be sensitive to sources such as coalescing compact binaries, the thermal noise limit here shown must be improved by at least two orders of magnitude.

The internal vibrational modes, instead, have resonant frequencies in the kHz region. In this case, the motion due to this mode is inversely proportional to $\sqrt{Q\,f\,m}$ and the mirror design has to carefully chose the product $\sqrt{Q\,m}$.

2.3 Detector Design Improvements

It has been shown in the previous three sections how seismic, thermal and shot-noise limit the sensitivity of the Michelson interferometer. For thermal noise, in particular, it was shown how materials with high quality factors are desired. Also, the design of a suspension system for the mirrors and a modification of the interferometer itself is necessary if an improvement of the SNR due to seismic and shot-noise is desired.

2.3.1 The Suspension System

As already seen, the limit $\tilde{h}_{seism}$ can be lowered by increasing the length l_0 being monitored. Another way to lower the limit is to suspend each mirror from a pendulum. By setting $F(s) = 0$ in eq.(2.3), the transfer function relating the motion of the mass $x(s)$ to the motion of the suspension point $x_0(s)$ is

$$\frac{x(s)}{x_0(s)} = \frac{\omega_0^{\,2}}{s^{\,2} + \omega_0^{\,2}} \tag{2.53}$$

which, in the limit $|s| >> |\omega_0|$, reduces to

$$\frac{x(s)}{x_0(s)} \simeq \frac{\omega_0^{\,2}}{s^{\,2}} \tag{2.54}$$

attenuating, by a factor $1/f^2$, the seismic motion. Particular attention is then made to the design of a pendulum with the lowest resonant frequency possible.

The attenuation factor of a mirror suspended from a pendulum can be improved if the mirror is suspended from a chain of pendula. For an ideal chain of M pendula (a real suspension system will be presented in sec.(4.4)), the transfer function is

$$\frac{x(s)}{x_0(s)} = \prod_{n=1}^{M} \frac{\omega_n^2}{s^2 + \omega_n^2} \tag{2.55}$$

where ω_n denotes the resonance of the n-th pendulum, resulting in an attenuation of

$$\frac{x(s)}{x_0(s)} \sim \frac{1}{s^{2M}} \tag{2.56}$$

for $|s| >> |\omega_M|$. The use of a chain of six filters would then attenuate by a factor of twelve orders of magnitude at 10 Hz. Ideally, a suspension system with as many harmonic oscillators as possible and with the lowest resonant frequencies is desired.

2.3.2 The Michelson Interferometer with Fabry-Perot Arms

In the previous section, it was shown how the use of a chain of harmonic oscillators attenuates and shifts the ground vibrations into lower frequencies. This section and the following describe how an improvement of the SNR due to shot-noise is possible by modifying the optical configuration of the interferometer.

One way to increase the optical path of light, without increasing the dimensions of the interferometer itself, is to use Fabry-Perot cavities (see Ch.3) in the place of the end mirrors, as shown

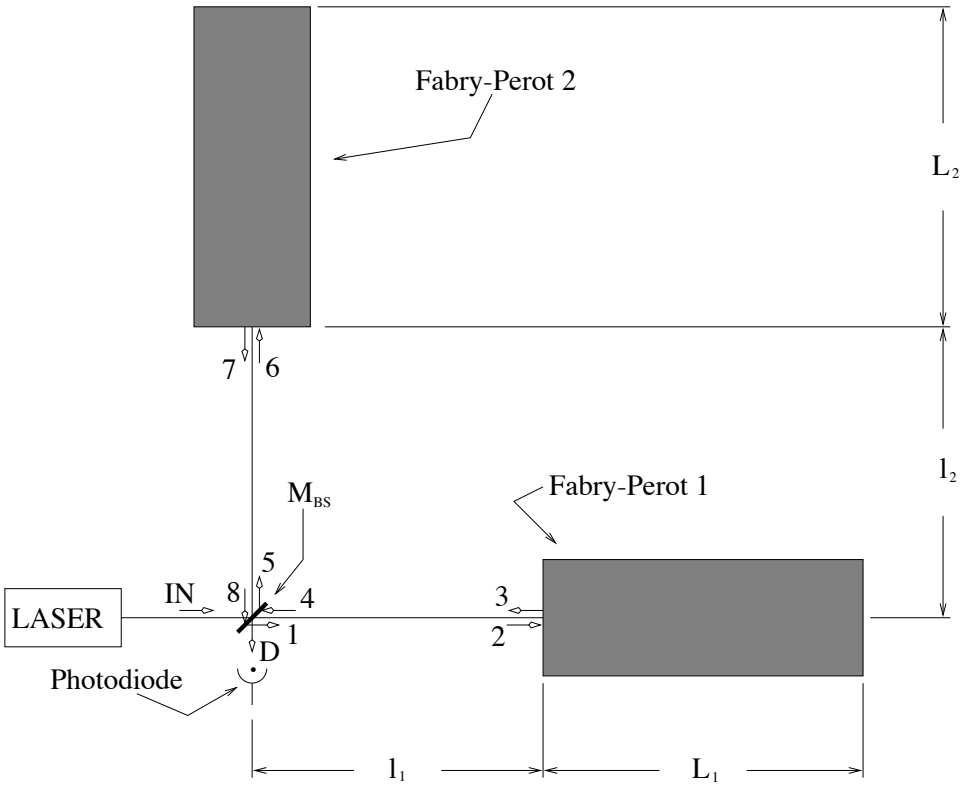

Figure 2.8: The Michelson Interferometer with Fabry-Perot arms.

in fig.(2.8). The electromagnetic field equations are now

$$\begin{aligned} \Psi_1 &= t_{BS}\,\Psi_{IN} & \Psi_5 &= i\,r_{BS}\,\Psi_{IN} \\ \Psi_2 &= \exp(-i\,k\,l_1)\,\Psi_1 & \Psi_6 &= \exp(-i\,k\,l_2)\,\Psi_5 \\ \Psi_3 &= \mathcal{A}_{R1}\,\Psi_2 & \Psi_7 &= \mathcal{A}_{R2}\,\Psi_6 \\ \Psi_4 &= \exp(-i\,k\,l_1)\,\Psi_3 & \Psi_8 &= \exp(-i\,k\,l_2)\,\Psi_7 \end{aligned} \tag{2.57}$$

where $\mathcal{A}_{Ri}$ is the complex reflectivity of the i-th Fabry-Perot

$$\mathcal{A}_{Ri} = A_{Ri}\,\exp(i\,\phi_{Ri}) \tag{2.58}$$

The power seen by the photodiode is found to be

$$|\,\Psi_D\,|^2 = r_{BS}^2\,t_{BS}^2\;|\,\Psi_{IN}\,|^2\left[A_{R1}^2 + A_{R2}^2 + 2\,A_{R1}\,A_{R2}\,\cos[(\phi_{R2} - \phi_{R1}) + \phi_{mic}]\right] \tag{2.59}$$

which can be written in the form

$$|\,\Psi_D\,|^2 = \frac{|\,\Psi_{IN}\,|^2}{2}\left[1 + C\,\cos[(\phi_{R2} - \phi_{R1}) + \phi_{mic}]\right] \tag{2.60}$$

where C is the contrast, $A_{R1} \simeq A_{R2} \simeq 1$ and $r_{BS} = t_{BS} = \sqrt{1/2}$. The expression in eq.(2.60) does not change from eq.(2.8).

By taking $L_{1,2} \gg l_{1,2}$, the induced length change caused by the passage of a gravitational wave is greater in the Fabry-Perot arms. For this reason, ϕ_{mic} can be neglected and the advantage in using such arm cavities appears evident in the phase $(\phi_{R2} - \phi_{R1})$ (refer to sec.(3.3.1)). By neglecting mirror losses, it can be shown that a small length perturbation δL around the operating point L_{res} (cavity length L corresponding to maximum stored power) generates, to first approximation, the change $\Delta\phi_R$

$$\phi_R(L_{res} + \delta L) \simeq \phi_R(L_{res}) + \Delta\phi_R \tag{2.61}$$

with

$$\Delta\phi_R \equiv \left.\frac{d\,\phi_R}{d\,L}\right|_{L_{res}} \delta L = -2\,k\left(\frac{2\,\mathcal{F}}{\pi}\right)\delta L \tag{2.62}$$

where $\mathcal{F}$ denotes the finesse, to be defined in eq.(3.22), assumed to be the same for both cavities.

A gravitational wave perturbation, just as in eq.(2.13), of the form

$$L_1 = L_0 + \delta L_1 = L_0 + \frac{1}{2}\,h_+\,L_0 \tag{2.63}$$

$$L_2 = L_0 - \delta L_2 = L_0 - \frac{1}{2}\,h_+\,L_0 \tag{2.64}$$

would generate the following phase change

$$\begin{aligned} \phi_{R2} - \phi_{R1} &\simeq \Delta\phi_{R2} - \Delta\phi_{R1} = \\ &= -2\,k\left(\frac{2\,\mathcal{F}}{\pi}\right)(\delta L_2 - \delta L_1) = 2\,k\left(\frac{2\,\mathcal{F}}{\pi}\right)h_+\,L_0 \end{aligned} \tag{2.65}$$

The phase $(\phi_{R2} - \phi_{R1})$ in eq.(2.60) needs to be compared to ϕ_{mic} shown in eq.(2.10). The distance L_0 being monitored results amplified by a factor $G = 2\,\mathcal{F}/\pi$ (known as the cavity power gain) as if monitoring an effective length $L_{eff} = G\,L_0$.

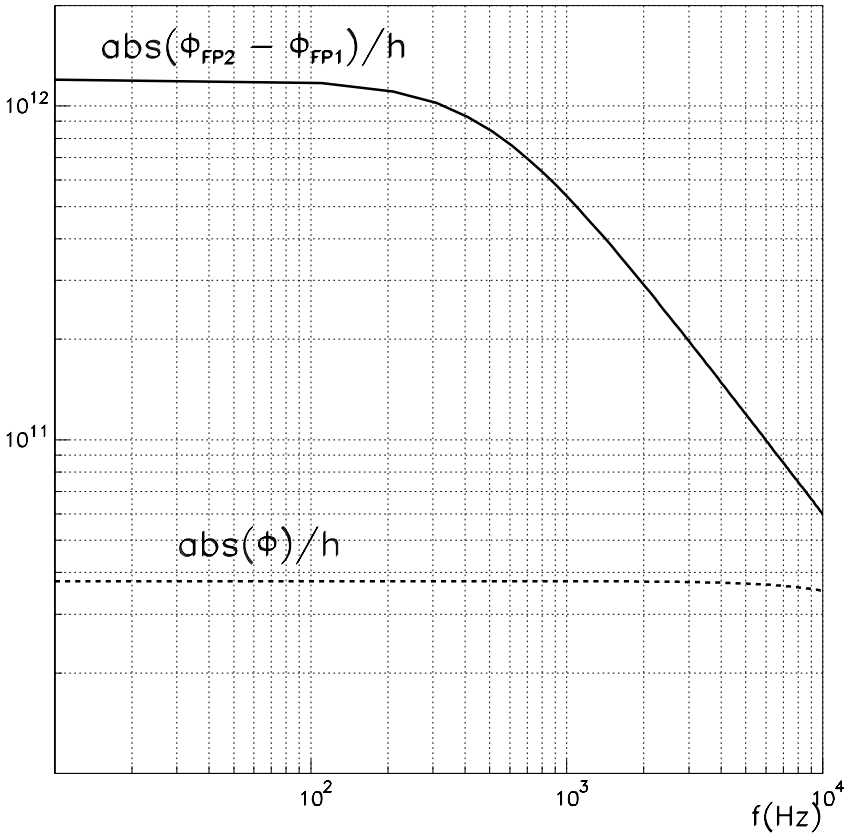

Figure 2.9: The plot of abs($\phi_{R2} - \phi_{R1}$)/h for a Michelson interferometer with Fabry-Perot arms of length $L_0 = 3$ km and finesse $\mathcal{F} = 50$ (continuous line) and the plot of abs($\Delta\phi_{mic}/h$) relative to a simple Michelson interferometer with arms of $l_0 = 3$ km (dotted line).

Eq.(2.65) is not exact because it does not take into account the travel time of photons, as shown in sec.(2.1.1). By dropping the assumption of infinite light speed, it is possible to show that the frequency response of the arms[13] to gravitational waves can be better approximated by

$$| \phi_{R2} - \phi_{R1} | = 2\,k \left(\frac{2\,\mathcal{F}}{\pi}\right) h\,L_0 \frac{1}{\sqrt{1 + \left[\omega_{gw}\,/\omega_{cav}\right]^2}} \tag{2.66}$$

where ω_{gw} is the gravitational wave angular frequency, $\omega_{cav} \equiv 1/\,\tau G$ is defined as the cavity pole and $\tau \equiv L_0\,/\,c$ is the light travel time from one mirror to the other. For VIRGO, the cavity pole is located at $\omega_{cav}/2\pi = 500$ Hz.

The plot of eq.(2.66) is shown in fig.(2.9), as well as eq.(2.25) for comparison. Even though the sensitivity for the Michelson with Fabry-Perot arms degrades for frequencies above the cavity pole, it is amplified by a factor $2\mathcal{F}/\pi$ with respect to the simple Michelson configuration.

The inevitable storage time difference between the two arms, caused by either a difference in finesse of the cavities or by a length difference in the arms, makes the output of the detector sensitive to frequency fluctuations. The sensitivity goal sets the requirements on the frequency fluctuation of the laser source, achieved by making use of several control systems in cascade.

However, the last control is performed by using the interferometer itself as a reference for the laser source. Due to the sophisticated suspension system, the interferometer is highly stable at high frequency. For an in-depth treatment, see [24].

2.3.3 The Recycled Michelson with Fabry-Perot Arms

In the previous section, it was shown how the gravitational wave signal can be amplified by replacing the terminal mirrors of the Michelson interferometer with Fabry-Perot cavities. This section introduces a recycling concept in order to improve the signal-to-noise ratio due to the photon *shot-noise*.

As the interferometer is operated in condition of dark fringe, most of the light is reflected back to the laser source. Adding a mirror right after the laser source, as shown in fig.(2.10), recycles the electromagnetic beam coming from both arms, inducing a power build up. Analytically, this can be written as

$$| \Psi_D |^2 = | \Psi_0 |^2 \ \cos^2 (\phi_{mic} / 2) \tag{2.67}$$

with

$$| \Psi_0 |^2 = \frac{t_0^2 \, | \Psi_{IN} |^2}{1 + r_0^2 \, \sin^2 (\phi_{mic} / 2) + 2 \, r_0 \cos (2 \, k \, l_r) \sin (\phi_{mic} / 2)} \tag{2.68}$$

where

$$l_r \equiv l_0 + \frac{1}{2} (l_1 + l_2) \tag{2.69}$$

while neglecting both the contrast defect and losses and assuming both Fabry-Perots in resonance, i.e. $A_R \simeq 1$, $\phi_R = \pi/2$ (see sec.3.3). In condition of destructive interference at the output photodiode, the power $| \Psi_0 |^2$ within the recycling cavity can be written as

$$| \Psi_0 |^2 = \frac{t_0^2}{(1 - r_0)^2} \, | \Psi_{IN} |^2 = G_{rec} \, | \Psi_{IN} |^2 \tag{2.70}$$

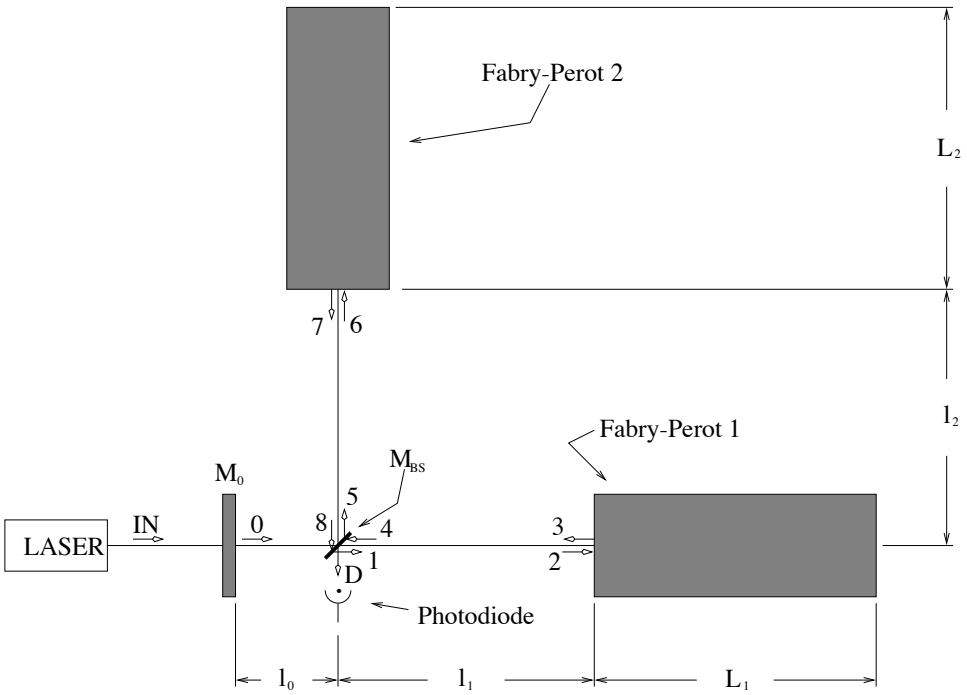

Figure 2.10: The Recycled Michelson Interferometer with Fabry-Perot arms.

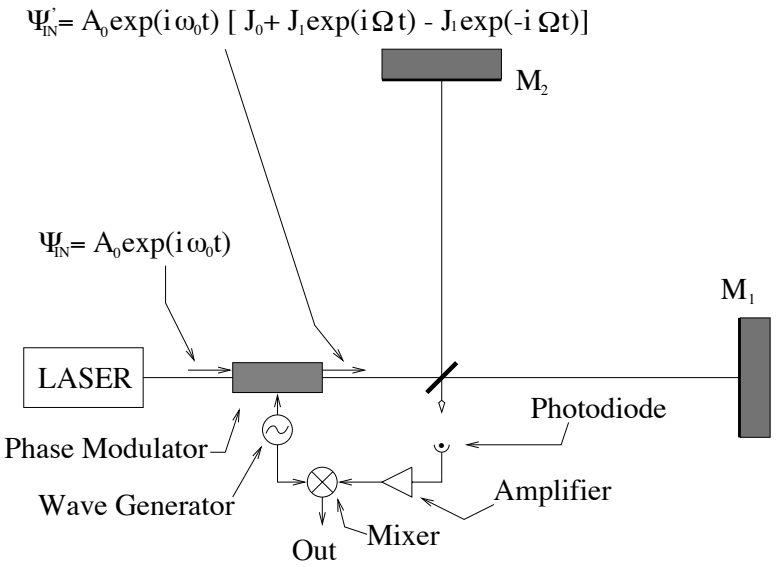

Figure 2.11: The Michelson interferometer in the frontal modulation scheme.

where G_{rec} is the power gain for the recycling cavity.

It can be shown[13] that there exists an optimal value r_0 for the reflectivity of the recycling mirror that maximizes the stored power. For this value

$$| \Psi_0 |^2 = \frac{1}{p_0^2 + p_{itf}^2} | \Psi_{IN} |^2 \tag{2.71}$$

where p_0^2 and p_{itf}^2 denote the power losses of the recycling mirror and of the interferometer respectively. In order to maximize the recycling gain, it is therefore necessary to limit the mirror losses as well as the interferometer losses.

2.4 The Frontal Modulation Scheme

A problem arises once the contrast $C < 1$. In sec.(2.2.2), it was shown how, when $C < 1$, the SNR is maximized when the interferometer is operated slightly detuned from destructive interference. As a consequence, the photodiode is sensitive to any power fluctuations of the laser source. In order to be shot-noise limited, the relative power fluctuations $\Delta P/P$ must satisfy the condition

$$\frac{\Delta P}{P} < \sqrt{\frac{\hbar\,\omega}{\eta\,P_C}} \tag{2.72}$$

where $P_C = (P_0/2)\sqrt{2\,(1-C)}$ is the power corresponding to maximal SNR with $1 - C = 10^{-4}$, $P_0 = 500$ W and $\eta = 1$. This leads to a requirement of $\Delta P/P \leq 10^{-10}/\sqrt{Hz}$. This condition is too demanding for the low frequency region due to laser amplitude noise and $1/f$ electronic noise. However, by implementing a modulation-demodulation scheme, it is possible to shift the detection from DC to the RF band ($> MHz$).

Many alternative detection schemes have been investigated, such as the internal, external and frontal modulation schemes[17]. All of them consist of phase modulation of the laser beam at different positions in the interferometer. One of them, the frontal modulation scheme, deserves particular attention. It consists of phase modulating the laser beam at the input of the interferometer and coherently de-modulating the output signal.

Let's consider the simple Michelson interferometer shown in fig.(2.11). The phase modulator consists of an electro-optical element that introduces two lateral frequency sidebands to the carrier.

It is made of a crystal whose index of refraction changes according to an applied voltage. If the incoming electromagnetic field Ψ_{IN} is described by

$$\Psi_{IN} = A_0\, e^{i\,\omega_0\,t} \tag{2.73}$$

where ω_0 is the angular frequency of the laser beam and A_0 its amplitude and if the applied voltage to the modulator is of the form

$$V = V_0\, e^{i\,\Omega\,t} \tag{2.74}$$

then the electromagnetic field after the modulator can be expressed as

$$\Psi'_{IN} = A_0\, e^{i\,(\omega_0\,t\,+\,m\,\sin\Omega\,t)} = A_0 \sum_{n=-\infty}^{\infty} J_n(m)\; e^{i\,(\omega_0\,+\,n\,\Omega)\,t} \tag{2.75}$$

where m is the modulation index and $J_n(m)$ are the Bessel functions. For values of $m << 1$, eq.(2.75) can be approximated by keeping the first three terms of the sum

$$\Psi'_{IN} \simeq A_0\,[\,J_0(m)\,e^{i\,\omega_0\,t} + J_1(m)\,e^{i\,(\omega_0\,+\,\Omega)\,t} + J_{-1}(m)\,e^{i\,(\omega_0\,-\,\Omega)\,t}] \tag{2.76}$$

Assuming $A_0 = 1$ and making use of the property

$$J_n \;=\; (-1)^n\,J_n \tag{2.77}$$

the electromagnetic field entering the interferometer can be written as

$$\Psi'_{IN} \simeq\; J_0(m)\,e^{i\,\omega_0\,t} + J_1(m)\,e^{i\,(\omega_0\,+\,\Omega)\,t} - J_1(m)\,e^{i\,(\omega_0\,-\,\Omega)\,t} \tag{2.78}$$

By propagating Ψ'_{IN} just as in sec.(2.1), the electromagnetic field Ψ_D seen by the output photodiode can be written as

$$\Psi_D = \Psi_0 + \Psi_+ e^{i\,\Omega\,t} + \Psi_- e^{-\,i\,\Omega\,t} \tag{2.79}$$

where

$$\begin{aligned}
\Psi_0 &= -J_0\left[\,\exp[+i\,\omega_0\,\delta l\,/\,c] + \exp[-i\,\omega_0\,\delta l\,/\,c]\,\right] \qquad (2.80)\\
\Psi_+ &= -J_1\left[\,\exp[+i\,(\omega_0\,+\,\Omega)\,\delta l\,/\,c] + \exp[-i\,(\omega_0\,+\,\Omega)\delta l\,/\,c]\,\right]\times\\
&\qquad\qquad\qquad\qquad\qquad\qquad\qquad\qquad\times\exp[+i\,\Omega\,(\,l_1\,+\,l_2\,)\,/\,c]\\
\Psi_- &= +J_1\left[\,\exp[-i\,(\omega_0\,-\,\Omega)\,\delta l\,/\,c] + \exp[-i\,(\omega_0\,-\,\Omega)\,\delta l\,/\,c]\,\right]\times\\
&\qquad\qquad\qquad\qquad\qquad\qquad\qquad\qquad\times\exp[-i\,\Omega\,(\,l_1\,+\,l_2\,)\,/\,c]
\end{aligned}$$

and for simplicity $\delta l \equiv l_2 - l_1$, $r_{BS} = t_{BS} = 1/\sqrt{2}$, $r_1 = r_2 = 1$, $J_i(m) = J_i$ and a global phase $\exp(i\omega_0(l_1+l_2)/c)$ has been neglected.

The power seen by the photodiode is then

$$\begin{aligned}
|\,\Psi_D\,|^2 \;=\;& |\,\Psi_0\,|^2 + |\,\Psi_-\,|^2 + |\,\Psi_+\,|^2 + \qquad (2.81)\\
&+\left[\,\Psi_+\,\Psi_0^* + \Psi_0\,\Psi_-^*\,\right]\exp[\,i\,\Omega\,t\,] \;+\; \left[\,\Psi_-\,\Psi_0^* + \Psi_0\,\Psi_+^*\,\right]\exp[\,-\,i\,\Omega\,t\,] +\\
&+\left[\,\Psi_+\,\Psi_-^*\,\right]\,\exp[\,2\,i\,\Omega\,t\,] \;+\; \left[\,\Psi_+^*\,\Psi_-\,\right]\,\exp[\,-\,2\,i\,\Omega\,t\,]
\end{aligned}$$

and contains a lot of information. It consists of a DC component made up of the square modulus of each frequency component and of modulated components at Ω and $2\,\Omega$. The Ω component is generated by the beating of the carrier with the sidebands and contains crucial information on

the status of the interferometer, while the $2\,\Omega$ component consists of the beating between the sidebands.

By defining

$$\delta l \equiv \Delta l + \delta l_{gw} \tag{2.82}$$

where $\Delta l \equiv n\,\lambda$, $n >> 1$ being an integer and $\delta l_{gw} << \lambda$ being the gravitational wave perturbation, it is possible to show

$$\begin{aligned}\left[\,\Psi_+\,\Psi_0^* + \Psi_0\,\Psi_-^*\,\right]\exp\left[\,i\,\Omega\,t\,\right] \quad + \quad \left[\,\Psi_-\,\Psi_0^* + \Psi_0\,\Psi_+^*\,\right]\exp\left[\,-\,i\,\Omega\,t\,\right] = \\ = 8\,J_0\,J_1\,r_1\,r_2\,\sin(\,\frac{\Omega}{c}\,\Delta l)\,\sin(\,2\,\frac{\omega_0}{c}\,\delta l_{gw}) \quad \times \\ \times \quad \left[\,\sin[\,\frac{\Omega}{c}\,(\,l_1\,+\,l_2\,)\,]\,\sin\,\Omega\,t - \cos[\,\frac{\Omega}{c}\,(\,l_1\,+\,l_2\,)\,]\,\cos\,\Omega\,t\right]\end{aligned} \tag{2.83}$$

In the presence of an asymmetry Δl in the arms, the term $\sin(\,\Omega\,\Delta l/c\,)$ is different from zero. This allows us to observe, in the demodulated components at Ω, the term $\sin(\,2\,\omega_0\,\delta l_{gw}/c) \simeq 2\,k\,\delta l_{gw}$. This mechanism can be explained in the following way. As the interferometer operates in destructive interference for the carrier, the asymmetry forces a leakage of the sidebands into the photodiode. Any change of the optical path would bring the carrier out of dark fringe, forcing it to beat against the sidebands.

Therefore, the frontal modulation scheme allows detection at RF where the electronic and amplitude noise of the laser are weaker. Furthermore, such a scheme can also be used to control the interferometer at low frequency as will be shown in the next chapter.

Chapter 3

The Optical Resonator: Response and Control

The objective of this chapter is to present and describe one of the key optical configurations for gravitational wave interferometry: the *two-mirror resonator* or *Fabry-Perot* cavity. The optical response of the outgoing electromagnetic (EM) fields to mirror movements will be given. In particular, the following two cases have been treated:

- the EM response to longitudinal movements of the mirrors (along the beam axis) by assuming a mode-matched laser beam to an aligned Fabry-Perot;
- the EM response to the angular mirror motion assuming a laser beam mode-matched and resonating in the optical system.

Throughout the thesis, this optical system will be often referred to.

An outline of well-known methods for cavity control will follow, consisting of

- the *Pound-Drever* technique[44] for the longitudinal control;
- the *Anderson*[45] and the *Ward*[46] techniques for the angular control.

Beforehand, a brief description of laser beam theory and resonators is necessary in order to fully comprehend the coupling of the incoming laser field with the optical system. It will be the task of Ch.5 to apply what is here presented to VIRGO's first optical configuration.

3.1 Propagation Modes of a Laser Beam

An ideal laser emits *coherent* and *monochromatic* electromagnetic radiation that can be expressed by the electromagnetic field $U(x, y, z)$. This function satisfies the wave equation

$$\nabla^2 U(x, y, z) + k^2 U(x, y, z) = 0 \tag{3.1}$$

where $k = 2\pi/\lambda$ is the propagation constant in the medium. Eq.(3.1) has an infinite set of solutions. One possible set of solutions for a light beam propagating along the z-direction consists of the *propagation modes* $U_{mn}(x, y, z)$ or TEM_{mn}, of order (m,n), which form a complete and orthogonal set of functions. Any monochromatic light distribution can be expressed as a linear combination of these modes.

The modes can be characterized in every point along the propagation axis by two parameters: $R(z)$ and $w(z)$. The first describes the radius of curvature of the wavefront that intersects the propagation axis, while the second parameter, with respect to the fundamental mode TEM_{00}, gives the radius for which the amplitude of the field has decreased by a factor $1/e$ with respect to the amplitude value along the propagation axis. Fig(3.1) shows the profile of a laser beam.

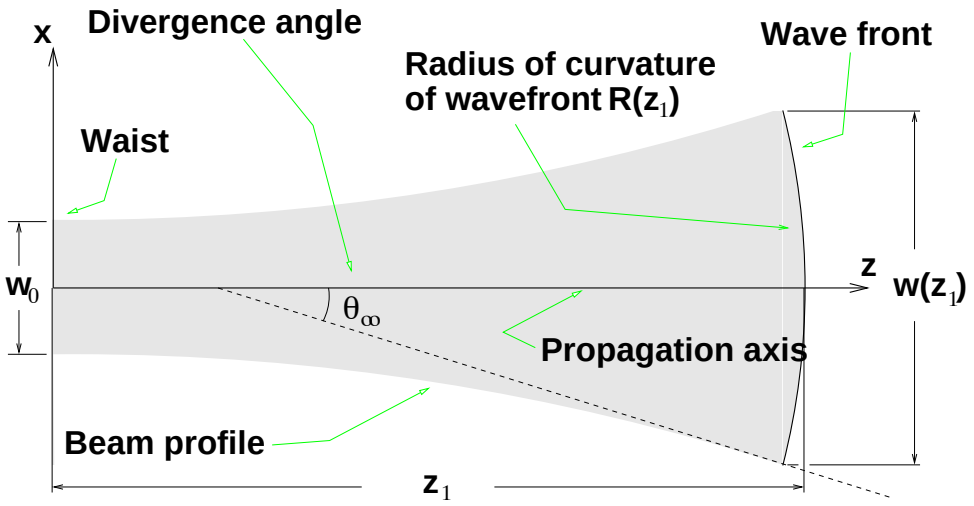

Figure 3.1: The laser beam profile.

The transversal intensity distribution of the laser beam has a Gaussian dependence and its radius $w(z)$ contracts to a minimum w_0 known as the *waist* of the beam. The two parameters $R(z)$ and $w(z)$ are determined by the waist size w_0 and by the distance z from the waist position, where

$$\begin{aligned} w^2(z) &= w_0^2 \left[1 + \left(\frac{\lambda\, z}{\pi\, w_0^2} \right)^2 \right] \\ R(z) &= z \left[1 + \left(\frac{\pi\, w_0^2}{\lambda\, z} \right)^2 \right] \end{aligned} \tag{3.2}$$

The beam profile, determined by the function $w(z)$, is a hyperbola with asymptotes forming an angle with the propagating axis of

$$\theta_\infty = \frac{\lambda}{\pi\, w_0} \tag{3.3}$$

which defines the divergence of the beam.

It can be demonstrated that for a given wavelength λ, waist w_0 and waist position z_0 (set to zero for simplicity), the propagation modes $U_{m\,n}(x, y, z)$ are

$$\begin{aligned} U_{m\,n}(x,y,z) = \frac{A_{m\,n}}{w(z)}\, H_m(\sqrt{2}\,\frac{x}{w(z)})\;\; H_n(\sqrt{2}\,\frac{y}{w(z)})\;\times \\ \times\; \exp\left[-\frac{x^2+y^2}{w^2(z)} - \frac{i\,k\,(x^2+y^2)}{2\,R(z)} - i\,(k\,z - \phi_{m\,n}(z)) \right] \end{aligned} \tag{3.4}$$

where

- $H_j(x)$ stands for the Hermite polynomial of order j in x, where the first few Hermite poly-

nomials are:

$$\begin{aligned} H_0(x) &= 1 \\ H_1(x) &= 2\,x \\ H_2(x) &= 4\,x^2 - 2 \\ H_3(x) &= 8\,x^3 - 12\,x \end{aligned} \tag{3.5}$$

- $\phi_{m\,n}(z)$ is the Guoy phase defined as

$$\phi_{mn}(z) \equiv (\, m + n + 1\,)\ \arctan\left(\frac{\lambda\ z}{\pi\ w_0^2}\right) \tag{3.6}$$

- and $A_{m\,n}$ is the normalization constant

$$A_{m\,n} = \left(\frac{2}{2^{n+m}\ n!\ m!\ \pi}\right)^{1/2} \tag{3.7}$$

Referring back to eq.(3.4), it is worth mentioning that $U_{m\,n}(x,y,z)$ is a function separable in the x and y variables. This is helpful when dealing with alignment problems: the x dimension can be treated separately from the y.

The approximation of a real laser field with plane wave formalism has already been presented in Ch.2. With eq.(3.4) it is possible to see the difference between the two. Obviously, they have a different power distribution, one being Gaussian while the other is constant. The most interesting difference is perhaps the phase difference γ:

$$\gamma\ =\ i\left[\ -\ \frac{k\,(x^{\,2}\ +\ y^{\,2})}{2\,R(z)}\ +\ \phi_{m\,n}(z)\ \right] \tag{3.8}$$

This arises from the Guoy phase, which depends both on the distance from the waist and the eigenmode in consideration, as well as the radius of curvature of the wavefront. By considering resonators with mirror curvatures coinciding with the beams' fundamental mode, the problem can really be seen as a plane wave incident to a plane mirror. In this case, the two formalisms are identical.

Also, the propagation modes take the simplest form at the position of the waist. By setting $z = 0$, the radius of curvature becomes $R(0) = \infty$ while $w(0) = w_0$. The electromagnetic field then takes the form

$$U_{m\,n}(x,y,0) = \frac{A_{m\,n}}{w_0}\ H_m(\sqrt{2}\ \frac{x}{w_0})\ H_n(\sqrt{2}\ \frac{y}{w_0})\ \exp\left[\ -\ \frac{x^{\,2}+y^{\,2}}{w_0^2}\ \right] \tag{3.9}$$

The Hermite-Gaussian modes are not the only solution to eq.(3.1). It is at times convenient to treat the problem in polar coordinates[42] where the eigenmodes can be expressed as Laguerre polynomials weighted by a Gaussian.

3.2 Geometrical Properties of Optical Resonators

The *Fabry-Perot* is the simplest of all optical resonators consisting of two partially reflective mirrors, a distance d apart. Once the cavity is illuminated, its length has to be adjusted with respect to the laser frequency, so as to allow a power build up. In this case, the reflected and transmitted beams exhibit interesting properties that are here presented. The concepts of stability and mode-matching are first introduced.

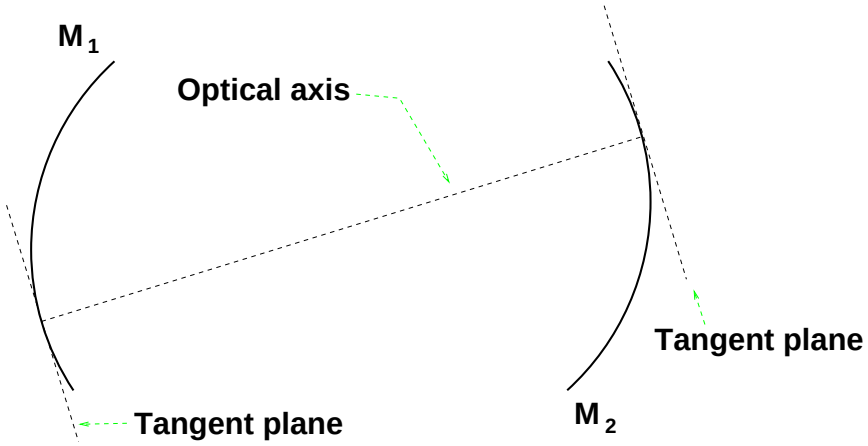

Figure 3.2: The optical resonator and its optical axis.

3.2.1 Resonator Stability

Let's define the *optical axis* of the cavity as the straight line perpendicular to the tangent planes of the mirrors, as shown fig.(3.2) where the surface of the mirrors is denoted by M_1 and M_2. Let's also define a *paraxial* ray as a ray with very small distance and angle, with respect to the optical axis. The resonator is then said to be *stable* if a paraxial ray experiences a periodic focusing action after an arbitrary number of reflections. It can be demonstrated[42] that this condition can be expressed as

$$0 < \left(1 - \frac{d}{R_1} \right) \left(1 - \frac{d}{R_2} \right) < 1 \tag{3.10}$$

where R_1 and R_2 are the curvature radii of the mirrors in figure and d their distance apart.

3.2.2 Cavity Modes

The modes of a resonator are defined as a stationary field configuration. If a mode can be represented by a wave propagating back and forth between the mirrors, the beam parameters $R(z)$ and $w(z)$ must be the same after one complete return trip of the beam. This is valid under the assumption that the resonator is stable and the mirror aperture is large compared to the beam spot size.

Fig(3.3) shows a resonator made of two mirrors M_1 and M_2 of radius of curvature R_1 and R_2 respectively, a distance d apart. These modes have a wavefront at the position of a mirror equal to the radius of curvature of the mirror in consideration. The dimensions of the spot size, at the position of the mirrors, is given[42] by

$$\begin{aligned} w_1^4 &= \left(\frac{\lambda\, R_1}{\pi}\right)^2 \frac{R_2 - d}{R_1 - d} \frac{d}{R_1 + R_2 - d} \\ w_2^4 &= \left(\frac{\lambda\, R_2}{\pi}\right)^2 \frac{R_1 - d}{R_2 - d} \frac{d}{R_1 + R_2 - d} \end{aligned} \tag{3.11}$$

where the waist w_0, shown in figure, is determined by

$$w_0^4 = \left(\frac{\lambda}{\pi}\right)^2 \frac{d\,(R_1 - d)\,(R_2 - d)\,(R_1 + R_2 - d)}{(R_1 + R_2 - 2d)^2} \tag{3.12}$$

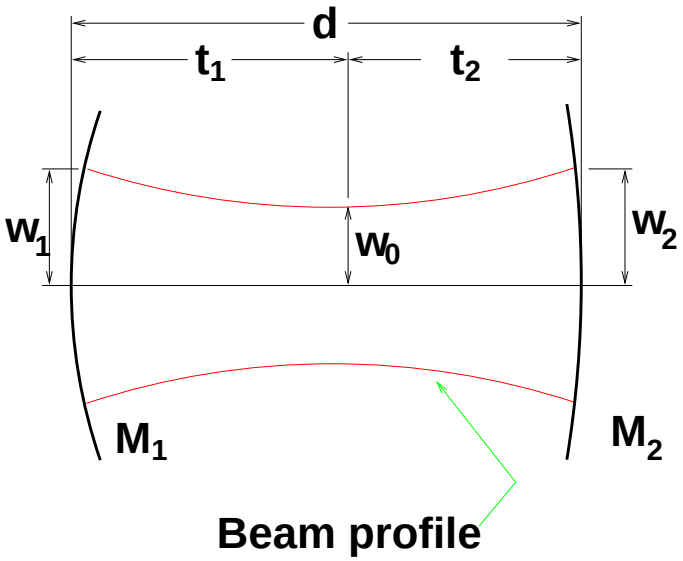

Figure 3.3: The resonator mode.

and is positioned inside the cavity at a distance t_1 from M_1 and t_2 from M_2 given by the expressions

$$\begin{aligned} t_1 &= \frac{d\,(R_2 - d)}{R_1 + R_2 - 2d} \\ t_2 &= \frac{d\,(R_1 - d)}{R_1 + R_2 - 2d} \end{aligned} \tag{3.13}$$

Therefore, the cavity is said to be *mode-matched* to an incoming beam, of wavelength λ, if the laser beam waist size and position coincide with that of the cavities.

In particular, the use of plane-concave cavities is common. Assuming M_1 to be a plane mirror with $R_1 = \infty$, the waist size expressed in eq.(3.12) becomes

$$w_0^2 = \left(\frac{\lambda}{\pi}\right)\sqrt{d\,(R_2 - d)} \tag{3.14}$$

and it will be positioned on the plane mirror M_1.

3.2.3 Resonance Condition

The laser beam is said to *resonate* inside a cavity of length d when the phase of light acquires 2π in a complete round trip. By using the convention that the beam acquires a $\pi/2$ shift in reflection, the resonance condition for a $\mathrm{TEM}_{m\,m}$ is

$$k\,d - \phi_{m\,n}(d) = \frac{\pi}{2}(2\,q - 1) \tag{3.15}$$

where q is an integer denoting the number of quarter wavelengths. Even though the $R(z)$ and $w(z)$ parameters describe every mode, the resonance condition is different for each mode due to the Guoy phase $\phi_{m\,n}(z)$. After some algebraic manipulation, it can be shown[42] that the mode $\mathrm{TEM}_{m\,n}$ resonant frequency $\nu_{m\,n}$ is

$$\frac{\nu_{m\,n}}{\nu_0} = \frac{1}{2}(2\,q - 1) + \frac{1}{\pi}\,(m + n + 1)\,\arccos\sqrt{(1 - \frac{d}{R_1})(1 - \frac{d}{R_2})} \tag{3.16}$$

where $\nu_0 = c\,/\,2\,d$ is the inverse of the light round trip travel time.

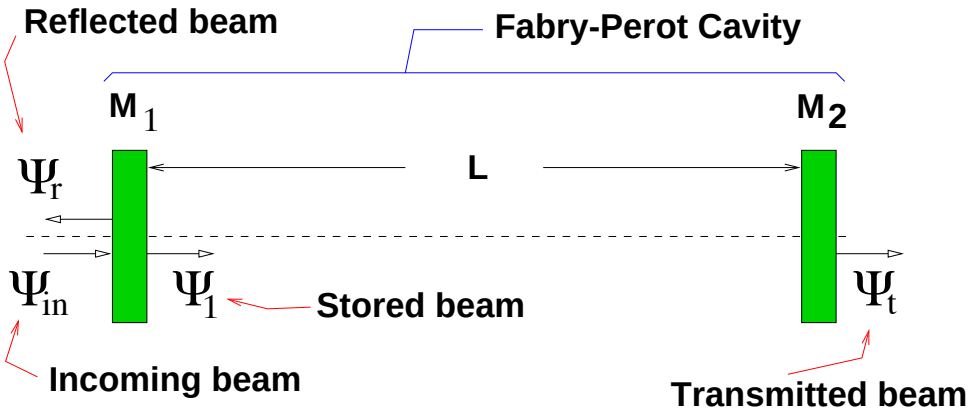

Figure 3.4: The Fabry-Perot: notations.

3.3 Optical response of a Fabry-Perot

This section presents the optical response of the simple resonator, the Fabry-Perot cavity, to mirror angular motions and along the beam axis. The longitudinal response is first presented.

3.3.1 The Longitudinal Response

The EM field dependence on longitudinal motions of the mirrors is described under the assumption that

- the incoming fundamental mode of the laser beam is mode-matched to the resonator;
- the cavity is aligned to the incoming light beam, or, in other words, that the optical cavity coincides with the beam axis.

Under these assumptions, the problem is simplified by describing the incoming light beam as a plane wave incident to a plane-plane cavity, as shown in fig.(3.4). According to the notation in the figure, the electromagnetic fields are

- the stored beam Ψ_1

$$\Psi_1(\phi) \;=\; \frac{t_1}{1 \,+\, r_1\, r_2\, \exp(-i\,\phi\,)} \;=\; \mathcal{A}_1(\phi) \;=\; A_1(\phi)\;\exp(\,i\,\phi_1\,) \tag{3.17}$$

- the transmitted beam Ψ_t

$$\Psi_t(\phi) \;=\; \frac{t_1\, t_2\, \exp(-i\,\phi\,/\,2\,)}{1 \,+\, r_1\, r_2\, \exp(-i\,\phi\,)} \;=\; \mathcal{A}_T(\phi) \;=\; A_T(\phi)\;\exp(\,i\,\phi_T\,) \tag{3.18}$$

- and the reflected beam Ψ_r

$$\Psi_r(\phi) \;=\; i\left[\,r_1 \,+\, \frac{r_2\, t_1^2\, \exp(-i\,\phi)}{1 \,+\, r_1\, r_2\, \exp(-i\,\phi\,)}\,\right] \;=\; \mathcal{A}_R(\phi) \;=\; A_R(\phi)\;\exp(\,i\,\phi_R\,) \tag{3.19}$$

where

- r_i^2, t_i^2 and p_i^2 are the power reflectivity, transmittivity and losses of the i-th mirror;
- $\phi \,=\, 2\,k\,L$ is the propagation phase accumulated in a complete round trip where L is the cavity length;

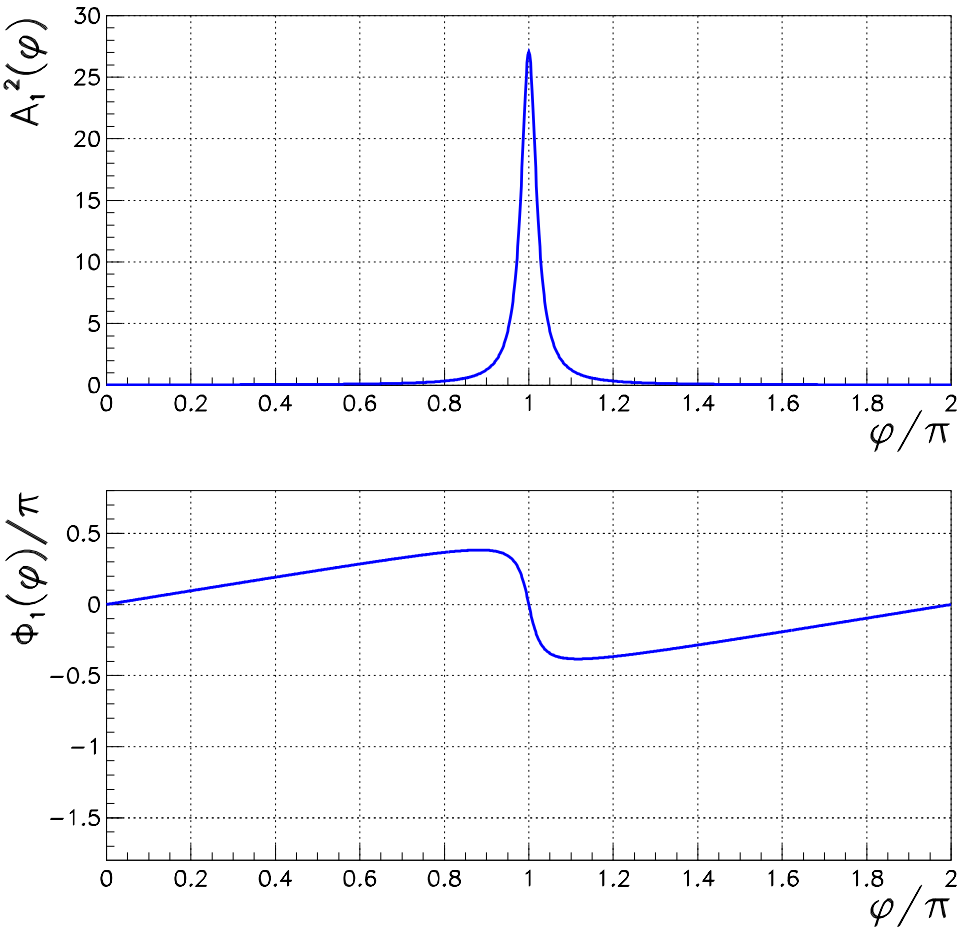

Figure 3.5: The cavity stored power A_1^2 with its corresponding phase ϕ_1 in the case $r_1^2 = 0.88$ and $r_2^2 = 0.99$ and no losses.

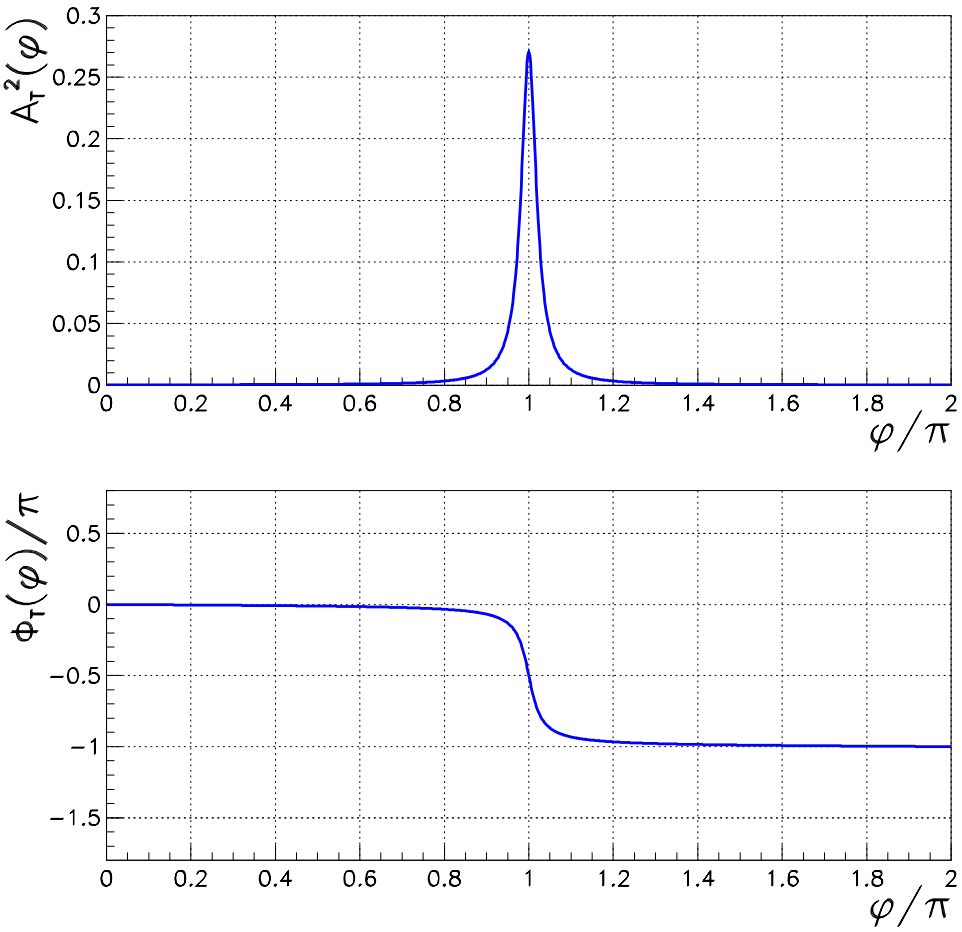

Figure 3.6: The transmitted power A_T^2 with its corresponding phase ϕ_T in the case $r_1{}^2 = 0.88$ and $r_2^2 = 0.99$ and no losses.

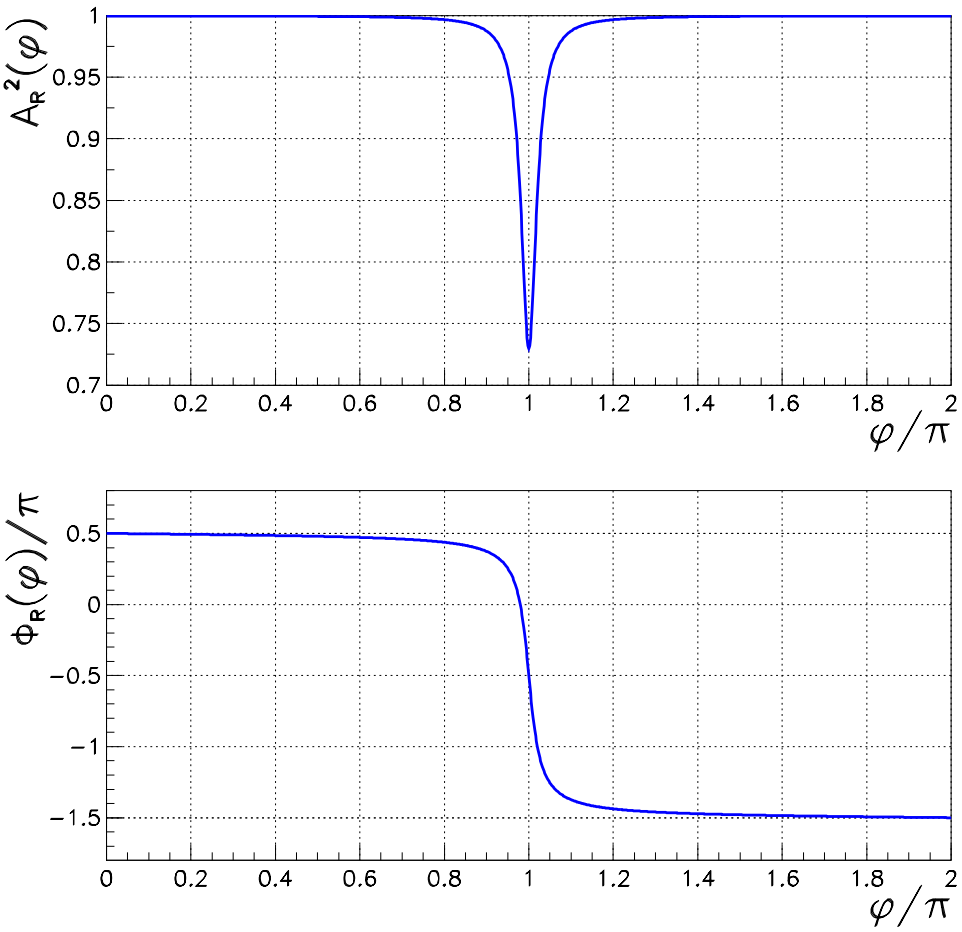

Figure 3.7: The reflected power A_R^2 with its corresponding phase ϕ_R in the case ${r_1}^2 = 0.88$ and $r_2^2 = 0.99$ and no losses.

- $\mathcal{A}_{1,R,T}(\phi)$ is the complex amplitude of the normalized stored, reflected and transmitted fields, whereas $A_{1,R,T}(\phi)$ is the modulo and $\phi_{1,R,T}(\phi)$ the phase of the corresponding fields;
- $\Psi_{in} = 1$ is the incoming field.

Fig(3.5), fig.(3.6) and fig.(3.7) show the plots of the square modulo of the stored A_1^2, transmitted A_T^2 and reflected A_R^2 fields, with their corresponding phases, as a function of the propagation phase ϕ. Notice that the curve in both fig(3.5) and fig.(3.6) delineate the *Airy Peak* [43]. For the plots, no mirror losses were taken into account, with power reflectivities for the mirrors of $r_1^2 = 0.88$ and $r_2^2 = 0.99$. From these plots and from eq.(3.17), eq.(3.18) and eq.(3.19), we remark that

- the functions are periodic modulo $2\,\pi$;
- the resonance condition occurs at $\phi = (2\,n + 1)\,\pi$, where n is an integer, and in this case
  i. power is built up inside the cavity:
  $$|\,\Psi_1(\pi)\,|^2 >> 1$$
  ii. the reflected power has a minimum, adding a phase of $-\pi/2$ to the reflected field (recall that a mirror adds a $\pi/2$ phase);
- the transmitted power $A_T(\phi)$ is proportional to the stored power $A_1(\phi)$;

It is in condition of resonance that the cavity shows special properties. Not only is the power within amplified but most importantly the reflected phase acquires a sensitivity to small length perturbations. It is also interesting to remark that out of resonance, the cavity behaves exactly like a mirror, reflecting all the power with a $\pi/2$ phase shift.

By introducing the concept of finesse $\mathcal{F}$, it is possible to simplify the expressions for the EM fields and their properties. The finesse $\mathcal{F}$ is defined as the ratio of the distance of between resonances and the full width at half maximum (FWHM) of a resonance. It can be shown that the FWHM of a resonance is

$$\text{FWHM} = \frac{1}{2\,k}\left(2\,\pi - 2\,\arccos\left[\frac{1 + r_1^2\,r_2^2 - 4\,r_1\,r_2}{2\,r_1\,r_2}\right]\right) \tag{3.20}$$

Hence, the finesse is

$$\mathcal{F} = \frac{\lambda\,/\,2}{\text{FWHM}} = \frac{\pi}{\pi - \arccos[\,(\,1 + r_1^2\,r_2^2 - 4\,r_1\,r_2\,)\,/\,(\,2\,r_1\,r_2\,)\,]} \tag{3.21}$$

In general, the reflectivities of optical resonators are chosen so that $1 - r_1\,r_2 << 1$. In this case, it is possible to expand eq.(3.21) so as to find an approximate form for the finesse. This turns out to be

$$\mathcal{F} \simeq \frac{\pi\sqrt{r_1\,r_2}}{1 - r_1\,r_2} \tag{3.22}$$

The mirror reflectivities of optical resonators dealt with here, satisfy the condition $1 - r_1\,r_2 << 1$. Therefore, throughout the thesis the approximate sign in eq.(3.22) will be replaced by the equal sign.

The introduction of the concept of finesse simplifies the expressions. The stored power, whose amplitude is expressed in eq.(3.17), can be rewritten in the form

$$|\,\Psi_1(\phi)\,|^2 = \text{G}\,\frac{1}{1 + (\,2\,\mathcal{F}\,/\,\pi\,)^2\,\sin^2(\,\phi\,/\,2\,)} \tag{3.23}$$

where G is the gain in power defined as the ratio between the stored and incident power in condition of resonance:

$$\mathrm{G} \equiv \frac{t_1^2}{(\,1 - r_1 r_2\,)^2} \tag{3.24}$$

Often, the mirror reflectivities not only satisfy the condition $1 - r_1 r_2 << 1$, but also the condition $1 - r_1 >> 1 - r_2$. In this case, it can be shown that the relationship between the gain G and the finesse $\mathcal{F}$ is

$$\mathrm{G} \simeq \frac{2\,\mathcal{F}}{\pi} \tag{3.25}$$

As already stated in Ch.2, the phase reflectivity of a Fabry-Perot plays a central role in interferometric detection. To first order approximation, it is possible to show that the phase change induced by a perturbation of the cavity length δL around resonance is

$$\phi_R(L + \delta L) - \phi_R(L) \simeq 2\,k\,\mathrm{G}\,\delta L \tag{3.26}$$

3.3.2 The Angular Response

The angular response is here presented by assuming that the incoming field is mode-matched to the resonator. It will be shown how a mirror misalignment generates a translation and rotation of the optical axis with respect to the beam axis inducing a coupling to the first order transverse modes.

The beam and optical axis

The optical systems that we will study consist of plane-concave cavities shown in fig.(3.8). This section will limit the discussion to such a configuration, treating angles only in one dimension.

Fig.(3.8) shows two possible mirror tilts. A tilt of an angle θ_2, as shown in fig.(3.8a), of the concave mirror M_2 generates only a translation of the axis. The induced translation is

$$a = R \sin\theta_2 \tag{3.27}$$

where R is the radius of curvature of mirror M_2. The mirror tilt induces also a length change ΔL of the cavity of

$$\Delta L = R\,(\,1 - \cos\theta_2\,) \simeq \frac{R\,\theta_2^2}{2} \tag{3.28}$$

approximated for small angles.

On the other hand, a tilt of angle θ_1 of the plane mirror M_1, as shown in fig.(3.8b), induces a rotation θ_1 of the axis as well as a translation of

$$a = (\,R - L\,) \sin\theta_1 \cos\theta_1 \tag{3.29}$$

causing a cavity length change ΔL of

$$\Delta L = (\,R - L\,)\,(\,1 - \cos\theta_1\,) \simeq \frac{(\,R - L\,)\,\theta_1^2}{2} \tag{3.30}$$

In both mirror tilts, the length change of the cavity is of second order in the angle.

The incoming field in the two reference systems

Misalignment effects are studied by making use of the property that the $\mathrm{TEM}_{m\,n}$ modes of the resonator form a complete and orthogonal set of functions. The incoming beam can then be expressed as a linear combination of these modes. The modal expansion can be performed at any point along the propagation axis. However, the analytical calculations are made easier

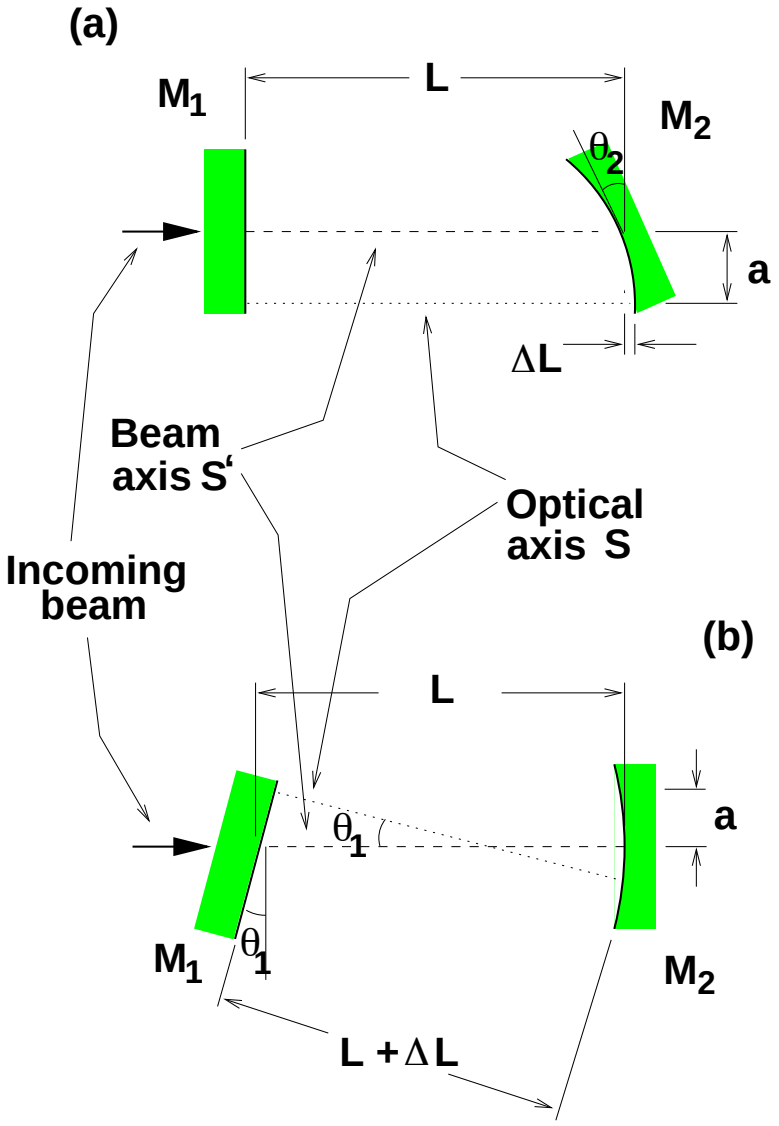

Figure 3.8: The optical axis as a function of mirror tilts: (a) the curved mirror M_2 is tilted by θ_2 generating a pure translation a of the optical axis with respect to the input axis and (b) the plane mirror is tilted by an angle θ_1 generating a translation a and angle θ_1 of the optical axis with respect to the input axis.

- when performed at the waist, since the expression of the modes becomes simplest, as shown in eq.(3.9);
- by considering misalignments in one plane only, the expression of the modes are separable functions in x and y;
- by making use of the approximation

$$\frac{a}{w_0} \ll 1 \qquad\qquad \frac{\theta}{\theta_\infty} \ll 1 \tag{3.31}$$

where a and θ are the translation and angle of the optical axis and w_0 and θ_∞ are the waist and divergence angle of the beam respectively. Second order terms of the expansion are neglected.

Let's first consider pure translations, as shown in fig.(3.8a). The two bases, defined by the primed beam axis S' and the unprimed optical axis S, are schematically shown in fig.(3.9a). The

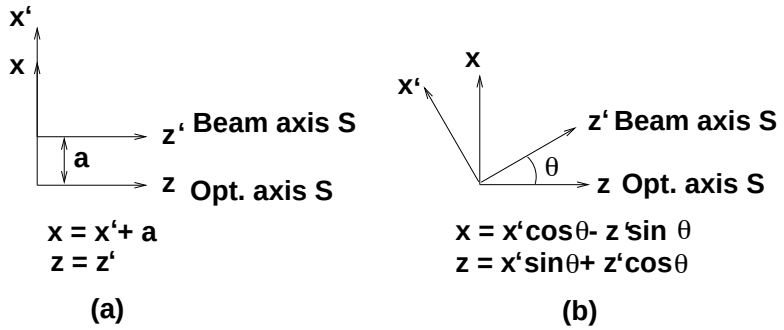

Figure 3.9: The reference systems defined by the beam axis S' and the optical axis S: (a) pure translation and (b) pure rotation.

transformation from one system to the other is simply

$$x = x' + a \qquad\qquad z = z' \tag{3.32}$$

In the S' reference system, the incoming laser beam is seen as a pure fundamental mode, which at the waist takes the form

$$\Psi_{in}(x') \;=\; U_{00}(x') \;=\; \frac{A_{00}}{w_0}\;\exp\Big[\;-\frac{x'^2}{w_0^2}\;\Big] \tag{3.33}$$

In the S reference frame, the incoming beam is

$$\begin{aligned} \Psi_{in}(x) \;&=\; U_{00}(x-a) = \\ &=\; \frac{A_{00}}{w_0}\;\exp\Big[-\Big(\frac{x-a}{w_0}\Big)^2\Big] = \\ &=\; \frac{A_{00}}{w_0}\;\exp\Big[-\frac{x^2}{w_0^2}\Big]\;\exp\Big[\frac{2\;x\;a}{w_0^2}\Big]\;\exp\Big[-\frac{a^2}{w_0^2}\Big] \end{aligned} \tag{3.34}$$

By making use of the approximation in eq.(3.31), a power expansion of the exponential term is performed up to first order. This leads to

$$\begin{aligned} \Psi_{in}(x) \;&\simeq\; \frac{A_{00}}{w_0}\;\exp\Big[-\frac{x^2}{w_0^2}\Big]\;\Big[1+\frac{2\;x\;a}{w_0^2}\Big] = \\ &=\; U_{00}(x) \;+\; \frac{a}{w_0}\,U_{10}(x) \end{aligned} \tag{3.35}$$

Any pure translation of the optical axis generates an *in-phase* coupling with the transversal mode $U_{10}(x)$ by an amount a/w_0.

Fig.(3.9b) shows schematically the beam axis S' tilted by an angle θ with respect to the optical axis S. We would like to express the beam from the S' base

$$\Psi_{in}(x') \;=\; U_{00}(x') \;=\; \frac{A_{00}}{w_0}\;\exp\Big[\;-\frac{x'^2}{w_0^2}\;\Big] \tag{3.36}$$

to the S base. The transformation equations relating the two reference systems are

$$x \;=\; x'\,\cos\theta \;-\; z'\,\sin\theta \qquad\qquad z \;=\; x'\,\sin\theta \;+\; z'\,\cos\theta \tag{3.37}$$

In this case, the phase and amplitude of the incoming beam need to be treated separately. The projection of the amplitude of the beam to the transverse plane of the optical axis is

$$\mid \Psi_{in}(x) \mid = \frac{\mid \Psi_{in}(x') \mid}{\cos\theta} \;\simeq \mid \Psi_{in}(x', y', 0) \mid (1 + \frac{\theta^2}{2} + ...) \tag{3.38}$$

consisting of a change in the second order in angle and will be neglected. However, the beam acquires a phase $\alpha(x)$ of

$$\alpha(x) = k\,x\,\sin\theta \;\simeq\; k\,x\,\theta \tag{3.39}$$

where the approximation in eq.(3.31) has been used. In the S reference system, the incoming beam becomes

$$\Psi_{in}(x) \;=\; U_{00}(x)\;\exp[i\,\alpha(x)] \tag{3.40}$$

By power developing eq.(3.40), this becomes

$$\Psi_{in}(x) \;=\; U_{00}(x) \;+\; i\,\frac{\theta}{\theta_\infty}\,U_{10}(x) \tag{3.41}$$

Pure rotations couple in *quadrature* phase with the transverse mode U_{10} by the amount θ/θ_∞. The difference with a pure translation lies in a $\pi/2$ phase shift in the coupling.

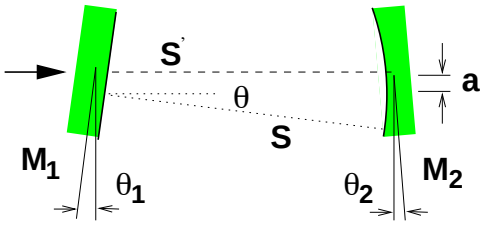

Figure 3.10: Misaligned Fabry-Perot: translation a and angle θ of the optical axis S with respect to the beam axis S'.

In general, for the misaligned Fabry-Perot in fig.(3.10), an incoming beam in the S' reference system expressed as

$$\Psi_{in}(x') \;=\; U_{00}(x') \tag{3.42}$$

is seen in the S reference system as

$$\Psi_{in}(x) \;=\; U_{00}(x) \;+\; \Big(\,\frac{a}{w_0} \;+\; i\,\frac{\theta}{\theta_\infty}\,\Big)\,U_{10}(x) \tag{3.43}$$

It is worth noticing that for the calculations here shown, the normalization factors have been neglected because of their dependence only on second order terms.

The transmitted and reflected beam of a misaligned cavity

Now that the expression of the beam in the optical base has been found, we are able to describe the response of the cavity, or how the transmitted and reflected beams look as a function of the misalignments.

By referring to fig.(3.10), the incoming beam expressed in the S frame is shown in eq.(3.43). The reflected beam Ψ_r in the S frame is

$$\Psi_r = \mathcal{A}_R^{00} U_{00}(x) + \left(\frac{a}{w_0} + i \frac{\theta}{\theta_\infty} \right) \mathcal{A}_R^{10} U_{10}(x) \tag{3.44}$$

where $\mathcal{A}_R^{00}$ and $\mathcal{A}_R^{10}$ are the complex reflectivity of the Fabry-Perot [eq.(3.19)] for the fundamental mode and the first transverse mode respectively. By performing a power expansion of the fundamental mode, it is possible to map back the field to the S' frame. The reflected beam is then

$$\Psi'_r = \mathcal{A}_R^{00} \left[U_{00}(x') - \left(\frac{a}{w_0} - i \frac{\theta}{\theta_\infty} \right) U_{10}(x') \right] + \left(\frac{a}{w_0} + i \frac{\theta}{\theta_\infty} \right) \mathcal{A}_R^{10} U_{10}(x') \tag{3.45}$$

In the same way, the transmitted field in S is

$$\Psi_t = \mathcal{A}_T^{00} U_{00}(x) + \left(\frac{a}{w_0} + i \frac{\theta}{\theta_\infty} \right) \mathcal{A}_T^{10} U_{10}(x) \tag{3.46}$$

which transformed back to S' becomes

$$\Psi'_t = \mathcal{A}_T^{00} \left[U_{00}(x') - \left(\frac{a}{w_0} + i \frac{\theta}{\theta_\infty} \right) U_{10}(x') \right] + \left(\frac{a}{w_0} + i \frac{\theta}{\theta_\infty} \right) \mathcal{A}_T^{10} U_{10}(x') \tag{3.47}$$

It is important to recall that once the fundamental mode resonates, the first order transverse mode anti-resonates. In this case, by referring to fig.(3.6), $\mathcal{A}_T^{10} \simeq 0$ and eq.(3.47) can be approximated as

$$\Psi'_t = -i A_T^{00} \left[U_{00}(x') - \left(\frac{a}{w_0} + i \frac{\theta}{\theta_\infty} \right) U_{10}(x') \right] \tag{3.48}$$

3.4 Longitudinal Locking: The Pound-Drever Method

In order to make use of the properties of the resonator, the fundamental eigenmode of the laser beam must resonate in the cavity. Laser frequency fluctuations, together with any mirror displacement noises, do not allow the beam to optically resonate. The *Pound-Drever*[44] method allows the stabilization of the cavity length to the laser source.

In VIRGO, the frontal modulation technique, presented in Ch.2, is used not only as a detection scheme but also as a means to longitudinally control the position of the mirrors. In particular, the Pound-Drever method consists in phase modulating the incoming beam, as shown in sec.(2.4)

- with both sidebands anti-resonating in the cavity
- while using the demodulated component of the reflected beam as an error signal useful for the cavity lock onto the laser frequency.

Assuming that the beam is mode-matched to the Fabry-Perot and that the cavity is aligned, we can study again the problem with the use of plane waves and a flat-flat cavity. Let a normalized modulated beam, of the form

$$\Psi_{in} = J_0 \, e^{i \, \omega_0 \, t} + J_1 \, e^{i \, (\omega_0 \, + \, \Omega) \, t} - J_1 \, e^{i \, (\omega_0 \, - \, \Omega) \, t} \tag{3.49}$$

impinge on the cavity, where $J_{0,1}$ is the amplitude of the carrier and sidebands and $\Omega/2\pi$ is the modulation frequency. By neglecting the global phase $\omega_0 \, t$, the reflected field is

$$\Psi_R = \Psi_0 + \Psi_+ \, e^{i \, \Omega \, t} + \Psi_- \, e^{-i \, \Omega \, t} \tag{3.50}$$

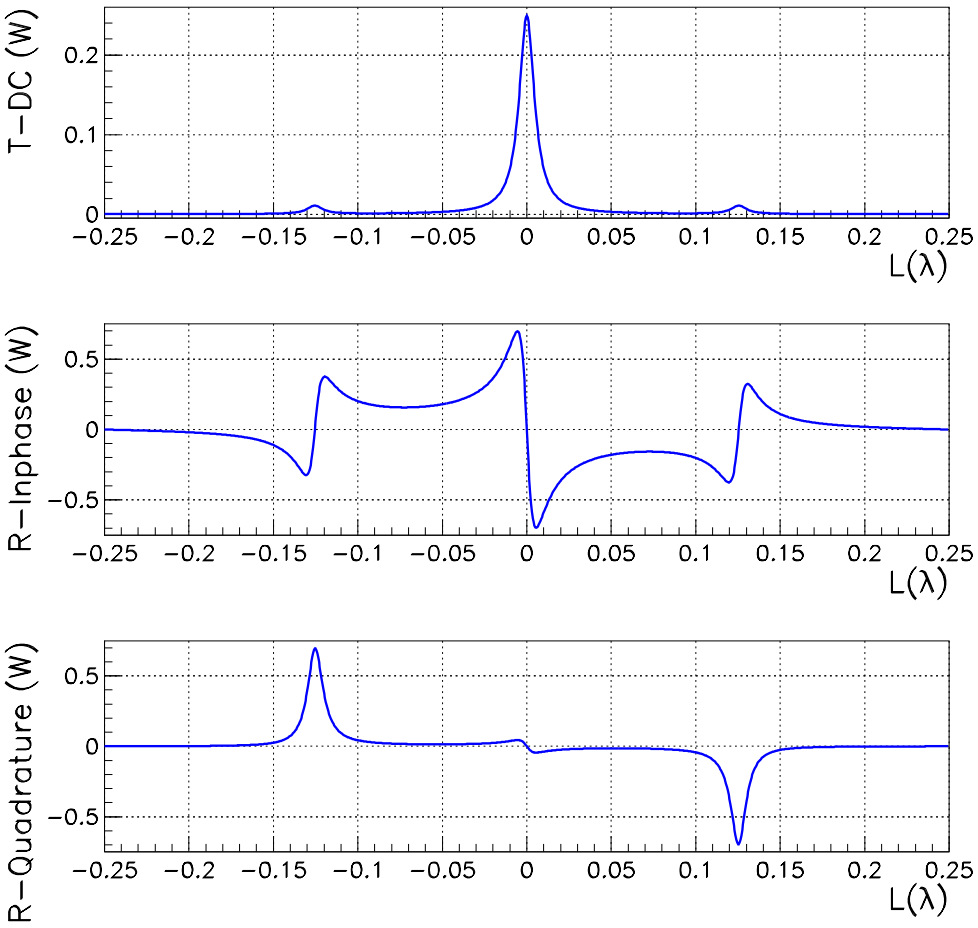

Figure 3.11: The Pound-Drever error signal of a Fabry-Perot with $r_1^2 = 0.88$, $r_2^2 = 0.99$ (no losses) as a function of cavity length (modulo λ). Top: transmitted power in DC. Middle: reflected in-phase signal. Bottom: reflected quadrature signal.

The power of the reflected beam is then

$$\begin{aligned} |\,\Psi_R\,|^2 \;=\; & |\,\Psi_0\,|^2 + |\,\Psi_-\,|^2 + |\,\Psi_+\,|^2 + \\ & + \Big[\,\Psi_+\,\Psi_0^* + \Psi_0\,\Psi_-^*\,\Big]\exp\left[\,i\,\Omega\,t\,\right] \;+\; \Big[\,\Psi_-\,\Psi_0^* + \Psi_0\,\Psi_+^*\,\Big]\exp\left[\,-\,i\,\Omega\,t\,\right] \end{aligned} \tag{3.51}$$

where the $2\,\Omega$ components have been neglected. The modulated components holding the signal for the length control can be re-written in simpler form as

$$\begin{aligned} \Big[\,\Psi_+\,\Psi_0^* + \Psi_0\,\Psi_-^*\,\Big]\exp\left[\,i\,\Omega\,t\,\right] \;+\; & \Big[\,\Psi_-\,\Psi_0^* + \Psi_0\,\Psi_+^*\,\Big]\exp\left[\,-\,i\,\Omega\,t\,\right] = \\ = \;\; & 2\,\Re\Big\{\,(\,\Psi_+\,\Psi_0^* + \Psi_0\,\Psi_-^*\,)\,\exp\left[\,i\,\Omega\,t\,\right]\Big\} = \\ = \;\; & 2\,\Re\{\,\Psi_+\,\Psi_0^* + \Psi_0\,\Psi_-^*\,\}\,\cos\Omega\,t \;-\; 2\,\Im\{\,\Psi_+\,\Psi_0^* + \Psi_0\,\Psi_-^*\,\}\,\sin\Omega\,t \end{aligned} \tag{3.52}$$

where $\Re\{\}$ and $\Im\{\}$ denote the real and imaginary part of the argument within parentheses.

The properties of the demodulated component $\Re\{\,\Psi_+\,\Psi_0^* + \Psi_0\,\Psi_-^*\,\}$, referred to as the *in-phase* component, and $\Im\{\,\Psi_+\,\Psi_0^* + \Psi_0\,\Psi_-^*\,\}$, referred to as the *quadrature* component, can be

physically understood as follows. Once the carrier is kept in resonance, both sidebands anti-resonate. Even though both the carrier and sideband amplitudes are reflected by almost the same amount, their phase change is different. The carrier gains a $-\pi/2$ phase shift while both sidebands gain, approximately, a $\pi/2$ phase shift, as seen in fig.(3.7). A length perturbation around resonance induces a phase change for the carrier only. This change generates a beating between the carrier and the sidebands which is at the origin of the error signal.

In fig.(3.11), the plot of the demodulated components of a Fabry-Perot with $r_1^2 = 0.88$, $r_2^2 = 0.99$ and no losses as a function of length is shown. The modulation frequency is $\Omega/2\pi = 6.28$ MHz. The DC transmitted power is also given to indicate the resonance location. It is important to notice that the in-phase signal is linear around resonance. A control system would then use such a signal to correct the cavity length. It can also be seen that the linearity is limited by the FWHM of the resonance:

$$\mathrm{FWHM} = \frac{\lambda}{2\,\mathcal{F}} \tag{3.53}$$

3.5 Automatic Alignment

We have presented the longitudinal response of the resonator as well as the Pound-Drever technique to stabilize the cavity length to the laser source. In the same way, this section presents two methods for the alignment of a Fabry-Perot. These are the *Anderson* and *Ward* techniques.

3.5.1 The Anderson Technique

This method[45] is based upon phase modulation of the incoming beam at a frequency equal to the frequency spacing between the TEM_{00} and TEM_{10} determined by the geometry of the resonator. As a consequence, the TEM_{10} of one sideband resonates at the same time as the TEM_{00} of the carrier. Unlike the Pound-Drever technique, the error signal is taken from the transmitted beam.

Assuming an incoming beam of the form

$$\Psi_{in} = J_0\,U_{00} + J_1\,U_{00}\,e^{i\,\Omega\,t} - J_1\,U_{00}\,e^{-i\,\Omega\,t} \tag{3.54}$$

where $\Omega/2\pi$ is the modulation frequency, then, by referring to eq.(3.48), the transmitted beam takes the form

$$\begin{aligned}\Psi_t = {} & -i\sqrt{\mathrm{G}}\,t_2 \times \\ & \times \left[J_0\,U_{00} - J_0\left(\frac{a}{w_0} + i\,\frac{\theta}{\theta_\infty}\right) U_{10} + J_1\left(\frac{a}{w_0} + i\,\frac{\theta}{\theta_\infty}\right) U_{10}\,e^{i\,\Omega\,t}\right]\end{aligned} \tag{3.55}$$

where G is the cavity gain factor, t_2 is the end mirror amplitude transmittivity and the sideband term at $-\Omega$ has been neglected. By taking the square modulo and neglecting second order terms in the misalignments, the demodulated components are

$$2\,J_1\,J_0\,U_{00}\,U_{10}\left[\left(\frac{a}{w_0}\right)\cos\Omega\,t - \left(\frac{\theta}{\theta_\infty}\right)\sin\Omega\,t\right] \tag{3.56}$$

It is possible to retrieve information for the alignment of the cavity from the demodulated components. In particular, the quadrature component holds information only on the tilt of the optical axis whereas the in-phase component holds information only on the translation of the axis. The in-phase and quadrature signals give orthogonal informations for the alignment. The drawback of this method is the constraint on the modulation frequency.

3.5.2 The Ward Technique

The Ward method[46] differs from the Anderson by taking the signal on reflection, not demanding the sidebands to resonate. The analytical expressions are rather complicated and we will limit ourselves only to an outline of the calculations.

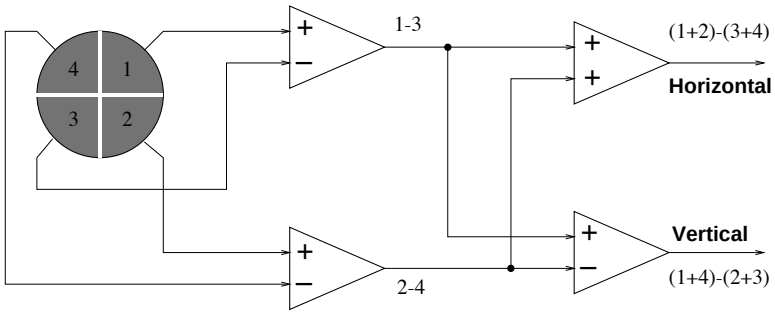

Figure 3.12: The quadrant photodiode.

Assuming an incident beam of the form

$$\Psi_{in} \;=\; J_0\, U_{00} \;+\; J_1 U_{00}\, e^{i\,\Omega\, t} \;-\; J_1\, U_{00}\, e^{-i\,\Omega\, t} \tag{3.57}$$

where $\Omega/2\pi$ is the modulation frequency, the reflected beam can be written as

$$\Psi_r \;=\; J_0\, \Psi_r^0\, e^{i\,\omega_0\, t} \;+\; J_1\, \Psi_r^+\, e^{i\,(\omega_0\,+\,\Omega)\, t} \;-\; J_{-1}\, \Psi_r^-\, e^{i\,(\omega_0\,-\,\Omega)\, t} \tag{3.58}$$

where

$$\begin{aligned} \Psi_r^0 \;&=\; -\,i\, e^{i\,\phi_{00}(z)} \left[U_{00} \;+\; \left(\;-\; \frac{a}{w_0} \;+\; i\, \frac{\theta}{\theta_\infty} \right) U_{10}\, e^{i\,\phi_{00}(z)} \right] \;+ \\ &\qquad\qquad i\, \left(\frac{a}{w_0} \;+\; i\, \frac{\theta}{\theta_\infty} \right) U_{10}\, e^{i\,\phi_{00}(z)} \\ \Psi_r^+ \;&=\; \Psi_r^- \end{aligned} \tag{3.59}$$

Here, the Guoy phase $\phi_{00}(z)$ has been put in evidence and all amplitudes in reflection have been approximated to unity. The square modulo of this expression leads to the following modulated components

$$J_0\, J_1\, U_{00}\, U_{10} \left[\left(\frac{\theta}{\theta_\infty} \right) \cos[\phi_{00}(z)] \;+\; \left(\frac{a}{w_0} \right) \sin[\phi_{00}(z)] \right] \sin\Omega\, t \tag{3.60}$$

Unlike the Anderson method, information on the rotation and translation of the optical axis comes from just the quadrature component with the mixing determined by the Guoy phase $\phi_{00}(z)$. In particular, the translation term is given by the coefficient of $\sin[\phi_{00}(z)]$ whereas the angle is given by the $\cos[\phi_{00}(z)]$ term.

The information on misalignment mixing depends upon the Guoy phase in which the observation is made. An optical telescope placed in front of the photodiode could adjust the phase. The main drawback is that in order to optimize the measurement, two photodiodes, one placed at a Guoy phase ϕ_1 while the other at $\phi_1 + \pi/2$, would be necessary. At the same time, the method offers the advantage of releasing the restraints on the modulation frequency.

3.5.3 The Quadrant Photodiode

Both with the Anderson and the Ward technique, a photodiode monitoring the power of a beam integrates on the transverse plane of the beam. However, the product $U_{00}(x) \times U_{10}(x)$ is an odd function of x and its integral is zero. A special photodiode, capable of integrating on the half plane, is therefore necessary. The quadrant photodiode, schematically shown in fig.(3.12), is able to integrate on the quarter plane. The sum of the signals coming from quadrant 1 with 2, 2 and 3, 3 and 4, and 4 and 1, give the power in the four half planes. By taking the difference between the

half planes horizontally and vertically, it is possible to recuperate the coefficient of the product $U_{00}(x) \times U_{10}(x)$. In particular, it can be shown that

$$\int_0^{\infty} U_{00}(x)\, U_{10}(x)\, dx \; - \; \int_{-\infty}^{0} U_{00}(x)\, U_{10}(x)\, dx \; = \; \sqrt{\frac{2}{\pi}} \tag{3.61}$$

Chapter 4

The VIRGO Project

The VIRGO project, supported by the Italian Istituto Nazionale di Fisica Nucleare (INFN) and the French Centre National de la Recherche Scientifique (CNRS), is a gravitational wave antenna to be built in Cascina (Pisa, Italy). Its objective is to directly detect gravitational waves and, in collaboration with other detectors, to perform gravitational wave astronomy with a planned sensitivity of $\tilde{h} = 10^{-21}/\sqrt{Hz}$ @ 10Hz and $\tilde{h} = 3 \times 10^{-23}/\sqrt{Hz}$ @ 500Hz.

This chapter describes the VIRGO detector, and in particular the optical configuration implemented, the suspension system for the mirrors, the laser system, the tube, the vacuum system and the foreseen sensitivity.

Particular attention is then given to the Global Control system. Its task is to monitor and supervise three phases: the acquisition of lock, the linear locking regime and autoalignment. An outline of the specifications for such a control is given as well as the software and hardware architecture of the system.

4.1 The Optical Configuration

The optical configuration of VIRGO consists of a Michelson interferometer with Fabry-Perot arm cavities [fig.(2.10)] with the following characteristics;

i. both Fabry-Perots of length $L = 3$ km and finesse $\mathcal{F} = 50$;

ii. a recycling cavity of length $l_r \equiv l_0 + (\frac{1}{2})(l_1 + l_2) = 12$ m and recycling gain $G_{rec} = (2\mathcal{F}_{rec})/\pi = 50$;

iii. an arm asymmetry of $\Delta l \equiv l_2 - l_1 = 0.8$ m;

The laser source will develop $P = 20$ W of light power in the fundamental mode to limit the equivalent shot-noise spectral density to

$$\tilde{h}_{shot} = \frac{1}{2k(2\mathcal{F}/\pi)L}\sqrt{\frac{\hbar\omega}{\eta G_{rec} P}} \simeq 10^{-23}\frac{1}{\sqrt{\text{Hz}}} \tag{4.1}$$

where $\lambda = 1.064\,\mu$m is the laser light wavelength and $\eta = 0.85$ is the photodiode efficiency. However, this performance is obtained only with the use of very low loss mirrors. By defining the *coupling factor*

$$\rho \equiv \frac{\mathcal{L}\mathcal{F}}{\pi} \tag{4.2}$$

where $\mathcal{L}$ denotes the Fabry-Perot losses, it can be shown[13] that eq.(2.62) holds only in the case of an under-coupled cavity, i.e. $\rho << 1$. Reasonable mirror losses of $\sim 2 \times 10^{-5}$ guarantee such under-coupling.

Furthermore, it can be shown[13] that the stored power in the recycling cavity is maximized as the recycling mirror reflectivity r_0 satisfies the condition

$$r_0^2 = (1 - p_0^2)(1 - p_{BS}^2)(1 - \rho) \tag{4.3}$$

where p_0^2 denotes the power losses of the recycling mirror and p_{BS}^2 the power losses for the beam splitter. This condition leads to *optimal recycling*, with a recycling gain G_{rec} inversely proportional to the total interferometer losses $\mathcal{L}_{itf}$

$$G_{rec} = \frac{1}{\mathcal{L}_{itf}} \tag{4.4}$$

The desire for under-coupled Fabry-Perot cavities with a recycling gain inversely proportional to the total losses demands the use of mirrors with losses lower than 10ppm.

Light is forced to make many passages in the optical substrates. For this reason, the quality of the optical components for VIRGO are on the limit of today's technology. Therefore, the substrates, and in particular those for the front mirrors of the Fabry-Perots and the recycling mirror, need to be extremely pure, with low diffusion and low absorption. Furthermore, the coatings must withstand large light power ($\sim$ 1kW in the recycling cavity) as well as a constraint on the surface deformation of less than $\sim \lambda/100$.

The modulation frequency for the locking and detection scheme has not been defined to date but will lie in the frequency rage $6 - 18$ MHz. It has been shown[26] that for a given modulation frequency Ω, the value of Δl for which there is maximal sideband leakage at the dark fringe port is

$$\cos\left(\frac{\Omega\,\Delta}{c}\right) = r_0\, r_{itf}(\omega_0 \pm \Omega) \tag{4.5}$$

where $r_{itf}(\omega_0 \pm \Omega)$ is the reflectivity of the interferometer for the two sidebands.

4.2 The Beam Source

The laser system is conceived to produce and adapt the beam to the interferometer. It consists of a laser source, an input bench and a mode-cleaner designed to provide light in the fundamental mode while fulfilling the specifications on the output power, the frequency and power fluctuations and beam jitter.

4.2.1 The Laser System

The chosen light source is a Nd:YAG laser of wavelength $\lambda = 1.064\,\mu$m with an output power of 20 W in the fundamental mode. It has been preferred over other sources, such as Argon sources, for its frequency and geometrical characteristics. To date, VIRGO has conceived and developed a 10 W mono-mode laser that will be used for the central area interferometer (CITF). The 20 W laser could be realized by phase locking two 10 W twin lasers.

The power comes out of a Nd:YAG slab, referred to as *slave* laser, which is pumped by a set of ten laser diodes phase locked, referred to as *injection locking*[19], to a commercial 700 mW Nd:YAG laser, known as the *master* laser. The optical cavity, within which the slab is placed, consists of four mirrors in a bow-tie configuration. This configuration has been chosen so as to optimize laser power with frequency characteristics.

4.2.2 The Input Bench

The input bench is an optical bench placed in vacuum, suspended by a superattenuator. It is made of three main components which need to be seismically and acoustically isolated:

- the input and output mode-cleaner mirrors;

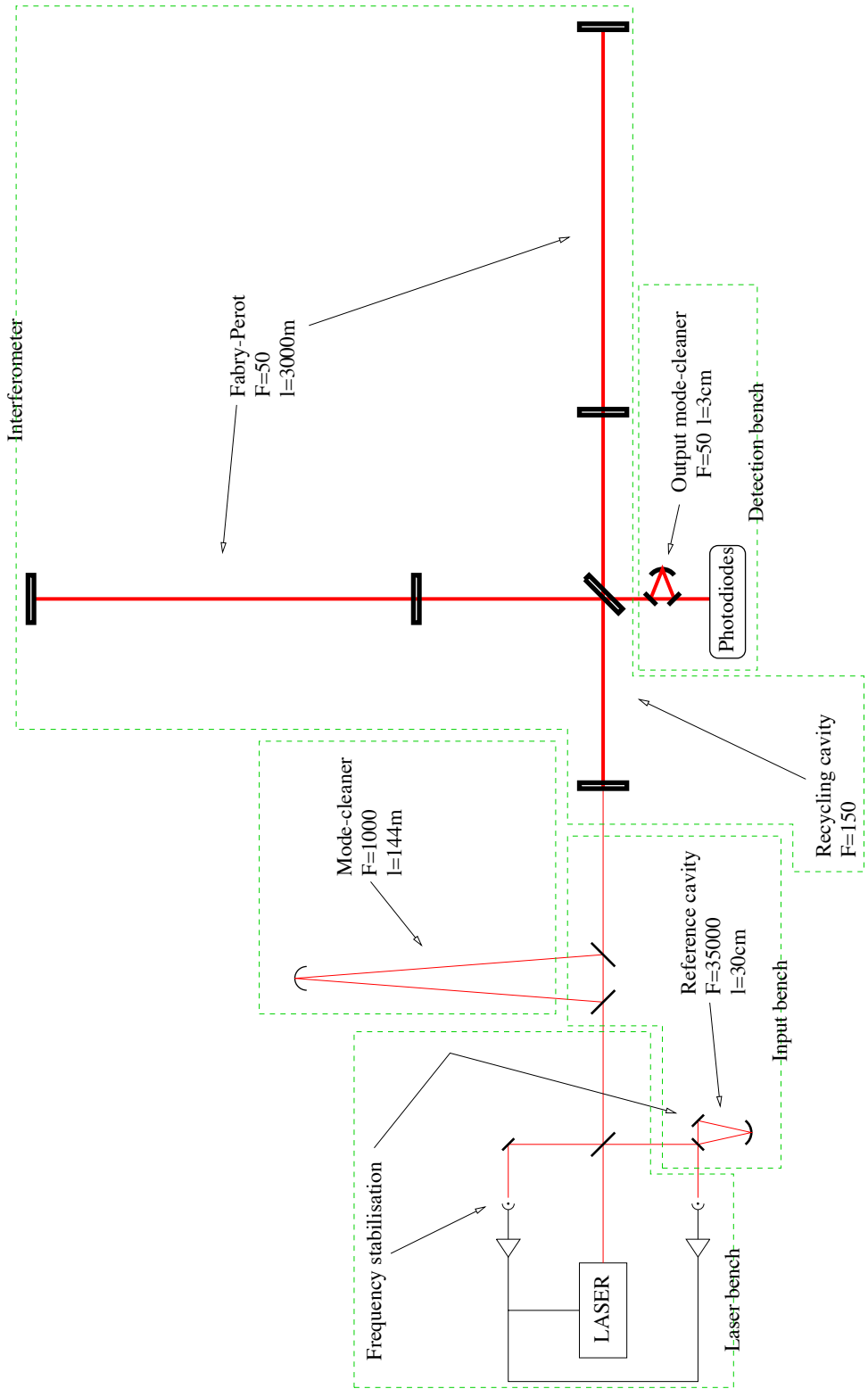

Figure 4.1: The optical configuration of VIRGO .

- the telescope adapting the beam from the mode-cleaner to the interferometer;
- the frequency pre-stabilization cavity rigidly attached to the bench.

The beam propagation is schematically shown in fig.(4.1). A pick-up plate is positioned along the output beam path. The plate reflects the beam from the laser source, sending it to the pre-stabilization cavity, along with the beam coming back from the interferometer. Both of these reflected beams are used for the frequency stabilization of VIRGO, see [24].

The beam transmitted by the plate is sent to the input mode-cleaner mirror. The light resonates in the cavity and is transmitted through the output plane mirror. An optical telescope then adapts and positions the beam waist to the input mirrors of both Fabry-Perot cavities.

4.2.3 The Input Mode-Cleaner

The Mode-Cleaner is a triangular cavity, 144 m long and with a finesse of $\mathcal{F} = 1000$. Its function is to filter the beam defects as well as the position noise. It consists of three mirrors: the two plane mirrors, input and output, located on the input bench, and a third concave mirror, suspended by a superattenuator located in the mode-cleaner tower.

All input geometrical beam fluctuations are seen by the mode-cleaner cavity axis as a linear combination of transverse modes. The main characteristic of the cavity is that once the fundamental TEM_{00} mode resonates, the higher order modes are all reflected back to the laser source, thus allowing the transmission of only the fundamental mode. The cavity acts as a spatial filter. A discussion of the mode-cleaner prototype, developed at LAL in Orsay, will be given in Ch.6.

4.2.4 Laser Source Requirements

The requirements on this system are indeed demanding. The presence of asymmetries in the two arms, such as the arm difference ΔL and finesse difference $\Delta\mathcal{F}$, make the interferometer output sensitive to frequency fluctuations $\delta\tilde{\nu}$. The equivalent spectral density noise can be simplified as

$$\tilde{h}_{\delta\nu} = \frac{\delta\tilde{\nu}}{\nu}\left(\frac{\Delta L}{L} + \frac{\Delta\mathcal{F}}{\mathcal{F}}\right) \tag{4.6}$$

where $\mathcal{F}$ is the average finesse, L is the arm length and ν the laser frequency. To prevent introduction of noise in the foreseen sensitivity curve $\tilde{h}$, the laser needs to satisfy the condition

$$\frac{\delta\tilde{\nu}}{\nu} < \frac{\tilde{h}}{\left(\Delta L\,/\,L + \Delta\mathcal{F}\,/\,\mathcal{F}\right)} \tag{4.7}$$

which, by assuming a total asymmetry of 1%, results in

$$\begin{aligned} \delta\tilde{\nu} &\leq 10^{-4} \quad [Hz/\sqrt{Hz}] \;@\; 10\,Hz \\ \delta\tilde{\nu} &\leq 10^{-6} \quad [Hz/\sqrt{Hz}] \;@\; 500\,\mathrm{Hz} \end{aligned} \tag{4.8}$$

Such requirement is met with the use of two control systems in cascade. The first consists of a pre-stabilization rigid cavity able to bring the fluctuations down to the $\delta\tilde{\nu} \leq 10^{-4}[Hz/\sqrt{Hz}]$ level. The second, instead, makes use of the interferometer itself as a reference. For an in-depth treatment refer to [24].

Furthermore, the RMS motion of the differential mode Δl causes an offset that couples with power fluctuations. By indicating with $\tilde{\phi_0}$ the spectral density phase change induced by the residual motion of the differential mode, the equivalent spectral density phase change can be written as

$$\tilde{\phi} = \frac{\delta\tilde{P}}{P}\,\tilde{\phi_0} \tag{4.9}$$

where P is the laser power and $\delta\tilde{P}$ its spectral fluctuations. By requiring shot-noise sensitivity, the power fluctuation with the differential motion must satisfy the condition

$$\tilde{\phi_0} \leq \sqrt{\frac{h\,\nu}{\eta\,P}} \Big/ \frac{\delta\tilde{P}}{P} \tag{4.10}$$

The requirements on the power fluctuations have been set to

$$\begin{aligned} \frac{\delta\tilde{P}}{P} &< 3\times10^{-5} \quad [1/\sqrt{Hz}] \quad @ \;\; 10\,\mathrm{Hz} \\ \frac{\delta\tilde{P}}{P} &< 3\times10^{-7} \quad [1/\sqrt{Hz}] \quad @ \;\; 500\,\mathrm{Hz} \end{aligned} \tag{4.11}$$

4.3 The Detection Bench

The main objective of the detection bench system is the measurement of dark fringe light power after an improvement in the contrast C. It will also

- separate the two output beams coming from the interferometer: the dark fringe and the reflected beam off of the second face of the beam splitter;
- adapt the beams;
- spatially filter the dark fringe so as to increase the contrast;
- perform the photodetection and signal treatment.

In order to fulfill these functions, a series of subsystems are necessary:

- a suspended optical bench, installed in the detection tower, in order to attenuate the acoustical noise and on which the following components are placed:
  - a mode-cleaner, shown in fig.(4.1), consisting of a triangular cavity, maintained in resonance, for the spatial filtering of the dark fringe;
  - an optical telescope for adapting the size of the beam to the mode-cleaner and to the photodetectors;
  - an optical system for the alignment of the bench in order to be able to follow the secondary beam;
- an external optical bench where all the photodetectors are situated;
- an amplification, filtering, demodulation and sampling system of the signals from the photodetectors.

4.3.1 The Output Mode-Cleaner

The mode-cleaner, of which a prototype has been developed and tested at VIRGO LAPP[25], consists of a monolithic triangular cavity of finesse 50 and length 3 cm, as shown in fig.(4.2). Its function is to improve the contrast defect generated by an asymmetry in the interferometer. The dominant phenomenon at the origin of the contrast is the wavefront deformation due to imperfections in the optical components. The wavefront defects generate the presence of high order modes in the beam. The property of the output mode-cleaner, just as the input one, is to transmit only the fundamental mode. The expected contrast defect after the filtering is

$$1 - C \sim 10^{-4} \tag{4.12}$$

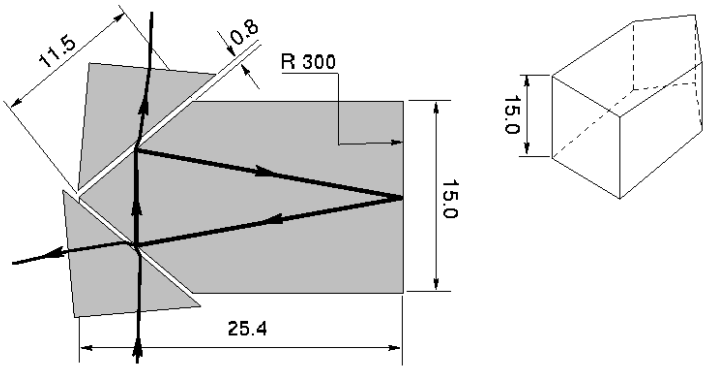

Figure 4.2: The output mode-cleaner with the propagating beam. All units in mm.

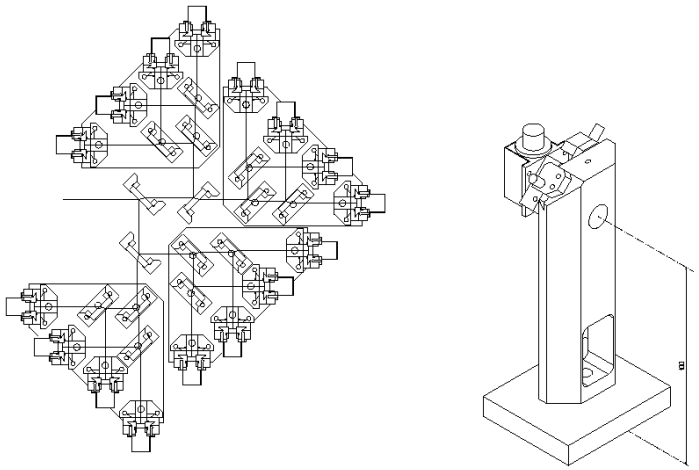

Figure 4.3: Left: the configuration of the 16 photodiodes needed for the photodetection of the dark fringe. Right: three dimensional view of a photodiode support.

4.3.2 The Photodiodes

The main function of the bench is photodetection and it must have

- a bandwidth larger than tens of MHz if the modulation frequency is of the order of MHz;
- a high quantum efficiency @ 1.064μm;
- the capability of detecting power of the order of 1 W.

By limiting the power on a photodiode to 100 mW, a set of 16 photodiodes is necessary for detection. The chosen configuration is shown in fig.(4.3).

4.4 The Superattenuator

None of the interferometric detectors under construction around the world implement a suspension system as sophisticated as VIRGO's superattenuator. It consists of a system of mechanical oscillators conceived so as to reduce the test mass movement down to 3×10^{-18} $[m/\sqrt{Hz}]$, corresponding to an equivalent strain of $\tilde{h}_{sis} = 10^{-21}[1/\sqrt{Hz}]$ @ 10 Hz. This is a critical frequency

region due to an expected abundance of gravitational wave sources, such as pulsars and coalescing binaries[7].

The superattenuator is made of a pre-isolator stage integrated with a chain of five pendula and is shown in fig.(4.4). It is designed so as to limit the resonant frequencies within a few Hertz, thus producing an attenuation of more than 10^{-10} above 10 Hz.

However, a chain of pendula does not attenuate the vertical and angular degrees of freedom. Due to the unavoidable mechanical couplings, these vibrations partially shift to the horizontal motion of the test mass. It is for this reason that the isolation system must attenuate in all degrees of freedom.

4.4.1 The Mechanical Filter

Each pendulum in the suspension chain is referred to as a *mechanical filter* and is shown in fig.(4.5) and fig.(4.6). It consists of a rigid steel cylinder suspended to its center of mass, designed to attenuate in the vertical, horizontal and angular degrees of freedom[33]. It is connected to the others via a steel wire 1.15 m long generating a resonance frequency at 0.46 Hz. The whole chain, once assembled, is about 9 m long.

Vertical attenuation is obtained by a set of converging triangular blade springs whose tips are attached to a vertical column capable of moving only in the vertical direction, as shown in fig.(4.6). The lower stages are then attached to this column. These blades are pre-bent so as to return flat and horizontal once they are loaded. In this way, the chain acts not only as a system of five pendula in the horizontal direction, but also as a chain of serially coupled oscillators in the vertical direction as well. However, the lowest resonant frequency of the blades lies around 1.5 Hz, which is above the pendulum resonant frequency of 0.45 Hz. A system of magnetic anti-springs is used to reduce the vertical stiffness of the blades in order to displace the main vertical resonant frequency of each filter below the pendulum one. In this way, the detection band will be limited by the horizontal motion of the chain and not by the vertical ones.

The anti-spring system[33] consists of two permanent magnets facing each other with opposite horizontal magnetic moment and constraint to move in the vertical direction. Once the magnets are perfectly aligned, the repulsive force has a null vertical component. However, once a magnet moves away from this unstable equilibrium point, a repulsive force appears along the vertical axis. This generates a resonant frequency f_0 for a vertical oscillator of the form

$$f_0 \equiv \frac{1}{2\,\pi\,\sqrt{m}}\sqrt{k - \frac{F_0}{d}} \tag{4.13}$$

where d is the distance between the magnets, F_0 is the repulsive force modulo, k the elastic constant of the blade springs and m the mass of the oscillator. By choosing appropriate values for F_0 and d, the resonant frequency is lowered to 0.4 Hz.

The chain acts as an angular attenuator as well. The filters are designed with a large moment of inertia and short lever arms between the two points where the wires are attached. Also, the two attachment points, which can be seen in fig.(4.6), are connected as close as possible to the filter center of mass. This design leads to tilt mode frequencies below 1 Hz. Furthermore, the low angular spring constant of the small diameter steel suspension wires lead to very low angular frequencies around the vertical axis.

4.4.2 The Pre-Isolator stage

The pre-isolator stage consists of three rigid columns, each connected to the ground through a flexible joint, and supporting a table. On the table-top lies a modified filter, named filter 0, acting as a vertical attenuator. This system forms the pre-isolator stage and can be seen in fig.(4.4). The chain of mechanical filters is then suspended from filter 0.

There are many advantages in the use of such a system. To begin with, assuming an elastic constant k for the joint and a length L of the inverted pendulum, the resonant frequency f_0 for

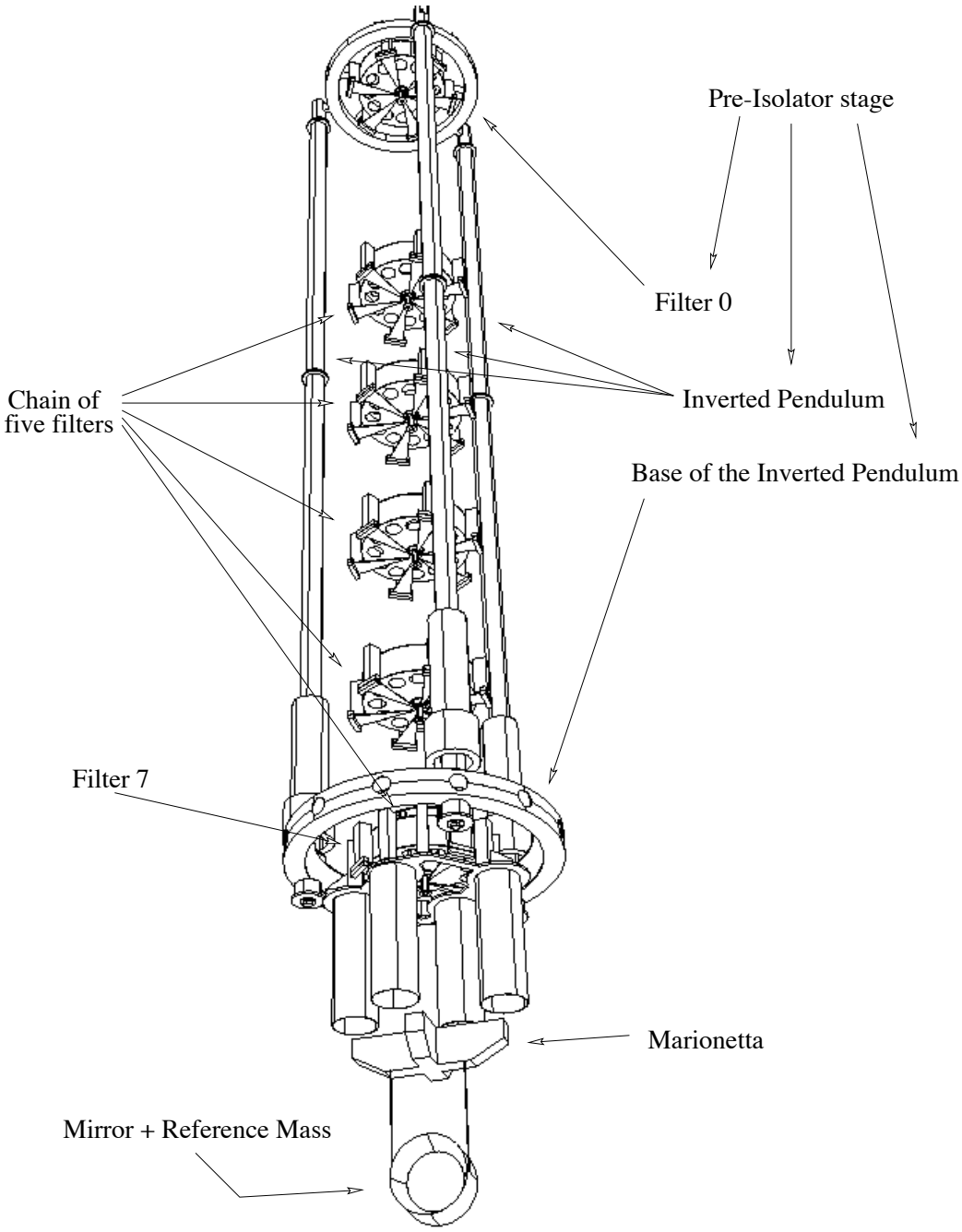

Figure 4.4: The superattenuator.

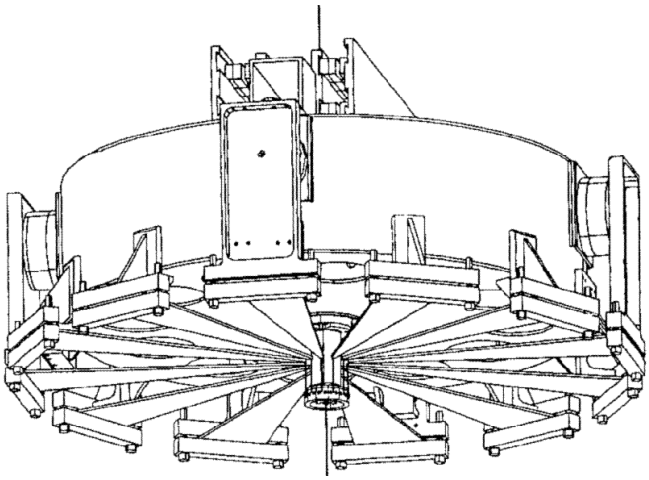

Figure 4.5: The mechanical filter: perspective view. Notice the twelve triangular blades.

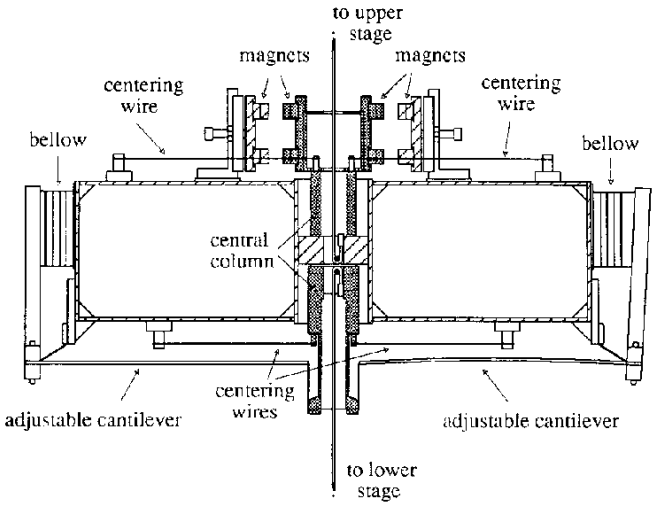

Figure 4.6: The mechanical filter: side view. The movable sections are shaded.

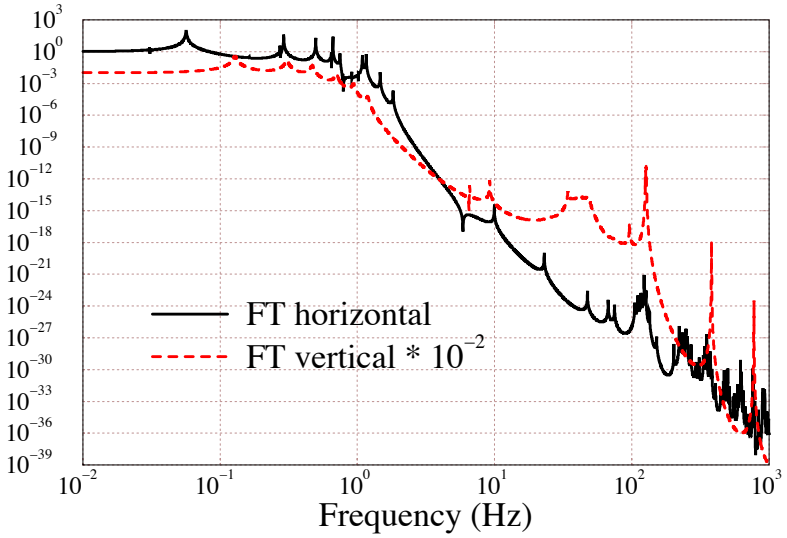

Figure 4.7: The calculated transfer function of the pre-isolator stage with a chain of five mechanical filters.

this oscillator is

$$f_0 = \frac{1}{2\,\pi}\sqrt{\frac{k}{M} - \frac{g}{L}} \tag{4.14}$$

where M is the load of the system. By properly tuning the parameters k, L and M, it is possible to shift the resonant frequency to a lower value, which is foreseen to be 30 mHz.

Secondly, this stage provides a movable suspension point for the superattenuator chain. Very low frequency ground motion may drift the mirror position ($\sim$1 mm) with respect to ground, once the interferometer is in operation. The inverted pendulum would then offer the possibility for the control of the suspension point. Furthermore, the system requires *low* forces in order to be controlled. Below its resonance frequency f_0, the force needed to displace the load of mass M a quantity δx is

$$F \simeq M\,\omega_0^2\,\delta x \tag{4.15}$$

This means that for a load mass $M = 1$ ton, frequency $f_0 = 30$ mHz, only 0.36 N are necessary in order to displace the suspension point of 1 cm.

A prototype[23] of the pre-isolator stage has been constructed in Pisa with promising results. Fig.(4.7) shows the calculated transfer function for a pre-isolator stage with a chain of five mechanical filters. The overall attenuation factor at 10 Hz is about 10^{-15}.

4.4.3 The Marionetta and Reference Mass/Mirror System

The last filter, known as filter 7, suspends the *marionetta*, the final stage supporting the mirror. It has been designed so as to steer and align the test mass once the interferometer is operative. It consists of a cross structure from which are suspended two wire loops holding the mirror and the reference mass. From filter 7, forces are applied so as to control the residual motions of the test mass up to 10μm in the frequency band 0.1-1 Hz without injecting noise into the system.

High frequency control ($>$ 1 Hz) is performed with the reference mass. Four coils are mounted on the reference mass facing the four magnets placed on the mirror, thus allowing a fine control of the test mass once the interferometer is running.

4.5 The Vacuum System

Any gas density fluctuations in the volume of air through which the laser beam travels induce fluctuations in the index of refraction, therefore causing a phase change in the electromagnetic beam. In order to limit such variations, the interferometer is operated under vacuum.

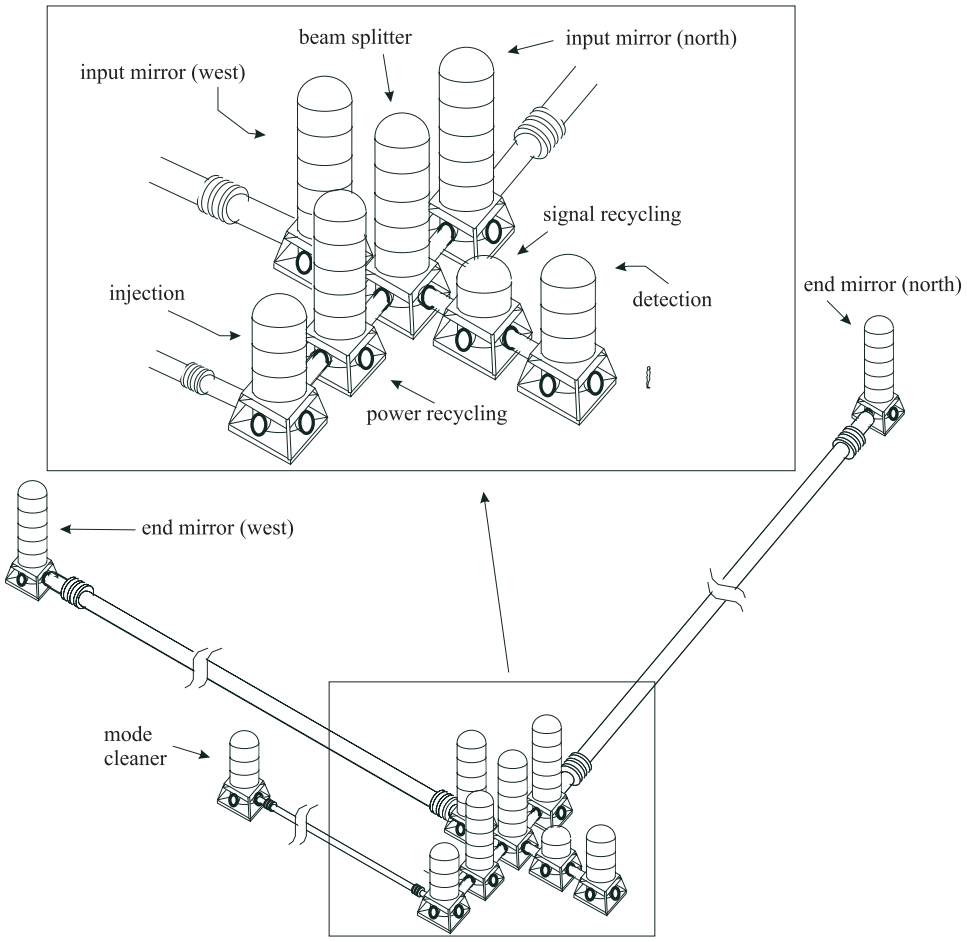

Figure 4.8: The vacuum system.

The vacuum system, as shown in fig.(4.8), is divided in two parts: the tube and the towers. The tube contains the propagating beam and is made of 15 m sections of 1.2 m in diameter, connected to each other by bellows and resting over special supports so as to allow dilation of the material during the baking procedure and dilation due to daily and seasonal temperature changes.

By requiring the noise fluctuations in the refractive index to be a factor 10 below the dominating noises, the limit for gas pressure is required to be 10^{-7} mbar. However, other considerations, such as the monitoring of mirror cleanliness and vacuum control lead to the design values:

- 10^{-9} mbar for hydrogen;
- 10^{-13} mbar for hydrocarbons;
- 10^{-10} mbar for the other gases.

The tube is also equipped with *baffles* designed to trap stray light. Any mirror imperfection would scatter light which would then be reflected by the vibrating pipe walls. If any of these reflected photons recombine with the main beam, a phase noise would arise. Such light traps,

made of an absorbing steel and shaped as truncated cones, are designed to absorb these spurious photons, thus avoiding their recombination with the main beam [34].

The towers hold the superattenuator and, due to the presence of a large number of devices and cables that outgas, will be maintained at a lower pressure with respect to the tube. A separating roof divides the ultra-high-vacuum of the tube from the 10^{-6} mbar pressure of the towers.

4.6 Foreseen Sensitivity of VIRGO

The thermal noise of the last stage suspension consists of three contributions:

1. the pendulum mode, dominant in the frequency region below 50 Hz;
2. the mirror internal modes, with resonances in the frequency range above 5kHz but with a significant tail contribution in the 50-500 Hz frequency range;
3. the violin modes, dominant in the intermediate frequencies, above 300 Hz.

An estimate of the noise contributions, performed by [21], resulted in

$$\tilde{h}_{pend} = \frac{5 \times 10^{-19}}{f^{5/2}} \quad [1/\sqrt{Hz}] \tag{4.16}$$

for the pendulum thermal noise for frequencies up to 50 Hz, and

$$\tilde{h}_{mir} = \frac{6 \times 10^{-22}}{f^{1/2}} \quad [1/\sqrt{Hz}] \tag{4.17}$$

for the mirror internal noise dominating in the frequency range between 50-500Hz.

The foreseen sensitivity curve for VIRGO is shown in fig.(4.9) with the contributions from the different sources of noise. The fundamental contributions are

- the seismic wall expected at 2 Hz;
- the *Newtonian noise*, contributing below 10 Hz, generated by low frequency mass density fluctuations which induce a stochastic gravitational field that couples directly to the mirrors (see [22]);
- pendulum thermal noise expected to dominate the frequency region between 10 and 30 Hz;
- mirror thermal noise which dominates between 30 and 500 Hz;
- shot noise dominating above 500 Hz.

The peaks present above 300 Hz are due to the violin mode resonances and their harmonics, whereas the first mirror internal resonance is found at 5 kHz. The peak found at 7 Hz is thermal noise associated to the main mode of the marionetta-mirror system.

4.7 Online/Offline Activities

The activities around the electronic output of all the sensors of the interferometer can be classified in the following way:

- online activity, concerning
  - interferometer control;
  - the acquisition, processing and monitoring of data produced by the sensors and the control processes;

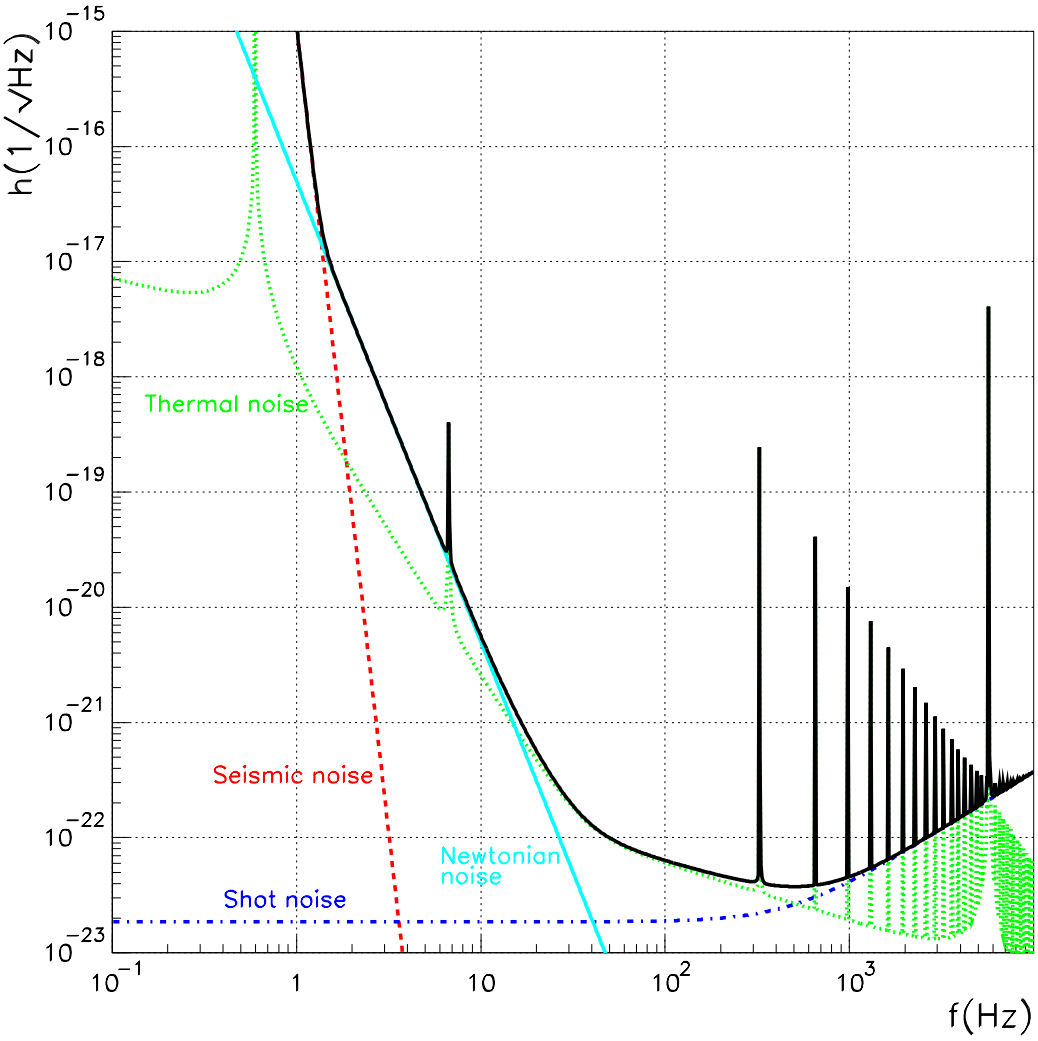

Figure 4.9: The foreseen VIRGO sensitivity curve.

- offline activity, whose main objective is the analysis of the collected data for the extraction of possible gravitational wave events;

- and simulation activity, for the study of the interferometer response to noise sources and excitation due to gravitational wave radiation.

In particular, the fundamental requirements for the online system are:

- a data acquisition with a sampling frequency of 20 kHz;

- a real time control performed at 10 kHz with fast processes involved;

- full data archiving;

- data quality check;

- data selection for particular gravitational wave sources.

Most of the signals produced by the different sensors around the detector are locally processed to compute and correct the local system in question within a given set of tolerances. The local suspension control and the vacuum system, to name a few, are examples of such local systems. A higher level control system, referred to as *Global Control*, guarantees the proper functioning of the interferometer by monitoring and acting upon both the laser system and the suspension system. This system is the subject of the section to come.

As an apparatus, VIRGO is composed of subsystems that have to run either on their own or as correlated components. All the subsystems are controlled and operated through the *Supervisor Control System*. Its main function is to keep track of, request, allow or inhibit modifications of the status of the various components of the interferometer in order to drive and maintain VIRGO in its functioning state. It is intended to provide the overall user interface with a graphic display of the status of all VIRGO components.

Also, the architecture of the control and read out systems must take into account the large distances separating the components. The controls must then be synchronized to a central *Timing System*: the knowledge of the precise timing of the various measurements and actions performed around the detector is of key importance.

The data produced by the sensors, as well as the corrections applied to the systems, are referred to as *raw* data and are collected and structured by a *Frame Builder*. A *frame* is a unit of information which records the detector behavior over a finite time interval, typically 2s. Each frame, organized as a C structure, consists of two sets of structures:

- all the raw data collected by the sensors;

- the *online* processing containing the reconstructed data set [t,h(t)] with the necessary auxiliary information.

The *Raw Data Archiving System* collects and stores all the frames produced by the Frame Builder. These data are necessary for a possible reprocessing due to an improvement of the off-line data analysis. The expected data flow rate is about 100 Gbyte/day and it will be archived.

The *Online Data Quality* task will survey constantly the quality of the produced data. It uses the signal induced by the calibrators and the environment monitoring, and runs data quality algorithms, thus providing a real time quality check. The corresponding information is stored in the data storage system to allow further data selection.

A *Data Selection* is necessary in order to reduce the amount of data for analysis. The goal would be a reduction in size of more than one order of magnitude. Trigger algorithms looking for burst events, such as binary coalescences and supernovae explosions, are necessary and the event candidates will be selected using simple and robust search algorithms.

4.8 Global Control

One of the main subsystems within VIRGO, Global Control enables and foresees the proper functioning of the interferometer. In particular, its tasks are:

1. *acquisition of lock* or *non-linear locking* whose objective is to bring the mirrors from their free running motion to a regime where the linear locking algorithm can be applied;

2. *linear locking*, the process that maintains the interferometer in operation by keeping

   i. light resonating in both Fabry-Perots as well as the recycling cavity;

   ii. a condition of dark fringe at the output of the interferometer;

3. *autoalignment* for the mirror angular control;

The objective of this thesis is the study of both the autoalignment and the acquisition of lock for the first phase of the VIRGO project, called the central area interferometer (CITF) which will be described in the next chapter.

4.8.1 Specifications

It has been shown how the superattenuator filters ground vibrations according to the transfer function shown in fig.(4.7). The residual motion will be concentrated below 1 Hz and in particular at the inverted pendulum frequency of 30 mHz, as shown in fig.(5.6a) and fig.(5.6b). The motion amplitude estimated is of the order of ten times the wavelength of light. A local damping control will be able to reduce such oscillations down to an amplitude of one wavelength. However, such damping will not be able to reach the requested precision. It is the task of the linear locking scheme to control the mirrors to within the specifications.

For the correct behavior of the interferometer, the following RMS conditions must be met:

1. by denoting with L the length of one of the Fabry-Perot, the length fluctuations δL of both cavities must satisfy the condition

$$\delta L \; < \; \frac{1}{10} \, \frac{\lambda}{4 \, \mathcal{F}} \; = \; 5 \times 10^{-4} \, \lambda \tag{4.18}$$

   where $\mathcal{F}$ is the finesse of both Fabry-Perots and λ the laser light wavelength. This condition is due to the requirement that the fluctuations be one tenth of half width at half maximum (HWHM) of the resonance peak;

2. by defining l_r as the recycling cavity length, its fluctuations δl_r must satisfy a similar condition:

$$\delta l_r \; + \; 2 \left(\frac{2 \, \mathcal{F}}{\pi} \right) \delta L \; < \; 8 \times 10^{-5} \, \lambda \tag{4.19}$$

3. any phase offset ϕ_{offset} from complete destructive interference couples directly with laser power fluctuations. To be shot-noise limited implies the following condition

$$\phi_{offset} \; = \; 2 \, k \left[\frac{2 \, \mathcal{F}}{\pi} \, (\, \delta L_2 - \delta L_1 \,) + \Delta l \right] \; < \; \sqrt{\frac{h \, \nu}{P_0}} \; / \; \frac{\delta P_0}{P_0} \tag{4.20}$$

   which leads to

$$\frac{2 \, \mathcal{F}}{\pi} \, (\, \delta L_2 - \delta L_1 \,) + \Delta l \; < \; 10^{-4} \, \lambda \tag{4.21}$$

   where Δl is the Michelson arm length difference.

Furthermore, it has been shown[26] that the maximum residual displacement tolerated for VIRGO with a sensitivity of a third of the required sensitivity, i.e.

$$\begin{aligned} \tilde{h} &= \frac{10^{-21}}{3} \quad [1/\sqrt{Hz}] \ @ \ 10\,\mathrm{Hz} \\ \tilde{h} &= \frac{3 \times 10^{-23}}{3} \quad [1/\sqrt{Hz}] \ @ \ 500\,\mathrm{Hz} \end{aligned} \tag{4.22}$$

leads to the following conditions for the spectral density linear displacement of the mirrors:

	@ 10 Hz	@ 500 Hz
Fabry-Perot Mirror (m/$\sqrt{\mathrm{Hz}}$)	10^{-18}	3×10^{-20}
Beam Splitter (m/$\sqrt{\mathrm{Hz}}$)	3×10^{-17}	9×10^{-19}
Recycling Mirror (m/$\sqrt{\mathrm{Hz}}$)	3×10^{-15}	8×10^{-17}

4.8.2 RIOT

The processes involved for the Global Control functionalities are located in the *RIOT* crate, shown in fig.(4.10) and whose acronym stands for Real tIme glObal conTrol, placed in the Central Building of VIRGO. RIOT will collect the signals coming from the various photodiodes around the interferometer, interpret them so as to compute the necessary corrections and send orders to the suspension and laser systems.

The functionalities are split into two types:

- the processes involving an action on the optical components, referred to as *action* processes:
  - *Longitudinal Locking* (10 kHz):
    for the longitudinal control of the mirrors within specifications;
  - *Autoalignment* (100 Hz):
    for the mirror angular control within the requirements;
  - *Non-Linear Locking* (100 Hz):
    to bring the interferometer into operation;
  - *Emergency Handler* (100 Hz):
    which in case of loss of lock is able to recuperate control, bringing the detector back into operation without going through the non-linear locking phase;
- the processes which analyze the running of the interferometer, referred to as *checking* processes:
  - *Longitudinal Monitor* (10 Hz):
    which supervises the proper running of Longitudinal Locking;
  - *Alignment Monitor* (10 Hz):
    which resembles the longitudinal monitoring;
  - *Strategy Handler* (1 Hz):
    where the new parameters for the control are computed.

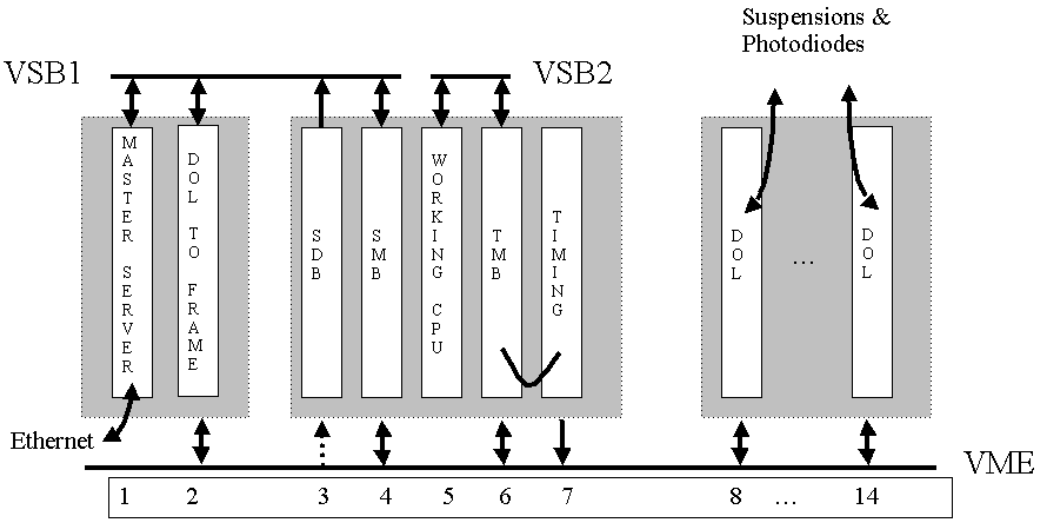

Figure 4.10: The RIOT crate.

Software and Hardware Architecture

The architecture design must be flexible enough so as to facilitate evolutions and must also minimize the data flow between processes. Furthermore, for the correct functioning of RIOT, it must separate all functions into mostly independent processes while minimizing the interferences. For this reason, processes such as the Longitudinal Locking must not be perturbed by the rest of the system.

In order to achieve this, the hardware architecture, shown in fig.(4.10), has been chosen as follows. The photodiode and actuator signals are sent and received by Digital Optical Links (DOLs) consisting of VME slave boards. A CES PowerPC board, referred to as *Working CPU*, performs the Longitudinal Locking task. However, the CPU in question is not able to quickly access and retrieve data due to the large amount of boards. For this reason, a fast data transfer board is necessary, consisting of a homemade board, the *Transparent Memory Board* (TMB), synchronized to the *Timing* board and able to quickly transfer the data from the VME to the VSB bus and vice versa. In this way, the Working CPU can quickly access the data.

A second CES PowerPC board, the *Master Server*, is in charge of Autoalignment, Non-Linear Locking, data access and distribution. In order to do this, two boards are introduced: the homemade *Spy Data Board* (SDB) and the *Shared Memory Board* (SMB). The SMB is a VME/VSB slave board that allows the transmission of status and command signals between the Working CPU and the Master Server while transmitting the Alignment and Non-Linear Locking corrections to the Working CPU.

The SDB, instead, is a VME spy/VSB slave introduced so as to perform a fast data retrieval without perturbing the synchronous processes. Once the data is available on the VSB bus, the Master Server is able to access it.

A workstation, not shown in figure, the *Global Control Survey* workstation, will perform the monitor functionalities: the Autoalignment Monitor, the Locking Monitor, the General Monitor, the Strategy Handler. The workstation will connect, through Ethernet, with RIOT.

Part II

Chapter 5

The Central Area Interferometer

VIRGO will first operate in a test configuration consisting of a recycled Michelson, referred to as the Central Area Interferometer (CITF), whose 'end' mirrors are placed at the location of the Fabry-Perot input mirrors. The detector will have the same suspension system, laser source (with an output power of 10 W), detection bench and acquisition system as the full VIRGO apparatus, providing

- a complete, full size test of all sub-systems;
- an opportunity to study the various noise contributions.

The CITF will be completely contained in the central building of VIRGO.

This chapter presents a study of the CITF optical response to the longitudinal and angular motions of the mirrors: the strategies of lock acquisition, locking and alignment need to take this response into account. In particular, it will be shown how

- when the CITF is in an unlocked state, the ratio of photodiode signals can be used to detect and lock the dark fringe regardless of the recycling stored power;
- an algorithm using an 8 quadrant photodiode configuration is presented capable of reconstructing the mirrors' angles once the CITF is locked.

A study on the CITF autoalignment will also be presented consisting of the control of the mirrors' angles by using the steering filter/marionetta system.

Before presenting these results, a description of the interferometer is given as well as the foreseen mirror displacements in free motion, the aimed sensitivity and the mirror control requirements. The reader is addressed to [35, 36] for further details.

5.1 The Longitudinal Control

The interferometer is schematically shown in fig.(5.1), where M_0 denotes the recycling mirror, M_{BS} the beam splitter and $M_{1,2}$ the end mirrors. The detector is said to be operational once it fulfills the specifications on

1. the condition of dark fringe implying the control of the phase

$$k\,\Delta l \tag{5.1}$$

   where $k = 2\,\pi\,/\,\lambda$ is the wave number and $\Delta l \equiv l_2 - l_1$ the arm length difference;

2. the condition of resonance in the recycling cavity, determined by the phase

$$k\,l_r \tag{5.2}$$

   where $l_r \equiv l_0 + (1/2)\,(l_1 + l_2)$ is the *mean* cavity length of the interferometer.

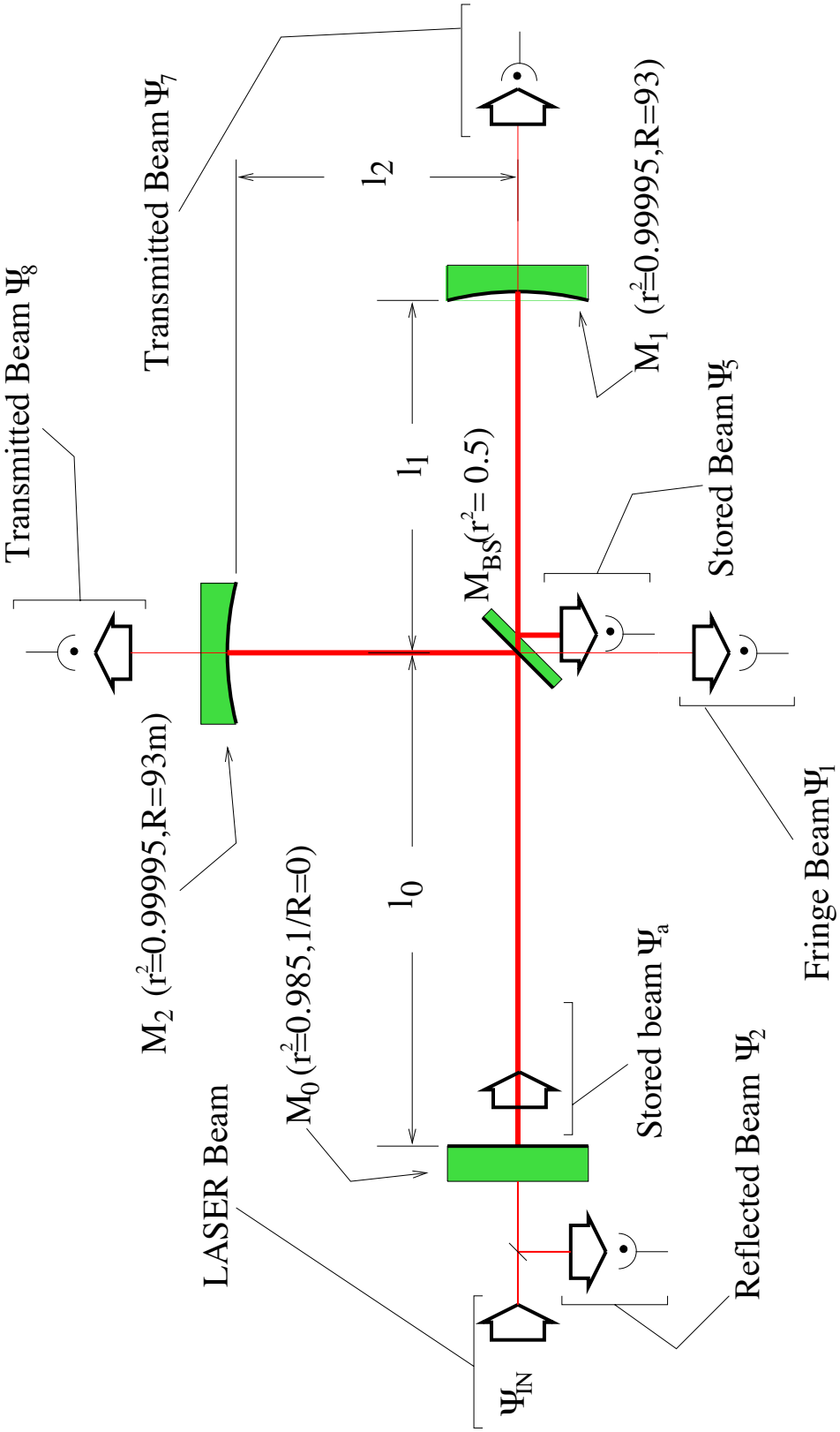

Figure 5.1: The CITF interferometer.

	M_0	$M_{1,2}$	M_{BS}
Coating side 1	$r_0^2 = 0.985$	HR	$t_{BS}^2 = r_{BS}^2 = 0.5 \pm 0.005$
Coating side 2	AR	AR	AR
Shape side 1	Flat	Concave R = 93 m	Flat
Shape side 2	Flat	Flat	Flat

Table 5.1: The mirror optical characteristics for the CITF. Side 1 refers to the side of the mirror shown in bold in the figure.

It will be shown in the sections to come that the low frequency components of the mirror displacements, if left free, will not allow the detector to operate within the requirements and therefore a control system is necessary. This low frequency control is referred to as *longitudinal locking*.

5.2 Optical Configuration

The main optical elements of the interferometer are described in tab.(5.1)[35], where r_i^2 and t_i^2 denote, respectively, the power reflectivity and transmittivity of the i-th mirror, AR indicates an anti-reflective coating, typically with $r^2 < 10^{-3}$ and HR a highly reflective coating with $10^{-5} < t_{1,2}^2 < 10^{-4}$. Here, coating side 1 refers to the side of the mirrors shown in bold in fig.(5.1). The finesse of the CITF, defined in condition of dark fringe, is

$$\mathcal{F} = \frac{\pi \sqrt{r_0\, r_{1,2}}}{1 - r_0\, r_{1,2}} \sim 400 \tag{5.3}$$

with a recycling factor $G_{rec} \equiv (2\,\mathcal{F}/\pi) \sim 260$. With a foreseen laser power of 10 W, the stored power in the recycling cavity is expected to be ~ 2.6 kW.

The optical paths, shown in fig.(5.1), are[35]:

$l_0 = 5952.75$mm	$l_1 = 6380.7$mm	$l_2 = 5532.8$mm

with a mean cavity length l_r and arm asymmetry Δl of

$l_r \equiv l_0 + \frac{1}{2}(l_1 + l_2)$	11909.5 mm
$\Delta l \equiv l_2 - l_1$	847.9 mm

Notice that the arm asymmetry, necessary for the frontal modulation technique, induces a beam mismatch: the beam curvature at the end of the arms differ from the mirror curvatures. This effect will be discussed in sec.(5.7).

The geometry of the laser beam has been chosen so as to mode match a plane-concave cavity of length l_r and of mirror curvature R = 93 m, and the beam waist is located at the input mirror.

λ	P	$\Omega / 2\pi$	m	J_0	J_1	w_0	$R(l_r)$
1.064 μm	10 W	12,586,274 Hz	0.5	0.93847	0.242268	3.244231 mm	93 m

Table 5.2: The characteristics of the laser beam, where λ is the light wavelength, P is the laser power, m is the modulation index, $J_{0,1}$ are the modulation amplitudes, w_0 is the beam waist and $R(l_r)$ is the wavefront curvature at the distance l_r.

The modulation frequency has been chosen to be $\Omega/2\pi = c\,/\,2\,l_r$ so as to allow simultaneously the recycling of both sidebands as well as the carrier. The presence of the arm asymmetry leads to a dark fringe condition for the carrier different from that of the sidebands, as already discussed in sec.(2.4). Tab.(5.2) shows the characteristics of the laser beam.

All output beams, as shown in fig.(5.1), are monitored by photodiodes for the locking and alignment of the system. The beams are:

- the fringe or output beam Ψ_1;
- the reflected beam Ψ_2 off of the recycling mirror M_0;
- the beam reflected off of the second face of the beam splitter Ψ_5;
- both transmitted beams Ψ_7 and Ψ_8;

We will use the following simplified model for the photodiodes and their signals: photodiode i will monitor beam Ψ_i, and its output is written in the form

$$d_i^{dc} \,+\, d_i^{ph}\,\sin\Omega t \,+\, d_i^{qu}\,\cos\Omega t \;\propto |\,\Psi_i\,|^2 \tag{5.4}$$

where d_i^{dc} denotes the DC component, $d_i^{ph,qu}$ denote the demodulated in-phase and quadrature components, and the $2\,\Omega$ terms have been neglected .

5.3 The Sensitivity Curve for the CITF

The sensitivity curve for the CITF, in phase and displacement units, is plotted in fig.(5.2) and fig.(5.3), where two different quality factors for the mirrors have been used for the top and bottom graphs. The uncertainty in the quality factor Q is due to the clamping of the mirrors to mirror holders, with a foreseen value anywhere from a pessimistic value of Q = 100 to an optimistic one of Q = 1000.

The sensitivity curve is limited by the seismic wall below 2 Hz and will approach, at high frequency, the phase shot-noise limit (see eq.(2.43)), of

$$\delta\tilde{\phi}_{shot} \;=\; \sqrt{\frac{\hbar\,\omega}{\eta\,G_{rec}\,P}} \;=\; 1.9\times10^{-11} \quad [rad/\sqrt{Hz}] \tag{5.5}$$

or, in displacement units,

$$\delta\tilde{l}_{shot} \;=\; 1.6\times10^{-18} \quad [m/\sqrt{Hz}] \tag{5.6}$$

where $l = 6$ m is the arm length and $\eta = 0.9$ is the photodiode quantum efficiency.

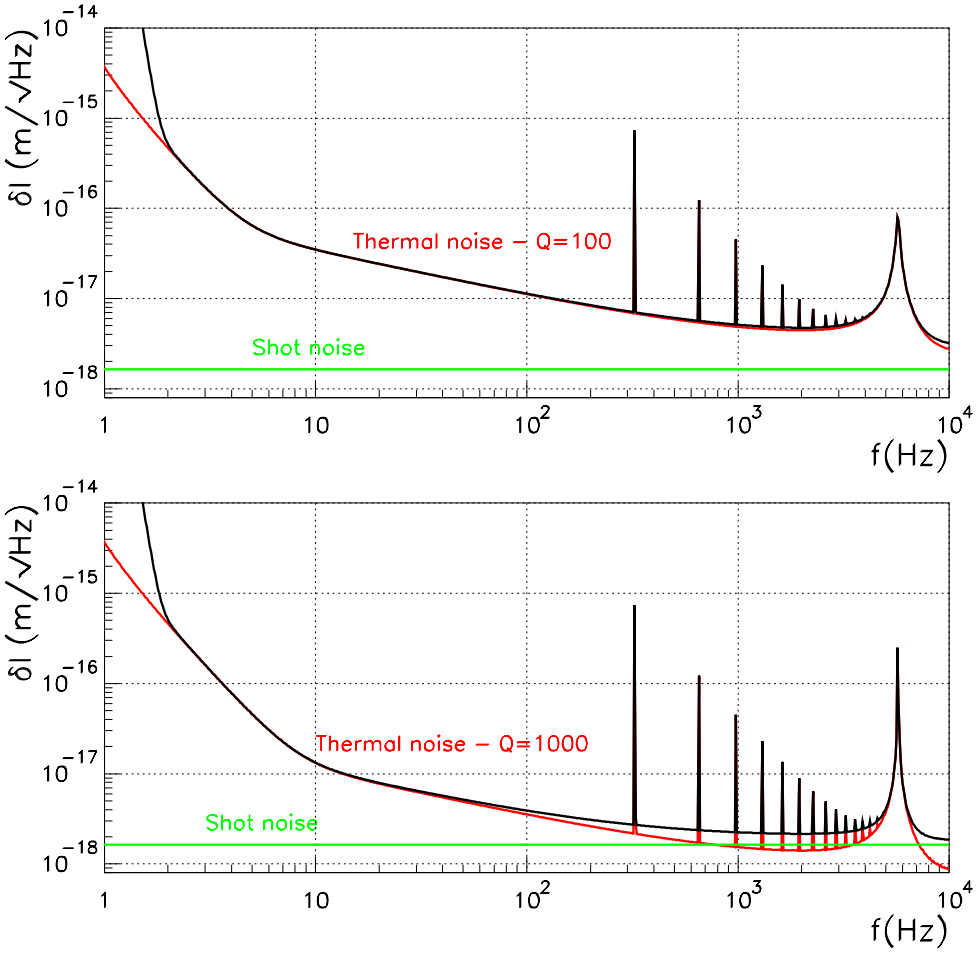

Figure 5.2: The foreseen CITF sensitivity curve, expressed in $m/\sqrt{Hz}$ units, for different values of the quality factor Q. Top graph: $Q = 100$; bottom graph: $Q = 1000$.

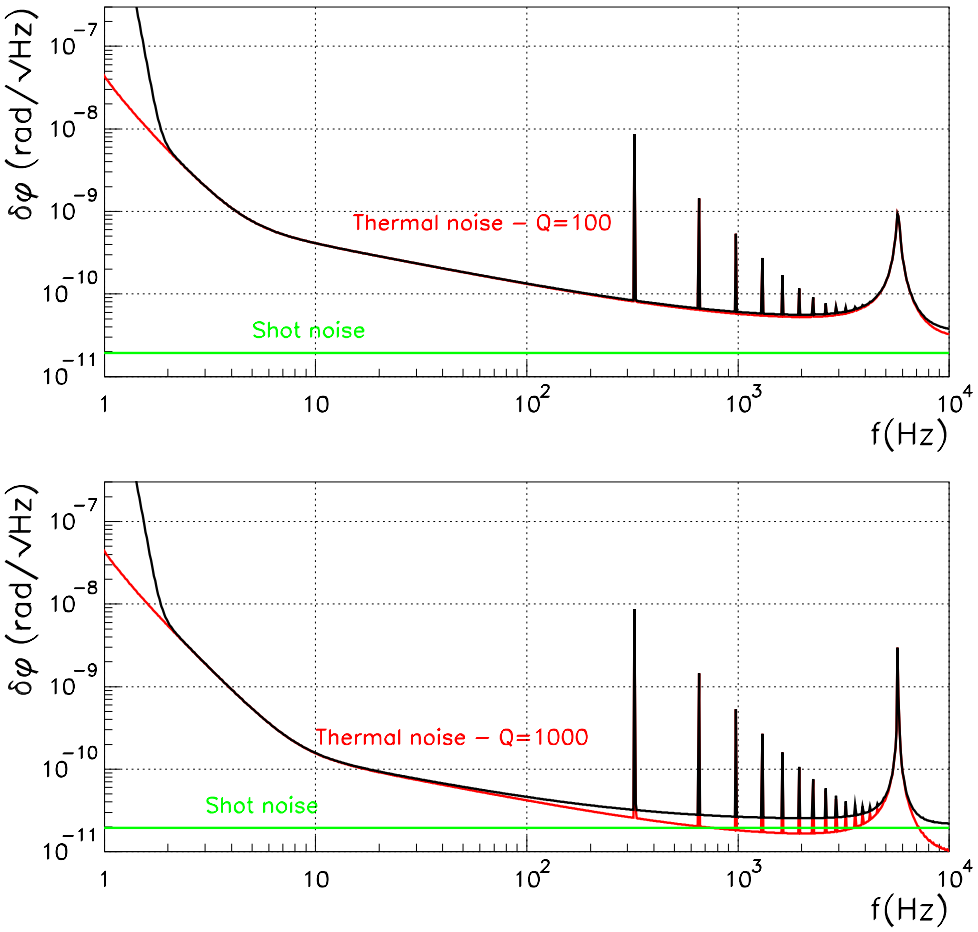

Figure 5.3: The foreseen CITF sensitivity curve, expressed in $rad/\sqrt{Hz}$ units, for different values of the quality factor Q. Top graph: $Q = 100$; bottom graph: $Q = 1000$.

5.4 Mirror Motion Specifications

As shown in the previous chapter, the specification for the fringe lock depend upon the laser power fluctuations. Assuming a noise of $\Delta\tilde{P}/P \sim 10^{-7}/\sqrt{\mathrm{Hz}}$, the tolerated fluctuations in Δl must be kept within[35]

$$\Delta(\, l_2 \, - \, l_1\,) \, < \, \frac{1}{10}\, 2\, k\, l\, \frac{\tilde{h}_{shot}}{\Delta\tilde{P}\,/\,P} \, \sim \, 10^{-12}\,\mathrm{m} \tag{5.7}$$

where a safety factor of 10 has been taken into account.

For the recycling cavity, the most stringent requirement comes from the dynamics of the electronics[35], giving a tolerance for the cavity length fluctuations of

$$\Delta(\, l_0 \, + \, \frac{1}{2}\,(\, l_1 \, + \, l_2\,)\,) \, < \, 10^{-11}\,\mathrm{m} \tag{5.8}$$

with a safety factor of 10 taken into account.

5.5 Mirror Displacement Noises

According to numerical calculations performed by A.Viceré and analytical computations performed by the Perugia group, whose results are shown in [36, 41], it is possible to estimate the mirror displacement in free motion due to thermal and seismic excitations. In this section, the amplitude spectral density of the mirror displacements are presented, in all degrees of freedom (DOF). The conventions in use are shown in fig.(5.4) and are

- the z or *longitudinal* axis along the beam;
- the y or *vertical* axis parallel to the suspension;
- the x or *horizontal* axis perpendicular to both longitudinal and vertical axes;
- the θ_i rotation angle around the i-th axis.

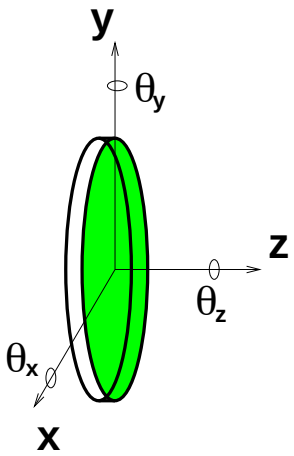

Figure 5.4: Conventions for the mirror's six degrees of freedom: x, y, z, θ_x, θ_y, and θ_z.

5.5.1 Thermal Noise

The mirror motion induced by thermal noise has been calculated with the following contributions for the different degrees of freedom:

1. along the longitudinal axis, the pendulum, violin and the mirror internal modes have been taken into account;
2. the horizontal motion has been approximated to be the same as the longitudinal one but the mirror internal modes have been neglected;
3. for the vertical motion, only the pendulum mode has been taken into account;
4. for the angular motions, only rotations around the vertical and horizontal axes have been computed.

Each mode contributing to one DOF has been added quadratically so as to obtain the total motion in the DOF in question.

Also, as already stated, the contribution of the mirror internal mode to the motion is not well defined for the CITF: the mirror mechanical support introduces frictions and stresses onto the mass, thus affecting the quality factor. A value of $Q = 1000$ at 1 kHz has been assumed in the calculations.

5.5.2 Seismic Excitation and Transfer Functions

The estimated residual motion of the mirror due to seismic excitation has been numerically calculated in all DOF with the superattenuator modeled as a chain of 15 rigid bodies: the 6 mechanical filters with their movable vertical system, the marionetta, the mirror and the reference mass. The rigid bodies are connected to each other by elastic elements: the triangular blades, the inverted pendulum, the centering and suspension wires. Such a model has not been completely validated by experimental data and makes use of the following approximations:

1. the quality factors of the resonances depend on the structural dissipation within each elastic body, not taking into account the effects due to clamping points;
2. the coupling parameters between the 6 DOF are approximated and are likely to change from suspension to suspension.

The output of the simulation consists of transfer functions relating an excitation applied at any level of the chain and in any of the 6 DOF to the motion of the mirror in all 6 DOF. The simulation allows a first estimate not only of the mirror motion due to seismic excitation but also of transfer functions for mirror control.

The seismic noise model used as input to the simulation is

$$\tilde{x}(f) \;=\; \tilde{y}(f) \;=\; \tilde{z}(f) \;=\; F(f) \;=\; \frac{10^{-6}}{f^2}\,\frac{f^2 + 0.01}{f^2 + 1.0} \qquad [m/\sqrt{Hz}] \tag{5.9}$$

which assumes equal contributions along the longitudinal, vertical and horizontal DOF. For the angle excitations, the following model has been assumed:

$$\tilde{\theta}_x(f) \;=\; \tilde{\theta}_y(f) \;=\; F(f)\,\frac{2\,\pi\,f}{v} \qquad [rad/\sqrt{Hz}] \qquad \tilde{\theta}_z(f) \;=\; 0 \tag{5.10}$$

where $v = 500\,m/s$ is the velocity of the seismic waves in the ground.

The motion along the 6 DOF is assumed to be uncorrelated since no experimental estimate of the cross-correlation of noises exists to date. The total mirror motion is the quadratic sum of the amplitude noise spectra weighted by the transfer functions. By defining $\tilde{s}_j(f)$ as the amplitude spectral density of ground vibrations along the j-th dimension and by defining $\mathcal{A}_{ij}(f)$ as the

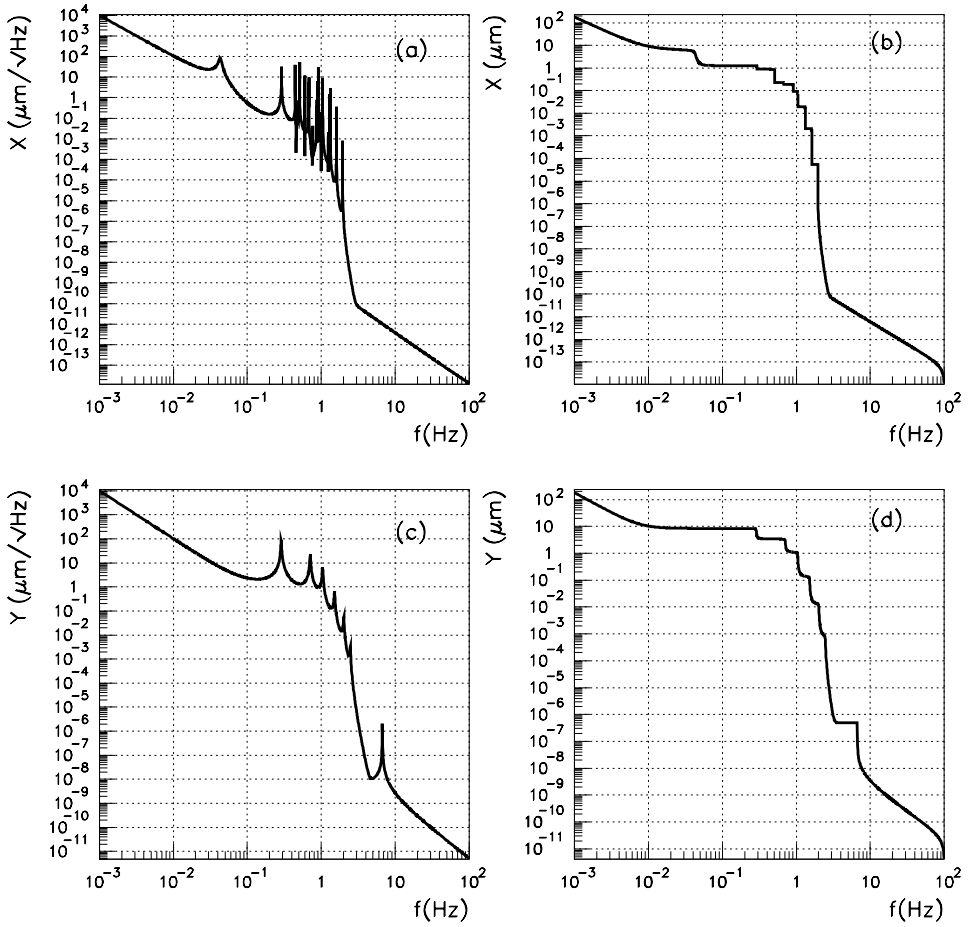

Figure 5.5: The calculated free mirror motion estimates due to seismic and thermal excitation: (a) the displacement amplitude spectral density along the horizontal axis and (b) its running RMS value; (c) the displacement amplitude spectral density along the vertical axis and (d) its running RMS value.

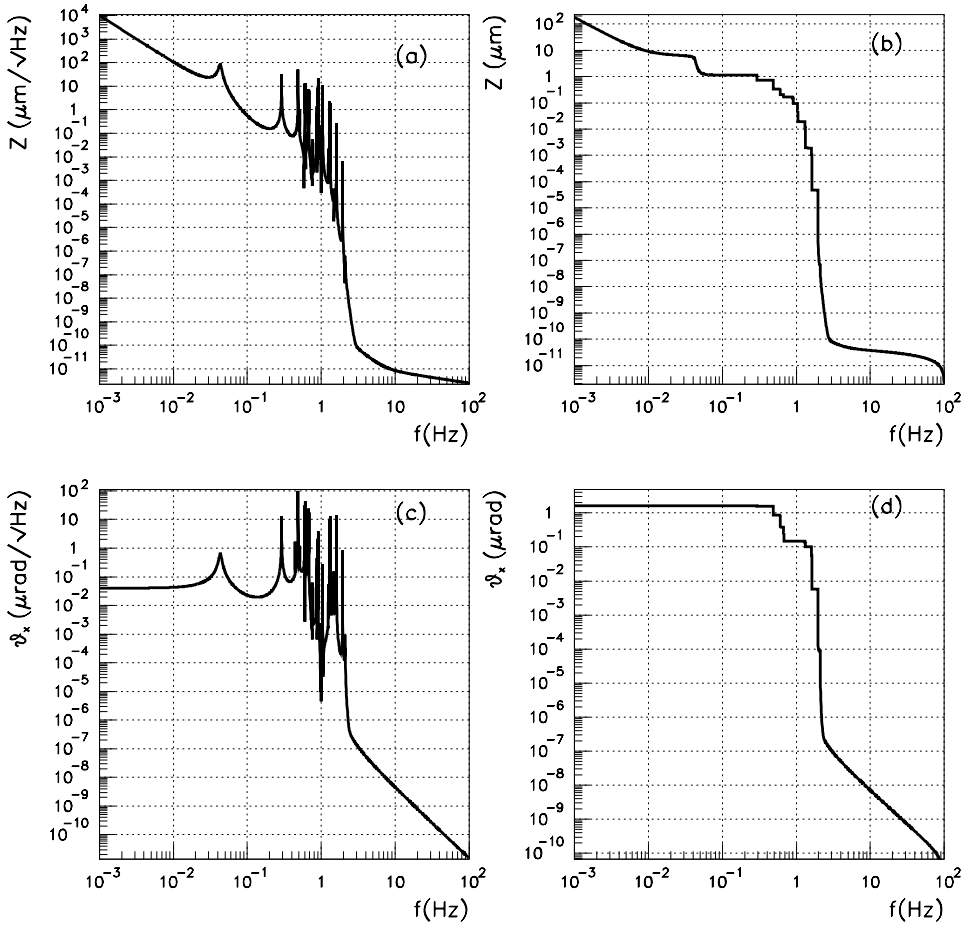

Figure 5.6: The calculated free mirror motion estimates due to seismic and thermal excitation: (a) the displacement amplitude spectral density along the longitudinal axis and (b) its running RMS value; (c) the angular amplitude spectral density around the horizontal axis with (d) its running RMS value.

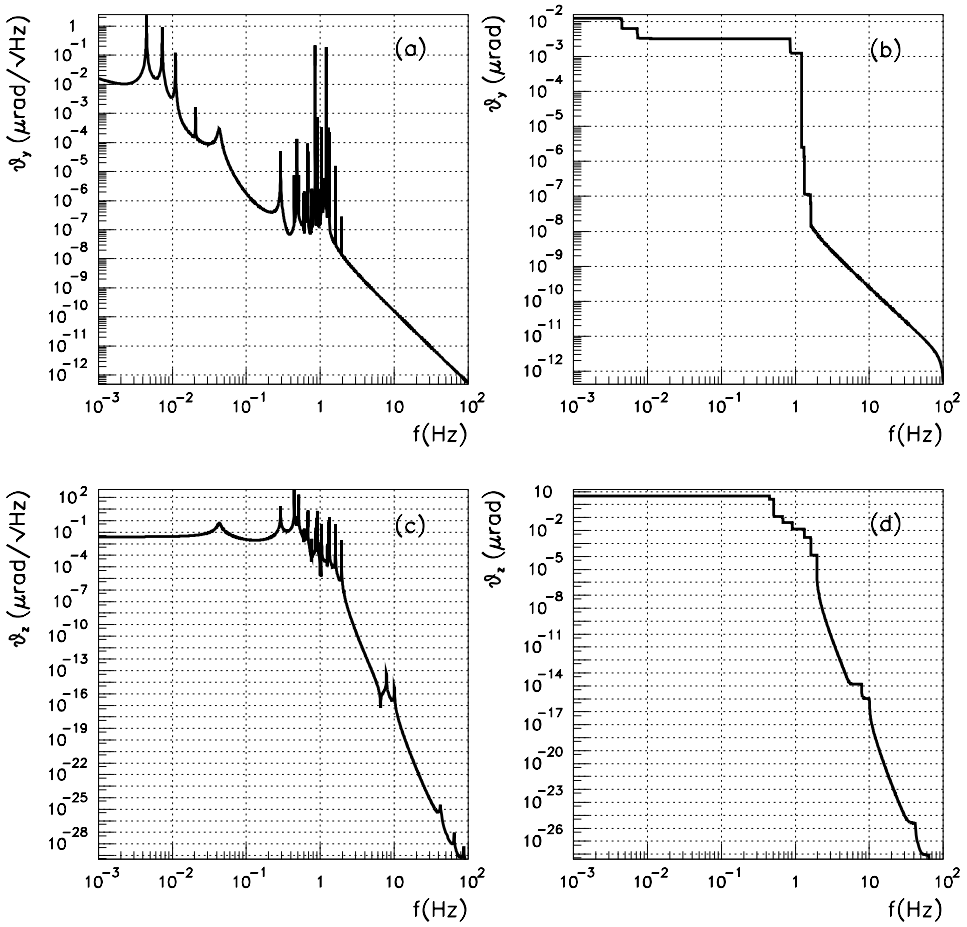

Figure 5.7: The calculated free mirror motion estimates due to seismic and thermal excitation: (a) the angular amplitude spectral density around the vertical axis and (b) its running RMS value; (c) the angular amplitude spectral density around the longitudinal axis with (d) its running RMS value.

transfer function relating the input excitation along j with the resulting mirror motion along i, the resulting spectral density linear displacement $\tilde{m}_i^{seis}$ is

$$\tilde{m}_i^{seis}(f) \;=\; \sqrt{\sum_j \left[\,\mathcal{A}_{ij}(f) \;\times\; \tilde{s}_j(f)\,\right]^2} \tag{5.11}$$

5.5.3 Mirror Motion Estimates

The seismic contribution to the mirror motion $\tilde{m}_i^{seis}(f)$ along the i-th direction is added quadratically to the thermal contribution $\tilde{m}_i^{ther}(f)$ along the same direction. The total movement of the mirror $\tilde{m}_i(f)$ is:

$$\tilde{m}_i(f) \;=\; \sqrt{\tilde{m}_i^{seis}(f)^{\,2} + \tilde{m}_i^{ther}(f)^{\,2}} \tag{5.12}$$

Fig.(5.5-5.7) show the amplitude spectral density along the 6 DOF with their corresponding running RMS values defined as

$$m_i^{rms}(f) \;=\; \sqrt{\left|\int_{100\,\mathrm{Hz}}^{f} \tilde{m}_i(f)^{\,2}\, df\right|} \tag{5.13}$$

The frequency spectrum up to at least the inverted pendulum resonance at $30\,mHz$ will be damped by a local control system: the *inertial damping*. From the estimates, the longitudinal RMS displacement value is foreseen to be 1 μm and dominated by a resonance at about $200\,mHz$. For the angular motion around the vertical and horizontal axis, the RMS value is expected to be kept within 1 μrad.

5.6 The Longitudinal Response and Ratio of Signals

The objective of this section is to present the optical response of the CITF to longitudinal motions of the mirrors. Assuming an equal curvature for the beam and the mirrors, with the incoming laser beam mode-matched to an aligned CITF, the longitudinal response can be studied by using a plane wave model.

Unlike the simple resonator, where the condition of resonance is obtained by adjusting the cavity length with respect to the laser frequency, two effects need to be controlled for the CITF: the dark fringe condition and the recycling cavity resonance. We represent the CITF, shown in fig.(5.8a), as a two mirror cavity, as shown in fig.(5.8b),

- made of the recycling mirror M_0 and an end mirror $M(\Delta l)$ whose complex reflectivity $\mathcal{R}(\Delta l)$ depend upon the arm length difference Δl;
- of length l_r;

Assuming that $\Psi_{in} = 1$, the stored field Ψ_{a} can then be written in the form

$$\Psi_a(l_r, \Delta l) = \frac{t_0}{1 + \; r_0\, \mathcal{R}(\Delta l)\; \exp(-2\, i\, k\, l_r)} \tag{5.14}$$

where the reflectivity $\mathcal{R}(\Delta l)$ of the end mirror, which depends only on the arm length difference, is

$$\mathcal{R}(\Delta l) = \; t_{BS}^2\, r_1\, \exp(i\, k\, \Delta l) \;-\; r_{BS}^2\, r_2\, \exp(-\, i\, k\, \Delta l) \tag{5.15}$$

The analogy with the Fabry-Perot can be seen by comparing the CITF stored EM field, expressed in eq.(5.14), with the Fabry-Perot stored field in eq.(3.17). The form of the two equations is identical; however, for the CITF, the reflectivity $\mathcal{R}(\Delta l)$ can vary both in amplitude and phase as

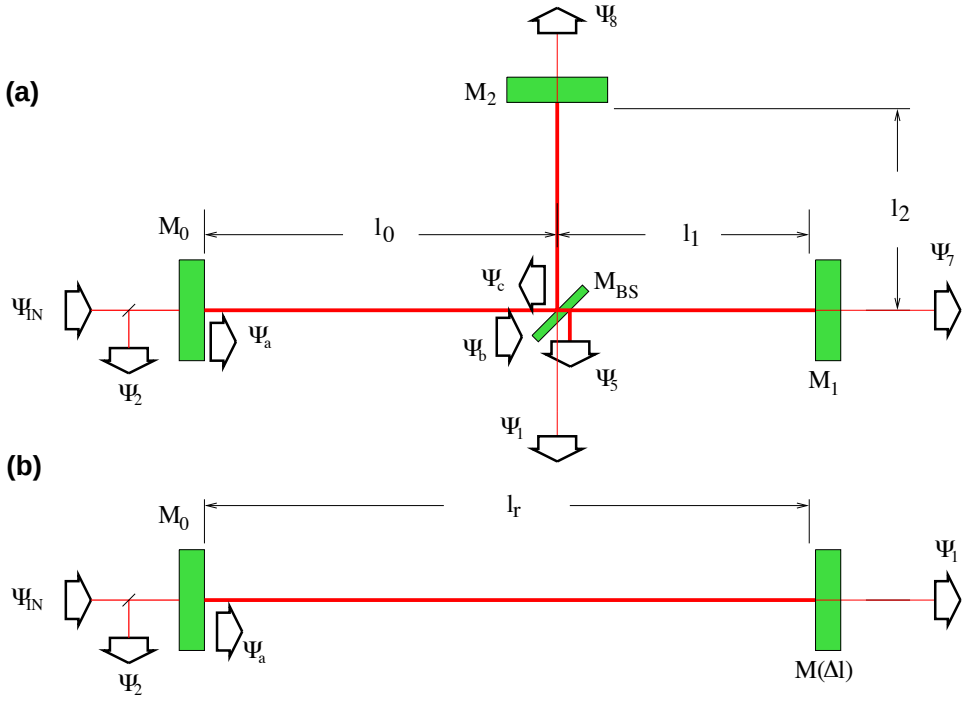

Figure 5.8: The CITF seen as a Fabry-Perot cavity.

Δl changes. This means that the condition of resonance depends not only on the mean cavity length l_r but also on the phase of $\mathcal{R}(\Delta l)$. In the same way, the finesse of the equivalent cavity depends necessarily on the amplitude reflectivity of the end mirror and is maximum in condition of dark fringe.

For simplicity, let $r_1 = r_2 = 1$ and $r_{BS} = t_{BS} = 1/\sqrt{2}$. In this case, the laser power can only leak out to photodiode 1 and $\mid \Psi_1 \mid^2$ can be written in the form

$$\mid \Psi_1 \mid^2 = \mid \mathcal{T}(\Delta l) \mid^2 \mid \Psi_a \mid^2 \tag{5.16}$$

where

$$\begin{aligned} \mid \mathcal{R}(\Delta l) \mid^2 &= \sin^2 k\,\Delta l \\ \mid \mathcal{T}(\Delta l) \mid^2 &= \cos^2 k\,\Delta l \end{aligned} \tag{5.17}$$

In other words, the DC component of $\mid \Psi_1 \mid^2$ is proportional to the stored DC power $\mid \Psi_a \mid^2$ and to the transmittivity $\mid \mathcal{T}(\Delta l) \mid^2$ of the end mirror. The condition of dark fringe is determined by $\mid \mathcal{T}(\Delta l) \mid^2$ regardless of the stored power. The monitoring of $\mid \mathcal{T}(\Delta l) \mid^2$ results in the knowledge of the dark fringe condition. By noting that

$$\mid \Psi_5 \mid^2 = \frac{AR}{2} \mid \Psi_a \mid^2 \tag{5.18}$$

where AR is the power reflectivity of the BS anti-reflective coating, $\mid \mathcal{T}(\Delta l) \mid^2$ can be written as

$$\mid \mathcal{T}(\Delta l) \mid^2 = \frac{\mathrm{AR}}{2} \frac{\mid \Psi_1 \mid^2}{\mid \Psi_5 \mid^2} \tag{5.19}$$

Therefore, the experimental ratio $\mid \Psi_1 \mid^2 / \mid \Psi_5 \mid^2$ gives information on the condition of dark fringe.

The CITF, whose configuration is described in sec.(5.2), has been simulated in the quasi-static approximation and some results are shown in fig.(5.9). Plots of d_1^{dc}, d_5^{dc} and their ratio are shown

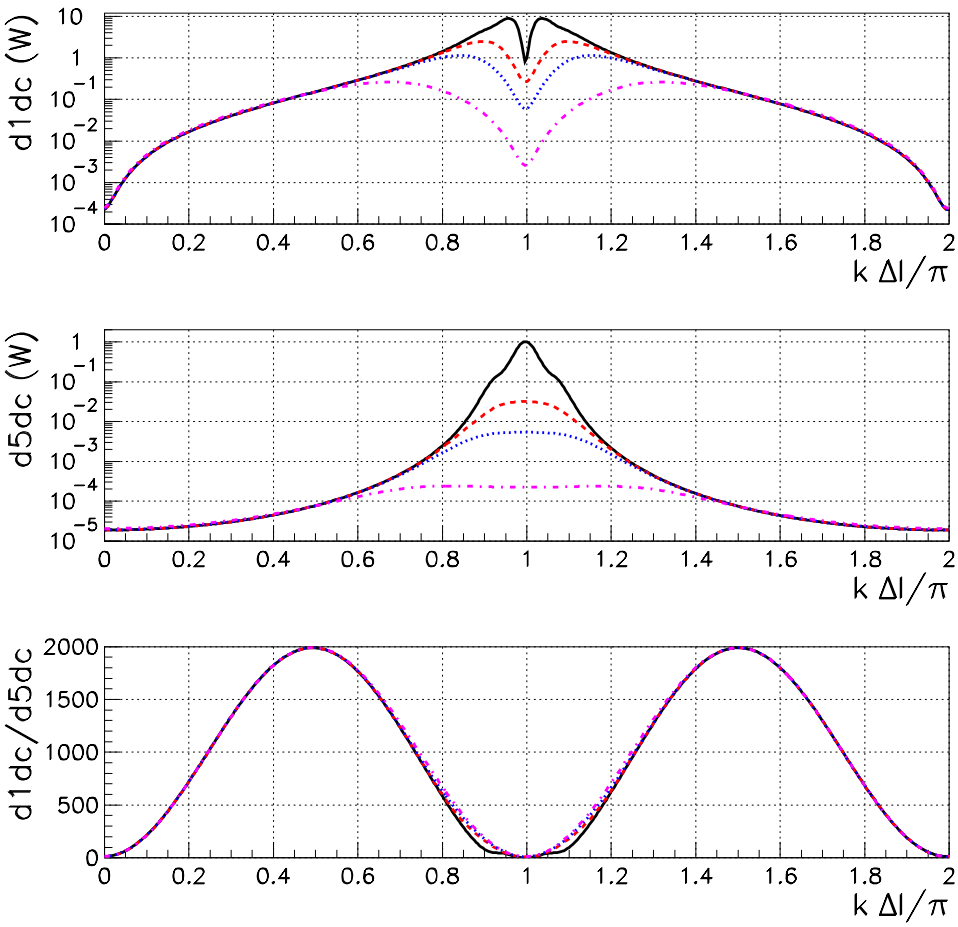

Figure 5.9: The ratio of $|\Psi_1|^2$ with $|\Psi_5|^2$ as a function of $k\Delta l$ and for different values of l_r: continuous line: $l_r = \lambda/4$; dashed line: $l_r = \lambda/4 + \delta l$; dotted line: $l_r = \lambda/4 + 2\,\delta l$; dot-dashed line: $l_r = \lambda/4 + 3\,\delta l$ ($\delta l = 4\times10^{-9} m$). Top graph: the DC power $|\Psi_1|^2$ as a function of the phase $k\Delta l$; middle graph: the DC power $|\Psi_5|^2$ as a function of the phase $k\Delta l$, where $AR = 10^{-3}$; bottom graph: the ratio of $|\Psi_1|^2$ with $|\Psi_5|^2$ as a function of $k\Delta l$.

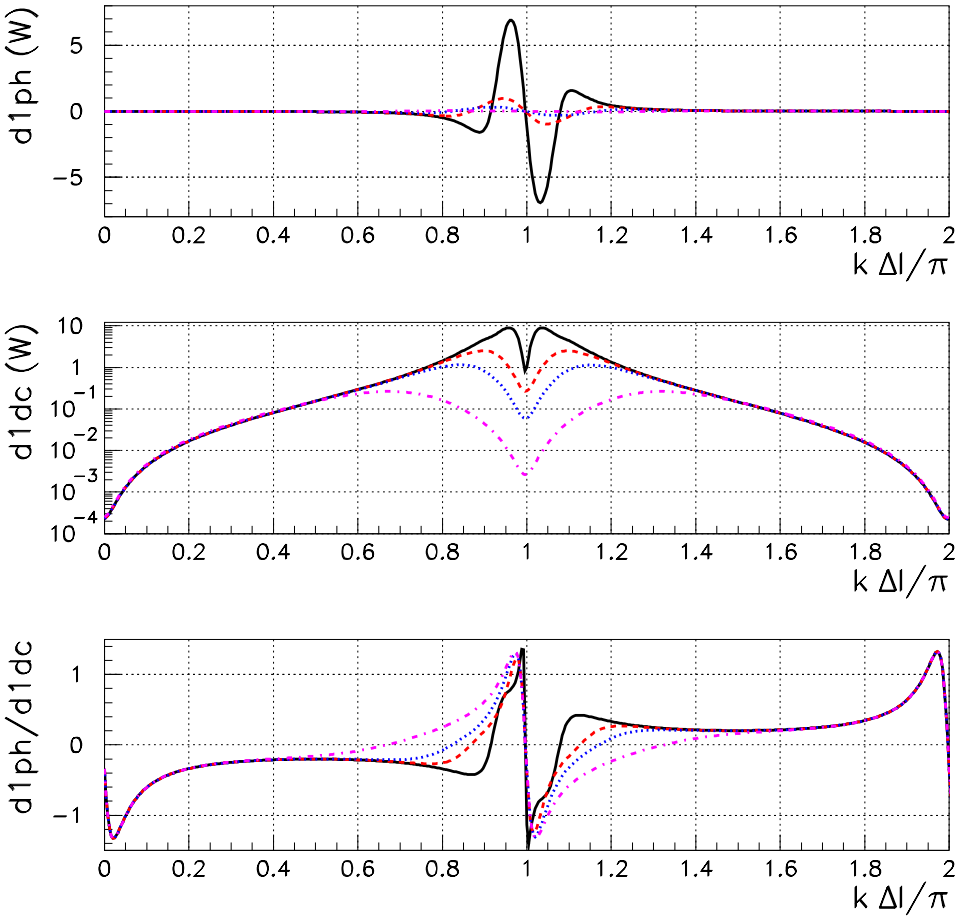

Figure 5.10: The ratio of the demodulated component d_1^{ph} with d_1^{dc} as a function of the phase $k\Delta l$ and for different values of l_r: continuous line: $l_r = \lambda/4$; dashed line: $l_r = \lambda/4 + \delta l$; dotted line: $l_r = \lambda/4 + 2\,\delta l$; dot-dashed line: $l_r = \lambda/4 + 3\,\delta l$ ($\delta l = 4 \times 10^{-9} m$). Top graph: the demodulated component d_1^{ph} as a function of the phase $k\Delta l$; middle graph: the DC component d_1^{dc} as a function of the phase $k\Delta l$; bottom graph: the ratio of the two signals.

as a function of the phase $k\,\Delta l$ and for different values of l_r. Notice how, to first approximation, the ratio is independent from l_r.

According to the conventions of the simulation program, which are different from the ones used here, dark fringe and maximum stored power occurs for

$$\begin{aligned} k\,\Delta l &= n\,\pi \\ 2\,k\,l_r &= (2\,n\,+\,1)\,\pi \end{aligned} \tag{5.20}$$

where n is an integer. For these values, $d_1^{dc} \simeq 1\,W$ due to the sideband leakage, and $d_5^{dc} \simeq 1\,W$ with a pessimistic value of $AR = 10^{-3}$. We would like to remark that for a fixed value of $l_r = \lambda/4 \pmod{\lambda/2}$, maximum recycling is possible for $k\,\Delta l = (2\,n\,+\,1)\,\pi$. On the other hand, for $k\,\Delta l = 2\,n\,\pi$, the recycling cavity anti-resonates. This is shown in fig.(5.9) and arises from the phase of the complex reflectivity $\mathcal{R}(\Delta l)$ which changes as a function of $k\,\Delta l$.

It is possible to use a demodulated signal as an error signal for the dark fringe control independent from the recycling condition. By defining

$$\Delta l \equiv \overline{\Delta l} + \delta l \tag{5.21}$$

where $\overline{\Delta l}$ is the arm asymmetry and $\delta l = \Delta l \pmod{\lambda}$, it is possible to show that the ratio between the in-phase signal d_1^{ph} with the DC component d_1^{dc} around dark fringe is, to first approximation

$$\frac{d_1^{ph}}{d_1^{dc}} \simeq K\,\delta l \tag{5.22}$$

For small values of the phase

$$\frac{\Omega}{c}\,\overline{\Delta l} << 1 \tag{5.23}$$

the constant K is

$$K = 2\,k\,\frac{J_0}{J_1}\,\frac{c}{\Omega\,\overline{\Delta l}} \tag{5.24}$$

The output of the simulation is given in fig.(5.10) where d_1^{ph}, d_5^{dc} and their ratio are shown as a function of $k\,\Delta l$ and for different values of l_r. The value of the constant K in eq.(5.24) is in good agreement with the simulation result.

5.7 The Angular Response

For a simple Fabry-Perot cavity, it has been shown in sec.(3.3.2) how any translation of the optical axis with respect to the incoming beam generates, to first order approximation, an in-phase coupling with the first order transverse mode. On the other hand, any rotation leads to a quadrature coupling with the first order transverse mode. For the CITF, it is not possible to have such a simple model. For this reason, the study here presented, with the exception of sec.(5.7.1), is based on numerical simulations[37]. These results correspond to an old CITF configuration with $l_0 = 6\,m$, $l_1 = 5.6\,m$, $l_2 = 6.4\,m$, $r_0^2 = 0.96$ and $J_1^2 = 0.01$.

This section describes the angular response for three different CITF configurations: *symmetric* with $l_1 = l_2$, asymmetric with $l_2 - l_1 = 0.8\,m$, but *mode-matched* to the incoming laser beam, and the *actual CITF configuration*. The asymmetry matrix for the actual CITF autoalignment will be presented in sec.(5.8).

5.7.1 Case 1: Symmetric CITF

Let's first consider the case of a symmetric recycled Michelson with $l_1 = l_2$ and $r_1 = r_2$, matched and aligned to an incoming U_0, where, for simplicity, $U_0 \equiv U_{00}$ and $U_1 \equiv U_{10}$. Due to its

symmetry, the beams transmitted and reflected by this optical system can be seen as the output beams of a simple Fabry-Perot cavity of the length l_r. A tilt θ of the Michelson recycling mirror induces the same effect as a tilt θ applied to the input mirror of the Fabry-Perot. In the same way, a tilt ϕ of the Fabry-Perot end mirror has the same effect as a tilt ϕ applied to both end mirrors of the Michelson. Therefore, we can see the CITF as an equivalent Fabry-Perot cavity and treat the problem as in sec.(3.3.2).

Let the incoming EM field be a pure U_0 which, according to the conventions in sec.(3.3.2), is expressed in the unprimed reference system of the laser

$$\Psi_{in} = J\, U_0 \tag{5.25}$$

where J is the beam amplitude. Let's also assume that the optical axis of the equivalent cavity is translated and rotated with respect to the incoming beam. At the waist location, the incoming field expressed in the primed reference system of the cavity is, up to first order approximation in a/w_0 and θ/θ_∞

$$\Psi'_{in} \;=\; J\left[\, U'_0 \,+\, \left(\, \frac{a}{w_0} \,+\, i\,\frac{\theta}{\theta_\infty}\,\right) U'_1\,\right] \tag{5.26}$$

where a and θ are the translation and angle of the axis. Denoting by $\mathcal{A}^i_R$ and $\mathcal{A}^i_T$ the complex valued cavity reflectivity and transmittivity of an incoming U'_i in the cavity reference system, as in sec.(3.3), the transmitted field can be written as

$$\Psi'_T \;=\; J\left[\, \mathcal{A}^0_T\, U'_0 \,+\, \mathcal{A}^1_T \left(\, \frac{a}{w_0} \,+\, i\,\frac{\theta}{\theta_\infty}\,\right) U'_1\,\right] \tag{5.27}$$

whereas the reflected beam takes the form

$$\Psi'_R \;=\; J\left[\, \mathcal{A}^0_R\, U'_0 \,+\, \mathcal{A}^1_R \left(\, \frac{a}{w_0} \,+\, i\,\frac{\theta}{\theta_\infty}\,\right) U'_1\,\right] \tag{5.28}$$

The two beams in the unprimed reference systems take the following form

$$\begin{aligned}
\Psi_T &= J\left[\, \mathcal{A}^0_T\, U_0 \,+\, \left(\, \frac{a}{w_0} \,+\, i\,\frac{\theta}{\theta_\infty}\,\right)\left(\mathcal{A}^1_T \,-\, \mathcal{A}^0_T\, e^{i\,\phi}\right) U_1\,\right] \\
\Psi_R &= J\left[\, \mathcal{A}^0_R\, U_0 \,+\, \left(\, \frac{a}{w_0}\,\right)\left(\mathcal{A}^1_R \,-\, \mathcal{A}^0_R\right) U_1 \,+\, i\left(\, \frac{\theta}{\theta_\infty}\,\right)\left(\mathcal{A}^0_R \,+\, \mathcal{A}^1_R\right) U_1\,\right]
\end{aligned} \tag{5.29}$$

By tuning the cavity so as to let the U_0 component resonate, we find

$$\begin{aligned}
\mathcal{A}^0_T &= -\,i\,A^0_T \\
\mathcal{A}^1_T &= A^1_T \\
\mathcal{A}^0_R &= -\,i\,A^0_R \\
\mathcal{A}^1_R &= i\,A^1_R
\end{aligned} \tag{5.30}$$

where $A^i_R \equiv \mid \mathcal{A}^i_R \mid$ and $A^i_T \equiv \mid \mathcal{A}^i_T \mid$. Eq.(5.29) reduces to

$$\begin{aligned}
\Psi_T &= J\left[\, -\,i\,A^0_T\, U_0 \,+\, \left(\, \frac{a}{w_0} \,+\, i\,\frac{\theta}{\theta_\infty}\,\right)\left(i\,A^0_T\, e^{i\,\phi} \,+\, A^1_T\right) U_1\,\right] \\
\Psi_R &= J\left[\, -\,i\,A^0_R\, U_0 \,+\, \left(\, \frac{\theta}{\theta_\infty}\,\right)\left(A^0_R \,-\, A^1_R\right) U_1 \,+\, i\left(\, \frac{a}{w_0}\,\right)\left(A^0_R \,+\, A^1_R\right) U_1\,\right]
\end{aligned} \tag{5.31}$$

The modulation frequency for the alignment will be the same as the longitudinal one, $\Omega\,/\,2\,\pi \;=\; c\,/\,2\,l_r$, and the incoming beam Ψ_{in}, for the three different frequency components, can be written in the form

$$\Psi^{(-,0,+)}_{in} = \begin{pmatrix} -\,J_1 \exp\left(-\,i\,\Omega\,t\right) \\ J_0 \\ J_1 \exp\left(i\,\Omega\,t\right) \end{pmatrix} \tag{5.32}$$

As a result, the transmitted and reflected beams for the carrier and the sidebands are :

$$\Psi_T^{(-,0,+)} = \begin{pmatrix} -J_1 \exp(-i\Omega t) \\ J_0 \\ J_1 \exp(i\Omega t) \end{pmatrix} \times \times \left[-iA_T^0 U_0 + \left(\frac{a}{w_0} + i\frac{\theta}{\theta_\infty} \right) \left(iA_T^0 e^{i\phi} + A_T^1 \right) U_1 \right] \tag{5.33}$$

$$\Psi_R^{(-,0,+)} = \begin{pmatrix} -J_1 \exp(-i\Omega t) \\ J_0 \\ J_1 \exp(i\Omega t) \end{pmatrix} \times \times \left[-iA_R^0 U_0 + \left(\frac{\theta}{\theta_\infty} \right) \left(A_R^0 - A_R^0 \right) U_1 + i \left(\frac{a}{w_0} \right) \left(A_R^0 + A_R^1 \right) U_1 \right]$$

Recalling that the demodulated components of the photodiode signals, shown in eq.(3.52) and eq.(5.4), consist of

$$\begin{aligned} \cos\Omega t \quad &\Rightarrow \quad 2\,\Re\left\{ \Psi^{0*}\,\Psi^{+} + \Psi^{0*}\,\Psi^{-} \right\} \\ \sin\Omega t \quad &\Rightarrow \quad 2\,\Im\left\{ \Psi^{0*}\,\Psi^{-} - \Psi^{0*}\,\Psi^{+} \right\} \end{aligned} \tag{5.34}$$

and that the products

$$\begin{aligned} \Psi_R^{0*}\,\Psi_R^{+} &= J_0 J_1 U_0 U_1 \left[-2 \left(\frac{a}{w_0} \right) A_R^0 \left(A_R^0 + A_R^1 \right) \right] \\ \Psi_R^{0*}\,\Psi_R^{-} &= -\Psi_R^{0*}\,\Psi_R^{+} \\ \Psi_T^{0*}\,\Psi_T^{+} &= -J_0 J_1 U_0 U_1 \left[\frac{a}{w_0} (A_T^0)^2 - \frac{\theta}{\theta_\infty} A_T^0 A_T^1 \right] \\ \Psi_T^{0*}\,\Psi_T^{-} &= -\Psi_T^{0*}\,\Psi_T^{+} \end{aligned} \tag{5.35}$$

we find that the in-phase signal, corresponding to the real part of the sum of the above components, cancels out. Since no imaginary components are present, the quadrature term is also zero. By recalling that the above analytical calculations are approximations to first order terms in a/w_0 and θ/θ_∞, we conclude that for a symmetric CITF, only second order terms or higher might be present in the demodulated signals. Just as for the frontal modulation scheme presented in sec.(2.4), an arm asymmetry is also necessary for the CITF alignment.

5.7.2 Case 2: Mode-Matched CITF

By introducing an arm asymmetry, the sidebands will behave differently from the carrier. In this section, we assume an arm asymmetry of $\overline{\Delta l} = 0.8\,m$ and we have chosen the radii of curvature of the end mirrors to $\sim 90\,m$ and $\sim 95\,m$ respectively, in order to match them to the curvature of the incoming laser beam. In this way, we can neglect the effect of the mismatch.

Before showing the results of the simulation runs, we define as *asymmetry* the up-down and left-right differences of the half-planes relative to a quadrant photodiode, described in sec.(3.5.3), demodulated at the modulation frequency, and normalized to the DC power. Since the asymmetries are linear functions of the misalignment angles (at least for small values of these angles), in the tables we report the proportionality constants that relate the asymmetries to the misalignment angle in units of the angular divergence (θ_∞).

Tab.(5.3) shows the asymmetries from quadrant photodiode 7, placed on one transmitted beam, and from quadrant photodiode 2, located on the beam reflected off of the recycling mirror. We notice that the in-phase signal depends strongly on the angle θ_0 and could be used to control M_0. Since the matrix is not diagonal, a χ^2 minimization procedure will use all error signals to reconstruct the mirror tilts.

beam		θ_0	θ_1	θ_2
Ψ_7	ph	$1.195 \cdot 10^{-2}$	$-8.734 \cdot 10^{-3}$	$-5.463 \cdot 10^{-3}$
	qu	$5.870 \cdot 10^{-4}$	$1.372 \cdot 10^{-2}$	$-1.467 \cdot 10^{-2}$
Ψ_2	ph	$-3.817 \cdot 10^{-1}$	$3.229 \cdot 10^{-2}$	$2.102 \cdot 10^{-2}$
	qu	$-6.244 \cdot 10^{-4}$	$5.797 \cdot 10^{-3}$	$-5.166 \cdot 10^{-3}$

Table 5.3: The asymmetry matrix for a CITF in the matched configuration: arm asymmetry of $\overline{\Delta l} = 0.8\,m$ and radius of curvature for the end mirrors of $\sim 90\,m$ and $\sim 95\,m$.

5.7.3 Case 3: The Actual CITF Configuration

In the actual CITF configuration, the radius of curvature of the end mirrors is set to $93\,m$ and a mismatch is present. The generated asymmetry matrix is shown in tab.(5.4) where both transmitted beams are shown as well as the reflected beam. No important differences are found when comparing tab.(5.3) with tab.(5.4).

5.8 The Asymmetry Matrix

In sec.(3.5.2), the Ward technique was introduced for the alignment of a Fabry-Perot cavity. The demodulated signal of the quadrant photodiode placed on the beam reflected off of the input mirror is (as shown in eq.(3.60)):

$$J_0\, J_1\, U_{00}\, U_{10} \left[\left(\frac{\theta}{\theta_\infty} \right) \cos[\phi_{00}(z)] + \left(\frac{a}{w_0} \right) \sin[\phi_{00}(z)] \right] \tag{5.36}$$

and depends on the misalignments a/w_0 and θ/θ_∞. The mixing of information on the translations and rotations is determined by the Guoy phase $\phi_{00}(z)$. For example, if the quadrant photodiode is placed at a Guoy phase $\phi_{00} = 0$, then the error signal contains information only on rotations:

$$J_0\, J_1\, U_{00}\, U_{10} \left[\frac{\theta}{\theta_\infty} \right] \tag{5.37}$$

A second photodiode placed at $\phi_{00} = \pi/2$ would then allow the retrieval of information on the translations of the system:

$$J_0\, J_1\, U_{00}\, U_{10} \left[\frac{a}{w_0} \right] \tag{5.38}$$

Therefore, in order to reconstruct both misalignments, two photodiodes are necessary, possibly placed at an arbitrary Guoy phase $\phi_{00} = \phi_1$ and $\phi_{00} = \phi_1 + \pi/2$.

For this reason, the CITF quadrant photodiode configuration, shown in fig.(5.11), also consists of two quadrant photodiodes placed on each beam. The transmitted beams are monitored, as well as the beam reflected off of M_0 and off of M_{BS}. The fringe beam, on the other hand, is neglected. All transverse modes arising from any optical defects leak out to the dark fringe and for this reason, its error signal is not used.

beam		θ_0	θ_1	θ_2
Ψ_7	ph	$1.186 \cdot 10^{-2}$	$-8.558 \cdot 10^{-3}$	$-5.541 \cdot 10^{-3}$
	qu	$1.024 \cdot 10^{-3}$	$1.350 \cdot 10^{-2}$	$-1.499 \cdot 10^{-2}$
Ψ_8	ph	$1.194 \cdot 10^{-2}$	$-5.472 \cdot 10^{-3}$	$-8.654 \cdot 10^{-3}$
	qu	$-1.491 \cdot 10^{-3}$	$1.601 \cdot 10^{-2}$	$-1.453 \cdot 10^{-2}$
Ψ_2	ph	$-3.834 \cdot 10^{-1}$	$2.738 \cdot 10^{-2}$	$2.585 \cdot 10^{-2}$
	qu	$-7.718 \cdot 10^{-4}$	$5.605 \cdot 10^{-3}$	$-5.308 \cdot 10^{-3}$

Table 5.4: The asymmetry matrix for a CITF configuration: $\overline{\Delta l} = 0.8\,m$ and radius of curvature for the end mirrors of $93\,m$.

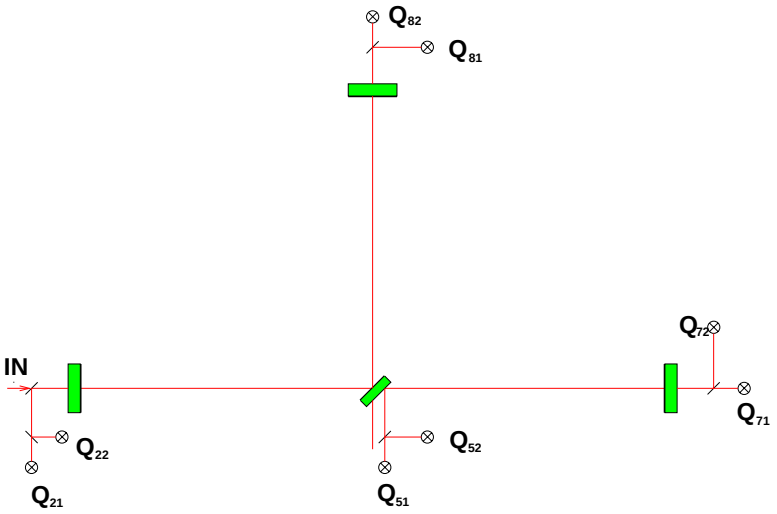

Figure 5.11: The quadrant photodiode configuration for the CITF. Two quadrant photodiodes are placed on each beam. The dark fringe is not monitored for the alignment.

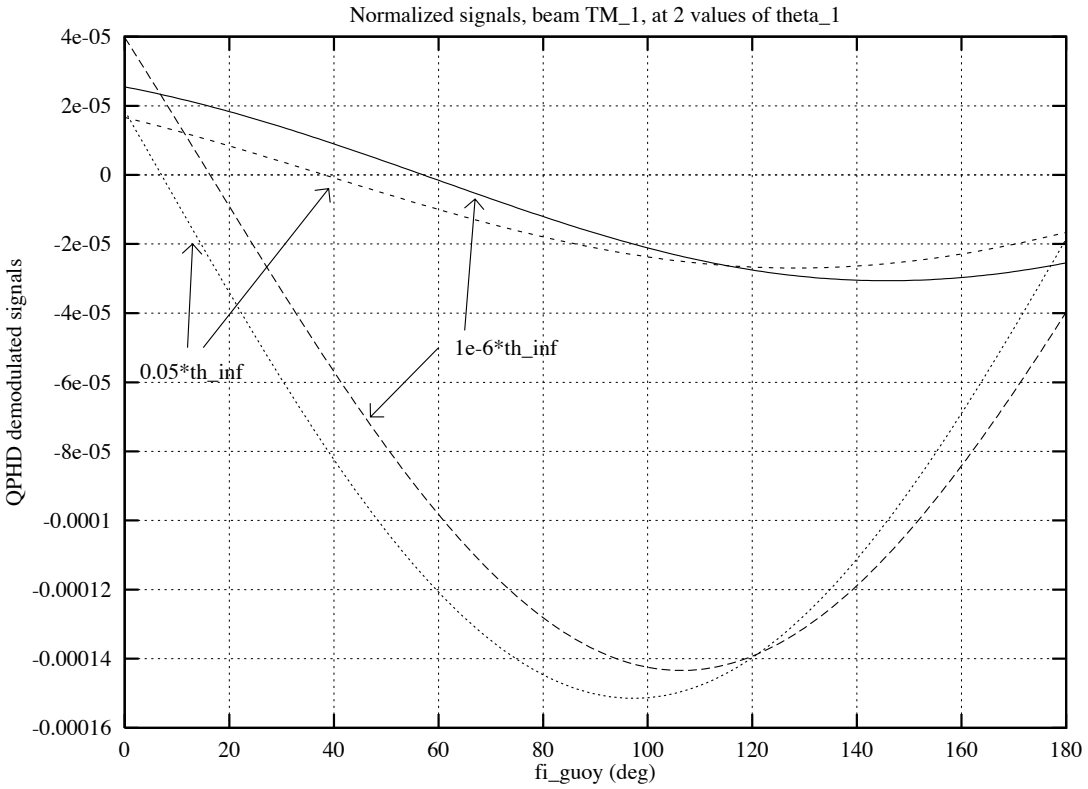

Figure 5.12: The demodulated signals from Ψ_7 as a function of ϕ_{00} and for two values of θ_1.

The chosen CITF asymmetry matrix[38] for the angular reconstruction, relative to the photodiode configuration shown in fig.(5.11), is presented in tab.(5.5), where ϕ_{00} indicates the Guoy phase and ϕ_D the demodulation phase of the photodiode signals. Considering mirror tilts in one plane only, the 8 quadrant configuration yields 3×16 elements.

The error signals, generated with the SIESTA module OPtestITF (see [49]) with the modal expansion limited to order $n + m = 4$, showed good linearity with misalignments up to $10^{-3}\,\theta_\infty$. A sizeable departure from linearity was observed for angles $10^{-1}\,\theta_\infty$.

The Guoy phase positioning of the quadrant photodiodes was chosen with the following criteria. Each pair of photodiodes is placed at a $\pi/2$ Guoy phase difference from each other so as to obtain orthogonal information on the misalignments. Since a departure from linearity is observed with increasing angles, the Guoy phase positioning of the photodiodes is chosen to prevent any change in sign for the asymmetries with increasing angle up to a maximum value. We see an example of sign change in fig.(5.12) where the demodulated signals from the photodiode placed on the transmitted beam are shown as a function of ϕ_{00} and for two values of θ_1.

It is possible to demodulate the photodiode signals at an arbitrary phase. Given the error signals A and B, the signals A' and B' demodulated at an arbitrary phase ϕ are such

$$A \cos\Omega t \,+\, B \sin\Omega t \,=\, A' \cos(\,\Omega t \,+\, \phi\,) \,+\, B' \sin(\,\Omega t \,+\, \phi\,) \tag{5.39}$$

where

$$\begin{aligned} A' \,&=\, A \cos\phi \,-\, B \sin\phi \\ B' \,&=\, A \sin\phi \,+\, B \cos\phi \end{aligned} \tag{5.40}$$

For the asymmetry matrix shown in tab.(5.5), the demodulation phase ϕ is chosen so as to minimize either an in-phase or quadrature term. The matrix terms minimized correspond to the zero values shown in the table.

5.9 The Reconstruction Procedure

The theory for the reconstruction procedure relative to the complete VIRGO interferometer has already been developed and experimentally verified [30, 40]. This section reviews and applies, through a numerical simulation, the procedure for the angle reconstruction for the CITF in one dimension using the asymmetry matrix shown in tab.(5.5).

The error signals y_i can be written in the form

$$y_i = \sum_j a_{ij}\,\theta_j \tag{5.41}$$

where θ_j is the misalignment angle for the j-th mirror, expressed in θ_∞ units, and a_{ij} is the asymmetry matrix shown in tab.(5.5). Given a set of n independent measurements y_n^* with statistical error δy_n, the best estimates for the parameters θ_j are those for which

$$\chi^2 = \sum_i \frac{(\,y_i^* - \sum_j a_{ij}\,\theta_j\,)^2}{\delta y_i^{\,2}} \tag{5.42}$$

is minimized[51]. By taking its first partial derivatives and setting them to zero

$$\left\{ \frac{\partial\,\chi^2}{\partial\,\theta_l} = 0 \right\} \quad \Rightarrow \quad \sum_k \frac{y_k^*}{\delta y_k^{\,2}}\,a_{kl} = \sum_j \left(\sum_i \frac{a_{ij}\,a_{il}}{\delta y_i^{\,2}} \right) \theta_j \tag{5.43}$$

a set of three equations in the three unknowns θ_l is obtained. This can be written in vectorial form as

$$\overline{P} = A\,\overline{\theta} \tag{5.44}$$

The parameters θ_j are then given by

$$\overline{\theta} = A^{-1}\overline{P} \tag{5.45}$$

with reconstruction errors $\Delta\theta_j$ equal to

$$\Delta\theta_j = \sqrt{\sum_k \left(\frac{\partial\theta_j}{\partial y_k} \right)^2 \delta y_k^{\,2}} \tag{5.46}$$

Let's assume that the noise on each photodiode is limited by the shot-noise. For the DC component attenuated to 3 mW, the shot-noise level corresponds to $\delta y_j = 1.7 \times 10^{-11}\,[W/\sqrt{Hz}]$. By referring to eq.(5.46), the angular reconstruction errors due to shot-noise limited signals is

$$\begin{aligned} \Delta\theta_0 &= 8.02 \times 10^{-9}\,\theta_\infty \;\; [1/\sqrt{Hz}] \\ \Delta\theta_1 &= 2.94 \times 10^{-8}\,\theta_\infty \;\; [1/\sqrt{Hz}] \\ \Delta\theta_2 &= 2.91 \times 10^{-8}\,\theta_\infty \;\; [1/\sqrt{Hz}] \end{aligned} \tag{5.47}$$

We also used a numerical simulation to estimate the reconstruction errors and compared the results with those given by eq.(5.47). The optical module OPtestITF, limited to modes $m + n = 4$, was used to calculate the in-phase and quadrature signals, as a function of mirror tilts, at the location of each quadrant photodiode. The misalignments were generated according to a Gaussian distribution with dispersion $\sigma = 10^{-5}\,\theta_\infty$ and are shown in the top graphs of fig.(5.13),

Q.Ph.	ϕ_{00}	ϕ_D (°)		θ_0	θ_1	θ_2
Q_7	40 °	$2.2313 \cdot 10^{+1}$	sin	$4.256 \cdot 10^{-3}$	$-7.6233 \cdot 10^{-3}$	0
			cos	$8.309 \cdot 10^{-4}$	$1.2325 \cdot 10^{-2}$	$1.4165 \cdot 10^{-2}$
	130 °	$-9.4122 \cdot 10^{-2}$	sin	$-9.1070 \cdot 10^{-3}$	$7.4093 \cdot 10^{-3}$	0
			cos	$4.9233 \cdot 10^{-4}$	$3.4013 \cdot 10^{-2}$	$3.4703 \cdot 10^{-2}$
Q_8	80 °	$7.5236 \cdot 10^{+1}$	sin	0	$3.2209 \cdot 10^{-2}$	$3.1723 \cdot 10^{-2}$
			cos	$2.3559 \cdot 10^{-3}$	$-4.3430 \cdot 10^{-3}$	$-5.7420 \cdot 10^{-3}$
	170 °	$1.7094 \cdot 10^{+2}$	sin	$-9.8263 \cdot 10^{-3}$	$6.4013 \cdot 10^{-3}$	$-4.3100 \cdot 10^{-3}$
			cos	0	$1.8201 \cdot 10^{-2}$	$1.8434 \cdot 10^{-2}$
Q_2	30 °	4.3053	sin	1.5220	$-5.3542 \cdot 10^{-1}$	$5.3138 \cdot 10^{-1}$
			cos	$1.1339 \cdot 10^{-1}$	0	$7.9673 \cdot 10^{-2}$
	120 °	4.1003	sin	1.1799	$-8.8540 \cdot 10^{-1}$	$8.8203 \cdot 10^{-1}$
			cos	$8.4472 \cdot 10^{-2}$	0	$1.2675 \cdot 10^{-1}$
Q_5	0 °	3.7661	sin	$-9.1743 \cdot 10^{-3}$	$5.8870 \cdot 10^{-3}$	$-4.9030 \cdot 10^{-3}$
			cos	0	$1.1568 \cdot 10^{-2}$	$1.1731 \cdot 10^{-2}$
	90 °	$1.8173 \cdot 10^{+2}$	sin	$-4.0353 \cdot 10^{-3}$	$2.8573 \cdot 10^{-3}$	$2.4385 \cdot 10^{-3}$
			cos	0	$3.4793 \cdot 10^{-2}$	$3.4940 \cdot 10^{-2}$

Table 5.5: The asymmetry matrix for the quadrant photodiode configuration shown in fig.(5.11). ϕ_{00} denotes the Guoy phase and ϕ_D refers to the demodulation phase. Notice that the dark fringe beam is not monitored.

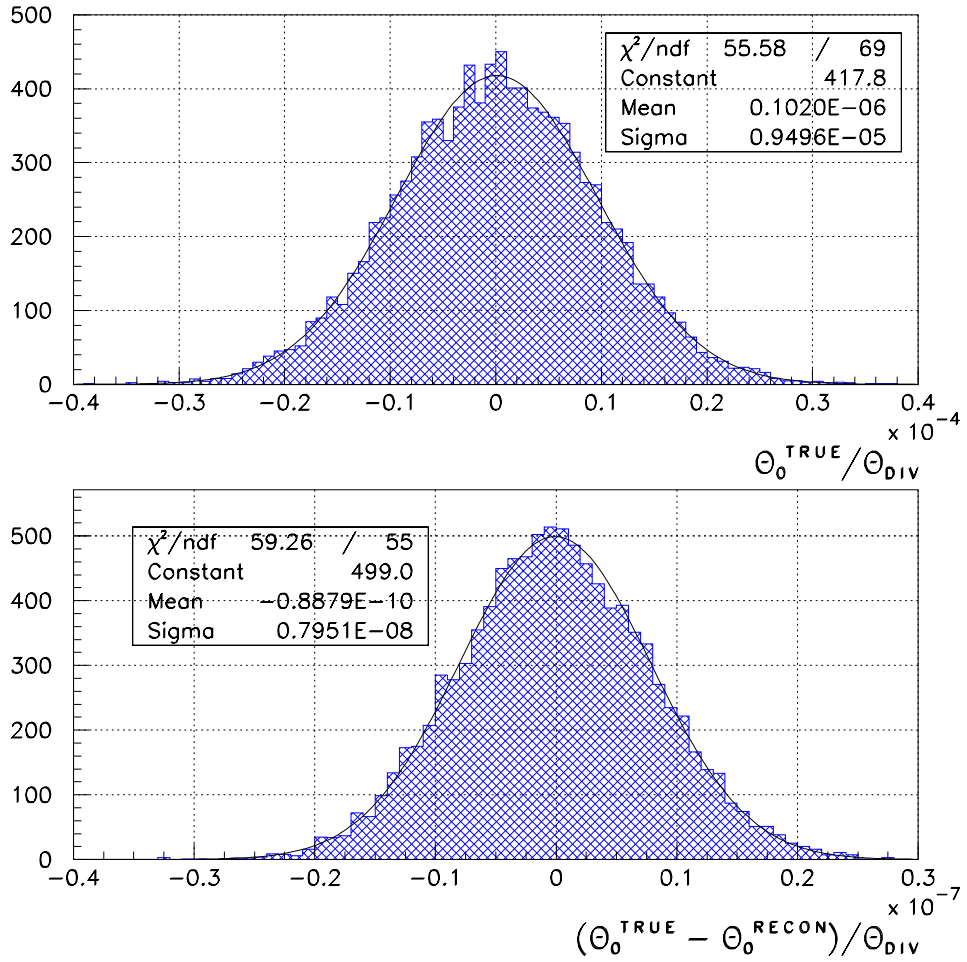

Figure 5.13: Distribution of the difference between the true angle $\theta_0^{\rm true}$ and the reconstructed angle $\theta_0^{\rm recon}$. Top graph: the distribution of the angle $\theta_0^{\rm true}$ with $\sigma_{\theta_0} = 10^{-5}\,\theta_\infty$ ($\theta_{DIV} \equiv \theta_\infty$). Bottom graph: the distribution of the error $(\,\theta_0^{\rm true} - \theta_0^{\rm recon}\,)\,/\,\theta_\infty$ with $\sigma = 7.95 \times 10^{-9}\,\theta_\infty$.

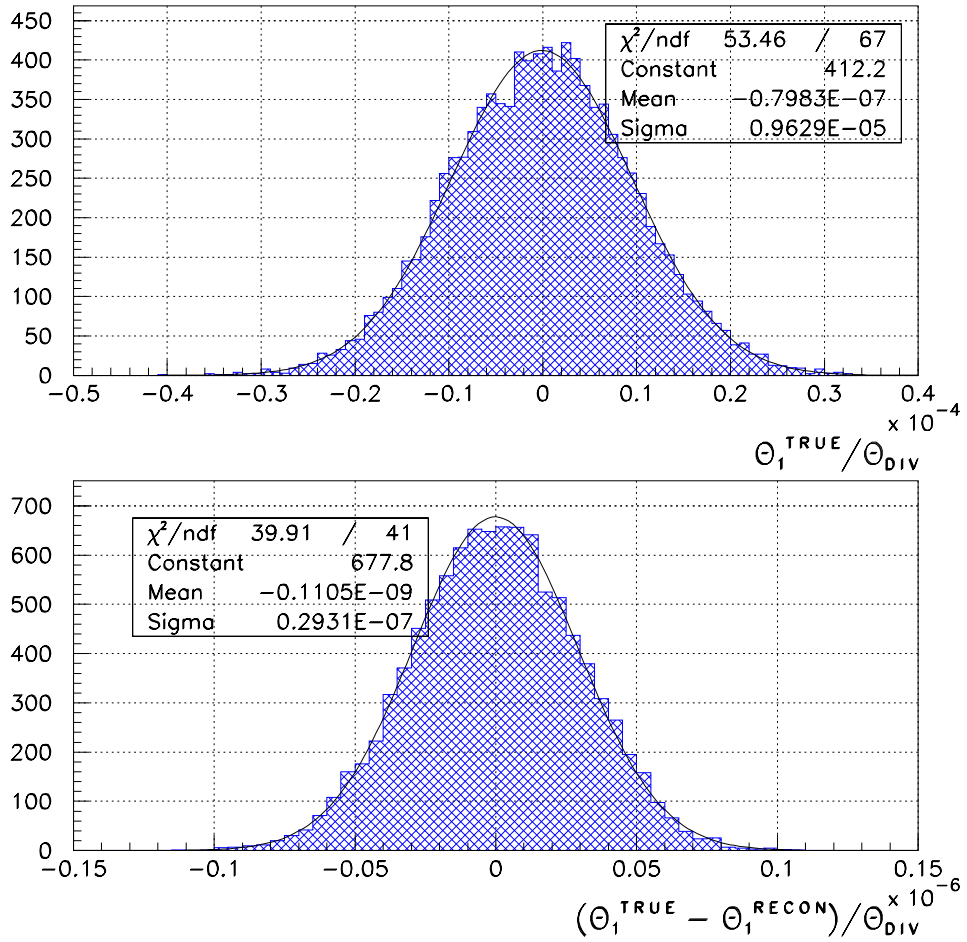

Figure 5.14: Distribution of the difference between the true angle $\theta_1^{\rm true}$ and the reconstructed angle $\theta_1^{\rm recon}$. Top graph: the distribution of the angle $\theta_1{}^{\rm true}$ with $\sigma_{\theta_1} = 10^{-5}\,\theta_\infty$ ($\theta_{DIV} \equiv \theta_\infty$). Bottom graph: the distribution of the error $(\,\theta_1{}^{\rm true} - \theta_1^{\rm recon}\,)\,/\,\theta_\infty$ with $\sigma = 2.93 \times 10^{-8}\,\theta_\infty$.

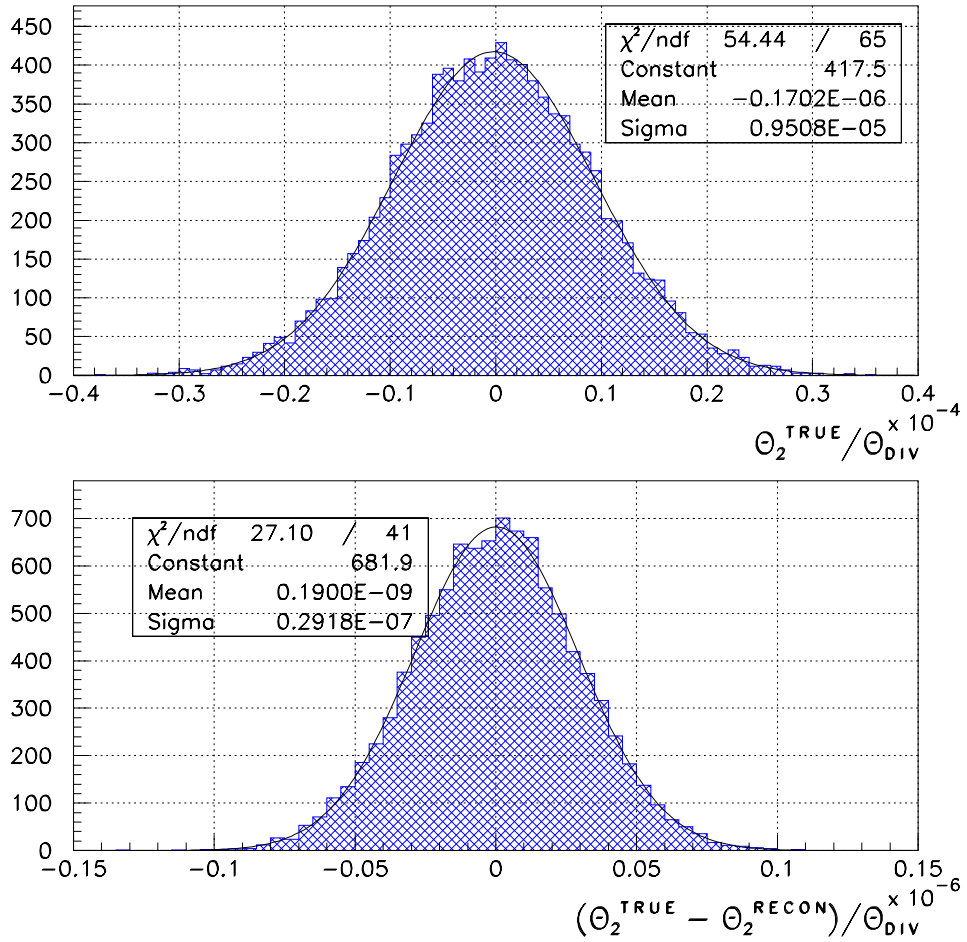

Figure 5.15: Distribution of the difference between the true angle $\theta_2^{\rm true}$ and the reconstructed angle $\theta_2^{\rm recon}$. Top graph: the distribution of the angle $\theta_2{}^{\rm true}$ with $\sigma_{\theta_2} = 10^{-5}\,\theta_\infty$ ($\theta_{DIV} \equiv \theta_\infty$). Bottom graph: the distribution of the error $(\,\theta_2{}^{\rm true} - \theta_2^{\rm recon}\,)\,/\,\theta_\infty$ with $\sigma = 2.92 \times 10^{-8}\,\theta_\infty$.

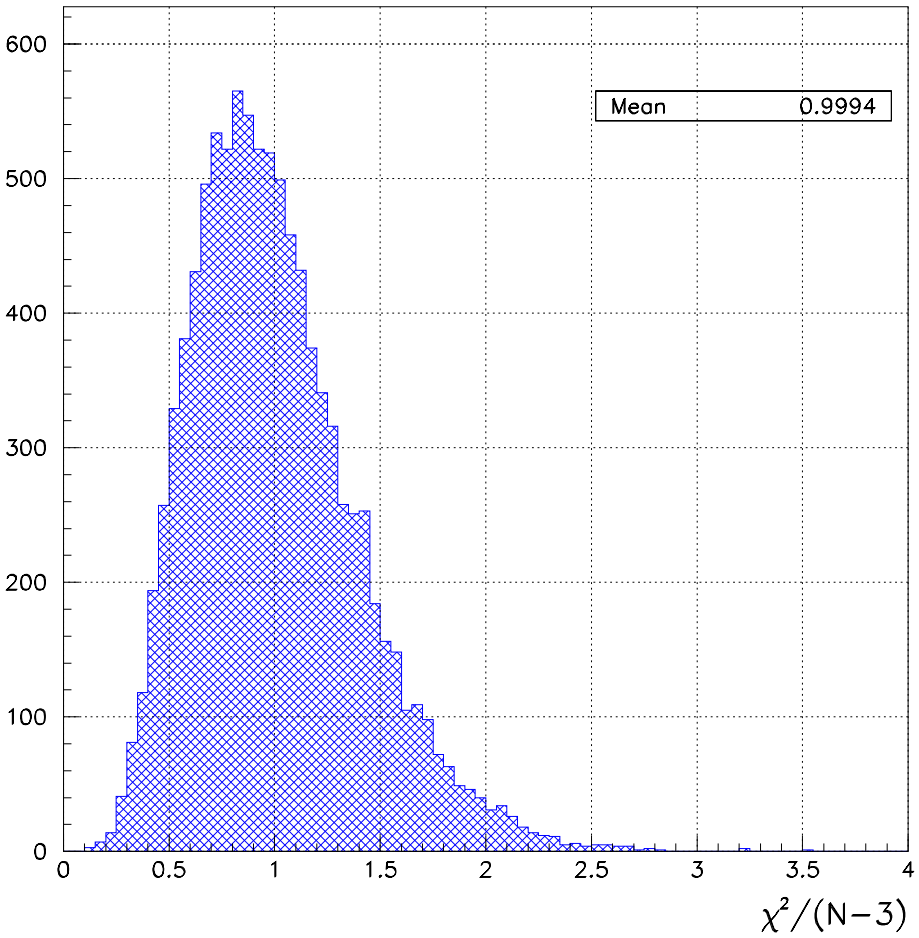

Figure 5.16: The χ^2 distribution for the angular reconstruction procedure.

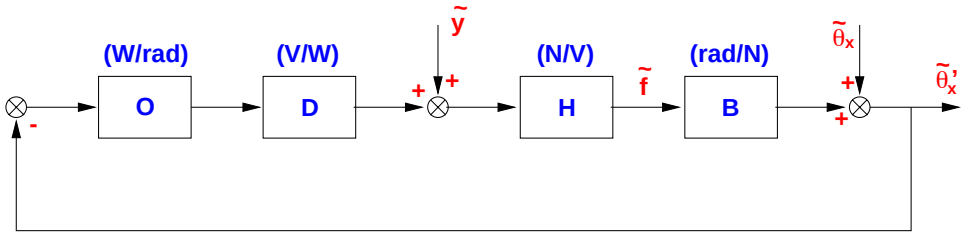

Figure 5.17: Block diagram for the mirror angular control.

fig.(5.14) and fig.(5.15). A reconstruction procedure then took the 16 error signals and used the asymmetry matrix in tab.(5.5) to reconstruct the misalignments. The distribution of the difference $(\theta^{\,\mathrm{true}} - \theta^{\,\mathrm{recon}})\,/\,\theta_\infty$ is shown in the bottom graphs of fig.(5.13), fig.(5.14) and fig.(5.15). By fitting the resulting distribution to a Gaussian, the reconstructed errors are

$$\begin{aligned} \Delta\theta'_0 &= 7.95 \times 10^{-9}\,\theta_\infty \;\; [1/\sqrt{Hz}] \\ \Delta\theta'_1 &= 2.93 \times 10^{-8}\,\theta_\infty \;\; [1/\sqrt{Hz}] \\ \Delta\theta'_2 &= 2.92 \times 10^{-8}\,\theta_\infty \;\; [1/\sqrt{Hz}] \end{aligned} \tag{5.48}$$

in agreement with the values found in eq.(5.47). The χ^2 distribution for the simulation run here presented is shown in fig.(5.16), with a mean value centered at 1. By plotting the χ^2 distribution for each error signal as a function of time, it is possible to monitor the behavior of each quadrant photodiode.

Concluding, this quadrant photodiode configuration allows to understand the angle misalignment for each individual mirror. These misalignments were taken from a Gaussian distribution with $\sigma = 10^{-5}\,\theta_\infty$. For larger angular values, the reconstruction error increases due to a change in the relation between misalignments and photodiode signals (see sec.(5.8)).

5.10 Angular Control

A preliminary study for the CITF angular control is here presented. It will be shown in sec.(6.1.1) and sec.(6.2) that the most stringent requirement for the alignment of the complete VIRGO interferometer comes from the coupling alignment/laser jitter: by assuming a laser beam jitter of $10^{-11}\,rad/\sqrt{Hz}$, the mirrors must be aligned to better than $10^{-8}\,rad$ RMS. For this reason, we would like to design a control system able to attenuate the CITF angular motion down to the $nrad$ RMS.

In this section, the main characteristics of the control system will be given as well as its performance in open and closed loop. It will be also shown how only the marionetta can be used for the control.

5.10.1 The Control System

Let $\tilde{\theta}_x$ represent the mirror angular density spectrum in open loop, as shown in fig.(5.6c). The objective is to attenuate this angular motion for the recycling mirror and both end mirrors once the CITF is longitudinally locked. This control could be achieved by using the reference mass as well as the steering filter piloting the marionetta. However, only the steering filter will be used: the reference mass does not have a sufficiently high dynamic range for this type of control, as shown below.

Let the control system be described by the block diagram shown in fig.(5.17) where

- O describes the CITF optical transfer function, assumed to be constant in this work, relating the mirror tilt with the output beam signals;

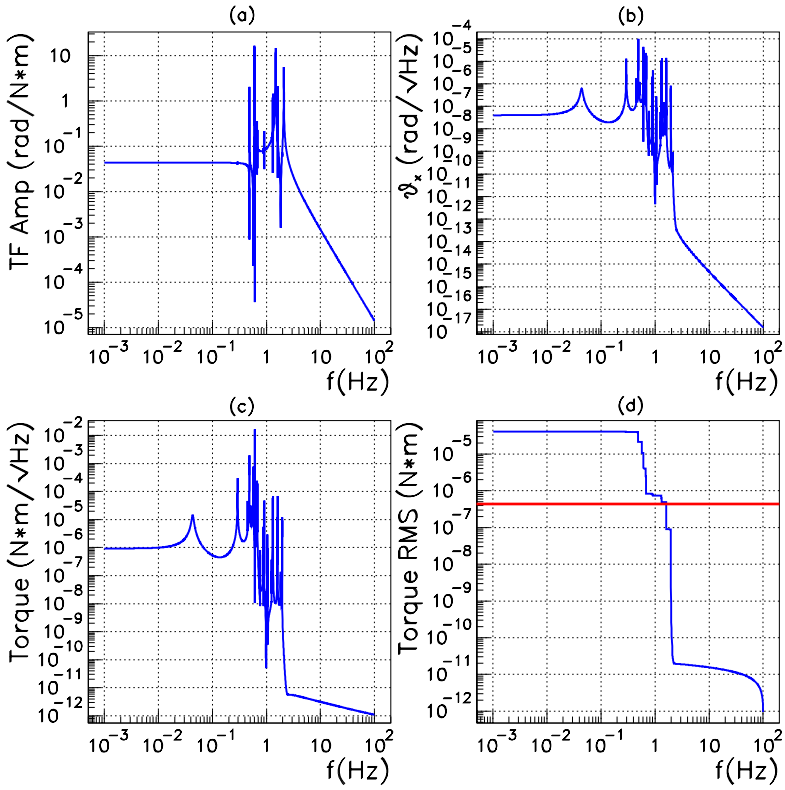

Figure 5.18: The estimated torque for the mirror angular control from the reference mass. In (a), the amplitude transfer function relating torque with angular displacement; (b) shows the estimated angular mirror spectrum $\tilde{\theta}_x$ in free motion; (c) shows the torque spectrum density once the loop is closed and (d) shows its corresponding running RMS value.

- D is the photodiode's transfer function, also assumed constant, transforming the incoming beam power from W to V;
- $\tilde{y}$ is the error contribution to the angle reconstruction due to shot-noise limited signals;
- H filters the incoming photodiode's voltage, with the error contribution, providing the output force $\tilde{f}$ to be applied to the marionetta from the steering filter;
- B is the mechanical transfer function transforming the force $\tilde{f}$ into angular motion;
- $\tilde{\theta}_x$ is the mirror angular density spectrum in open loop;
- $\tilde{\theta}'_x$ is the mirror angular density spectrum in closed loop.

Once the system is in closed loop, the resulting angular mirror motion $\tilde{\theta}'_x$ is

$$\tilde{\theta}'_x = \left(\frac{1}{1+G}\right)\tilde{\theta}_x + \left(\frac{H\,B}{1+G}\right)\tilde{y} \tag{5.49}$$

where $G \equiv O\,D\,H\,B$ is the open loop transfer function. The force for the control is

$$\tilde{f} = -\left(\frac{H\,O\,D}{1+G}\right)\tilde{\theta}_x + \left(\frac{H}{1+G}\right)\tilde{y} \tag{5.50}$$

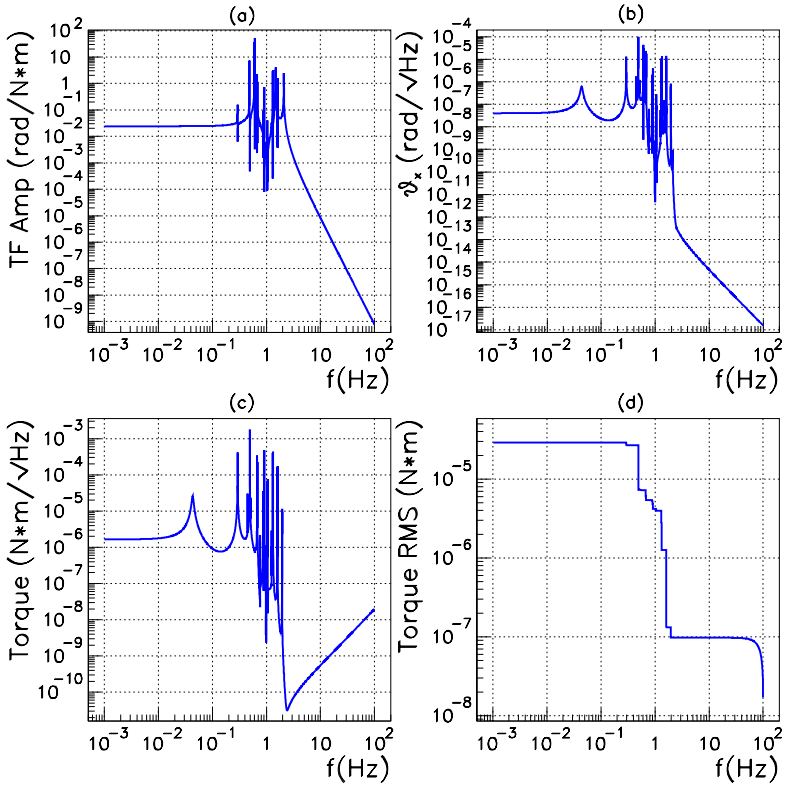

Figure 5.19: The estimated torque for the mirror angular control from the steering filter of the superattenuator. In (a), the B amplitude transfer function relating the torque with the angular displacement; (b) shows the estimated angular mirror spectrum $\tilde{\theta}_x$ in free motion; (c) shows the torque spectrum density once the loop is closed and (d) shows its corresponding running RMS value.

If the design of H is such that within a given bandwidth

$$| G | \gg 1 \tag{5.51}$$

then eq.(5.49) and eq.(5.50) can be approximated as

$$\begin{aligned} \tilde{\theta}'_x &\simeq \left(\frac{1}{G}\right)\tilde{\theta}_x + \tilde{y} \\ \tilde{f} &\simeq -\left(\frac{1}{B}\right)\tilde{\theta}_x + \left(\frac{1}{O\,D\,B}\right)\tilde{y} \end{aligned} \tag{5.52}$$

From the above, the angular motion in open loop will be attenuated by a factor G and will be limited by the shot-noise value. Furthermore, within the bandwidth in question, the necessary force for the control will be proportional to the seismic excitation $\tilde{\theta}_x$ and inversely proportional to the mechanical transfer function B.

Marionetta or reference mass?

The simulation program used for the mirror motion estimates, described in sec.(5.5.2), can be used to estimate the transfer functions (referred to as B in the block diagram in fig(5.17)) necessary for the mirror control from the reference mass as well as from the steering filter. Therefore, it is possible to estimate the forces involved from both control systems.

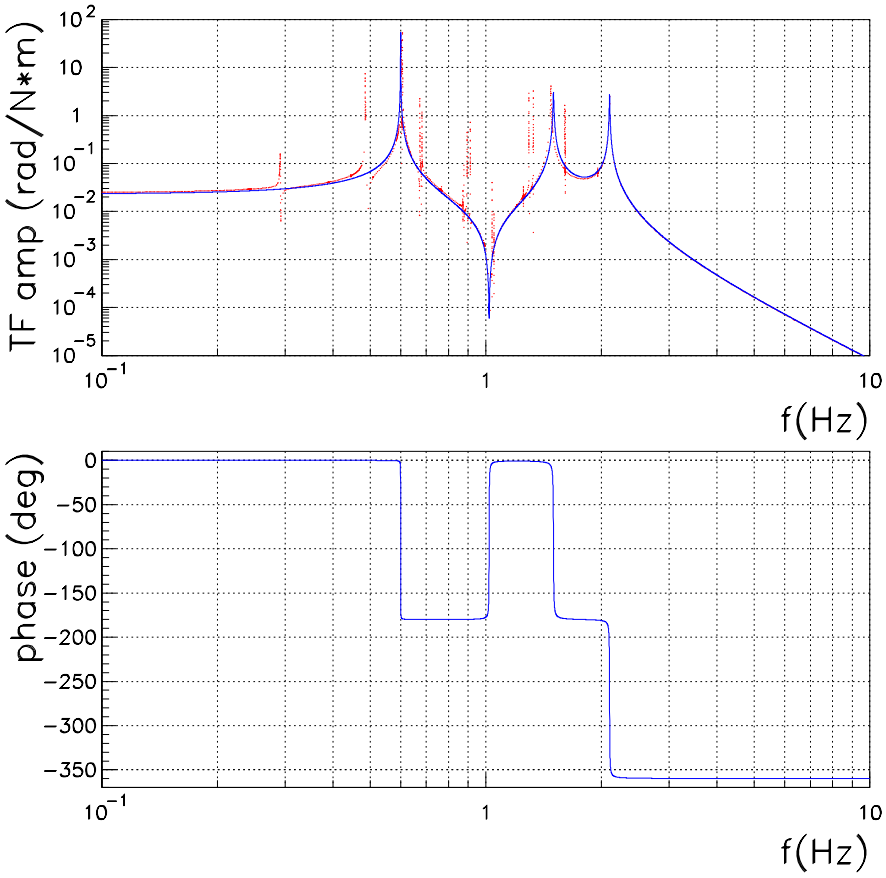

Figure 5.20: The B transfer function relating the torque applied from the steering filter to the mirror tilt θ_x. Top: the transfer function amplitude: dots: simulation output; continuous line: approximation. Bottom graph: transfer function phase. Only the approximated behavior is shown.

Fig.(5.18a) shows the amplitude transfer function relating the torque to the mirror angular displacement from the reference mass. By dividing the expected seismic noise, shown in fig.(5.18b), with the amplitude transfer function in fig.(5.18a), we obtain the torque spectrum density shown in fig.(5.18c). Integrating the latter leads to the graph shown in fig.(5.18d) which gives the expected running RMS torque for the reference mass. According to [39], the maximum allowed torque for the reference mass and the steering filter are

$$\begin{aligned} \text{reference mass} &\rightarrow 4.41 \times 10^{-7}\,(N\,m)\ \text{RMS} \\ \text{steering filter} &\rightarrow 0.84 \times 10^{-3}\,(N\,m)\ \text{RMS} \end{aligned} \tag{5.53}$$

For the reference mass, this maximum value is shown in the figure by the gray line. This means that from frequencies above $1.5\,Hz$, the reference mass could be used for the control. However, it clearly is not suited for the angular control of the CITF, where all the angular motion is concentrated below $1.5\,Hz$.

On the other hand, we show in fig.(5.19) the results relative to the control from the marionetta. The limit set in eq.(5.53) is well above the foreseen RMS torques necessary. As a consequence, in this preliminary study we will only make use of the marionetta to pilot the mirror.

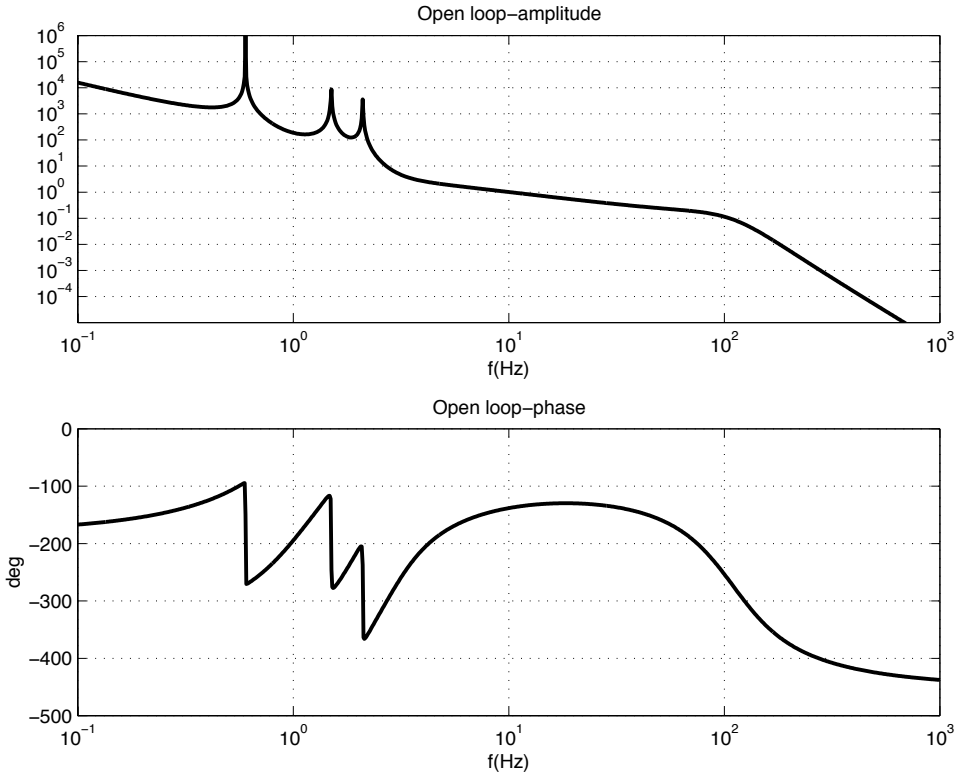

Figure 5.21: The open loop transfer function G for the mirror angular control.

The H filter

The amplitude transfer function for the mirror control from the marionetta, shown in fig.(5.19a), is also shown by the dots in the top graph of fig.(5.20). Its essential behavior is shown on the same plot by the continuous line and can be characterized by a set of 3 double-poles (the peaks at $0.6\,Hz$, $1.5\,Hz$ and $2.1\,Hz$) and one double-zero (the notch at $1\,Hz$). The remaining characteristics arise from sets of pole-zero, close enough to each other to cancel their combined effect.

In order to prevent instabilities, the notch must not cross the unitary gain. Also, the mirror motion is mostly concentrated around $1\,Hz$ so that, if a bandwidth of tens of Hz is desired, it is necessary to compensate the notch to some degree. This implies a very good knowledge of the transfer function around $1\,Hz$ in order to guarantee that the feedback system is robust.

We have assumed, for simplicity, that we know B exactly and we have chosen the poles and zeros of H to consist of

- a double pole at the origin in order to attenuate the low frequency region as much as possible;
- two poles to compensate the notch at $1\,Hz$;
- a set of 7 zeros to let the open loop transfer function descend as $1/s$ when crossing the UGF;
- four poles to limit the H filter dynamic from about $100\,Hz$.

The filter H can be written as

$$H(s) = K\,\frac{(s-a)\,(s-a^*)\,(s-b)\,(s-b^*)\,(s-c)\,(s-c^*)\,(s-d)}{s^2\,(s-e)\,(s-e^*)\,(s-f)\,(s-f^*)\,(s-g)\,(s-g^*)} \tag{5.54}$$

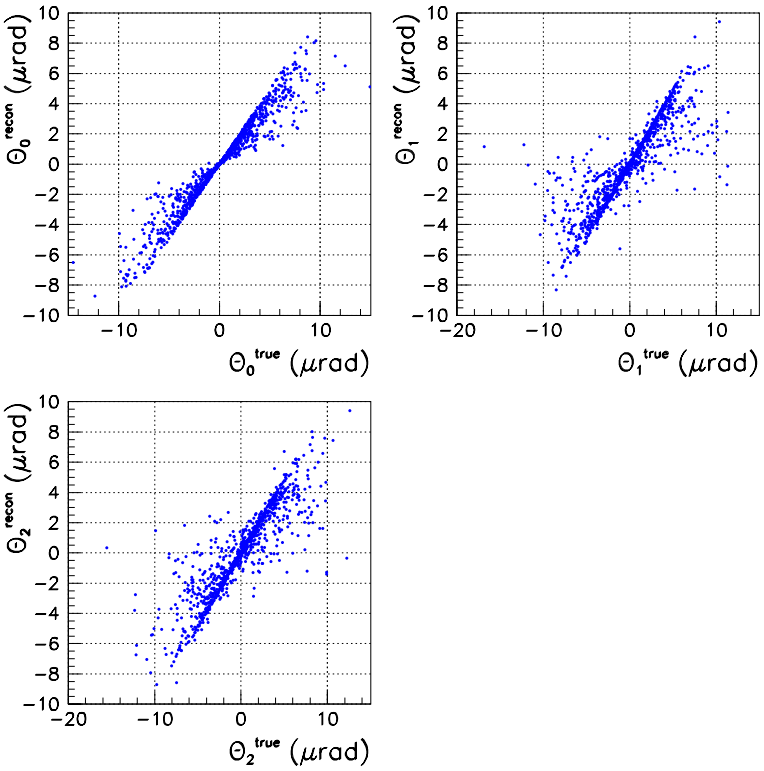

Figure 5.22: The angle reconstruction as a function of the real angular value.

where

$$\begin{aligned} K &= 2 \times 10^{11}\,[N/V] \\ a &= -3.1 + i\,5.4 \\ b &= -7.2 + i\,17.4 \\ c &= -4.8 + i\,11.6 \\ d &= -9.4 \\ e &= -6.4 \times 10^{-2} + i\,6.4 \\ f &= -3.1 \times 10^{2} + i\,5.4 \times 10^{2} \\ g &= -3.8 \times 10^{2} + i\,6.5 \times 10^{2} \end{aligned} \tag{5.55}$$

with the poles and zeros in rad/s units. The resulting open loop transfer function is shown in fig.(5.21). The gain is 10^4 at $10^{-1}\,Hz$ with the UGF at $10\,Hz$ and a gain and phase margin of $6\,db$ and 40^o respectively.

5.10.2 Autoalignment: Open and Closed Loop

We present the results of the model presented thus far, sketched in fig.(5.17), once it was implemented within the SIESTA engine. Before presenting the closed loop performance, a discussion of the open loop case will be given.

The optical model described in sec.(5.8) and the angle reconstruction procedure discussed in sec.(5.9) will be used. We let the recycling mirror and both end mirrors follow the motion

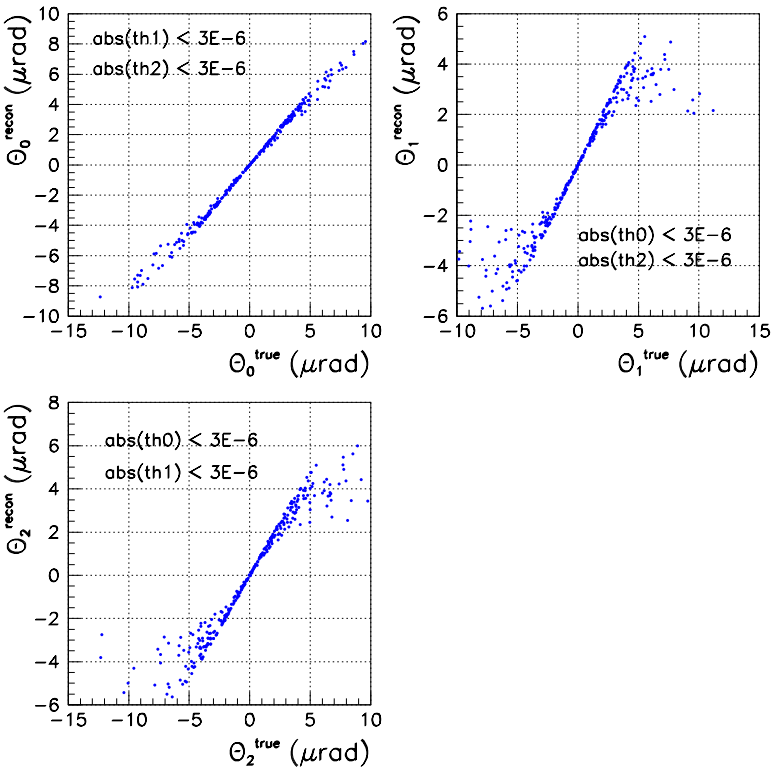

Figure 5.23: The angle reconstruction as a function of the real angular value and with the angular cuts shown.

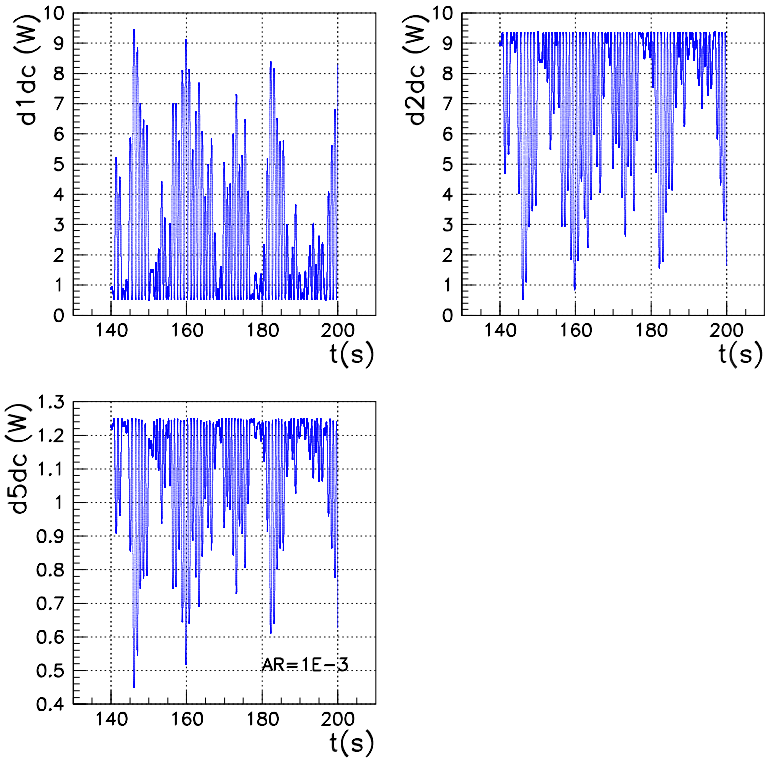

Figure 5.24: The DC power fluctuations as the mirrors move in free motion.

described by the spectrum shown by the continuous line in fig.(5.25), which is an approximation of fig.(5.6c). As the simulation evolved in time, the angular tilts of the three mirrors followed the motion described by the angular spectrum given. At each tick of the simulation's clock, an adjustment was made on Δl and l_r so as to optimize dark fringe and maximize recycling, therefore simulating the locked state.

Angle reconstruction for mirrors in free motion

In order to study the performance of the angle reconstruction, we extracted the mirrors' tilts from a white and Gaussian distribution with $\sigma = 4 \times 10^{-6}\, rad$ RMS. The results of a simulation run are shown in fig.(5.22) and fig.(5.23). The reader can observe that in the plots of fig.(5.22), the mirror tilts can go up to $10^{-5}\, rad$. Even though for these large angular values the reconstruction percent error reaches errors as high as 90%, the reconstructed angles always have the correct sign. For this reason, no difficulties in the acquisition of control are expected.

In fig.(5.23) we show how the reconstruction can be improved if an angular cut on the true angular positions is introduced. For example, the reconstruction of θ_1 is improved when the excursions of the real values of θ_0 and θ_2 are limited.

DC power fluctuations in open loop

It is also interesting to observe the DC power fluctuations for a free motion run with the mirrors following the open loop spectrum density shown by the continuous curve of fig.(5.25), consisting of an approximation of the spectrum shown in fig.(5.6c). Each mirror moves with an angular motion of $1.5\, \mu rad$ RMS. The DC power fluctuations are shown in fig.(5.24) where d_1^{dc} refers to

the photodiode on the dark fringe, d_2^{dc} is the photodiode on the beam reflected off of the recycling mirror and d_5^{dc} is the photodiode placed on the beam reflected off of the BS ($AR = 10^{-3}$). The DC power fluctuations for the dark fringe detector can go as high as $9\,W$. This is explained by the fact that any high order transverse mode generated by the misalignments is leaked directly out to the dark fringe, thus inducing large DC power fluctuations, as discussed below.

The CITF can be seen as a Fabry-Perot whose input mirror is the CITF recycling mirror and whose virtual end mirror transmittivity t is simply $d_1^{dc}/2 * d_5^{dc} * 1000$ where $2 * d_5^{dc} * 1000$ is the DC power incident to the BS. The stored DC power of the Fabry-Perot is then the DC power stored in the recycling cavity. It is then clear that, the more power is leaked out of the dark fringe, the higher the transmittivity of the Fabry-Perot virtual mirror, inducing a decrease in the stored power.

For example, at about $160\,s$

$$\begin{aligned} d_1^{dc} &\simeq 9\,W \\ d_5^{dc} &\simeq 0.52\,W \\ d_2^{dc} &\simeq 0.9\,W \end{aligned} \tag{5.56}$$

At that instant, about $t^2 = 9/1040 \simeq 0.87\%$ of power is lost in higher order modes, mainly through the dark fringe port (neglecting the transmitted beam contributions and assuming no absorption losses). The stored power P is then

$$P = 10\,W\,\frac{t_0^2}{(1 - r_0\sqrt{1-t^2})^2} \simeq 1070\,W \tag{5.57}$$

The reader will recall that the desired power buildup for the locked and aligned CITF is $2.6\,kW$.

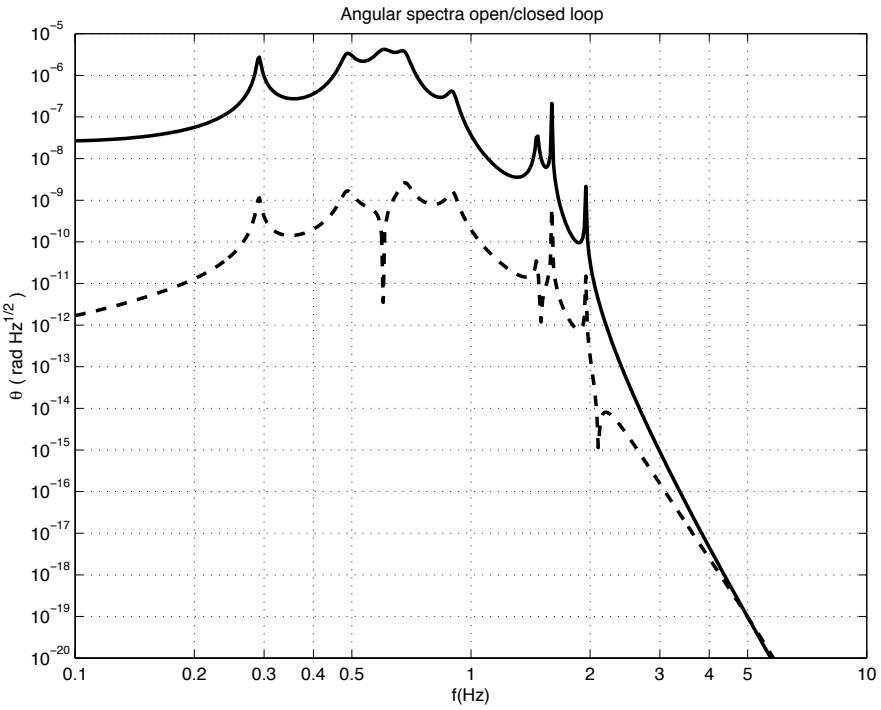

Figure 5.25: The angular density spectrum in open/closed loop. Continuous line: open loop $\tilde{\theta}_x$; dotted line: closed loop $\tilde{\theta}'_x$

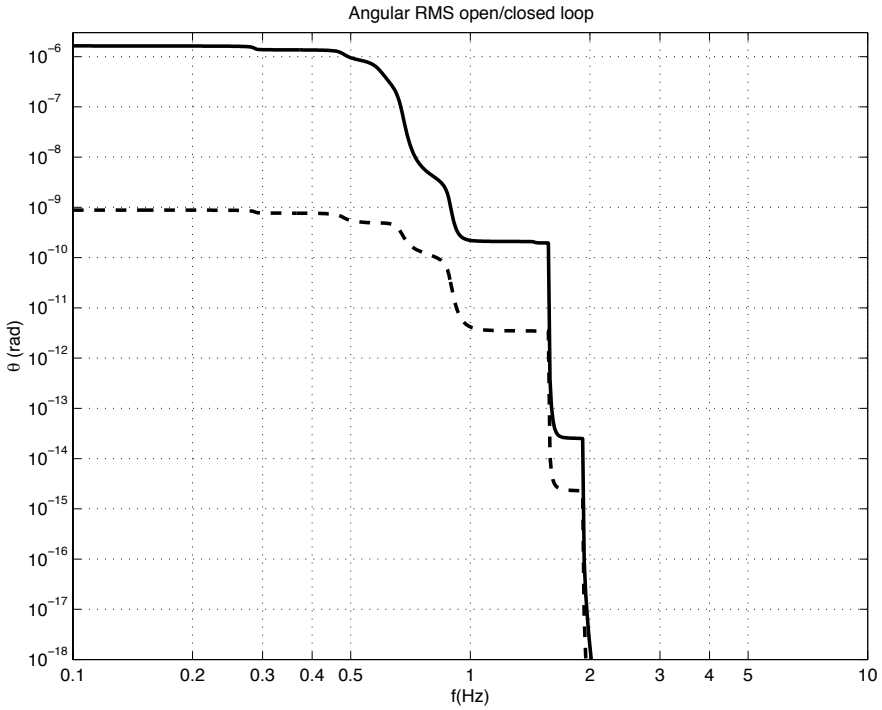

Figure 5.26: The angular displacement running RMS value. Continuous line: open loop θ_x; dotted line: closed loop θ'_x.

The closed loop performance

The performance of the control system in closed loop is here presented. The seismic angular density spectrum noise used is an approximation of the spectrum shown in fig.(5.6c) and it is shown by the continuous curve in fig.(5.25). The continuous curve in fig.(5.26) shows its running rms value, resulting in $1.5\,\mu rad$ RMS. Once the loop is closed (dotted curves in the figures), the open loop RMS value is attenuated down to to $10^{-9}\,rad$.

Fig.(5.27) shows the histogram of the three mirror angles, once in closed loop, with a resulting angular motion for each of $10^{-9} rad$ RMS. In the same figure, the distribution of the dark fringe DC power fluctuations are limited to within 10^{-5}.

5.11 Conclusion

In this chapter, we presented a study on the optical response to longitudinal and angular mirror motions. We showed that, when the CITF is in a non-linear state, by taking the ratio of photodiode signals it is possible to detect dark fringe and obtain an error signal useful for its control, regardless of the power buildup in the recycling cavity. The results of this investigation will be used to guide the CITF from a non-linear state to the locked state.

Furthermore, by examining the CITF angular response, we were able to design an algorithm using an 8 quadrant photodiode configuration, capable to angularly reconstruct, in one dimension, the mirror tilts once the CITF is in a locked state.

This algorithm was then implemented in an angular control system for the CITF. We have shown how only the marionetta can be used and that the piloting of the mirror from the steering filter requires a very good knowledge of the transfer function in question if the bandwidth of the system is to be limited to within some tens of Hz.

Therefore, assuming a good knowledge of the transfer function for the control, we have designed a filter for the autoalignment capable of attenuating the angular fluctuations down to the $10^{-9} rad$

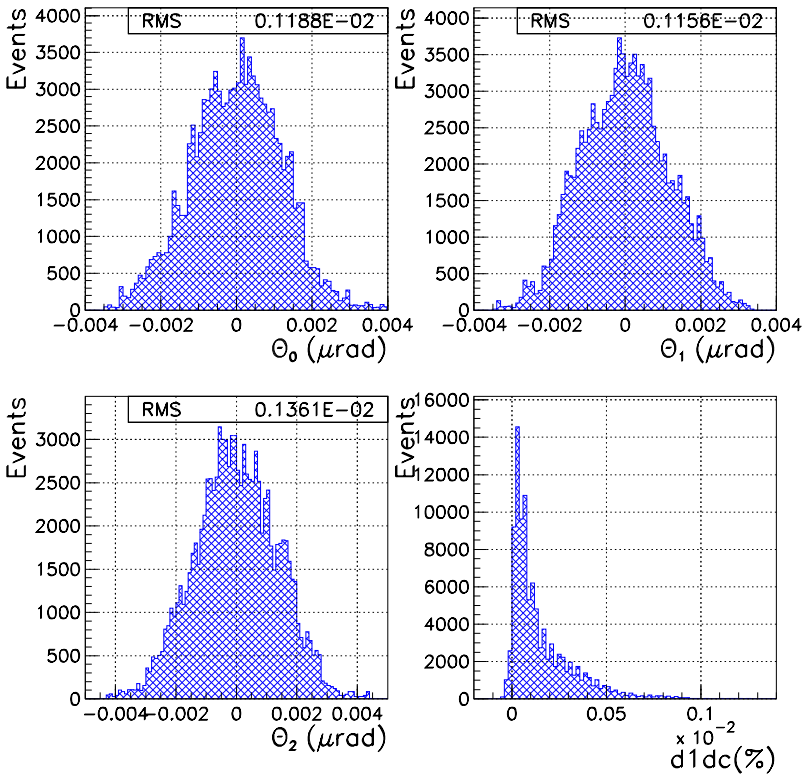

Figure 5.27: The angular RMS values in closed loop and the dark fringe DC power fluctuations expressed in percent.

RMS as required by the coupling laser jitter/misalignment.

We also observed that in open loop, the foreseen angular spectral density for each mirror causes large DC power fluctuations. However, even for these large angular values, the model was able to reconstruct them with the correct sign: no difficulties acquiring control are expected.

Chapter 6

The Mode-Cleaner Prototype

One of the first suspended cavities within the VIRGO project is the Orsay mode-cleaner prototype. It served as a test bed for

- mirror local control systems;
- longitudinal locking;
- automatic alignment.

The structure of this chapter is threefold. First, the motivations for the use of a mode-cleaner are given together with a brief description of its VIRGO configuration. Next, the Orsay mode-cleaner (MC30) is characterized, in particular its optical response, the local mirror controls, and the servo system for the longitudinal control. Finally, and most importantly, the simulations performed for the study of the acquisition of lock are discussed. For a brief overview of feedback design, refer to Appendix A.

6.1 Why a Suspended Mode-Cleaner?

Fig.(6.1) represents the mode-cleaner optical configuration. It consists of a suspended three mirror

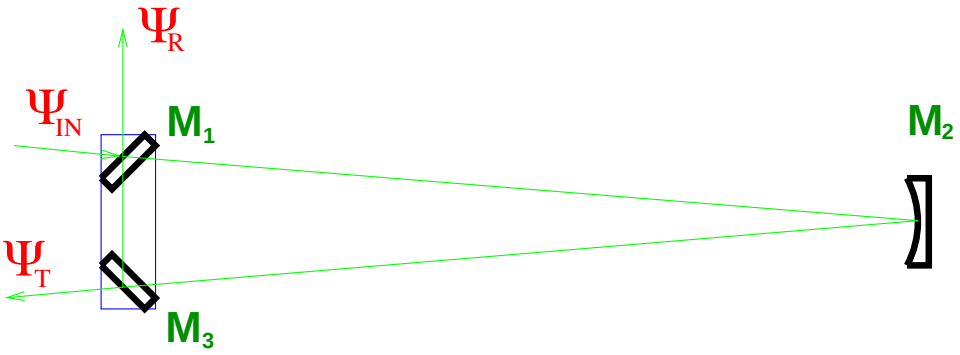

Figure 6.1: The mode-cleaner optical configuration.

ring cavity of perimeter 2L as implemented in most gravitational wave interferometers. In fig.(6.1), M_1 and M_3 denote both input and output mirrors, with the same transmittivity and reflectivity, whereas M_2 indicates the terminal mirror whose reflectivity is set to 1. The objective of this optical configuration is to

- transmit the fundamental TEM_{00} mode while reflecting all higher order modes;

- attenuate both frequency and power fluctuations;
- attenuate beam jitter by at least 3 orders of magnitude.

6.1.1 Beam Jitter and Optical Defects

In order for the incoming light beam to couple completely to the interferometer, it is necessary to spatially filter it. The main sources of noise arise from

1. beam distortions generated by the optical elements;
2. the laser beam *jitter*.

As already stated in Ch.(3), every monochromatic light distribution can be expressed as a linear combination of the propagation modes $\mathrm{TEM}_{m\,n}$. The effect of the passage of light in the many optical components, such as the phase modulator, induces beam distortions which can be expressed as a linear combination of high order modes. The mode-cleaner would transmit only the fundamental one.

For simplicity, the triangular cavity can be seen as a two mirror cavity with the same input and output mirrors as the triangular one but a distance L apart, as shown in fig.(6.2). In this case, from eq.(3.23), we can write the transmitted power $P_{m\,n}$ for a $\mathrm{TEM}_{m\,n}$ as

$$P_{m\,n} \;=\; \frac{P_{00}}{1 \,+\, (\,2\,\mathcal{F}\,/\,\pi\,)^{\,2}\,\sin^{2}(\,2\,\pi\,\Delta\nu_{m\,n}\,L\,/\,c\,)} \tag{6.1}$$

where P_{00} is the power transmitted for a resonant TEM_{00} mode and $\Delta\nu_{m\,n}$ is the frequency spacing between the TEM_{00} and the $\mathrm{TEM}_{m\,n}$ modes [refer to eq.(3.16)]:

$$\frac{\Delta\nu_{m\,n}}{\nu_0} \;=\; \frac{1}{\pi}\,(\,m \,+\, n\,)\;\arccos\sqrt{(\,1 \,-\, \frac{L}{R}\,)} \tag{6.2}$$

where $\nu_0 \,=\, c\,/\,2\,L$ is the inverse of the light round trip travel time.

In order for the optical system to *mode-clean* the input beam while transmitting all the incoming TEM_{00} power, it must

- maximize the factor

$$\left(\,\frac{2\,\mathcal{F}}{\pi}\,\right)^{\,2}\,\sin^{\,2}\left[\,2\,\pi\left(\,\frac{L}{c}\,\right)\Delta\nu_{m\,n}\,\right] \tag{6.3}$$

  present in eq.(6.1) by choosing

  - a large value for the finesse $\mathcal{F}$;
  - a *non-degenerate* optical configuration such that the resonance frequency of the higher order modes be different from the fundamental one (and possibly anti-resonant);

- transmit all the incoming TEM_{00} power by setting equal transmittivity for the input and output mirrors;

The triangular geometry is introduced so that the reflected beam is not injected back to the laser source.

The second source of noise comes from the laser beam jitter or beam positioning fluctuations. In sec.(3.3.2) it was shown how a TEM_{00} is seen, in the optical axis of a misaligned cavity, as a linear combination of higher order modes. In the same way, any input jittering beam is seen by the cavity as composed of a linear combination of transverse modes. It has been shown[47, 48] that for an aligned interferometer, any beam fluctuations introduce second order terms at the output

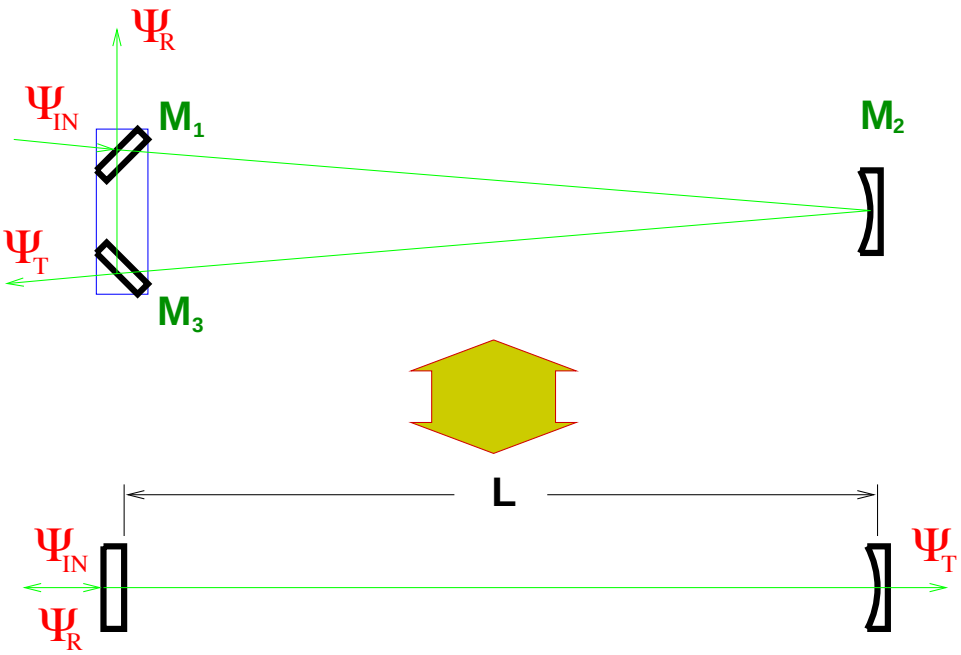

Figure 6.2: The mode-cleaner seen as a Fabry-Perot cavity.

port of the interferometer. However, any misalignment of the interferometer couples directly with the beam jitter, as can be seen in the expression for the phase noise at the output port:

$$\delta\tilde{\phi} \simeq 2\left(\frac{1 - r_0 A_R^{00}}{1 + r_0 A_R^{01}}\right)\left[\frac{\tilde{\theta}}{\theta_\infty}\left(\frac{a_1 - a_2}{w_0}\right) + \frac{\tilde{a}}{w_0}\left(\frac{\theta_1 - \theta_2}{\theta_\infty}\right)\right] \tag{6.4}$$

where

- r_0 is the reflectivity of the recycling mirror M_0;
- A_R^{00} and A_R^{01} are the amplitude reflectivities of the Fabry-Perot cavities for the TEM_{00} and TEM_{01} modes respectively;
- $\tilde{\theta}$ and $\tilde{a}$ are the angular and lateral fluctuations of the incoming beam;
- a_i and θ_i are the lateral and angular translations of the optical axis of the i-th Fabry-Perot;
- w_0 and θ_∞ are the beam waist and angular divergence.

Beam jittering and interferometer misalignments have a different frequency dependence: the former is caused by the mechanical vibrations of the laser source, with spectral components within the detection bandwidth of the interferometer. The latter, instead, is dominated by the frequency spectrum of the suspension system, concentrated in the low-frequency region. The misalignments, compared to the jitter, can be considered as a static contribution causing, by referring back to eq.(6.4), the jitter to contribute to the noise at first order.

The mode-cleaner is then required not only to spatially filter the laser field, but also to provide a stabilized beam positioning at the input of the interferometer. The mode-cleaner transmitted beam will have the same stability as the mode-cleaner optical axis. The mode-cleaner mirrors must be suspended so that the mode-cleaner optical axis displacements have only low frequency components.

6.1.2 Frequency and Power Fluctuation Filtering

As shown in eq.(2.66), the Fabry-Perot cavity behaves as a low-pass filter of the form

$$H(f) \sim \frac{1}{\sqrt{1 + (f / f_{cav})^2}} \tag{6.5}$$

for both frequency and power fluctuations with a pole $f_{cav} = c/(4\mathcal{F}L)$. By increasing the product $L\mathcal{F}$, it is possible to shift the pole of the cavity to lower frequencies and thus increase the attenuation factor.

6.2 The VIRGO Mode-Cleaner

The VIRGO mode-cleaner (MC144) is a triangular Fabry-Perot cavity 144 m long that can be schematically represented by fig.(6.1). It consists of three mirrors: the two plane mirrors, input and output, located on the input bench and a third concave mirror ($R = 181\,m$) located in the mode-cleaner tower. The input bench and the concave mirror are both suspended by special superattenuators. The input and output mirrors have a power reflectivity of $r^2 = 0.997$ (with the end-mirror power reflectivity $r^2 \sim 1$) corresponding to a cavity finesse of $\mathcal{F} = 1000$.

The optical system must satisfy the specifications on

- laser jitter:
  the specifications on the jitter of the beam at the interferometer input (θ_{beam}) are strictly connected to the gain of the automatic alignment of VIRGO. This can be seen as follows. The phase noise induced by the coupling misalignment/jitter [eq.(6.4)] must be less than the shot-noise level of [see eq.(4.1)]

  $$\tilde{\phi}_{shot} \sim 10^{-11} \qquad [rad/\sqrt{Hz}] \tag{6.6}$$

  or in other words

  $$\tilde{\theta}_{beam}(a_1 - a_2) < 3 \times 10^{-16} \qquad [m\,rad/\sqrt{Hz}] \tag{6.7}$$

  where only the dominant term in eq.(6.4) has been kept. Assuming a laser jitter of $\tilde{\theta}_{beam} \simeq 10^{-8}\ rad/\sqrt{Hz}$[31] which after mode-cleaning is reduced to $\theta_{beam} \simeq 10^{-11}\ rad/\sqrt{Hz}$, the requirement on the alignment becomes

  $$(a_1 - a_2) < 3 \times 10^{-5}\,m \tag{6.8}$$

  From eq.(3.27), $a = R\,\theta$, so the control on the angle must be better than 10^{-8} rad.

- sidebands:
  not only must the optical system be able to filter the beam but it must allow the sidebands to be transmitted as well. Therefore, the modulation frequency must be a multiple of the free spectral range, i.e. $c/2L$.

- cavity pole:
  as already stated, a large value of L and $\mathcal{F}$ would shift the cavity pole to lower frequencies, thus improving the attenuation factor for frequency and power fluctuations. For L = 144 m and $\mathcal{F} = 1000$, the cavity pole is $c/4\mathcal{F}L \simeq 500$ Hz, corresponding to an attenuation factor of ~ 20 at 10 kHz.

6.3 The Mode-Cleaner Prototype

The properties and requirements for mode-cleaning the laser beam have been presented in the previous sections. This section will briefly describe the Orsay mode-cleaner prototype (MC30),

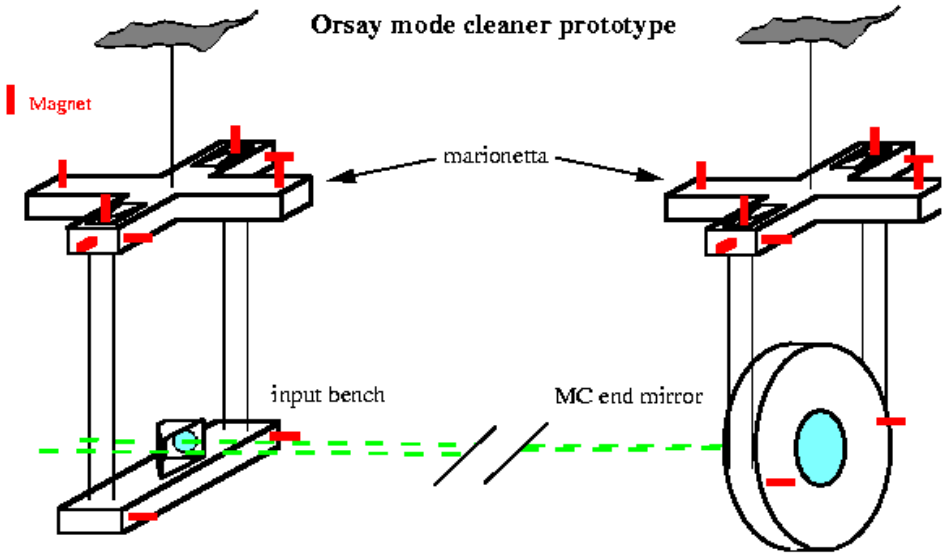

Figure 6.3: Sketch of the mode-cleaner prototype MC30.

sketched in fig.(6.3). In particular, its optical configuration will be given as well as an outline of the local controls and alignment necessary for the longitudinal lock of the cavity with respect to the laser frequency.

The optical configuration of the prototype has been chosen as close as possible to the VIRGO mode-cleaner. It consists of a triangular ring cavity of 30 m in length. Tab.(6.1) allows a comparison between the principal characteristics of the two mode-cleaners. The laser source is a Nd:YAG providing 300 mW in the fundamental mode. A rigid ULE cavity of 30 cm is used as a reference for the frequency prestabilization of the laser.

The MC30 consists of two masses placed in two vacuum chambers connected by a tube 30 cm in diameter. Mass 1 is the mass holding an optical bench where the two plane mirrors are placed. Mass 2 contains the concave mirror held by a cylindrical holder (see fig.(6.3)).

Both masses are suspended by a double pendulum system. The first stage is referred to as the *marionetta* stage and is similar to the marionetta found in the VIRGO superattenuator. The local control, necessary for the local damping of the mirror motion, uses a magnet-coil system where the magnets are on the marionetta and the coils are rigidly connected to the ground. The masses are controlled in all six degrees of freedom: the three translations and the three rotations around the axes.

The two-stage suspension system is seen as two coupled oscillators in the horizontal direction. In the vertical direction, only one attenuation stage is provided by the metal blades placed on the marionetta.

By rotating the polarization state of the incoming light beam, from the p state, where the electric field is parallel to the plane of the incident and reflected beams, to the s state, where the electric field is perpendicular to it, the finesse of the cavity can be changed. A finesse of 1600 was found for the s-state whereas a finesse of 120 was found for the p-state. This allowed a study of the MC30 acquisition of lock phase for different finesse values.

6.3.1 Local Controls

The two-stage suspension system provides an attenuation of seismic noise above the pendulum frequencies that are at 0.5 Hz and 1 Hz along the beam axis and at 2 Hz along the suspension axis. The mirror dynamics in free motion is dominated by these resonances, resulting in motion amplitudes as high as hundreds of a light wavelength. For this reason, before stabilizing the cavity

	MC30	MC144
Length L (m)	30	144
Finesse $\mathcal{F}$ (s)	$\sim$ 1600	1000
Finesse $\mathcal{F}$ (p)	$\sim$ 100	
Suspensions	2 stages	3 stages and inverted pendulum
Geometry	triangular	triangular
Mass 1	2 plane mirrors	2 plane mirrors
Mass 2	concave mirror R = 112 m	concave mirror R = 181 m
Laser	Nd:YAG 300 mW	Nd:YAG 10 W
Prestabilization	ULE non-suspended	ULE suspended

Table 6.1: The prototype MC30 configuration is shown with respect to the VIRGO MC144.

length to the laser frequency, it is necessary to damp the resonance contributions *locally*, that is relative to the ground, in all six degrees of freedom.

The local controls used for the MC30 function as follows:

1. the mirror position in the six degrees of freedom is measured[52] by observing, with the aid of a CCD camera,
   - reference marks placed on the mass;
   - the reflected beams injected by two auxiliary lasers;
2. the digitized signals from the camera are processed to find the mirror displacements and to compute the corrections to be applied;
3. once the corrections are computed, an appropriate current is sent to the coils.

The residual motion per mirror after local control is 0.5μm RMS for the three axes, 1μrad RMS around the vertical and transversal axes and 20μrad RMS around the beam axis.

6.4 Cavity Control Elements and Models

The main objective of this chapter is the study of the acquisition of lock process for the MC30 prototype, once the local controls are on, in both s and p polarization states. This process is achieved modeling the control system for the cavity stabilization with respect to the laser frequency. A basic description of the electrical, mechanical and optical elements involved is here given as well as the system's block diagram.

A numerical calculation, performed with the SIESTA engine, made it possible to model the overall system. The simulation results of each block element, as well as of the overall system in open and closed-loop, were compared to experimental results [24].

6.4.1 The Control System

The goal of the feedback system is to stabilize the MC30 to the incoming laser frequency ν_{las}: the cavity must follow, within the specifications, the evolution of ν_{las}. The block diagram for the system in question, shown in fig.(6.4), is made of the following signals and transfer functions:

- a *reference* signal $r(s)$, namely the laser frequency ν_{las};
- a photodiode, described by the transfer function $H(s)$, whose objective is to provide an error signal $\epsilon(s)$, generated by phase modulating the incoming beam at 6.25 MHz and observing the demodulated signal reflected off the cavity (the Pound-Drever technique);
- an electronic (analog) filter or *compensator*, whose transfer function is denoted by $G(s)$, to appropriately filter and amplify the error signal $\epsilon(s)$;
- the coil amplifier's transfer function $A(s)$ providing a force generated by coils placed on the ground and applied directly onto the mirror;
- the mechanical transfer function $M(s)$ which relates an incoming force with the mirror movement;
- the suspension transfer function $P(s)$ describing the filtering of seismic noise;
- the cavity transfer function $C(s)$ characterizing the optical response of the prototype.

In order to conceive the feedback control, it is necessary to know the transfer functions of each element here listed. Measurement and simulation are compared.

Seismic noise, the mechanical $M(s)$ and pendulum $P(s)$ transfer functions

By Laplace transforming the differential equations of the double pendulum system pictorially shown in fig.(6.5), it is possible to derive the transfer functions

- $M(s)$ for the mirror control, defined as the ratio between the mass displacement x(s) and the force F(s):

$$M(s) \equiv \frac{x(s)}{F(s)} \tag{6.9}$$

- $P(s)$ for the filtering of seismic noise, defined as the ratio between the suspension point movement $x_0(s)$ and the mass displacement $x(s)$:

$$P(s) \equiv \frac{x(s)}{x_0(s)} \tag{6.10}$$

The pendulum transfer function $P(s)$ consists of two double-poles corresponding to the two resonances and it can be written in the form:

$$P(s) = \frac{{\omega_1}^2}{\left(s^2 + \frac{\omega_1}{Q_1}s + {\omega_1}^2\right)} \frac{{\omega_2}^2}{\left(s^2 + \frac{\omega_2}{Q_2}s + {\omega_2}^2\right)} \quad [m/m] \tag{6.11}$$

where

$$\begin{aligned} \omega_1 &= 2\,\pi \cdot 0.5234\,\mathrm{Hz} \qquad Q_1 = 2 \\ \omega_2 &= 2\,\pi \cdot 1.1349\,\mathrm{Hz} \qquad Q_2 = 3 \end{aligned} \tag{6.12}$$

The quality factors of the resonances are really the effective quality factors: they depend upon the attenuation factor of the local controls.

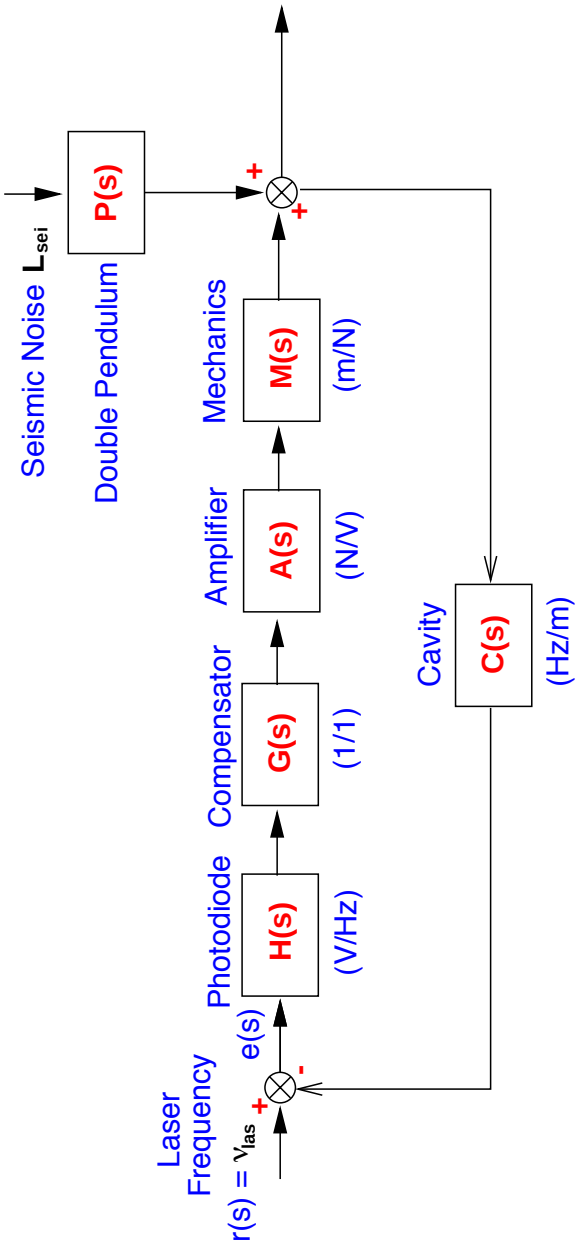

Figure 6.4: The mode-cleaner MC30 block diagram.

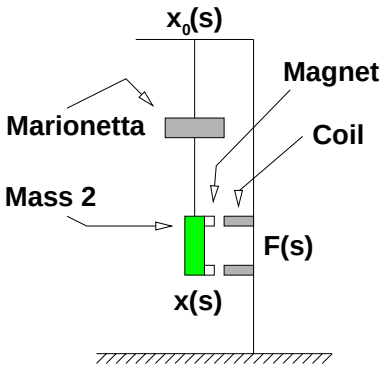

Figure 6.5: The MC30 mirror suspension system and the magnet-coil system for the longitudinal control of the cavity.

An experimental measurement of the cavity length noise was obtained by locking the laser frequency onto the mode-cleaner. In order to change the laser frequency, there is an actuator with a dynamic range corresponding to a length change of about 25 μm and a large bandwidth (MHz). The length variations, induced by seismic noise, are of the order of $1\mu m$ RMS in a low frequency range, where the correction signal sent to the laser is proportional to the length. In fig.(6.6), the amplitude spectral density of the cavity length, measurement and numerical simulation, is shown. The model simulated two identical suspensions for the mass 1 and 2, both described by eq.(6.11) and using, for the amplitude spectral density of ground motion, the model

$$\tilde{x}_0 \;=\; 3 \times 10^{-7} [m/\sqrt{Hz}] \tag{6.13}$$

Here, the discrepancies between the measurement and the model are due to the uncertainties in the local control gain and to the presence of other resonances (3 Hz, 5 Hz) arising from the angular motion that couples to the cavity length motion. Fig.(6.7) shows the running RMS of fig.(6.6) whose values ΔL for the cavity displacement at 0.01 Hz are

$$\begin{aligned} \Delta L_{exp} &= 0.3\,\mu m \\ \Delta L_{the} &= 0.7\,\mu m \end{aligned} \tag{6.14}$$

The mechanical transfer function $M(s)$ is the transfer function whose input is the computed force for the correction and whose output is the displacement of mass 2. It consists of two double-poles and one double-zero:

$$M(s) \;=\; P(s) \cdot \frac{\left(s^2 \;+\; \dfrac{\omega_3}{Q_3}\, s \;+\; \omega_3^{\,2} \right)}{\omega_3^{\,2}} \qquad [m/N] \tag{6.15}$$

where

$$\omega_3 \;=\; 2\,\pi \cdot 1.0986\,\mathrm{Hz} \qquad\qquad Q_3 \;=\; 111 \tag{6.16}$$

The presence of the double-zero causes a driving force at ω_3 to weakly excite the mirror motion. In the case of the VIRGO reference mass, for example, this is not the case: the transfer function relating the driving force from the reference mass to the mirror position is that of a simple pendulum.

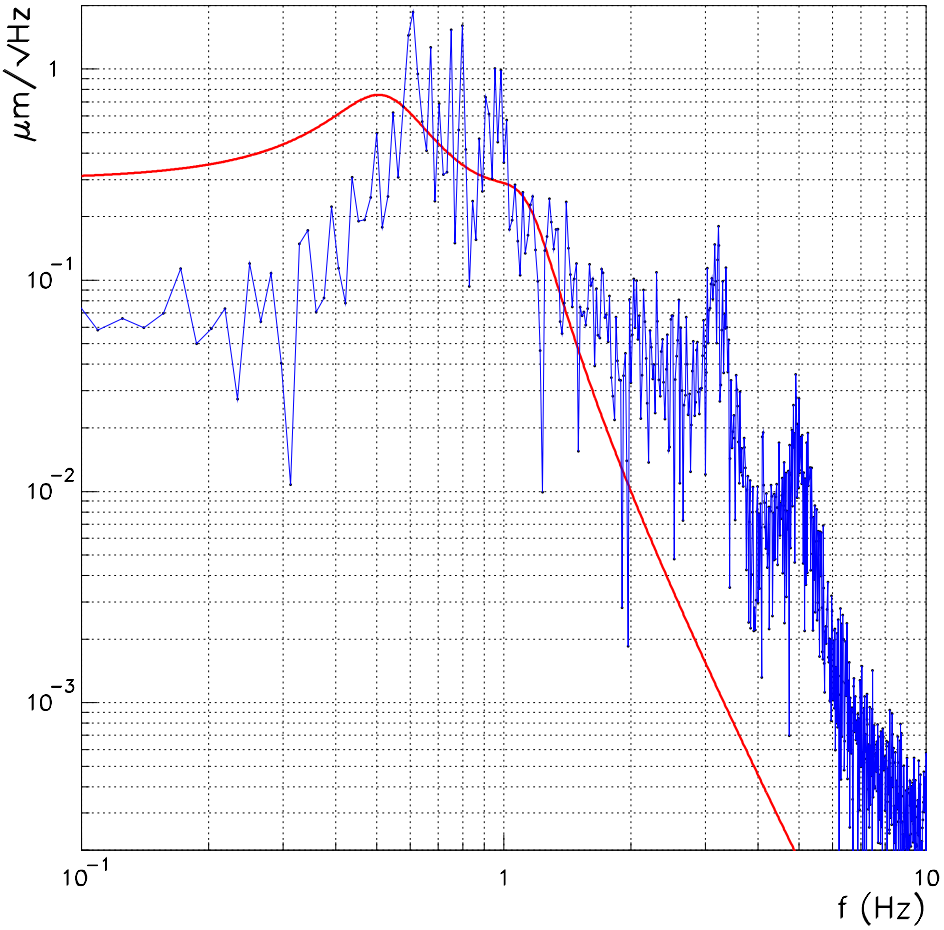

Figure 6.6: The MC30 amplitude spectral density of the length fluctuations. Continuous line: simulation. Continuous line with dots: measurement.

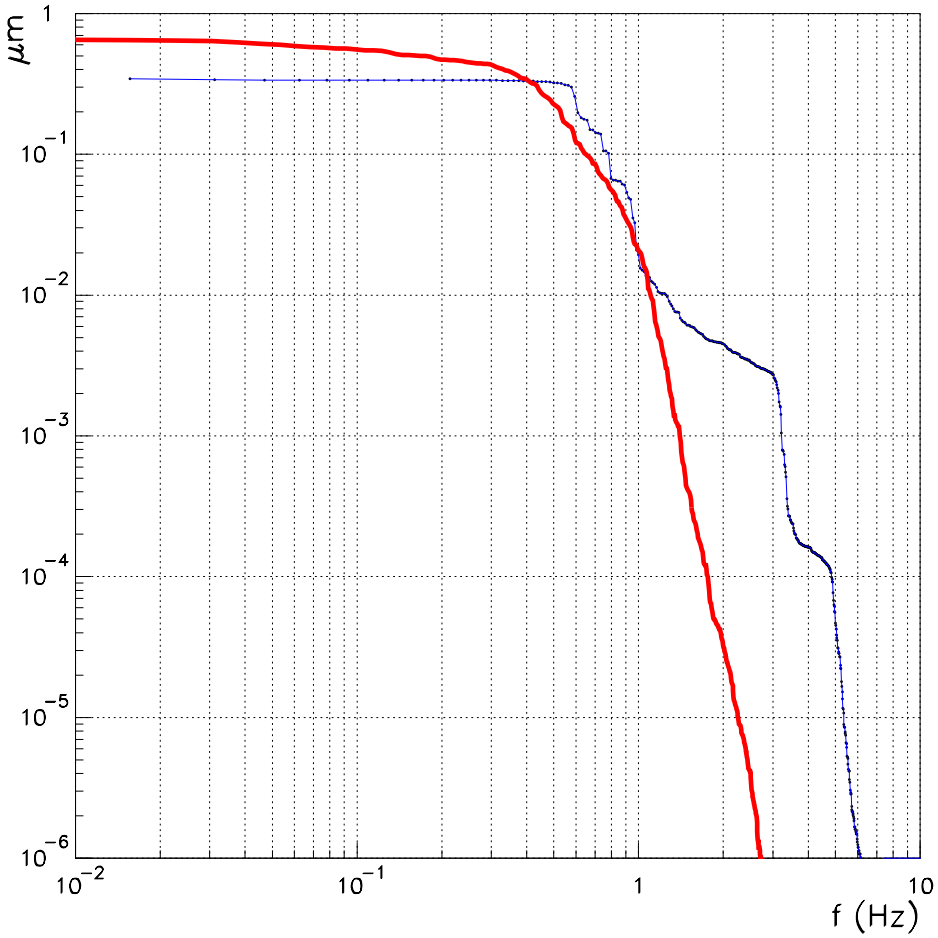

Figure 6.7: The MC30 running RMS of the mirror displacement amplitude spectral density. Continuous line: simulation. Continuous line with dots: measurement.

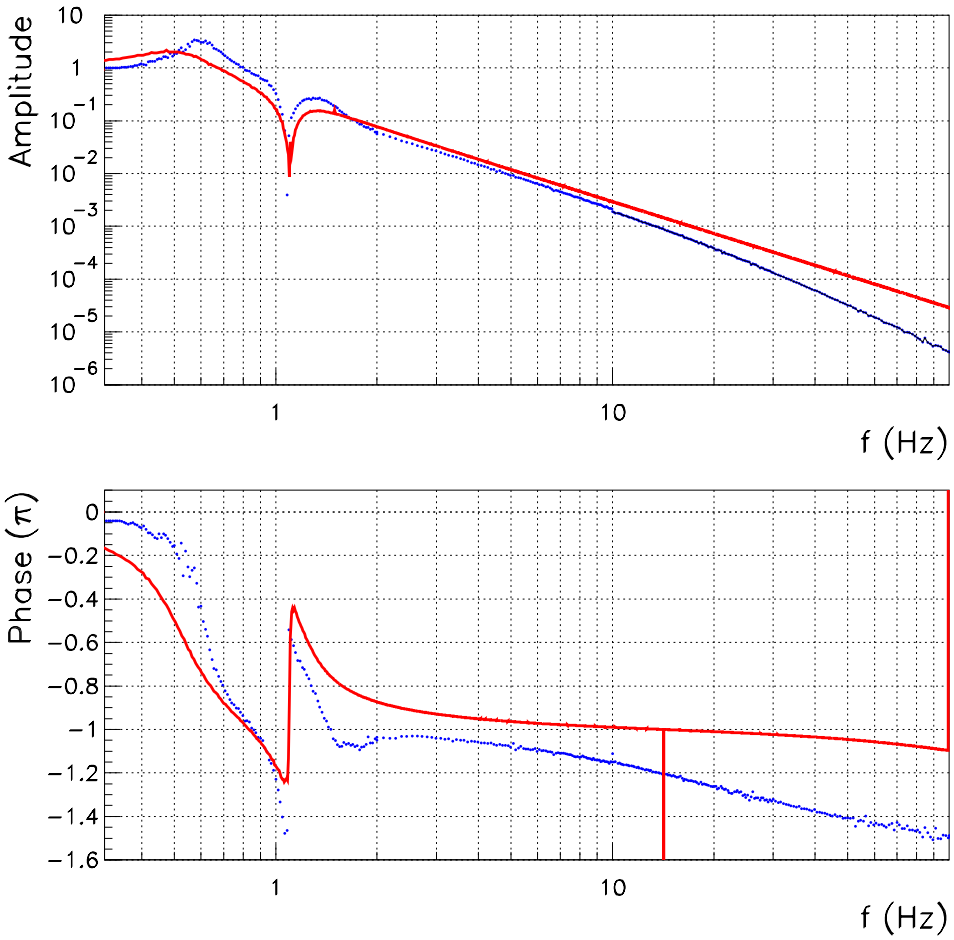

Figure 6.8: The MC30 measured and simulated mechanical transfer function $M(s)$. Continuous line: simulation. Points: measurement

The cavity transfer function $C(s)$

The cavity response is represented by the transfer function $C(s)$. It basically relates the cavity length $L(s)$ with its frequency equivalent $\nu(s)$:

$$C(s) = \frac{\nu(s)}{L(s)} = \frac{\left(\frac{c}{2\,L}\right)}{\left(\frac{\lambda}{2}\right)} \frac{\omega_{cav}}{(s + \omega_{cav})} \qquad [Hz/m] \tag{6.17}$$

where $\omega_{cav}/2\pi$ is the cavity pole with values

$$\frac{\omega_{cav}}{2\,\pi} = \frac{c}{4\,\mathcal{F}\,L} = \begin{cases} 25 \text{ kHz} & \text{for } \mathcal{F} = 100 \\ \\ 1.6 \text{ kHz} & \text{for } \mathcal{F} = 1600 \end{cases} \tag{6.18}$$

For the control, we are interested in the low frequency region, with a bandwidth of 100 Hz. For

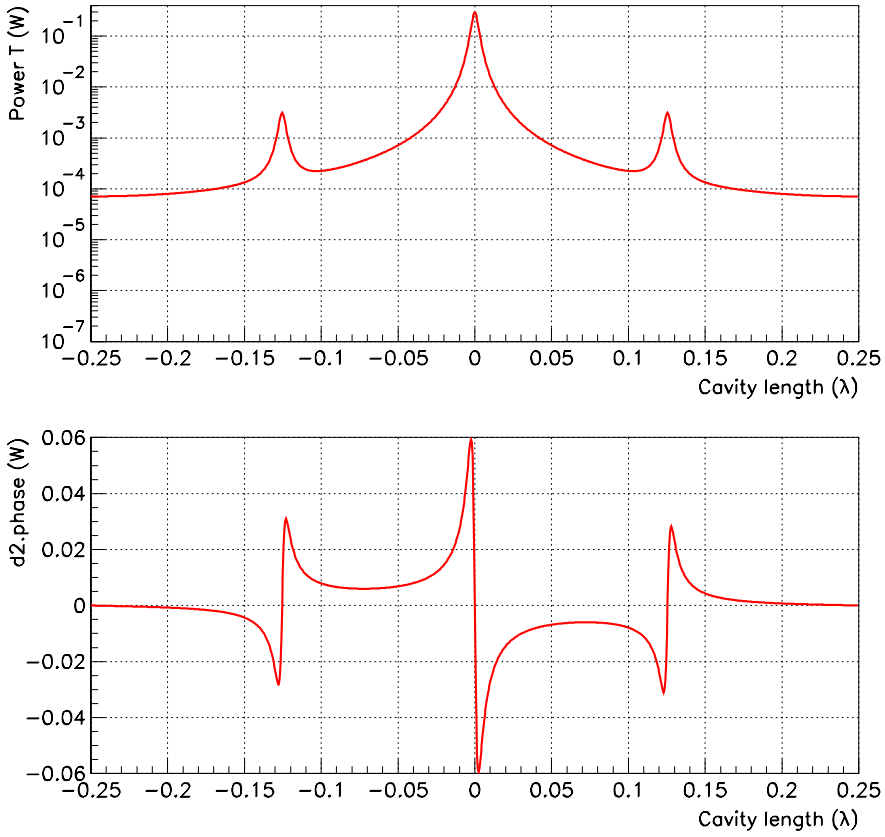

Figure 6.9: The calculated MC30 transmitted power and error signal. Top graph: transmitted power as a function of cavity length. Bottom graph: the Pound-Drever error signal as a function of cavity length.

this reason, the cavity transfer function can be seen as just a multiplicative factor, independent of frequency, mapping length into frequency.

The Pound-Drever error signal for the mode-cleaner in the p state has been simulated by the SIESTA engine and shown in fig.(6.9). The chosen optical module made use of the plane wave and static approximation. The parameters used were

$$\begin{aligned} r_1^2 &= r_2^2 = 0.97 \\ P_{in} &= 300\ mW \\ J_1 &= 0.1 \end{aligned} \tag{6.19}$$

where $r_{1,2}$ is the amplitude reflectivity of the mirrors, P_{in} is the incident power of the laser and J_1^2 is the percentage of power in each sideband.

The coil driver $A(s)$

The control of the cavity is achieved by controlling the mirror mass 2 position with the aid of a set of coils and magnets. In particular, the coils are driven from the ground while the magnets, applied directly to the mass, allow its direct control (unlike the local controls that pilot the mass through the marionetta).

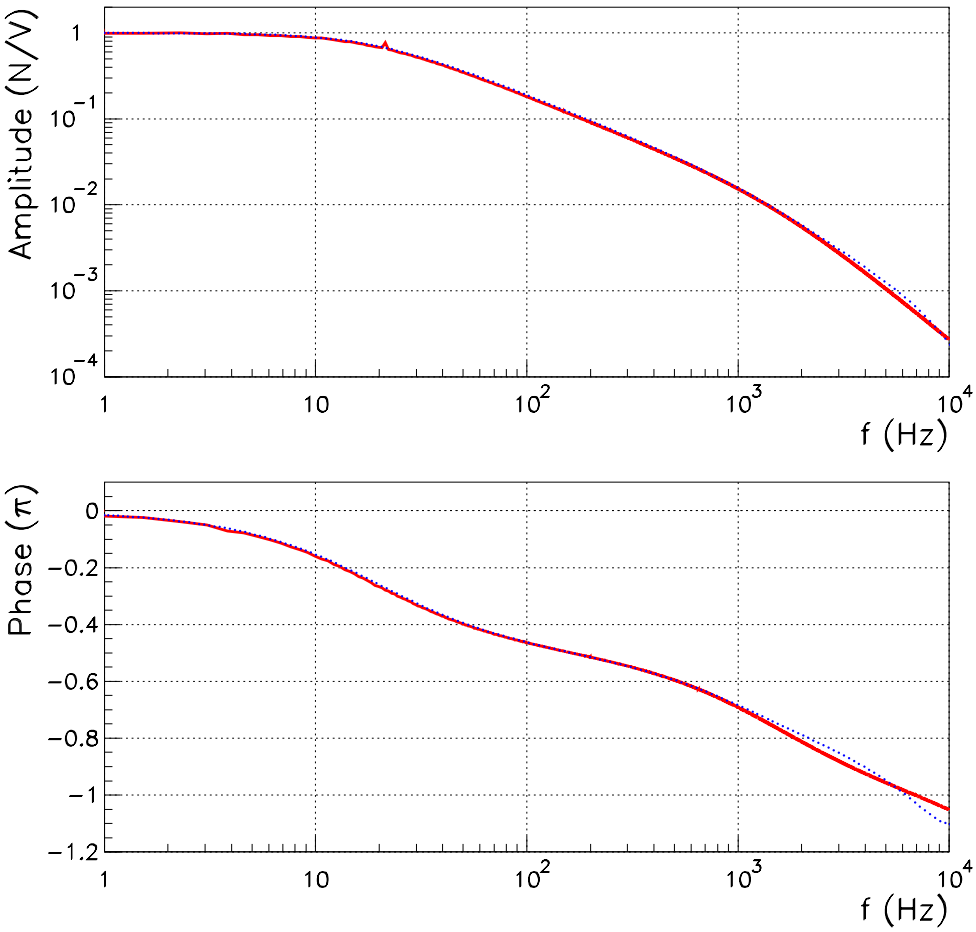

Figure 6.10: The MC30 measured and simulated coil driver transfer function relating the incoming compensator signal (V) to an outgoing force (N) applied to the mass. Continuous line: simulation. Points: measurement.

The transfer function relating the input voltage of the amplifier to the force delivered by the coils is of the form

$$A(s) = \frac{\omega_1}{(s+\omega_1)} \frac{\omega_2}{(s+\omega_2)} \qquad [N/m] \tag{6.20}$$

where

$$\begin{aligned} \omega_1 &= 2\pi \cdot 18.5\,\mathrm{Hz} \\ \omega_2 &= 2\pi \cdot 1.5\,\mathrm{kHz} \end{aligned} \tag{6.21}$$

and an overall gain has been neglected. This function relates an incoming signal, expressed in V and generated by the compensator $G(s)$, to an outgoing force, in N. Fig.(6.10) shows both measurement and simulation of the amplitude and phase of $A(s)$. The agreement between the two is satisfactory.

The photodiode $H(s)$ and compensator $G(s)$ transfer function

For simplicity, the transfer function $H(s)$ describing the photodiode response consists of just a multiplicative factor, transforming the signal from Hz to V. The role of the compensator $G(s)$ is of key importance. It is designed to fulfill

- the specifications of the control;
- the stability criteria.

In the locked regime, we require the residual cavity length fluctuations ΔL to be much smaller than the HWHM of the resonance:

$$\Delta L << \text{HWHM} = \frac{\lambda}{4\,\mathcal{F}} \sim \begin{cases} 10^{-9}\ \text{m} & \text{for } \mathcal{F} = 100 \\ \\ 10^{-10}\ \text{m} & \text{for } \mathcal{F} = 1600 \end{cases} \tag{6.22}$$

This means that a double-zero would compensate the $1/s^3$ behavior, after 18.5 Hz, of $A(s)\,M(s)$.

Assuming a RMS displacement per mass of 0.5μm (with local controls) concentrated below 1 Hz, the required loop gain G must be

$$G >> \sqrt{2} \times 0.5\mu\text{m} \begin{cases} /10^{-9}\ \text{m} \sim 700 & \text{for } \mathcal{F} = 100 \\ \\ /10^{-10}\ \text{m} \sim 7000 & \text{for } \mathcal{F} = 1600 \end{cases} \tag{6.23}$$

where the motion of the masses has been assumed uncorrelated.

The design of the compensator used for the p polarization state of MC30 is[24]

$$G(s) = K \frac{\omega_1^{\,2}}{\left(s^2 + \dfrac{\omega_1}{Q_1}\,s + \omega_1^{\,2}\right)} \frac{\omega_2^{\,2}}{\left(s + \omega_2\right)} \frac{\left(s^2 + \dfrac{\omega_3}{Q_3}\,s + \omega_3^{\,2}\right)}{\omega_3^{\,2}} \qquad [1/1] \tag{6.24}$$

where

$$\begin{aligned} K &= 1.5 \times 10^4 \\ \omega_1 &= 2\,\pi \cdot 700\,\text{Hz} \qquad Q_1 = 0.5 \\ \omega_2 &= 2\,\pi \cdot 26.5\,\text{kHz} \\ \omega_3 &= 2\,\pi \cdot 30\,\text{Hz} \qquad Q_3 = 0.5 \end{aligned} \tag{6.25}$$

Furthermore, in order to maintain a relatively large phase and amplitude margin, the 1/s behavior is kept from about 30 Hz to 300 Hz, with the UGF placed at 100 Hz. Fig.(6.11) shows the corrector used for the control of MC30 once in p state. A notch (double-zero) was introduced at 3.4 kHz in order to compensate for a mechanical resonance. For the simulation study, both the notch and the resonance were neglected.

6.5 Performance of Control

Fig.(6.4) can be put in simpler form by defining the following products of functions

$$\begin{aligned} G'(s) &\equiv H(s) \cdot G(s) \cdot A(s) \cdot M(s) \\ H'(s) &\equiv C(s) \end{aligned} \tag{6.26}$$

The resulting block diagram is shown in fig.(6.12). It is possible to express the cavity length $L(s)$

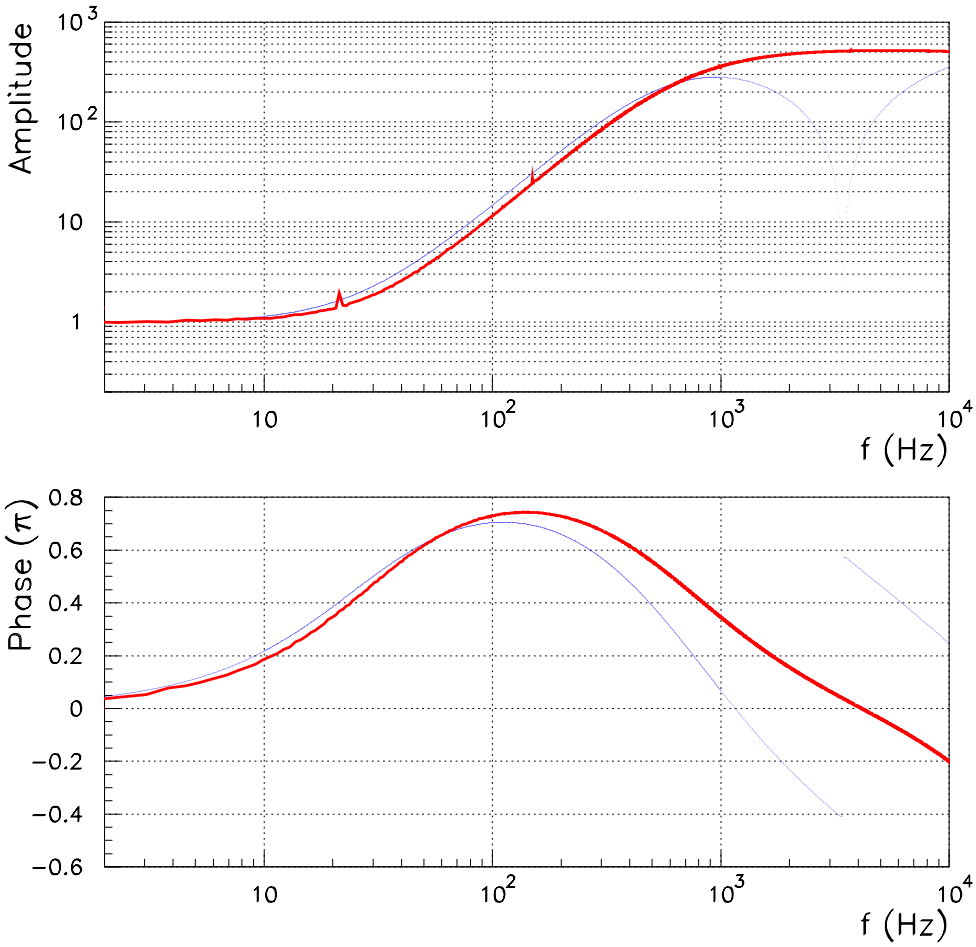

Figure 6.11: The corrector $G(s)$ used for the control, in the p state, of MC30[24]. Continuous line: simulation. Points: measurement. Notice the presence of a notch (double-zero) at 3.4 kHz in the measurement, necessary to compensate a mechanical resonance found at that frequency. For the simulation study, the notch and the mechanical resonance were neglected.

as a function of the reference signal $r(s) = \nu(s)$, where $\nu(s)$ is the laser frequency, and the cavity length fluctuations $P(s) \cdot n(s)$ due to seismic noise:

$$L(s) \;=\; \left[\frac{G'(s)}{1 \,+\, G'(s)\,H'(s)}\right] \nu(s) \;+\; \left[\frac{1}{1 \,+\, G'(s)\,H'(s)}\right] P(s)\, n(s) \tag{6.27}$$

where

$$G'(s)\,H'(s) \tag{6.28}$$

is the open-loop transfer function, defined in eq.(A.1), and

$$\frac{G'(s)}{1 \,+\, G'(s)\,H'(s)} \tag{6.29}$$

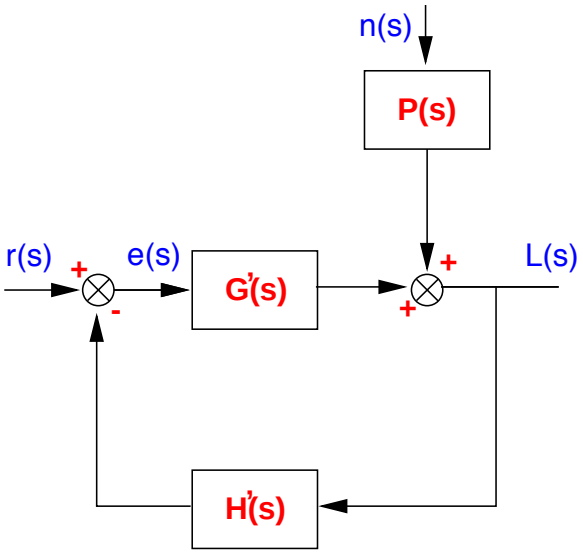

Figure 6.12: The block diagram for the longitudinal control of MC30.

is the closed-loop transfer function, defined in eq.(A.2). For frequencies such that the open-loop transfer function has an elevated gain, i.e.

$$| G'(s)\, H'(s) |>> 1 \tag{6.30}$$

the cavity length $L(s)$ can be written as

$$L(s) \simeq \frac{1}{H'(s)}\nu(s) + \frac{P(s)}{G'(s)\, H'(s)}\, n(s) \tag{6.31}$$

In our case, $H'(s)$ is the cavity transfer function, which we assumed to be a constant. On the other hand, the noise contribution is attenuated by the factor $1/G'(s)H'(s)$ by virtue of eq.(6.31). As a result, in closed-loop, the seismic noise is attenuated and the cavity fluctuations follow the laser frequency. Throughout this chapter, no frequency fluctuations have been assumed.

6.5.1 The Open-Loop Transfer Function

Fig.(6.13) shows the Bode plot[1] of the open-loop transfer function $G'(s)\, H'(s)$. Most of the properties of the feedback control can be understood from these plots. The gain at DC is 1.5×10^4 and the unit gain frequency is 100 Hz. Notice the 1/f behavior from about 30 Hz up to 300 Hz. The amplitude and phase margin of 4.5 and 40° respectively a reasonable stability and robustness. Notice the notch at 1.1 Hz originating from the transfer function $M(s)$. The gain must be high enough so that the notch does not go below the unity gain, otherwise the system will be unstable.

6.5.2 The Closed-Loop Transfer Function

The closed-loop transfer function $G'(s)/(1 + G'(s)\, H'(s))$ is shown in fig.(6.14). The cavity length $L(s)$ follows the laser frequency $\nu(s)$ up to 100 Hz, where an overshoot appears.

The transfer function $1/(1 + G'(s)\, H'(s))$, instead, gives the attenuation factor of the mirror displacement due to seismic noise $(P(s) \cdot n(s))$ and is plotted in fig.(6.15).

[1] Bode plots consist of amplitude and phase plots of the transfer function.

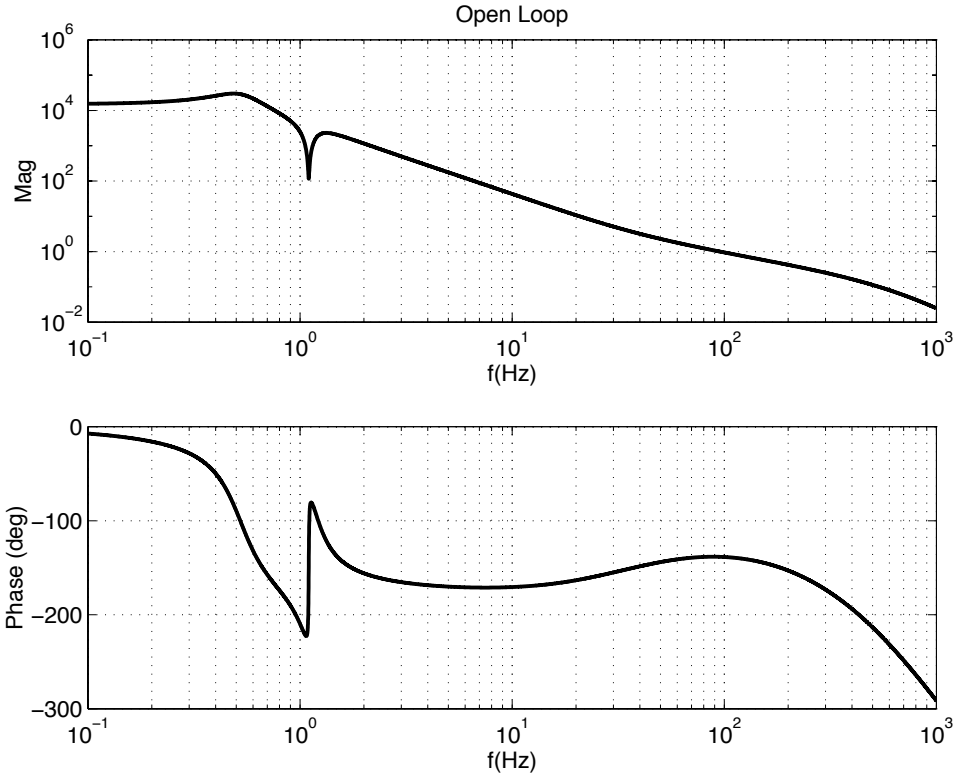

Figure 6.13: The open-loop transfer function $G'(s)\,H'(s)$ for the MC30. Upper graph: the amplitude $\mid G'(s)\,H'(s)\mid$. Lower graph: the phase $\arg[G'(s)\,H'(s)]$. The amplitude and phase margins are 4.5 and 40° respectively.

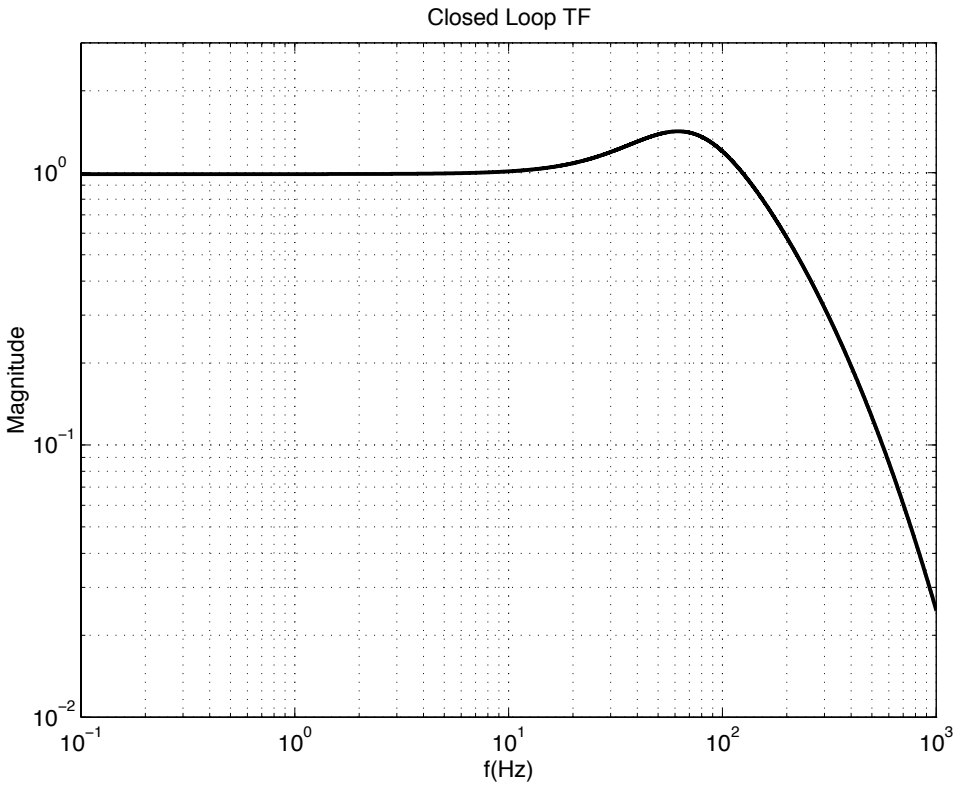

Figure 6.14: The closed-loop transfer function $G'(s)/(1 + G'(s)\,H'(s))$ for the MC30.

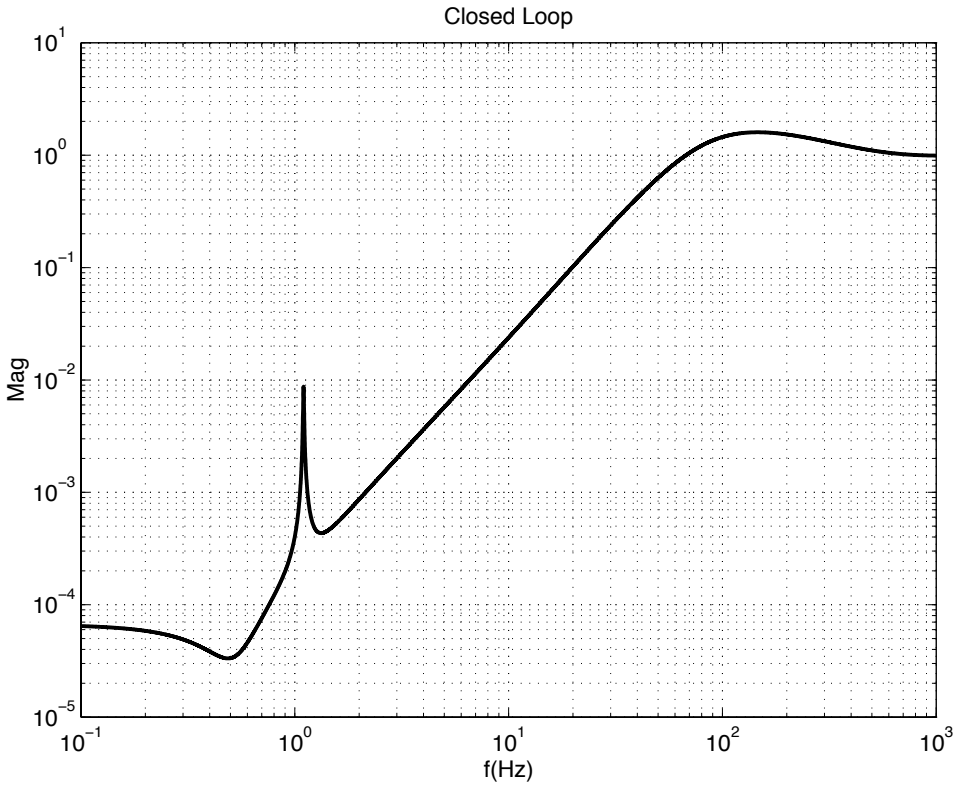

Figure 6.15: The seismic noise attenuation factor $1/(1 + G'(s)\,H'(s))$ for the MC30.

6.6 The Acquisition of Lock Problem

So far, the overall description of the mode-cleaner prototype was given, as well as the performance of the control system in closed-loop. The only noise that was taken into account was the seismic excitation of the masses.

This section presents the acquisition of lock problem. In particular, we would like to understand what parameters play a role in the lock acquisition time. The simulation results are then compared to the experimental.

The problem is two-fold. To begin with, it is necessary to understand how fast the control system is. In other words, assuming an incoming linear error signal, how long will the control system take in order to control the cavity length?

Secondly, the error signal, and precisely the Pound-Drever signal, is linear only close to the fundamental resonance. Outside of the FWHM of the peak, the signal is non-linear, as can be seen in fig.(6.9). It is natural to ask how the control system would react to such a non-linear signal.

6.6.1 The Control System Time Response

In order to describe the time response of a control system, it is necessary to define a parameter that characterizes such a response. The *settling time*, defined as the time required for the response of the system to be within 5% of the final value, can be used as such a parameter.

One way to quantify the settling time of the system in question is to send, as a reference signal,

$z_1 = -1.9 \times 10^2$	$p_1 = -1.7 \times 10^5$
$z_2 = -3.1 \times 10^{-2} + 6.9\,i$	$p_2 = -8.8 \times 10^3$
	$p_3 = -6.8 \times 10^3$
	$p_4 = -1.8 \times 10^3$
	$p_5 = -3.5 \times 10^2 + 3.0 \times 10^2\,i$
	$p_6 = -1.5 \times 10^2$
	$p_7 = -3.1 \times 10^{-2} + 6.9\,i$

Table 6.2: The poles and zeros (in rad/s) for the closed-loop transfer function $\mathcal{C}(s)$ in eq.(6.33).

the unit step function $u(t)$

$$r(t) \equiv u(t) = \begin{cases} 0 & \text{for } t < 0 \\ \\ 1 & \text{for } t \geq 0 \end{cases} \tag{6.32}$$

whose Laplace transform is $\mathcal{L}[u(t)] = 1/s$ and observe the reaction time of the feedback. Recalling the closed-loop transfer function, defined as

$$\mathcal{C}(s) \equiv \frac{L(s)}{\nu(s)} = \frac{G'(s)}{1 + G'(s)\,H'(s)} \tag{6.33}$$

then the unit step response of the system is just

$$L(s) = \frac{1}{s}\,\frac{G'(s)}{1 + G'(s)\,H'(s)} \tag{6.34}$$

By Laplace transforming eq.(6.34) to the time domain, the time response of the system is found.

For the control system in question, the problem is difficult to treat. The polynomial order of the closed-loop transfer function is $\mathcal{O}(s^4)/\mathcal{O}(s^9)$ and the analytical expression is complicated. Nonetheless, it is possible to simplify the problem.

Let's neglect the photodiode and cavity transfer functions because they are constant. The factored closed-loop transfer function then becomes

$$\begin{aligned} \mathcal{C}(s) &= \frac{G(s)\,A(s)\,M(s)}{1 + G(s)\,A(s)\,M(s)} \\ &= \frac{(s - z_1)^2\,(s - z_2)\,(s - z_2^*)}{(s - p_1)\,(s - p_2)\,(s - p_3)\,(s - p_4)\,(s - p_5)\,(s - p_5^*)\,(s - p_6)\,(s - p_7)\,(s - p_7^*)} \end{aligned} \tag{6.35}$$

where p_i and z_i denote the i-th pole and zero of the function and p_i^* and z_i^* their complex conjugates. The values of the poles and zeros are shown in tab.(6.2).

It is possible to approximate the closed-loop transfer function by referring to tab.(6.2). To begin with, remark that the pole p_7 is sufficiently close enough to the zero z_2. This double-pole and double-zero cancel out. In the same way, to first approximation, we can assume that the pole p_6 cancels out the zero z_1. By so doing, we say that these poles and zeros do not contribute to the system.

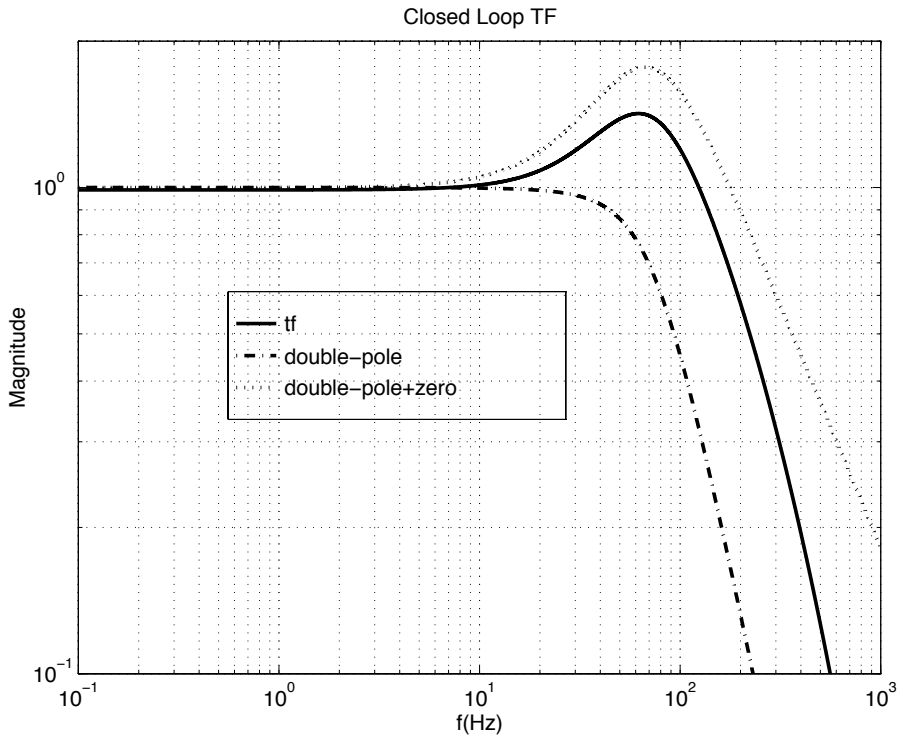

Figure 6.16: The amplitude of the MC30 closed-loop transfer function $\mid \mathcal{C}(s) \mid$ and its two approximations: (double-pole) denoting the transfer function with only the double-pole p_5 and (double-pole+zero) denoting the double-pole p_5 with the zero z_1.

Furthermore, the bandwidth of the system is about 100 Hz. It is, therefore, useless to consider the poles and zeros which are found above this frequency. This implies that the contribution of the poles p_1, p_2, p_3 and p_4 can be neglected as well. Thus, eq.(6.35) reduces to

$$\mathcal{C}(s) \simeq \frac{|\, p_5 \,|^2}{z_1} \frac{(s - z_1)}{(s - p_5)(s - p_5^*)} \tag{6.36}$$

To appreciate the approximation, a plot of the closed-loop transfer function amplitude $|\, \mathcal{C}(s) \,|$ is shown in fig.(6.16), with the approximation in eq.(6.36) and the amplitude of

$$\mathcal{C}(s) \simeq |\, p_5 \,|^2 \frac{1}{(s - p_5)(s - p_5^*)} \tag{6.37}$$

as well.

Moreover, the transfer function consisting of just the two poles can serve as an order of magnitude behavior of the system. A transfer function of this type is really describing a damped harmonic oscillator and can be re-written in the form

$$\begin{aligned} \mathcal{C}(s) &\simeq |\, p_5 \,|^2 \frac{1}{(s - p_5)(s - p_5^*)} \\ &= \frac{\omega^2}{s^2 + \dfrac{\omega}{Q} s + \omega^2} = \frac{\omega^2}{s^2 + 2\,\delta\,\omega\, s + \omega^2} \end{aligned} \tag{6.38}$$

where $\omega/2\,\pi = |p_5|/2\,\pi$ and $Q = 1/2\,\delta = -|p_5|/2\,\Re(p_5)$ is the resonance frequency and quality factor of such an oscillator. By reducing the closed-loop transfer function to such a simple system, many properties can be easily understood. To begin with, only two parameters play a role in the closed-loop transfer function: the resonance frequency $\omega/2\pi$ and the quality factor Q. Therefore, also the time response must depend on two parameters.

It can be shown that if the closed-loop transfer function is described by a harmonic oscillator transfer function, then the response of the system to a step excitation leads to

$$L(s) = \frac{1}{s} \frac{\omega^2}{s^2 + 2\,\delta\,\omega\, s + \omega^2} \tag{6.39}$$

The Laplace transform mapping back to the time domain gives as a result

$$\mathcal{L}^{-1}[L(s)] = L(t) = 1 - A \exp(-\delta\,\omega\, t) \sin(\tilde{\omega}\, t + \phi) \tag{6.40}$$

where

$$\begin{aligned} A &\equiv \frac{1}{\sqrt{1 - \delta^2}} \\ \tilde{\omega} &\equiv \sqrt{1 - \delta^2}\,\omega \\ \phi &\equiv \arccos\delta \end{aligned} \tag{6.41}$$

Fig.(6.17) shows the step response as a function of ωt and for different values of δ.

From eq.(6.40) and its plot in fig.(6.17) we see that there are two components to the step response: a sinusoidal term and an exponential term. The response has a marked oscillation for high values for the quality factor $1/2\,\delta$. For relatively low values of the quality factor, the exponential term dominates the response time of the control. In other words, recall that a relatively high quality factor corresponds to low dissipative forces in the oscillator model. Once the system is excited, relatively long damping times are expected. On the other hand, with low quality factors, the energy of the system is quickly dissipated. It is natural to think that for the closed-loop system, a low quality factor is desired. The goal is to follow the time evolution of the reference signal with as few oscillations as possible and as quickly as possible. Therefore, for stable systems, the model

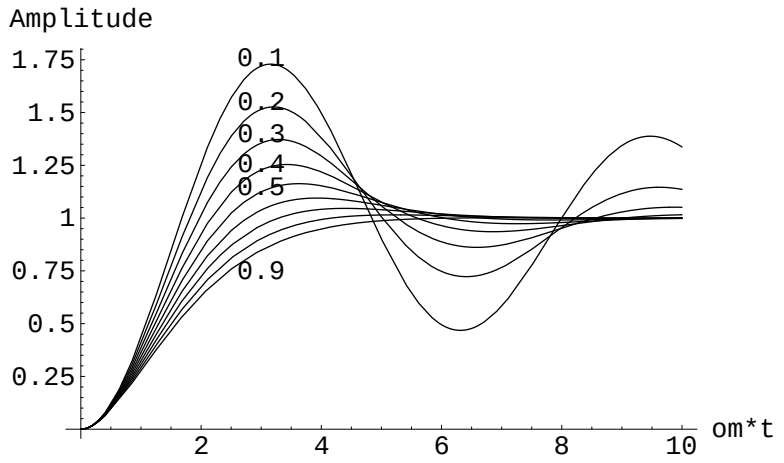

Figure 6.17: The step response of a harmonic oscillator as a function of $\omega\, t$ and for different values of δ.

must have a relatively low quality factor. In the end, the only parameter that determines the time response of the model is the resonance frequency ω appearing in the exponential term. In such a simple model, the bandwidth is almost equal to the resonating frequency ω, so, as expected, the bandwidth of the system plays a central role in the step response.

We approximated the closed-loop transfer function with a harmonic oscillator of quality factor $1/2\delta$ and resonance frequency ω. The model was used as an example to get the main characteristics of the system. We computed the time response to the step function of eq.(6.36), thus including the effect of the zero z_1 and comparing it to the results obtained for the harmonic oscillator (see fig.(6.18)). The presence of the zero introduces an overshoot; however, the settling time of the system remains about the same, $10ms$, corresponding to the inverse of the bandwidth.

6.6.2 The Error Signal

The second consideration in the acquisition of lock is the nature of the error signal. It has been mentioned that the linearity of the signal is limited to the FWHM of the resonance peak, shown in fig.(6.9). If the non-linear contribution of the signal is negligible, or if the signal is relatively weak outside of resonance, then it is clear that only the width of the resonance plays a role in the acquisition times.

On the other hand, if the signal has a non-negligible non-linear component of the correct sign, then this component helps the acquisition process. The latter is the case for the mode-cleaner prototype in the p state, relative to the finesse $\mathcal{F} = 100$. Outside resonance, as far as $\sim \lambda/10$ from resonance, the error signal has non-negligible values with the correct sign. The cavity, once outside the FWHM but still within the $\sim \lambda/10$, will give an error signal not proportional to the correction to be applied but with the correct sign. It is expected that the control system applies forces with the correct sign.

6.7 The Acquisition of Lock: $\mathcal{F} = 100$

The simulation for the acquisition of lock of the mode-cleaner prototype in the p polarization state is described as follows. The transfer functions used have been described in sec.(6.4) and the model is shown in fig.(6.19).

For this study, the laser frequency has been assumed constant, and the only noise considered was the seismic noise exciting the mirror positions. At the beginning of the simulation, performed in the time domain, the mirrors were left free to follow their motion induced by seismic noise.

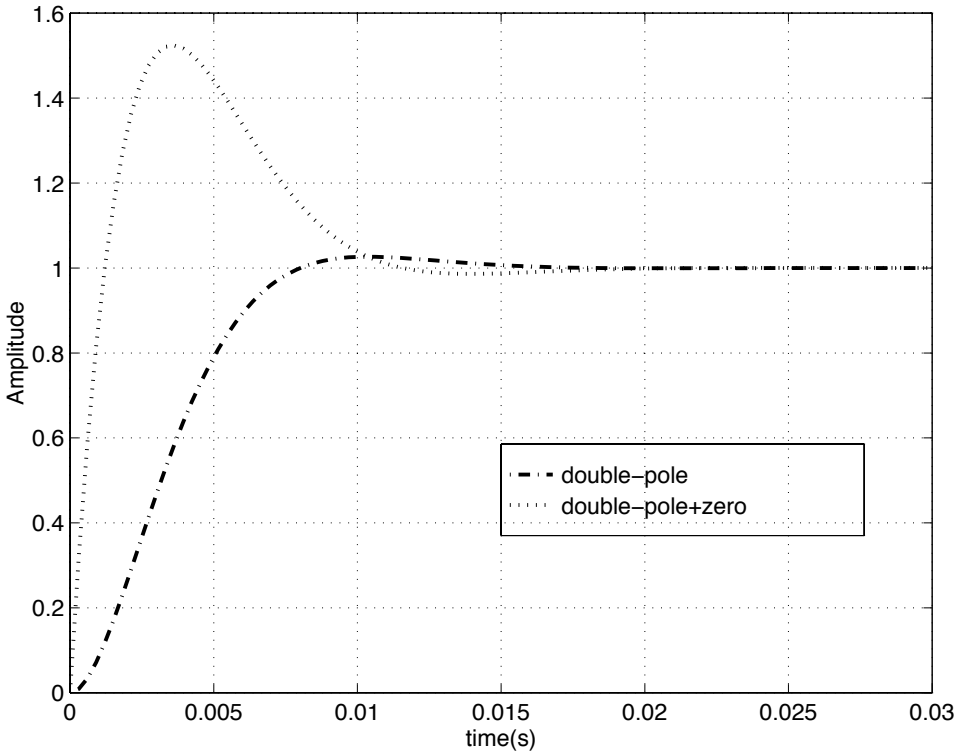

Figure 6.18: The step response of the closed-loop transfer function $\mathcal{C}(s)$. The simple harmonic oscillator model is compared to the transfer function with a double-pole and the zero. The settling time is about the same and is the inverse of the bandwidth of the system in question.

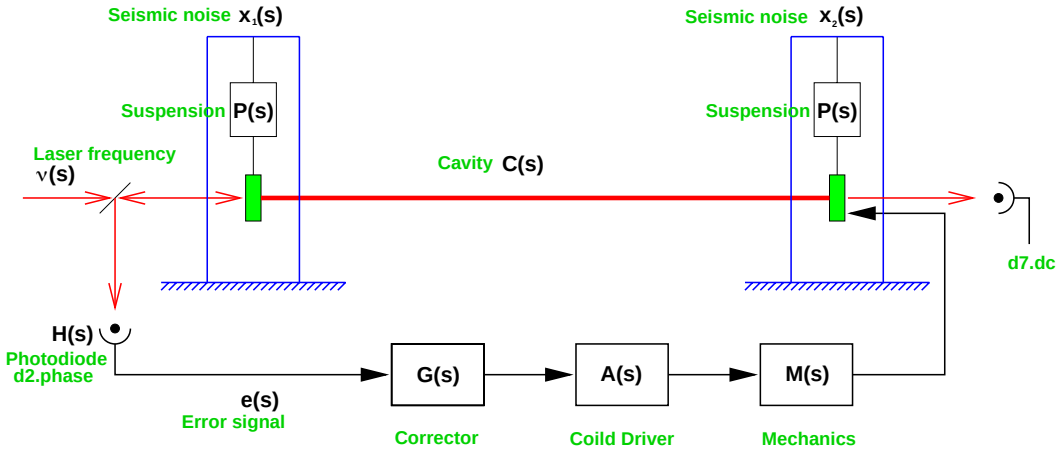

Figure 6.19: The MC30 model used for the acquisition of lock simulation in the p polarization state ($\mathcal{F} = 100$). Seismic noise excited the mirror positions, while the laser frequency has been assumed constant.

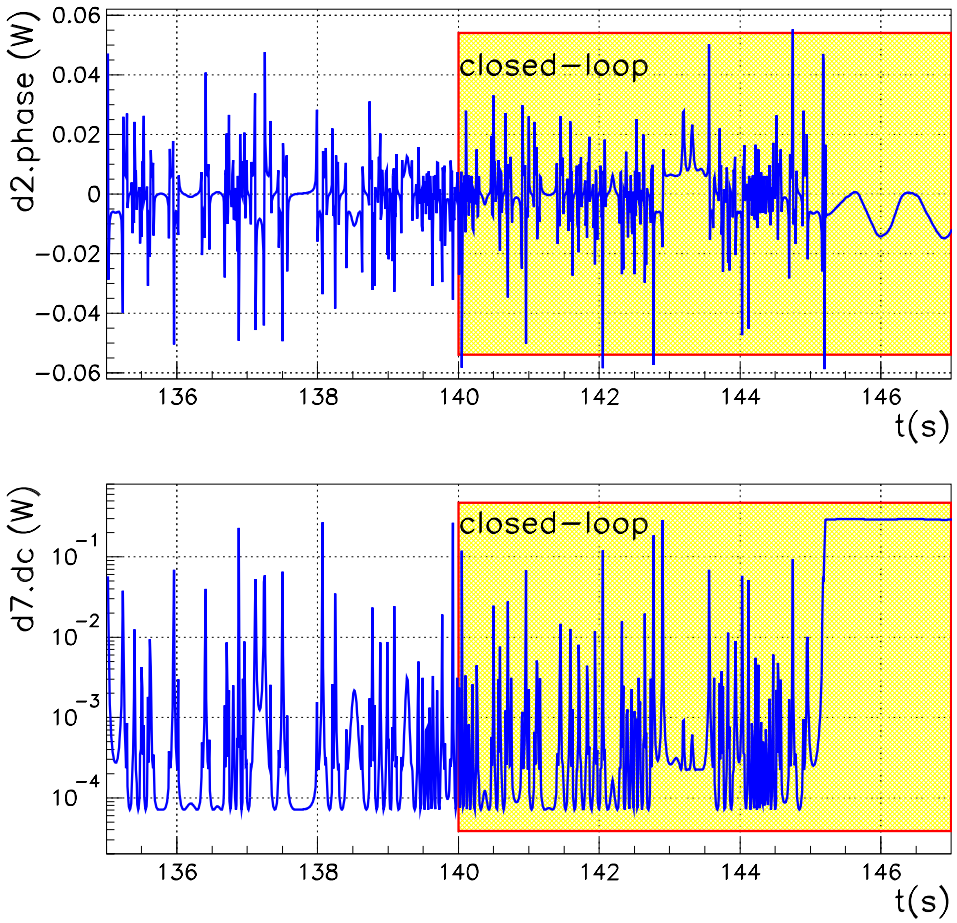

Figure 6.20: First example of lock acquisition from the simulation run of MC30 with $\mathcal{F} = 100$: the time evolution of the error signal d_2^{ph} and the transmitted DC power d_7^{dc} as the loop is closed at t= 140 s.

After an arbitrary time, the control loop was closed (by controlling the end mirror) and the first attempt to lock the cavity began. The feedback was left closed for 50 s, after which the mirror was released. After allowing it to freely move again and establish its natural motion, the procedure was repeated. Briefly, the simulation consisted of

1. letting the two masses relax and follow their natural motion for an arbitrary time Δt_i (open-loop);

2. closing the loop once the system relaxed regardless of the state of the cavity with respect to the laser frequency which is constant;

3. maintaining the loop closed for τ seconds and saving the time evolution of

   (a) the photodiode signals d_7^{dc} and d_2^{ph};

   (b) the cavity length $L(t)$;

4. releasing the controlled mirror (the terminal mirror 2) by opening the loop and letting the system relax again.

The relaxing time Δt_i was chosen randomly from a uniform distribution with values ranging as

$$\Delta t_i \in [100, 140] \text{ s} \tag{6.42}$$

whereas the time the loop was closed was chosen to be $\tau = 50$ s. During a simulation run of 3000 s, the loop was closed 17 times. Throughout the chapter, we will refer to as *event* the ensemble of signals (such the beam power, the cavity length, the correction signals etc.) relative to times when the loop is closed.

The result of the simulation showed that for each event, or in other words every time the loop was closed, the cavity was successfully locked with a mean time for lock acquisition of $\overline{t}_{acq} = 3$ s and a maximum time of 10 s. For the mode-cleaner prototype in Orsay, mean acquisition times of 10 s were experimentally observed[55].

The agreement between simulation and experiment is more than acceptable taking into account all the uncertainties in the parameters used in the model. Not only did this study allow the estimation of acquisition times, but it also offered a means to understand the process behind the acquisition of lock. In the following, 2 events out of the 17 will be presented as typical events, thus allowing the main characteristics of the process to be put in evidence.

6.7.1 Example: t = 140 s

Out of all the events, the one presented here is perhaps the most interesting. Fig.(6.20) shows the time evolution of the error signal d_2^{ph} in the top graph, as well as the transmitted DC power d_7^{dc} in the bottom graph. The system is in open loop, with both masses freely moving. At t = 140 s, the loop is closed. It takes the feedback about 5 s to achieve control. The transmitted power, at t $\geq$ 145 s, is equal to the incoming laser power of 300 mW corresponding to the complete transmission of all the power.

Not much can be understood from both graphs of fig.(6.20) apart from a distinct behavior around t = 143 s. On the other hand, by plotting the time evolution of the cavity length L(t), it is possible to get an insight into the process. Two curves are plotted in fig.(6.21), both depicting L(t) in λ units as a function of time. The dotted curve describes the time evolution L(t) in open loop. In this case, the loop is never closed and the masses are free to move. On the other hand, the continuous curve describes L(t) with the loop closed at t = 140 s. By plotting the two curves at the same time, it is possible to better understand the locking process. Notice that the fundamental mode resonance corresponds to L(t) = 0 and all multiples of $\lambda/2$.

There are two characteristics of the graph in question:

1. the difference between the curves describing the cavity length in open and closed loop increase as the relative velocity of the mirrors decreases; in other words, the control system is able to substantially change the cavity length only when the two mirrors slow down with respect to each other;

2. the control system can "kick" the cavity out of resonance.

In all the events studied, the relative velocity of the mirrors plays an important role in the lock acquisition process.

Fig.(6.22) focuses in the region around the kick. The plot of the error signal d_2^{ph} as well as the DC transmitted power d_7^{dc} is shown together with the cavity evolution. It is worth noticing that for $t \in [142.2s : 142.8s]$ the cavity crosses six resonances, with a relative velocity that goes up to 8λ/s. In this time interval, the control system has a negligible effect on the cavity length as can be seen by the fact that the two curves almost overlap.

Once the relative velocity goes to zero, the feedback begins to act, as shown in a further close-up in fig.(6.23). When the cavity approaches the resonance at $L = -1.5\,\lambda$, the velocity decreases and goes to zero before the sideband resonance. The cavity then goes back toward the resonance

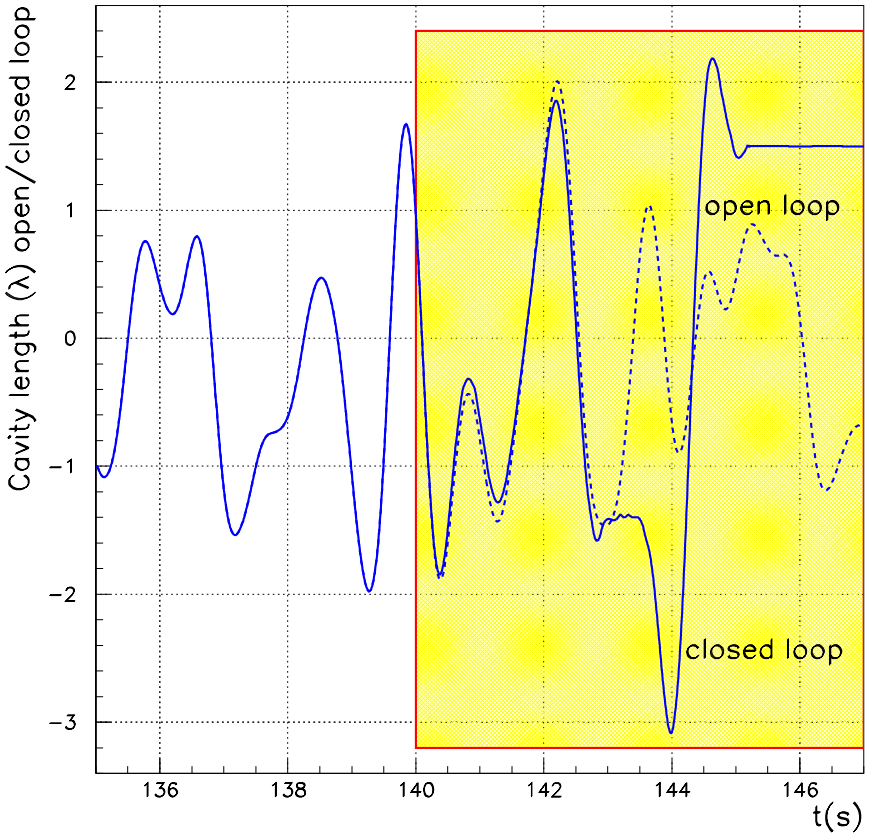

Figure 6.21: First example of lock acquisition from the simulation run of MC30 with $\mathcal{F} = 100$: the cavity length, in λ units, as a function of time. The dotted curve is the cavity time evolution in open loop whereas for the continuous curve the loop is closed at t= 140 s.

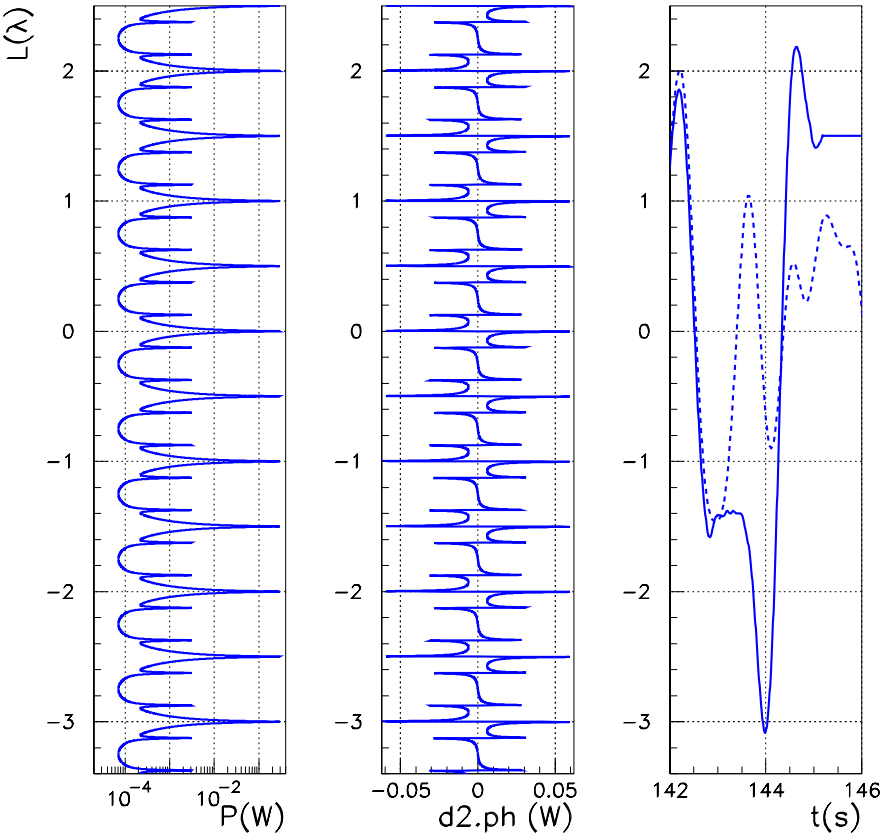

Figure 6.22: First example of lock acquisition from the simulation run of MC30 with $\mathcal{F} = 100$: a close-up in the region around the kick. Right: the cavity length L(t) as a function of time; center: the corresponding error signal d_2^{ph} as a function of length L; left: the corresponding DC transmitted power d_7^{dc} as a function of cavity length L.

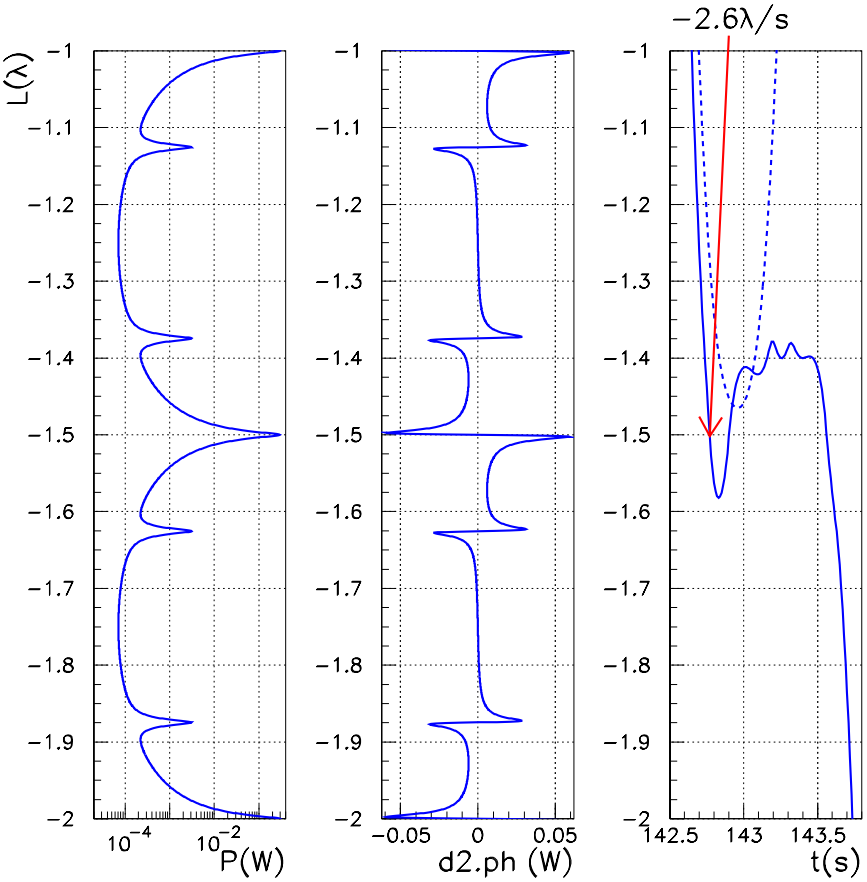

Figure 6.23: First example of lock acquisition from the simulation run of MC30 with $\mathcal{F} = 100$: a close-up in the region around the kick. Right: the cavity length L(t) as a function of time; center: the corresponding error signal d_2^{ph} as a function of length L; left: the corresponding DC transmitted power d_7^{dc} as a function of cavity length L.

again but the servo system is unable to stop it at resonance. The cavity expansion continues until the other sideband resonance is approached. Here, the two curves begin to differ completely. We would like to recall that the cavity length L(t) in closed loop consists of two contributions: one originating from seismic noise, and the other from the control system. The seismic contribution can be observed from the open-loop curve (the dotted one) in fig.(6.21) and fig.(6.22), whereas the sum of both contributions is described by the closed-loop curve (continuous one). Now, by referring to fig.(6.23) we notice that as the sideband resonance is approached, the cavity, due to the seismic contribution only, begins to expand. In closed-loop, the cavity also expands until the error signal increases due to the sideband. Here, the feedback is able to revert the expansion at t = 143 s. As a consequence, as the sideband resonance is left behind, the error signal decreases and the seismic contribution begins to dominate. The error signal increases, an oscillatory behavior begins and the cavity finds itself in an unstable position from t = 143 s to t = 143.5 s. At the end (t = 143.5 s), the relative velocity of the mirrors in open-loop decreases, as can be seen in fig.(6.21), and the control system does not have enough time to react accordingly, resulting in a forceful kick to the terminal mirror.

Fig.(6.24) focuses on the moment when the control system acquires lock. The relative velocity of the masses decreases in the region around the resonance at L=1.5λ. Here, the non-linear region due to the sideband contribution plays a role again: the cavity is guided into lock from outside the FWHM of the fundamental resonance.

In conclusion, we observed that the effect of the servo system is noticeable when the relative velocity of the mirrors is low. Furthermore, in all the events, the Pound-Drever error signal outside of the FWHM of the fundamental resonance contributed to the acquisition of control. Only 2 events out of the 17 were observed where the mirror was forcefully kicked away from resonance.

6.7.2 Example: t = 825 s

Most of the 17 events resemble this one. The plot of the error signal as well as the DC power as a function of time are shown in fig.(6.25). In this case, only 2.5 s were necessary in order to acquire lock. The cavity length evolution, in both closed and open loop, is presented in fig.(6.26). Again, once the relative velocity reaches low values, the control system begins to play a role. If, at the same time, the value of the error signal is non-negligible, the feedback is able to guide the cavity into lock. Fig.(6.27) shows the behavior in question. The relative speed decreases as the resonance at L = λ is approached and the cavity length begins to oscillate from one sideband to the other. It is clear that the non-linear component of the error signal plays a role in the process.

6.8 Acquisition of Lock: $\mathcal{F} = 1600$

The lock acquisition process was also studied in the case of $\mathcal{F} = 1600$. By going from a finesse $\mathcal{F} = 100$ to a finesse of $\mathcal{F} = 1600$, the resonance FWHM decreases by more than one order of magnitude. Fig.(6.28) shows both the transmitted DC power as well as the error signal for the two polarization states. As a consequence, the gain of the control must be adjusted so as to limit the length fluctuations to within $(\lambda/2)/\mathcal{F} = 3 \times 10^{-4}\,\lambda$ once the loop is closed. One way to increase the gain while leaving the bandwidth of the system at $100\,Hz$ is to multiply the open-loop transfer function by the filter

$$\frac{s + \omega}{s} \tag{6.43}$$

where $\omega/2\pi = 18.5\,Hz$.

A simulation run of t = 3000 s, just as in sec.(6.7), was used to study the lock acquisition process. The same MC30 model was used, only with the finesse modified to $\mathcal{F} = 1600$ and the open-loop transfer function, discussed in sec.(6.5.1), multiplied by the filter in eq.(6.43). The result of the simulation showed that the control system was unable to acquire lock. Experimentally, unacceptably long lock acquisition times were observed with the control system described in this chapter.

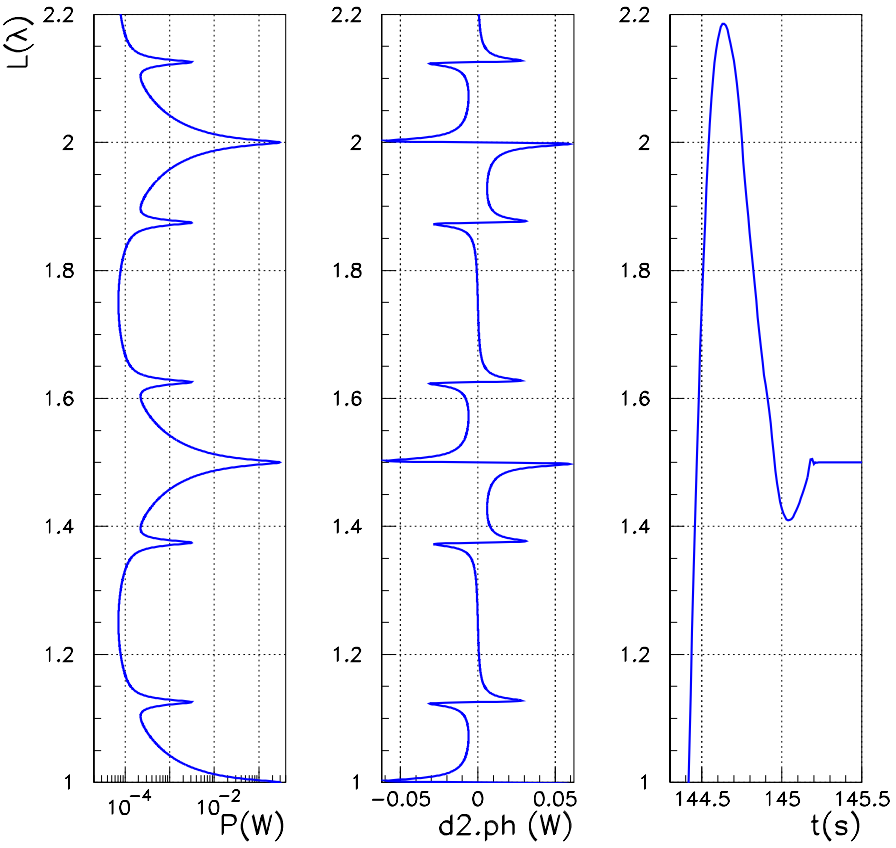

Figure 6.24: A close-up of the acquisition of lock region. Right: the cavity length L(t) as a function of time; center: the corresponding error signal d_2^{ph} as a function of length L; left: the corresponding DC transmitted power d_7^{dc} as a function of cavity length L.

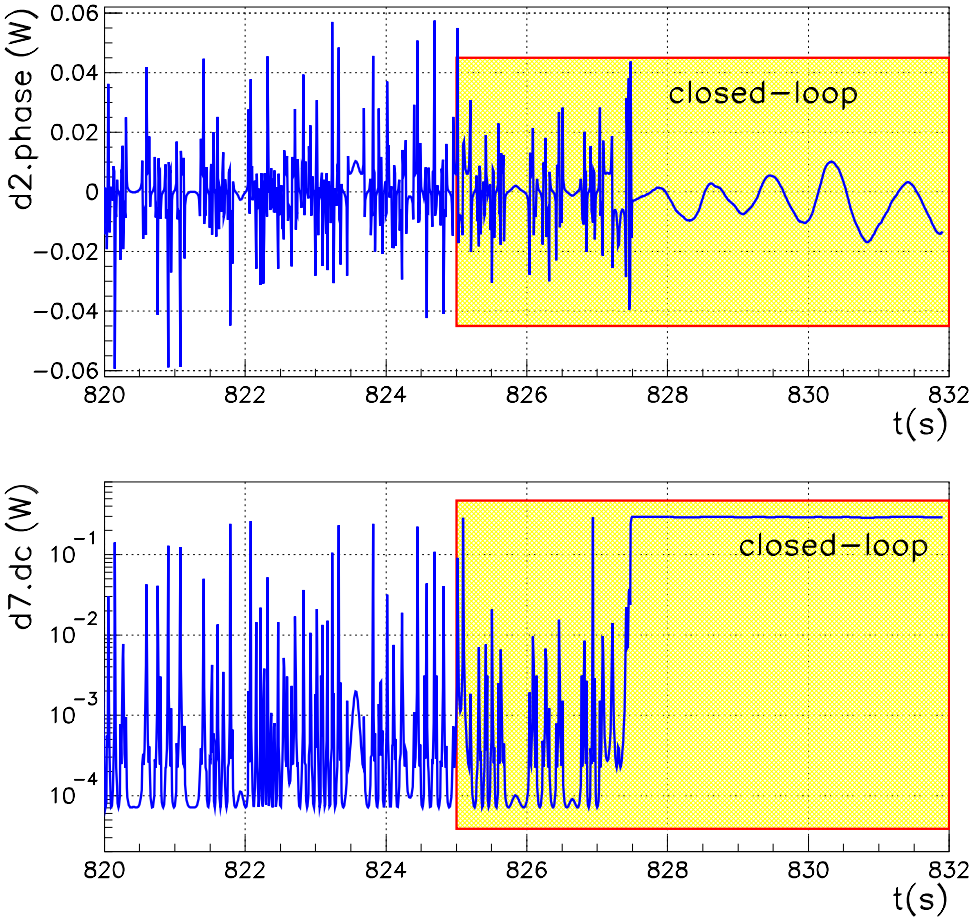

Figure 6.25: The time evolution of the error signal d_2^{ph} and the transmitted DC power d_7^{dc} as the loop is closed at t= 825 s.

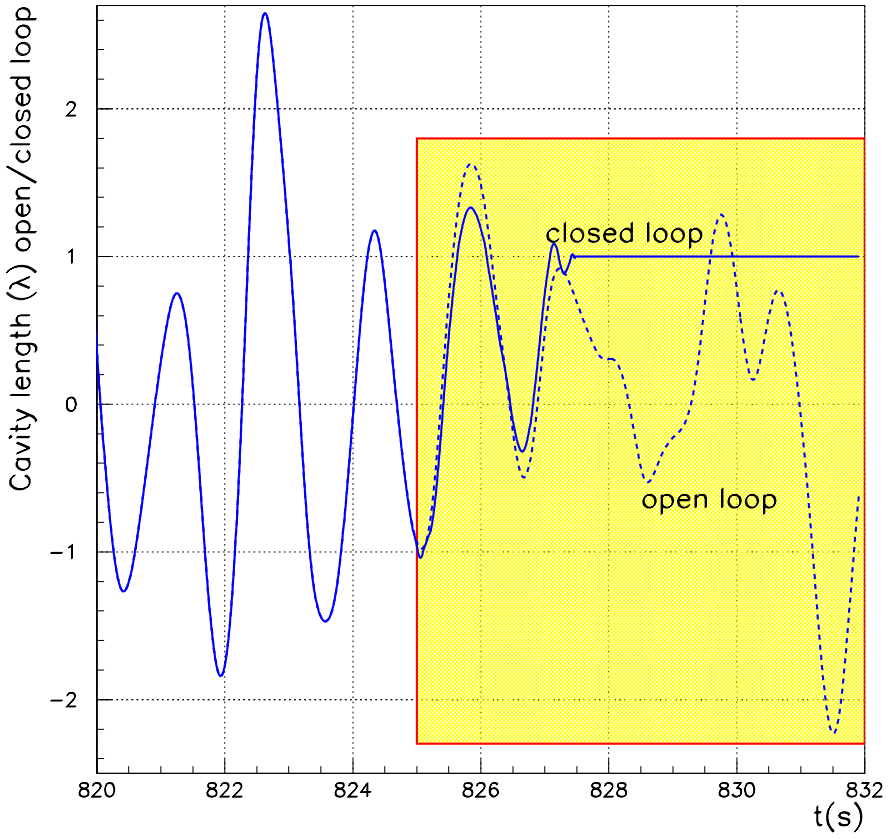

Figure 6.26: Second example of lock acquisition from the simulation run of MC30 with $\mathcal{F} = 100$: the cavity length, in λ units, as a function of time. The dotted curve is the cavity time evolution in open loop whereas for the continuous curve the loop is closed at t= 825 s.

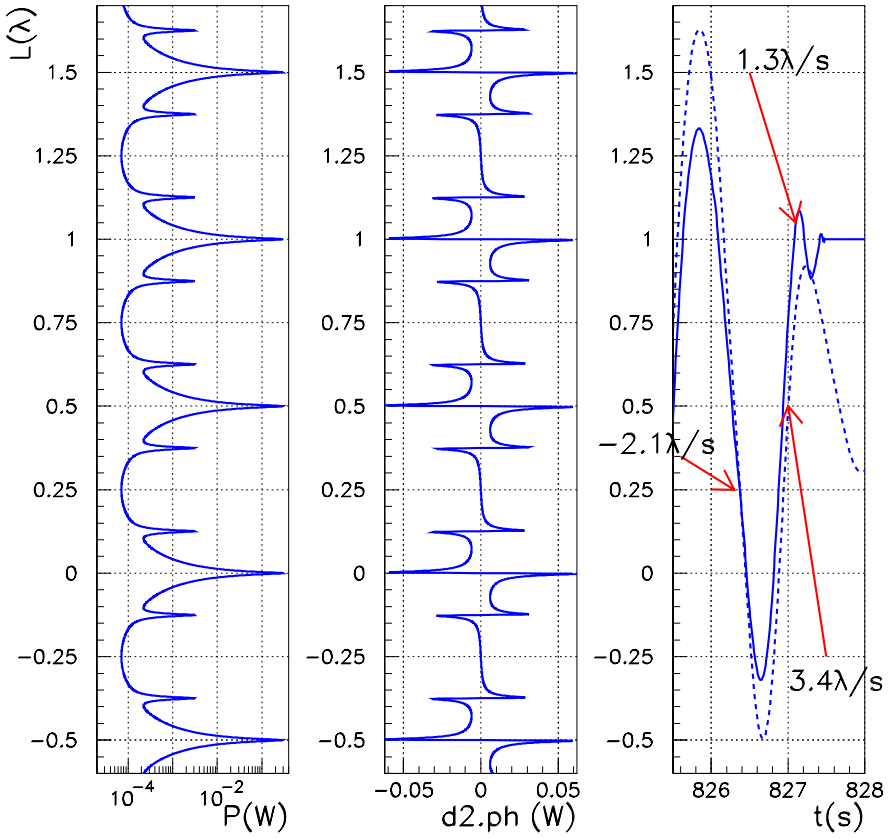

Figure 6.27: A close-up in the region around the acquisition of lock. Right: the cavity length L(t) as a function of time; center: the corresponding error signal d_2^{ph} as a function of length L; left: the corresponding DC transmitted power d_7^{dc} as a function of cavity length L.

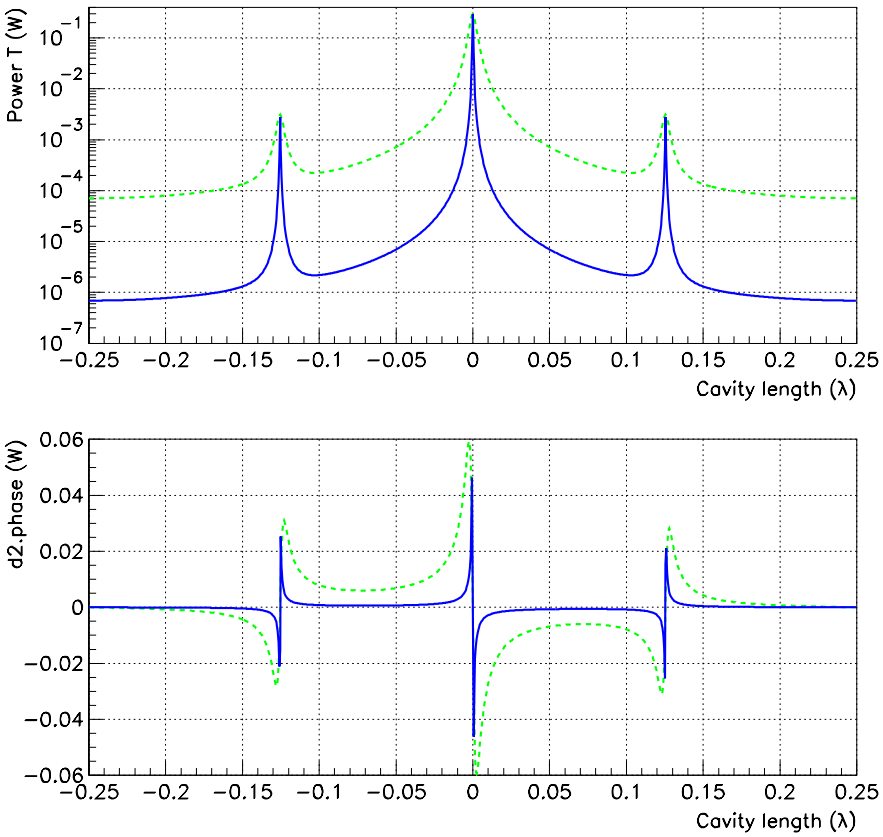

Figure 6.28: The calculated MC30 transmitted DC power and the error signal as a function of the cavity length. Dotted line: $\mathcal{F} = 100$. Continuous line: $\mathcal{F} = 1600$.

This was expected and it can be understood by referring to fig.(6.28). For the two polarization states, not only the two resonance FWHM but also the non-linear components of their error signals differ. In the case of $\mathcal{F} = 1600$, the Pound-Drever error signal can be neglected outside of the resonance because of its low value. The threshold velocity $v_{\rm thr}$, defined in eq.(6.46) is, in this case

$$v_{\rm thr} = B * \frac{\lambda/2}{\mathcal{F}} = 3 \times 10^{-2}\,[\lambda/s] \tag{6.44}$$

As an estimate, for the mirror motion concentrated at $1\,Hz$ with an RMS value of $1\,\mu m$, the mean velocities expected are of the order of $3\,\mu m/s$, which is two orders of magnitude above the threshold value, and therefore very long acquisition times are expected.

6.9 Conclusion

The model of the mode-cleaner prototype MC30 in the p polarization state has been presented as well as a simulation of the acquisition of lock process. The numerical study resulted in a mean acquisition time $\overline{t}$ and a maximum acquisition time t_{max} of

$$\begin{aligned} \overline{t} &= 3\ \text{s} \\ t_{max} &= 10\ \text{s} \end{aligned} \tag{6.45}$$

This has been confirmed on the MC30 prototype with acquisition times of the order of 10 s[55].

The simulation results also showed that

1. the control system plays a role only when the relative speed of the mirrors is low;
2. the non-linear contribution of the error signal also plays a role
   (a) by causing the control system to inject noise into the system (as for example forcefully kicking the mirror away from the closest resonance) even though only 2 out of the 17 events showed such behavior;
   (b) by helping the control system to guide the cavity into lock with oscillations of the cavity length ranging from sideband to sideband.

It is possible to give an estimate for the acquisition times once the response of the control system, the relative speed of the mirrors and the error signal are known. Assuming that the error signal has a negligible component outside of the FWHM of the resonance, then there exists a threshold speed $v_{\rm thr}$ below which the control system is able to acquire lock. Such a threshold can be defined as follows:

$$v_{\rm thr} \equiv B * \text{FWHM} \tag{6.46}$$

where B is the bandwidth of the control. If the mirror speed v is such that

$$v < v_{\rm thr} \tag{6.47}$$

then the feedback is able to follow and correct the evolution of the cavity dynamics.

For the mode-cleaner prototype with $\mathcal{F} = 100$, acquisition times are difficult to estimate. This is due to the fact that the error signal outside of the FWHM does contribute to the locking. By assuming that an error signal is limited to the distance between the sideband resonances, $\sim \lambda/4$, then the threshold velocity is

$$v < v_{\rm thr} \simeq B * \frac{\lambda}{4} = 25\,[\lambda/s] \tag{6.48}$$

For seismic displacements concentrated around $1\,Hz$ with a RMS value of $1\,\mu m$, the mean velocities expected are of the order of $3\,\mu m/s$, well below the threshold limit, and short acquisition times

are expected. From the simulation, acquisition of lock was possible from velocities ranging up to 5 λ/s.

On the other hand, the results of the numerical calculations showed that for the mode-cleaner prototype with $\mathcal{F} = 1600$, the control system was unable to acquire lock. Experimentally, unacceptable acquisition times were observed with the control system described in this chapter. This was anticipated: the non-linear contribution of the error signal is negligible so that the threshold velocity is $v_{\rm thr} = 3 \times 10^{-2}\,[\lambda/s]$, well below the mean velocity of $3\,\mu m/s$. Long acquisition times are therefore expected.

Chapter 7

The Ringing Effect

Before making the step from the MC30 prototype to the CITF as regards the lock acquisition process, let us consider a phenomenon which occurs on the mode-cleaner in high finesse. Prior to the lock acquisition of the MC30 prototype, the mirrors move in free motion, inducing the cavity length to sweep the optical resonance at different rates of expansion. If the relative velocity between the mirrors is constant, the DC transmitted power delineates the *Airy peak* as a function of time. This was observed for the optical system with $\mathcal{F} = 100$. However, during the experimental work on the MC30 prototype with $\mathcal{F} = 1600$, a deformation of the Airy peak, similar to a ringing, was observed. Fig.(7.1) shows an experimental measurement of the transmitted power as a function of time, as the cavity length swept the optical resonance at an unknown expansion rate.

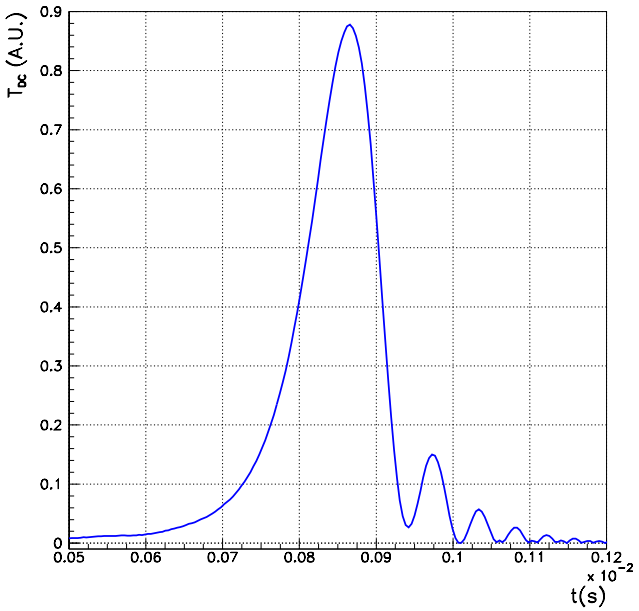

Figure 7.1: The observed *ringing effect* on the transmitted DC power of the MC30 prototype. The transmitted power is shown as a function of time as the cavity length sweeps the optical resonance at an unknown rate.

Both [56, 57] and references therein discuss this phenomenon. Briefly, this effect arises once the cavity sweeps the optical resonance in a time τ_{sweep} of the order of or less than the cavity

storage time $\tau_{\text{storage}} \simeq \mathcal{F}\, L\,/\,c$, i.e.

$$\tau_{\text{sweep}} \leq \tau_{\text{storage}} \tag{7.1}$$

This effect is observed when the rate of expansion is so high that, as resonance is approached, the cavity doesn't have enough time to completely fill itself. It is the beating between the incoming laser field and the evolving stored field that gives rise to this oscillatory behavior.

This effect created difficulties in the measurement of the finesse for the s polarization state. In the p polarization state, it was possible to measure the resonance FWHM, thus allowing the determination of this parameter. However, for relatively high finesse values, the Airy peak distortion introduced by the ringing effect modifies the resonance FWHM, impeding the estimate.

In this chapter, we present a numerical study on the ringing effect. This study allowed the determination of

- the MC30 finesse for the s polarization state, whose result is then compared to that of an alternative method[56];
- an empirical expression to resolve the cavity expansion rate.

These two parameters, $\mathcal{F}$ and v, define the behavior of the oscillations. We begin the chapter by describing the model used for this study.

7.1 The Ringing Effect Model

In order to model this phenomenon, the photon travel time within the cavity needs to be taken into account. Just as in Ch.(6), a two-mirror Fabry-Perot of length $L_0 = 30\,m$, sketched in fig.(7.2), was chosen to simulate the mode-cleaner. Assuming a negligible mirror displacement for times of

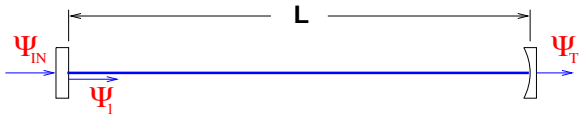

Figure 7.2: The model used for the study of the MC30 ringing effect.

the order of the round trip time of light $\tau = 2L_0/c = 0.2\,\mu s$, the stored field $\Psi_1(t)$ at time t can be written as

$$\Psi_1(t) \;=\; t_1\,\Psi_{in} \;+\; r^2\,\exp(-2\,i\,k\,L\,)\,\Psi_1(t\,-\,\tau) \tag{7.2}$$

where r denotes the amplitude reflectivity for each mirror, Ψ_{in} is the incoming laser field, and L is the cavity length. Assuming that the cavity expands at a constant rate v, we can write

$$L \;=\; L_0 \;+\; v\,t \tag{7.3}$$

and solve eq.(7.2) iteratively, for different velocities v and finesse $\mathcal{F}$.

By setting the Fabry-Perot finesse to a fixed value and plotting the stored DC power as a function of cavity length ΔL for different expansion rates, it is possible to reproduce the oscillatory behavior shown in fig.(7.1). In particular, fig.(7.3) shows this plot for three velocities: $v = 0$ (static approximation), $v = 1\lambda/s$, and $v = 2.6\lambda/s$, with $\mathcal{F} = 4000$. The curve labeled *static*, corresponding to $v = 0$, was generated by neglecting the travel time of light, assuming an infinite speed of light. The two other curves, on the other hand, were simulated according to the dynamical model here presented. Notice how the main peak height decreases, its width increases and its position shifts ahead of the resonance. These changes are greater for larger velocities.

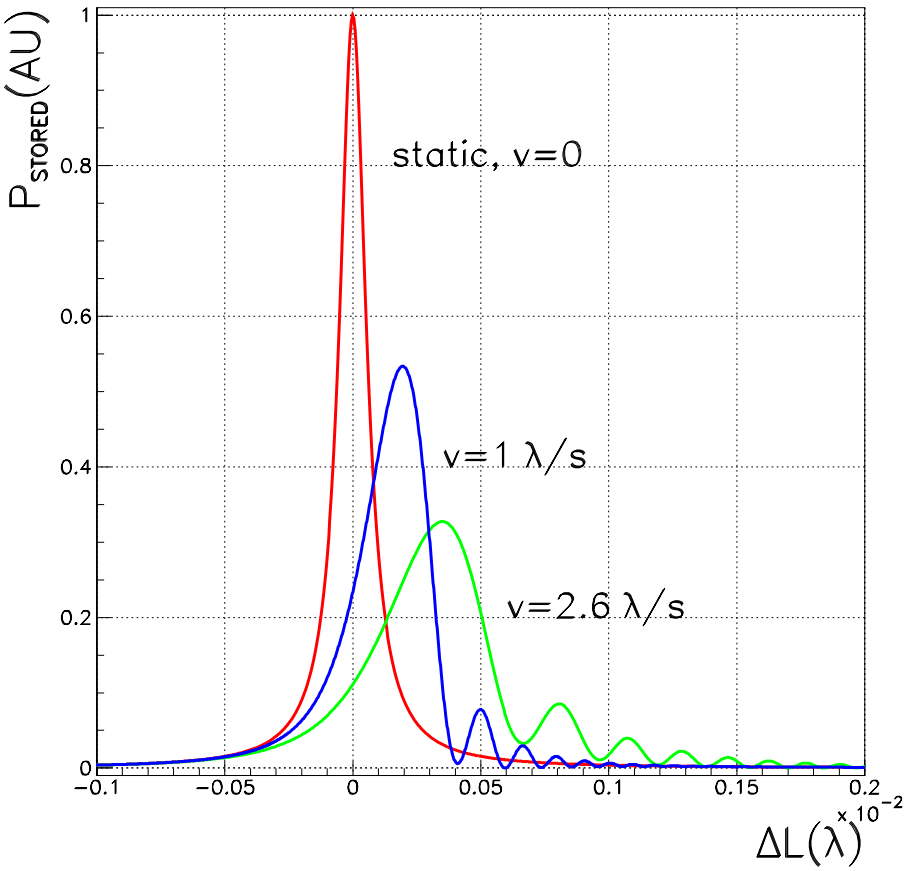

Figure 7.3: The calculated Fabry-Perot transmitted power, with $\mathcal{F} = 4000$, as a function of cavity length ΔL as the resonance is swept at $v = 0$ (static approximation), $v = 1\lambda/s$, and $v = 2.6\lambda/s$. In the figure, $\Delta L = 0$ corresponds to resonance.

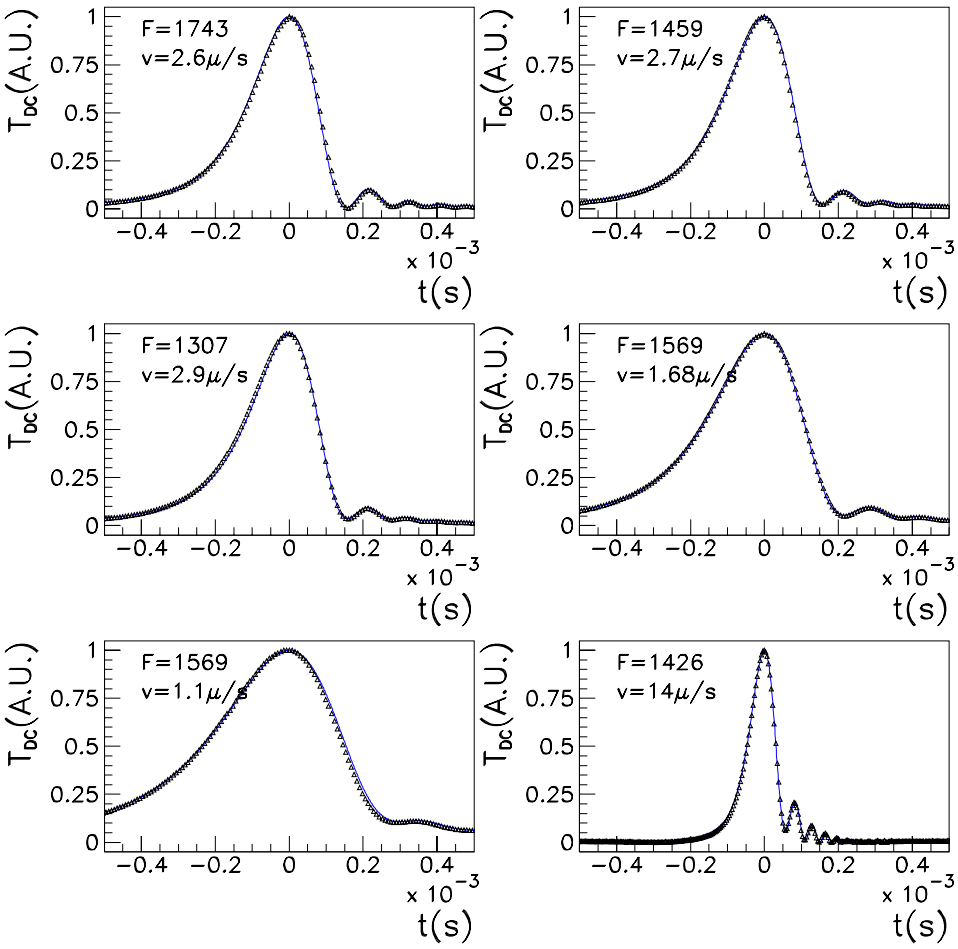

Figure 7.4: The observed ringing effect for the MC30 prototype: measurements and eye fits. The finesse and velocity values are shown for each graph.

7.2 Measurement Fits

The first goal of this work was to reproduce the observed ringing effect on the MC30 prototype and estimate the cavity finesse as well as the relative mirror velocities. Figs.(7.4-7.5) show ten measurements of the transmitted power, with the principal peak height normalized to one, and their eye fits performed with the simulation. The good agreement between actual measurements and simulation outputs confirm the validity of the model in use. By averaging the fit results, the mean finesse is

$$\overline{\mathcal{F}} = 1554 \pm 160 \tag{7.4}$$

Here the error arises from the fact that the state of the alignment changes from each resonance crossing, generating different cavity losses per crossing. This finesse value was later confirmed by a measurement of the cavity pole[58].

The fits also allowed an estimate of the relative velocities. We can observe that the time difference between minima and maxima decreases with increasing velocity.

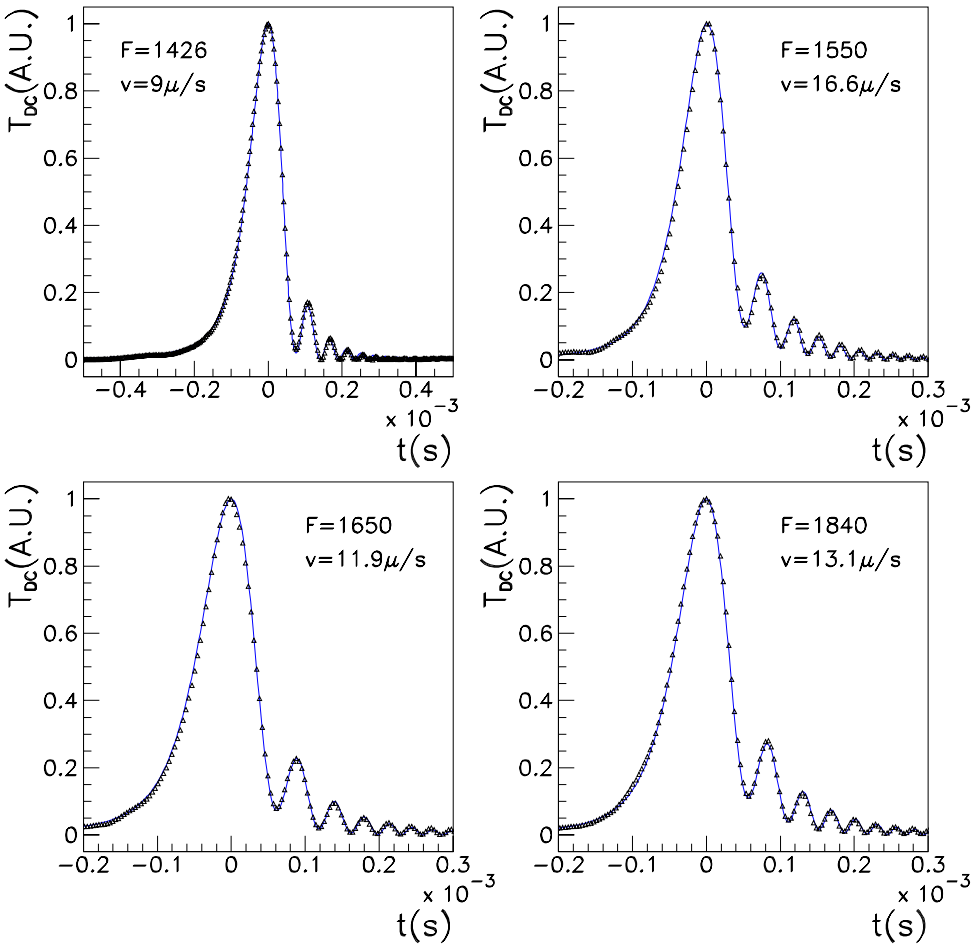

Figure 7.5: The observed ringing effect for the MC30 prototype: measurements and eye fits. The finesse and velocity values are shown for each graph.

Finesse $\mathcal{F}$ set in simulation	Finesse estimated from eq.(7.5)	Error
1000	828	20%
1500	1316	12%
2000	1845	8%
2500	2452	2%
3000	2960	1%
3500	3480	0.5%

Table 7.1: The precision of eq.(7.5) as a function of finesse, using simulation outputs instead of measurements. The rate of expansion used was $v = 10\,\lambda/s$.

7.3 Measuring the Finesse: An Alternative Method

An alternative method for the measurement of (relatively) high finesses from the observation of the ringing effect, described in [56], was used. According to the authors, by measuring the first and second peak height, I_1 and I_2 respectively, as well as their time difference Δt, then

$$\mathcal{F} = \frac{\frac{2\,\pi\,c}{L}\,\Delta t}{\frac{I_1}{I_2} + 2 - e} \tag{7.5}$$

where L is the cavity length. This method also yielded a mean finesse of $\overline{\mathcal{F}} \simeq 1600$ with a maximum spread of 20%.

This method is biased towards high finesse values, which can be observed by using eq.(7.5) with simulation outputs instead of measurements, thus allowing the comparison of the known finesse with the finesse obtained by this method. Tab.(7.1) shows the results for 6 different finesse values with the same cavity expansion rate $v = 10\,\lambda/s$. The reader can observe that the error decreases as the finesse increases with values that go below 1% for finesse values above 3000.

7.4 The Properties of the Effect

We would now like to discuss a property of the ringing effect observed from the simulation runs. Fig.(7.3) graphs the stored power as a function of cavity length for a given finesse and for different values of velocity. We can now plot the stored power as a function of time, setting the velocity to a fixed value, but varying the finesse. One example is given in fig.(7.6). The top graph of this figure shows the stored power as a function of time, for an expansion rate set to $v = 10\,\lambda/s$, for three different finesse values: $\mathcal{F} = 1000$, $\mathcal{F} = 2000$, and $\mathcal{F} = 3000$. The bottom graph is the curves' time derivative. From these plots, we remark a particular characteristic of the phenomenon: the position of the minima and maxima, with the exception of the main peak, are almost independent from the finesse value.

Furthermore, going back to fig.(7.3), we can now note that the derivative zeros depend only on the relative mirror velocity. Therefore, the output of the simulation can be easily adjusted so as to fit any measurement. As a matter of fact, by modifying the cavity rate of expansion, it is

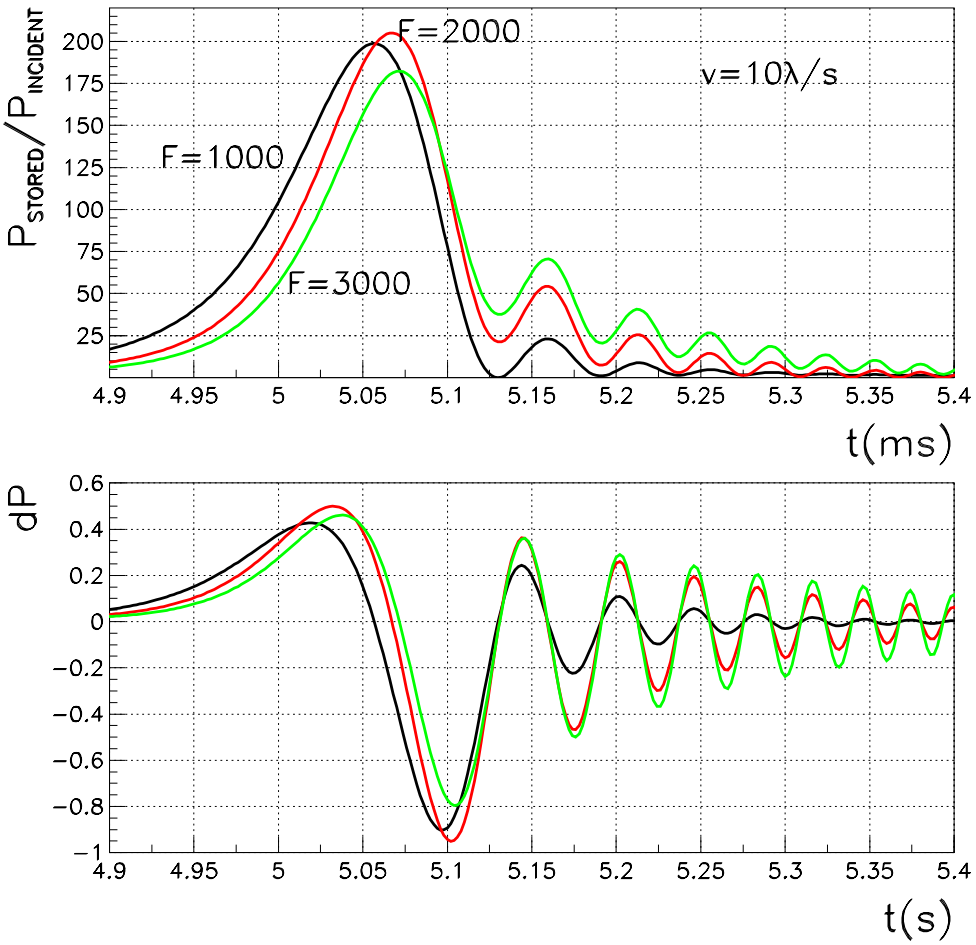

Figure 7.6: The calculated stored power as a function of time, with a fixed expansion rate set to $v = 10\lambda/s$, for different finesse values: $\mathcal{F} = 1000$, $\mathcal{F} = 2000$, and $\mathcal{F} = 3000$. Top graph: the stored power. Bottom graph: the stored power time derivative.

possible to increase or decrease the frequency of the oscillations so as to match the experimental position of minima and maxima. Once these positions are found, changing the finesse allows the adjustment of the peak heights.

7.4.1 The Relative Velocity Estimate

The simulation output shown in fig.(7.6) not only shows how the derivative zeros are independent, at least to first approximation, from the finesse, but it also shows a particular regularity in the spacing between the minima and maxima. The upper graph of fig.(7.7) shows the simulated stored power of a cavity with $\mathcal{F} = 3500$, expanding at a rate $10\lambda/s$. Let the position of the curve's derivative zeros, $t_{\rm zero}$, be labeled by the index n, so that, for the first zero, positioned at $t_{\rm zero} \simeq 5.07\,ms$, $n = 0$, for the second zero, located at $t_{\rm zero} \simeq 5.103\,ms$, $n = 1$ and so on. Then, the bottom graph of fig.(7.7) shows the plot of index n as a function of time. We remark that the n-th zero of the derivative is a quadratic function of the zero crossing time $t_{\rm zero}$:

$$n \propto t_{\rm zero}^2 \tag{7.6}$$

By fitting the simulation outputs to the expression

$$n_{\rm zero} = p_1 + p_2\, t_{\rm zero} + p_3\, t_{\rm zero}^2 \tag{7.7}$$

where $p_{1,2,3}$ are fitting parameters, we empirically found that the coefficient p_3 can be written as

$$p_3 = \frac{c\,v}{\lambda\,L} \tag{7.8}$$

where L is the cavity length and v is the cavity expansion rate (an example of this fit is shown in the bottom graph of fig.(7.7)). Therefore, an estimate of coefficient p_3 would also give us an estimate of the relative velocity v.

Now, going back to the measurements discussed in sec.(7.2) and shown in figs.(7.4 - 7.5), it is possible to fit them with eq.(7.7) to estimate the relative velocity v. For 5 measurements, figs.(7.8 - 7.12) show, on the left, the measured transmitted power as a function of time and on the right, the fit results of $t_{\rm zero}$ as a function of n. In these figures, what is referred to as coefficient P_3 refers to the inverse of eq.(7.8). From the 5 fit results, the estimate of p_3 gives an estimate on the velocity. The velocity error derives from the accuracy within which the minima and maxima are located. For this work, this was set to half of the oscilloscope's sampling time. The fit results for the velocity reconstruction are shown in tab.(7.2), with their corresponding χ^2/ndf values, and are in agreement with the eye fits shown in fig.(7.4 - 7.5).

7.5 Conclusion

In this chapter, we investigated a phenomenon, which we called *ringing effect*, observed on the MC30 transmitted DC power as the mirrors moved in free motion. By fitting the behavior with SIESTA's outputs, we were able to give a first estimate of the cavity's finesse

$$\overline{\mathcal{F}} = 1554 \pm 160$$

Furthermore, the numerical results showed how the position of the oscillations' minima and maxima, when plotted as a function of time, weakly depend on the finesse value and are completely determined by the cavity expansion rate as the resonance is being crossed. In particular, we showed how a simple empirical formula can determine the cavity expansion rate by observing these minima and maxima. For the same set of measurements used for the finesse, the results from the empirical formula and the eye-fits were in agreement.

This chapter's results may be useful for a possible acquisition of lock algorithm relative to VIRGO's mode-cleaner prototype. We remark that the velocity reconstruction here shown gives information only on its amplitude and not on its sign. In order to obtain information on the velocity sign, the same empirical formula must be applied to the demodulated signals.

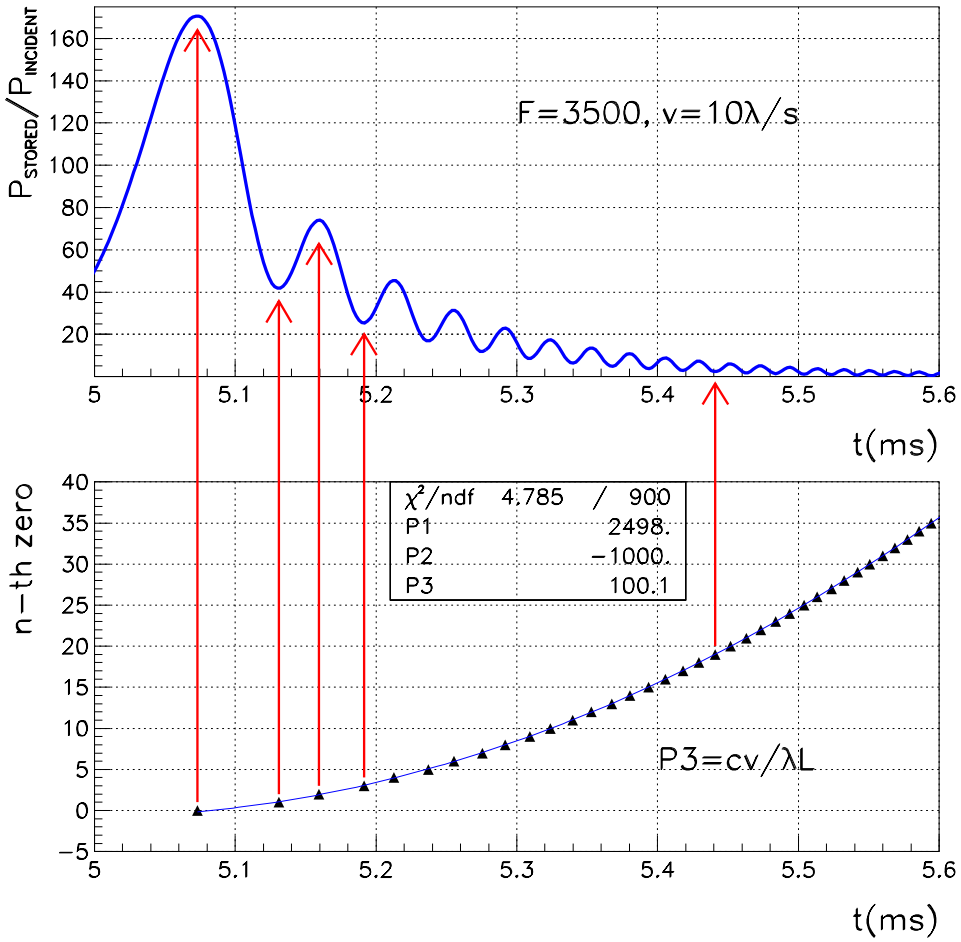

Figure 7.7: The simulated stored power of a Fabry-Perot, expanding at a constant rate $v = 10\,\lambda/s$, with $\mathcal{F} = 3500$. Top graph: the stored power as a function of time. Bottom graph: the index n, corresponding to the n-th derivative zero, as a function of time. The curve is fit to the expression $n = p_1 + p_2\,t + p_3\,t^2$. Notice that $p_3 = c\,v\,/\lambda\,L = 100\,[1/ms^2]$.

	fig.(7.8)	fig.(7.9)	fig.(7.10)	fig.(7.11)	fig.(7.12)
v (μ/s) (from eye fit)	2.6	2.7	16.6	11.9	13.1
v (μ/s)	$2.5 \pm 3 \cdot 10^{-4}$	$2.7 \pm 3 \cdot 10^{-3}$	$13.9 \pm 3 \cdot 10^{-2}$	$10.9 \pm 7 \cdot 10^{-3}$	$12.8 \pm 8 \cdot 10^{-3}$
χ^2/ndf	7.3	8.7	1.6	0.8	0.9

Table 7.2: Fit results for the mirror relative velocity reconstruction: the estimated velocity v and the corresponding χ^2/ndf value.

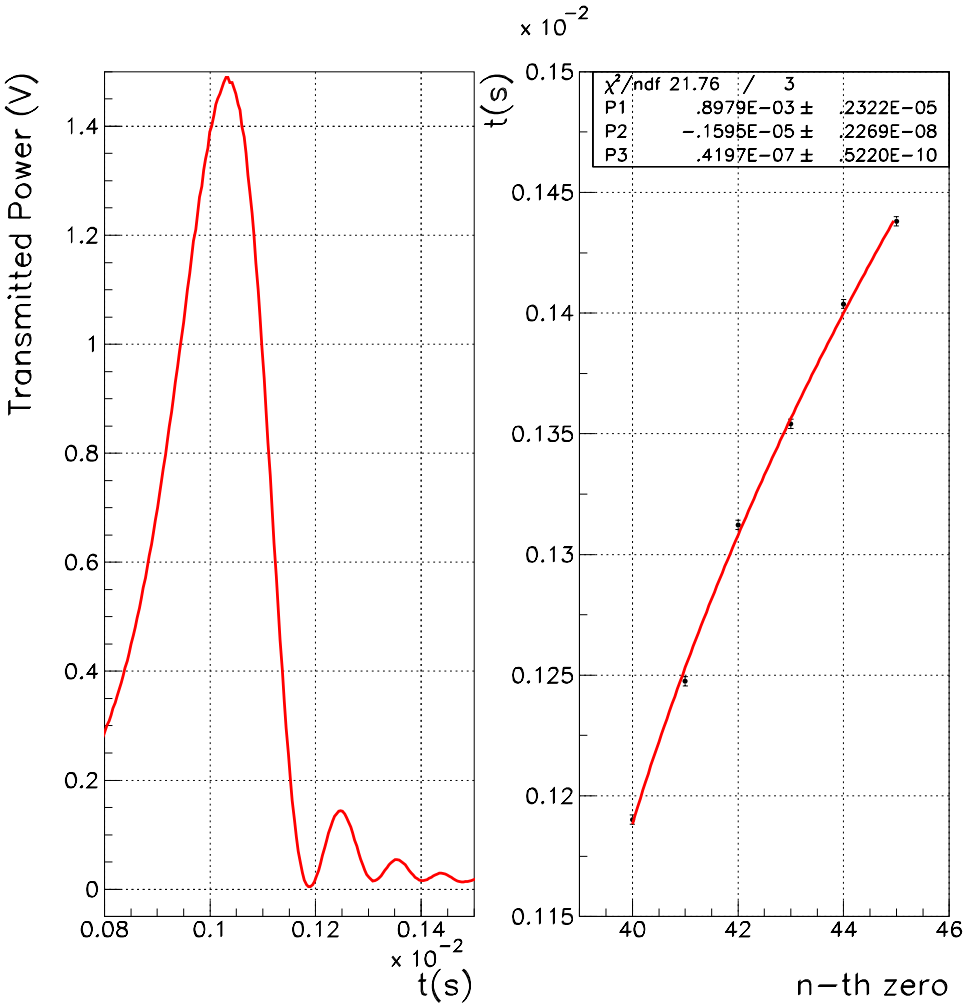

Figure 7.8: Fit results for the mirror relative velocity reconstruction.On the left: The measured DC transmitted power. On the right: the plot of t_{zero} as a function of index n. The error bars correspond to half of the oscilloscope's sampling time.

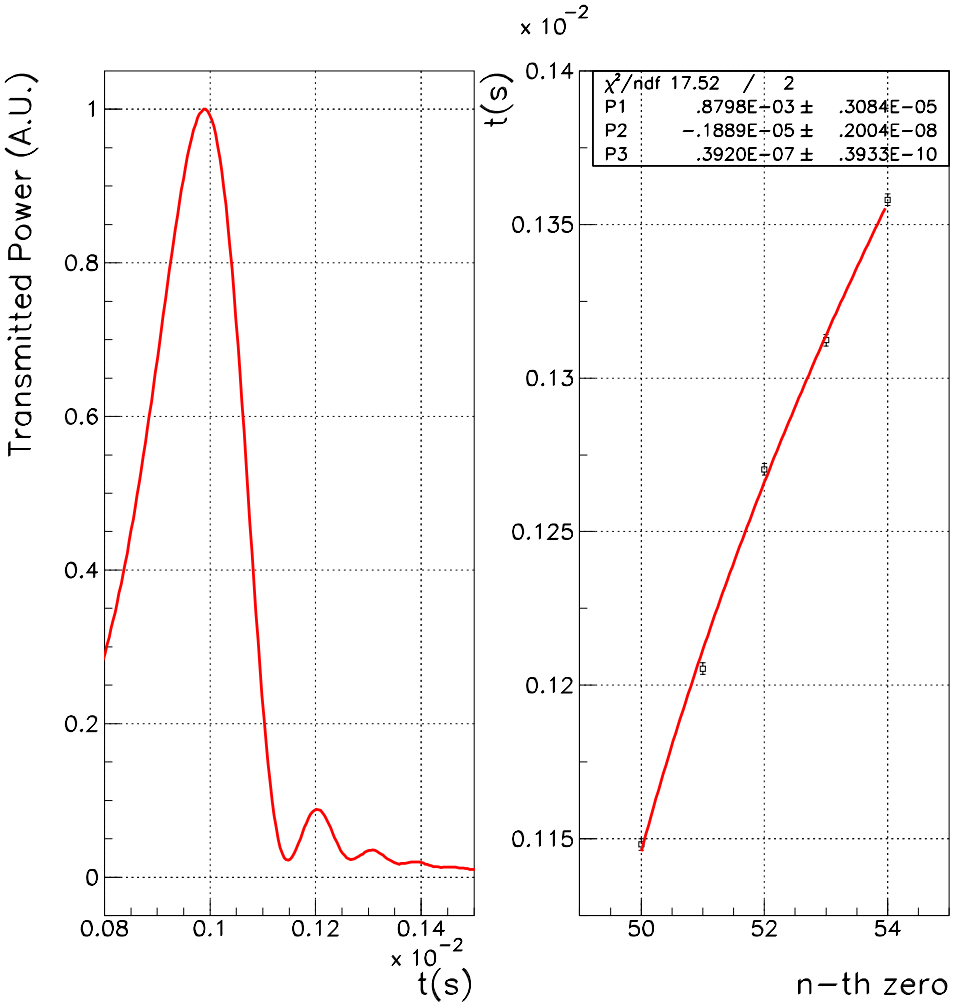

Figure 7.9: Fit results for the mirror relative velocity reconstruction.On the left: The measured DC transmitted power. On the right: the plot of t_{zero} as a function of index n. The error bars correspond to half of the oscilloscope's sampling time.

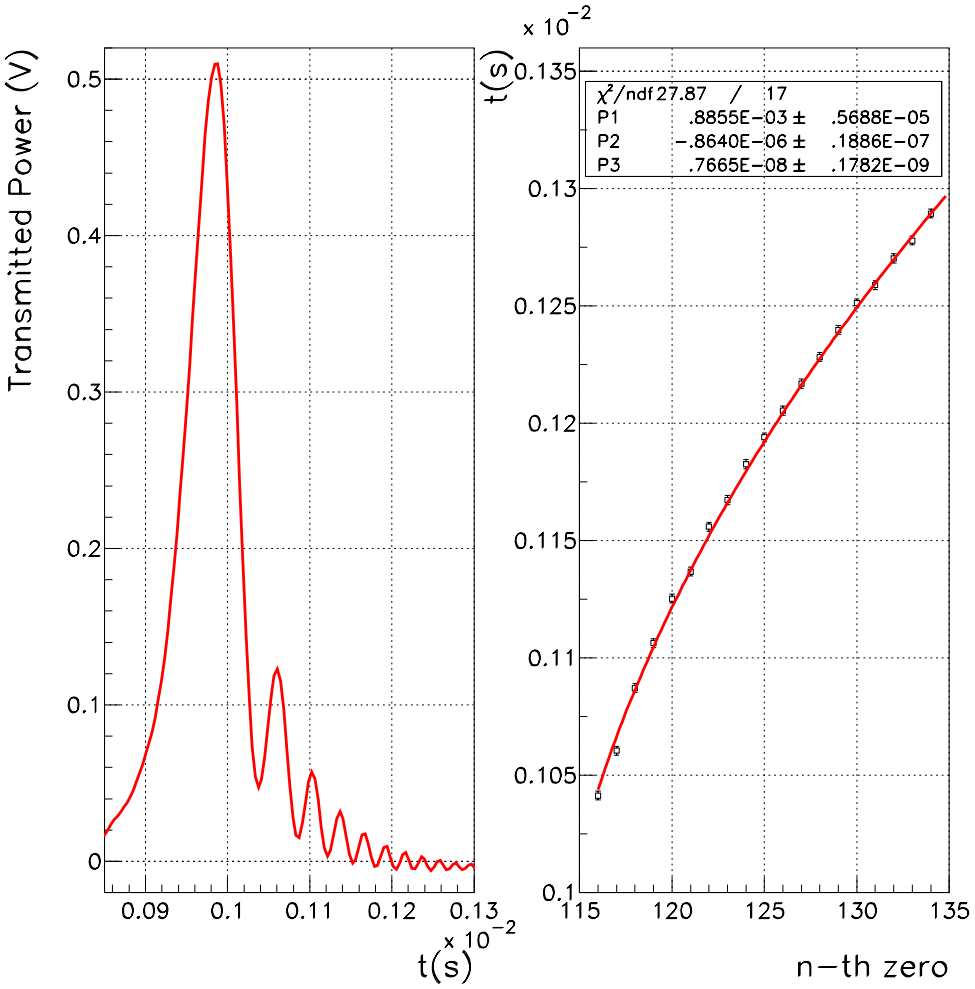

Figure 7.10: Fit results for the mirror relative velocity reconstruction.On the left: The measured DC transmitted power. On the right: the plot of t_{zero} as a function of index n. The error bars correspond to half of the oscilloscope's sampling time.

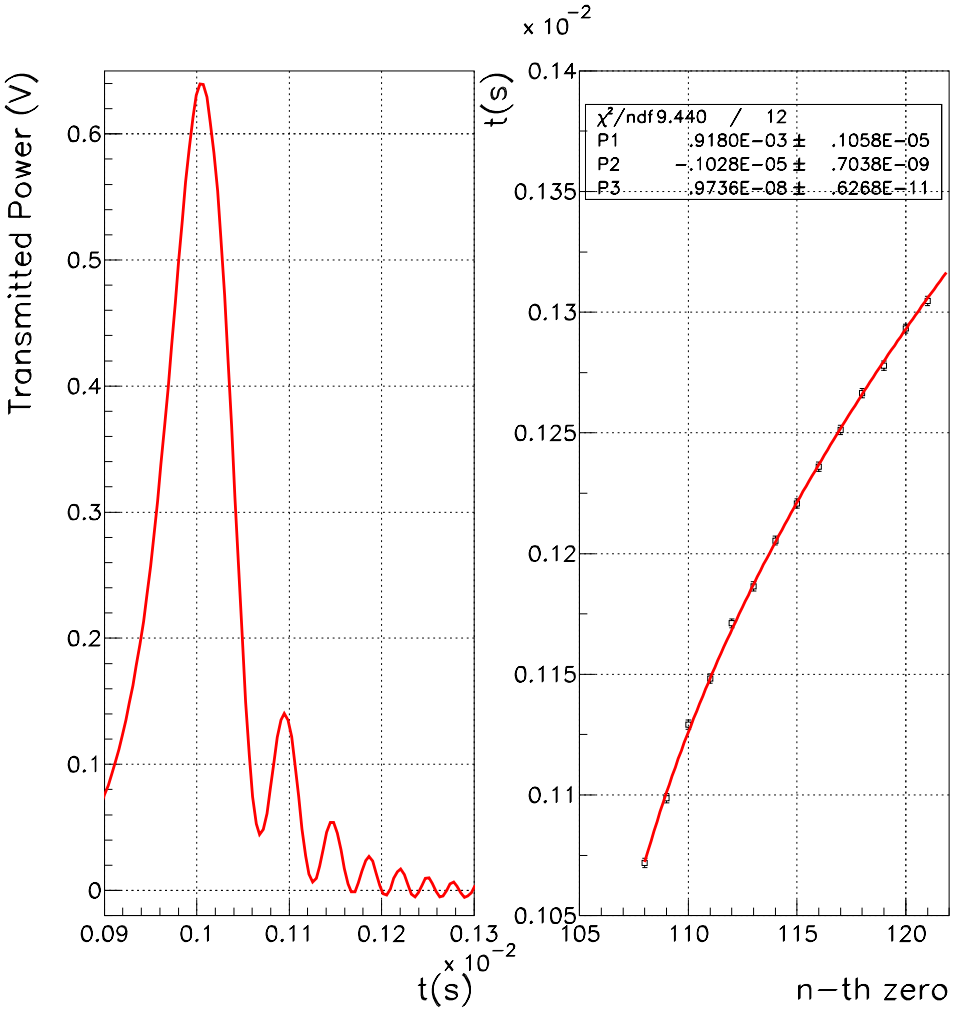

Figure 7.11: Fit results for the mirror relative velocity reconstruction.On the left: The measured DC transmitted power. On the right: the plot of t_{zero} as a function of index n. The error bars correspond to half of the oscilloscope's sampling time.

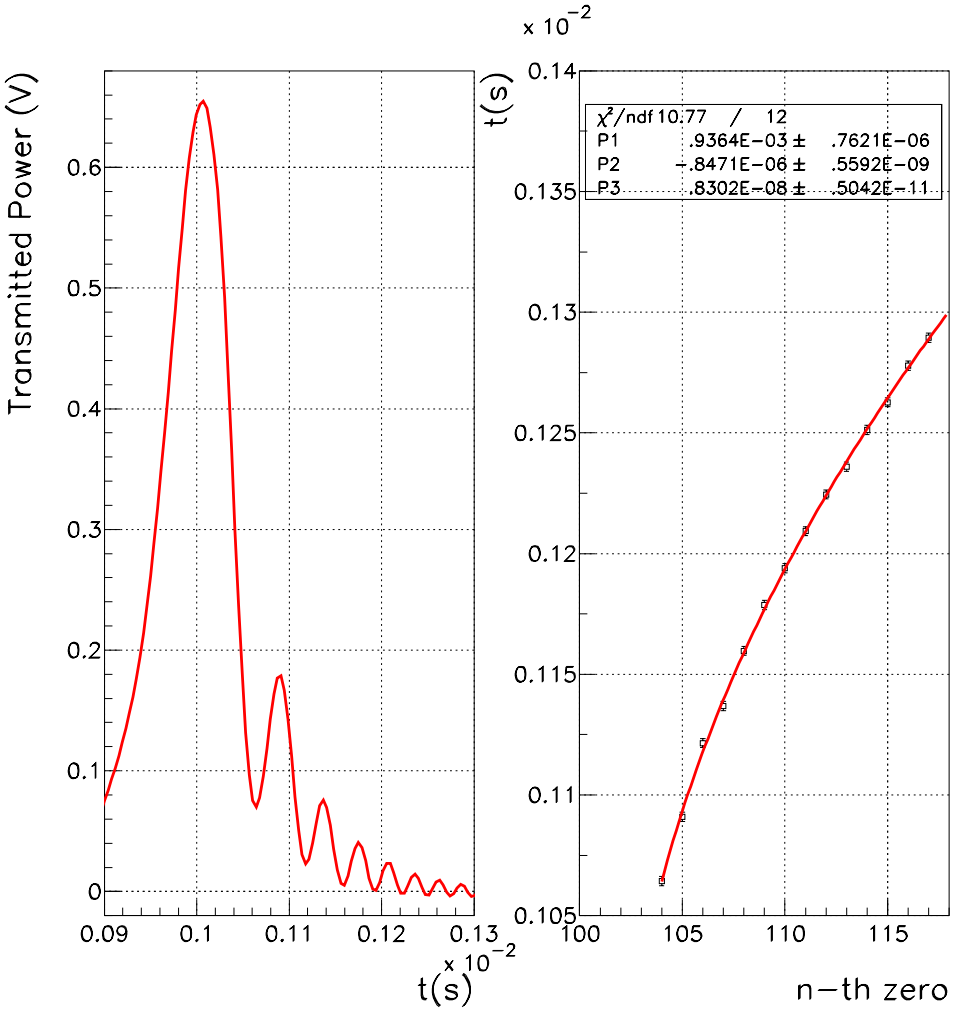

Figure 7.12: Fit results for the mirror relative velocity reconstruction.On the left: The measured DC transmitted power. On the right: the plot of t_{zero} as a function of index n. The error bars correspond to half of the oscilloscope's sampling time.

Chapter 8

Lock Acquisition Strategy

The study of the mode-cleaner prototype in ch.(6) allowed an understanding of the acquisition of lock process for the two polarization states. It has been shown how, given a spectral density displacement for the longitudinal motion of the mirrors, the acquisition time depends on

- the bandwidth of the control system;
- the finesse of the optical system.

Once these parameters are set, it is possible to estimate the acquisition time.

This chapter discusses this process for the CITF, and presents a non-linear lock acquisition strategy inspired from a work[59] developed within the LIGO collaboration. At first, the strategy is simulated by modeling a VIRGO Fabry-Perot. Then, once the scheme is presented, it is applied to the CITF case. The simulation results close the chapter.

8.1 Acquisition Time Estimate

As previously stated, the lock acquisition time depends on the bandwidth of the control system and the finesse of the optical system. However, in order to give an estimate of such a time period, it is also necessary to estimate the mirrors' relative velocity distribution and to observe how many resonance crossings, per unit time, have a velocity below a certain threshold.

For the CITF with mirrors in free motion, the displacement noise is concentrated below $3\,Hz$, as shown in the CITF sensitivity curve in fig.(5.3). Ideally, a control bandwidth of a few Hertz is desired. In this way, noise injection into the detection bandwidth is limited and the first violin mode excitation ($300\,Hz$) is avoided. A study[62] already exists on linear locking for the complete VIRGO interferometer with a $20\,Hz$ control bandwidth. For this reason, in this chapter we assume a linear locking bandwidth for the CITF also of $20\,Hz$. It is clear that for such a low bandwidth, the control system will necessarily have a slow reaction time.

Once the CITF is operated in dark fringe, the resonance FWHM for the recycling cavity is

$$\text{FWHM} = \frac{\lambda\,/\,2}{\mathcal{F}} \sim 10^{-3}\,\mu m \tag{8.1}$$

where $\mathcal{F} = 400$. Assuming a negligible contribution of the error signal outside of the linear region, the velocity threshold v_{thr} is

$$v_{\text{thr}} \sim 20\,Hz \times \text{FWHM} \sim 2 \times 10^{-2}\,[\mu m/s] \tag{8.2}$$

By referring to the mirror amplitude spectral density displacement model used for the simulations, shown in fig.(8.2), the mirror motion, in open-loop, has an RMS value of $A \simeq 1.6\,\mu m$ dominated

by a resonance at $f = 200\,Hz$. If we assume that the mirror displacement $x(t)$ is described by a simple sinusoidal model of the form

$$x(t) \;=\; A\,\sin(2\,\pi\,f\,t) \tag{8.3}$$

then the mean mirror velocity $\overline{v}_x$ is

$$\overline{v}_x \;=\; 2\,\pi\,f\,A \times \frac{1}{T}\int_0^T \;\mid \cos(2\,\pi\,f\,t)\mid\; dt = 4\,A\,f \sim 1.3\;[\mu m/s] \tag{8.4}$$

and the relative mirror velocity $\overline{v} = \sqrt{2}\,\overline{v}_x = 1.8\,\mu m/s$. The mean time $\overline{\Delta t}$ between each resonance crossing is

$$\overline{\Delta t} \;=\; \frac{\lambda\,/\,2}{\overline{v}} \;\sim\; 0.3\,s \tag{8.5}$$

In the sections to come, it will be shown that less than 0.1% of all crossings have a relative mirror velocity below the velocity threshold. This means an acquisition time $t_{\rm acq}$ no less than

$$t_{\rm acq} \;=\; \frac{\overline{\Delta t}}{0.1\%} \;\sim\; 300\,s \tag{8.6}$$

Acquisition times this long are not acceptable and a means of improvement is necessary.

There are three possibilities for the improvement of the acquisition time:

i. increase the linear range of the error signal;

ii. increase the bandwidth of the control system;

iii. decrease the mirror relative velocity.

This chapter presents a non-linear locking scheme for the improvement of the CITF acquisition time by damping the relative motion of the mirrors, thus facilitating the acquisition of control by the linear servo system. The goal of this chapter is to first present and simulate the scheme for a VIRGO Fabry-Perot and then extend it to the CITF.

8.2 The VIRGO Fabry-Perot Model

We here present the model, shown in fig.(8.1), used for the Fabry-Perot simulation[60]. In particular, the simulation

1. computed the mirror motion due to seismic noise, thermal noise and the possible presence of forces induced by the reference mass coils;

2. computed the optical response of the cavity;

3. treated the photodiode signals, filtering and sending them, if necessary, to the reference mass coils.

8.2.1 Mirror Dynamics and Control

The two mirrors M_1 and M_2, $3\,km$ apart, are suspended by identical superattenuators. By low-pass filtering white noise according to a power law of the form f^{-2}, seismic noise is simulated and filtered through the superattenuator transfer function. The noise contribution due to thermal excitation was simulated as well, even though it is negligible for the lock acquisition study. The amplitude spectral density displacement $\tilde{x}_{1,2}$ for both mirrors $M_{1,2}$ is shown in fig.(8.2), corresponding to an RMS value for the displacement of $1.6\mu m$ integrated down to $200\,mHz$. Having injected

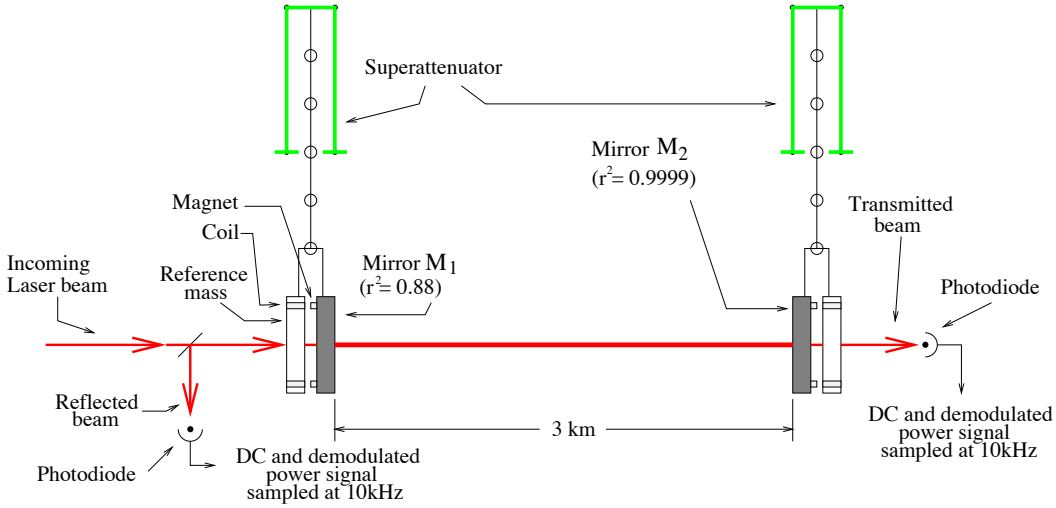

Figure 8.1: The model used for the Fabry-Perot non-linear locking scheme. The mirror amplitude spectral density displacement is shown in fig.(8.2).

uncorrelated noise, the RMS value for the cavity length fluctuations is $2.3\,\mu m$. Notice also that the thermal noise contribution has been added quadratically and contributes from about $3\,Hz$.

A system of coils and magnets allows position control of the mirror through a reference mass, as can be seen in fig.(8.1). The mirror displacement induced by the force applied from the reference mass is computed according to a transfer function that takes into account the mirror's mass, the quality factor $Q(10^6)$ and to the resonance frequency $(0.6\,Hz)$ of the pendulum system. It is assumed that no energy is injected in the superattenuator upper stages as the reference mass acts on the mirror.

8.2.2 The Optical Response and The Linear Control System

A phase-modulated (modulation frequency $\Omega/2\pi = 6.27\,MHz$) $10\,W$ laser beam (wavelength of laser light $\lambda = 1.064\,\mu m$) is injected into the optical system. Due to the plane-wave characteristics of the model used, the cavity is assumed to be aligned and matched to the incoming beam. In the optical configuration given, the mirror power reflectivities are $r_1^2 = 0.88$ and $r_2^2 = 0.9999$, corresponding to a finesse of $\mathcal{F} \simeq 50$. Since the photon storage time is about $\mathcal{F}\,L\,/\,c \sim 1\,ms$ and the foreseen relative mirror velocities are below $10\,\mu m/s$, no ringing effect is expected and the quasi-static approximation is used for the optical module of the simulation.

Two photodiodes monitor the reflected and transmitted beams. The only error measurement taken into account is the statistical fluctuations in the number of photons detected, the beams shot-noise. The signals coming from the photodiodes are digitized at a $10\,kHz$ sampling rate.

The error signal is the Pound-Drever error signal, using the demodulated component on reflection. Fig.(8.3) shows its dependence on the cavity length as it is swept over time at a constant velocity. Due to the low finesse of the system, the non-linear component contributes to the lock acquisition process.

Assuming a bandwidth for the linear control system of $20\,Hz$, the threshold velocity is $20\,Hz \cdot \mathrm{FWHM} \sim 0.2\,\mu m/s$ if we neglect the non-linear contribution of the error signal. However, the non-linear component does play a role, just as in the case of MC30 with $\mathcal{F} = 100$, and the threshold velocity must be higher. Long acquisition times are not expected for this system.

8.2.3 Lock Acquisition Strategy

An algorithm is here introduced to aid the linear control system acquire cavity lock. The algorithm consists of

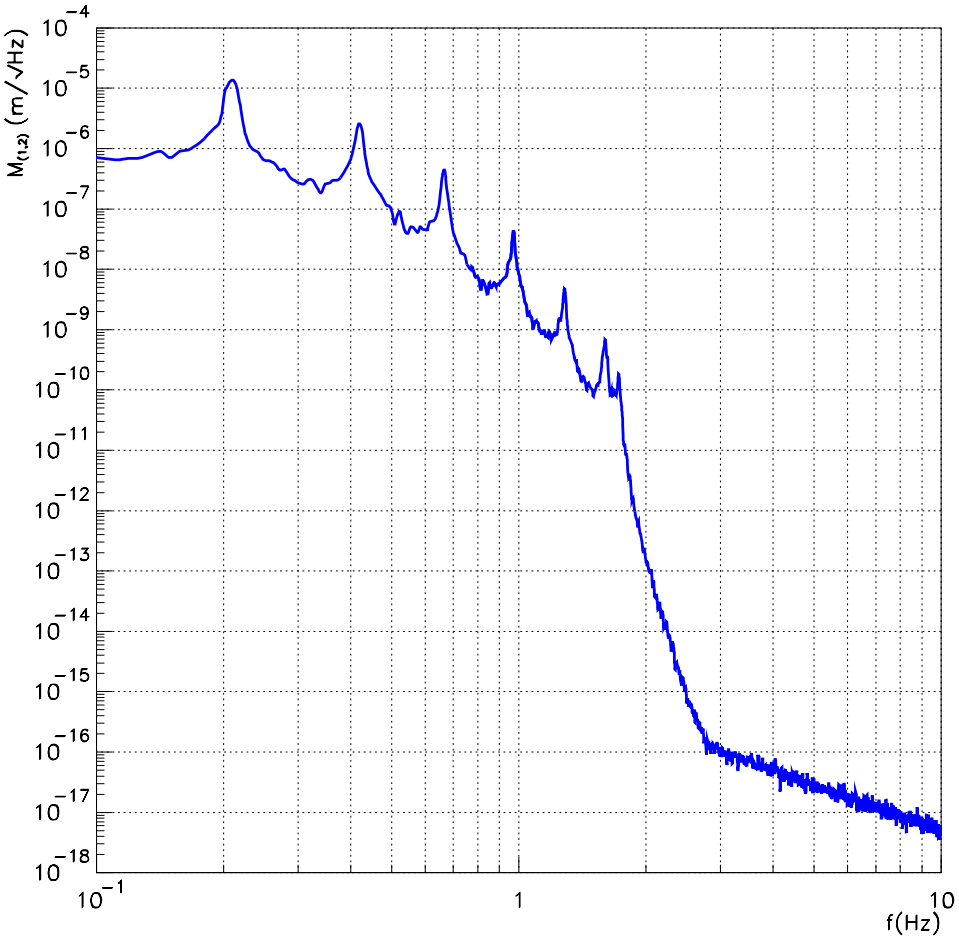

Figure 8.2: The simulated displacement amplitude spectral density for each mirror. The RMS cavity length displacement is $2.3\,\mu m$ dominated by the resonance at $200\,mHz$.

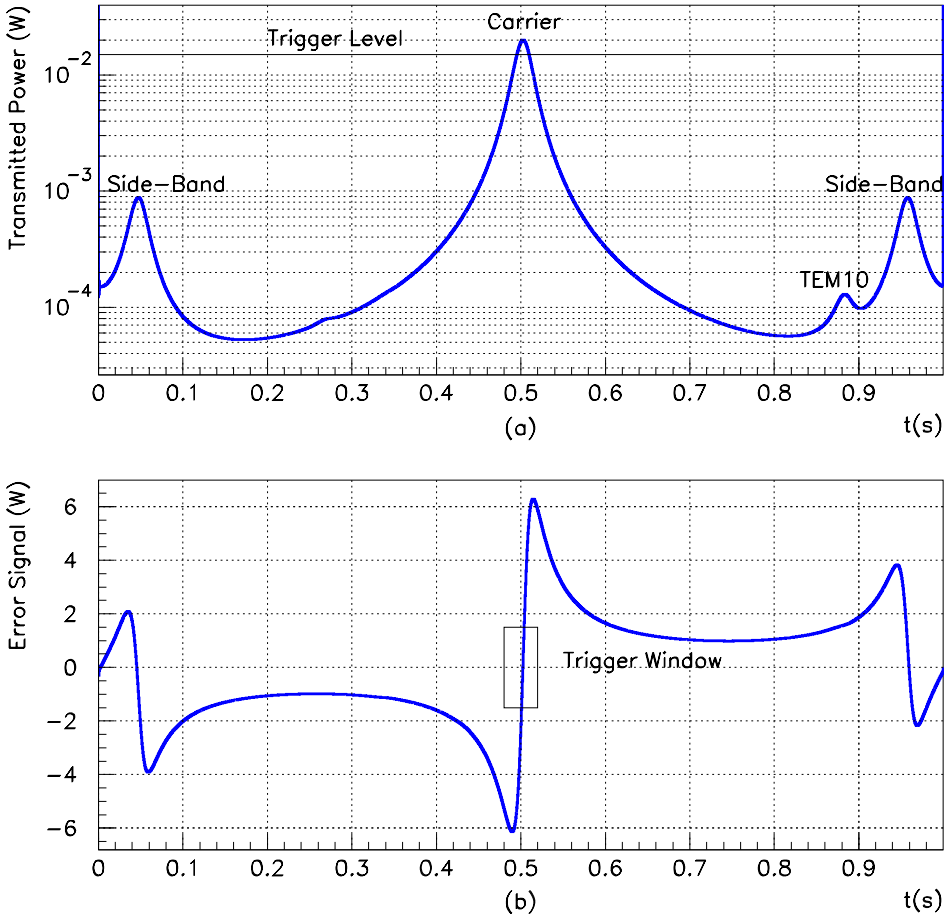

Figure 8.3: The simulated transmitted DC power and the Pound-Drever error signal for the VIRGO Fabry-Perot cavity. The trigger on transmission is set to the resonance half-maximum while the window on the error signal is opened for values below $1.5\,W$. The presence of a TEM_{10}, due to a slight misalignment, is also shown.

- an *analysis* procedure;
- an *acting* procedure.

The objective of the first procedure is to reconstruct the relative mirror velocity. The acting procedure then uses the reconstructed value to damp the relative mirror motion to within the velocity threshold. Once this is done, the linear control system is enabled.

8.2.4 The Analysis Procedure

In order to understand how fast the mirrors are moving with respect to each other, we must be able to monitor the linear region of the Pound-Drever error signal. This is possible only when the cavity length is within the FWHM of resonance and which is not frequent because the mirrors move freely and the full spectral range of the cavity is swept completely. One way to monitor just the linear region of the error signal is to recognize when a fundamental mode resonance is being crossed as the mirrors move in free motion. This is achieved by simply triggering the transmitted power at a particular value. Once the transmitted power is above a particular threshold, the cavity is about to resonate and the error signal can be used to determine the relative velocity. However, for this to be possible the power of both sidebands, as well as that of any high order transverse modes, must be below the threshold level.

Fig.(8.3a) shows the transmitted power as a function of time as the cavity length is swept. A trigger is set at the half-maximum level of the resonance. Once this trigger is satisfied, the cavity is within the resonance FWHM and the error signal can be monitored. Notice how the trigger level is higher than the power of resonating sidebands. The presence of a TEM_{10}, generated by a small misalignment, is also shown. Fig.(8.3b) shows the Pound-Drever error signal.

As the trigger placed on the transmitted power is satisfied, a window on the error signal opens and the values of the error signal are stored until the window closes. At this point, a least-square fit to a straight line reconstructs the velocity. In other words, by defining as y_i the value of the error signal at the sampled time t_i and considering a model of the form

$$y(t) \;=\; a \,+\, b\,t \tag{8.7}$$

then the merit function

$$\chi^2 \;=\; \sum_i \Big[\, y_i \,-\, (\,a \,+\, b\,t\,)\,\Big]^2 \tag{8.8}$$

gives a measure of how well the model fits the sampled data. By minimizing eq.(8.8) with respect to the parameters a and b, we obtain

$$\begin{aligned} a \;&=\; \frac{\sum_i t_i^2 \sum_i y_i \,-\, \sum_i t_i \sum_i t_i y_i}{N \sum_i t_i^2 \,-\, \Big(\sum_i t_i\Big)^2} \\ b \;&=\; \frac{N \sum_i t_i y_i \,-\, \sum_i t_i \sum_i y_i}{N \sum_i t_i^2 \,-\, \Big(\sum_i t_i\Big)^2} \end{aligned} \tag{8.9}$$

where N is the number of sample points within the window. The value of parameter b allows the estimate of the mirrors relative velocity.

Fig.(8.3b) shows an example of a window which opens on the error signal once the trigger on the transmitted power is enabled. In this figure, the window is set to $\pm 1.5\,W$.

We would like to remark that it is possible to reconstruct the velocity correctly only if we assume that it is constant within the time interval of the resonance crossing. Since the motion is mostly concentrated around $200\,mHz$, the relative velocity can be considered constant for time intervals much smaller than $1/200\,mHz = 5\,s$.

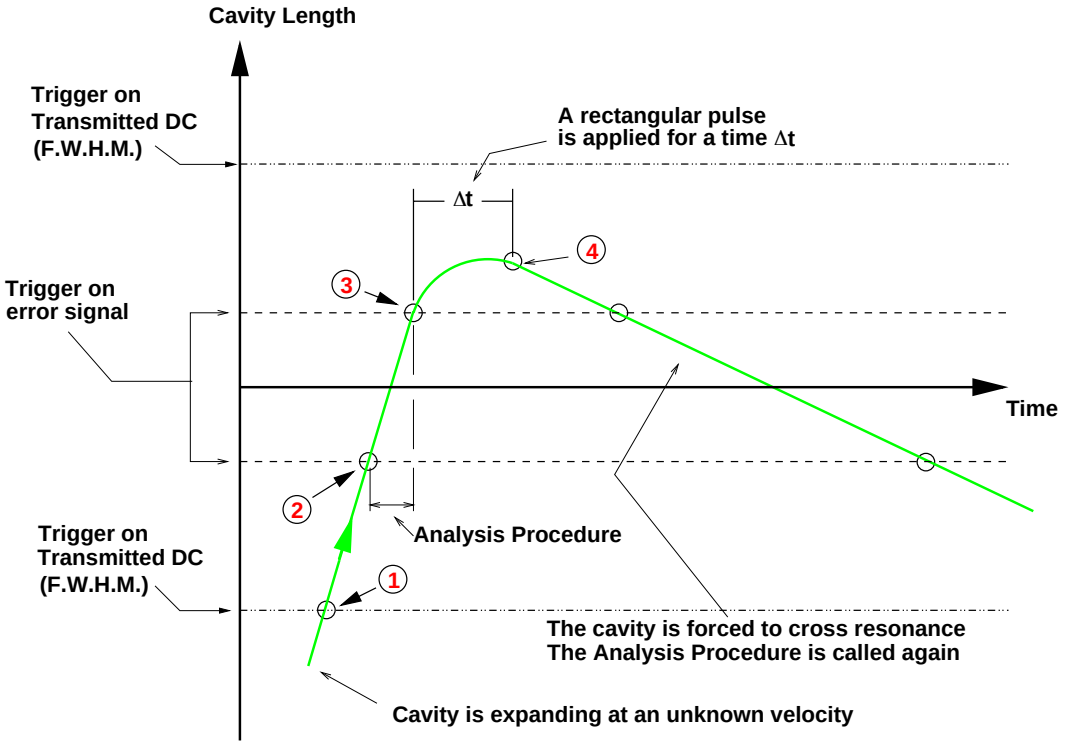

Figure 8.4: The effect of the application of a single pulse to a mirror. (1) The cavity is expanding at an unknown velocity and at this point the transmitted power is above threshold. (2) A window opens on the error signal and the analysis procedure begins. (3) The analysis procedure ends and the χ^2 minimization procedure determines the rate of expansion $\vec{v}$. The acting procedure begins and a pulse in current is sent to the reference mass coils. (4) The pulse ends here. The cavity is now expanding at the rate $-\varepsilon\vec{v}$ and it is forced to cross resonance again.

8.2.5 The Acting Procedure

Once the relative velocity is reconstructed, the algorithm has the option of enabling the linear feedback or not, according to the reconstructed value. If the reconstructed velocity is below the threshold value, the linear feedback is enabled. If not, a pulse of current is sent to the coils of the reference mass so as to damp the relative motion of the mirrors. If the analysis procedure reconstructed an expansion of the cavity at a rate $\vec{v}$, a rectangular pulse of amplitude $\vec{F}$ is sent for a time Δt with

$$\vec{F} = -\frac{m\,\vec{v}}{\Delta t}\,(1+\varepsilon) \tag{8.10}$$

where m is the mass of the mirror and ε is a parameter. The result of such a pulse application causes the relative velocity to change from $\vec{v} \rightarrow -\varepsilon\,\vec{v}$. As can be seen, the relative motion will be damped for values of $\varepsilon \in [0,1)$. Fig.(8.4) shows graphically the effect of the application of a single pulse.

In principle, any value of $\varepsilon \in [0,1)$ is suitable. Setting $\varepsilon = 0$ would momentarily stop the relative motion of the masses and the linear feedback could take over without a problem. However, this would imply a very good knowledge of the optical system, the reconstruction and the acting procedure as well. For this reason, we opted for an iterative application of pulses, i.e., an iterative analysis and acting procedure. The result is the periodic control of the optical system, damping the relative motion of the mirrors below the threshold value.

This iterative procedure cannot be applied for an infinite amount of time: after a few pulses,

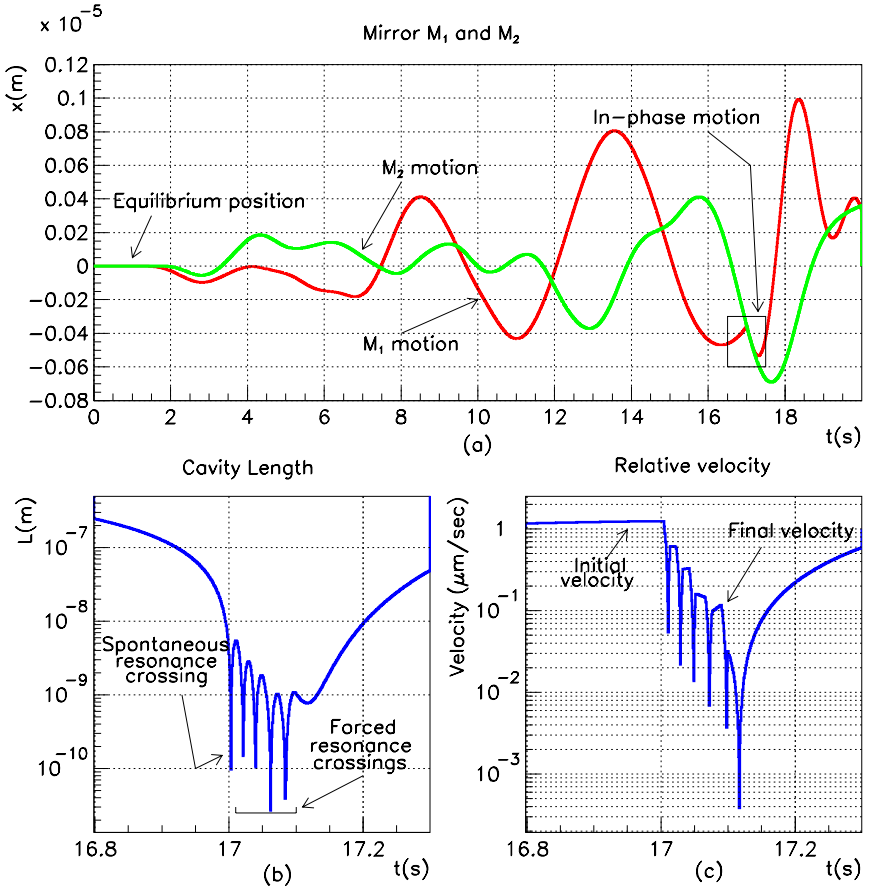

Figure 8.5: A brief simulation shows the effect of the algorithm with pulses sent to mirror M_1. In graph (a), the two mirror positions are shown as a function of time. At $t = 17\,s$, pulses are sent to mirror M_1 forcing it to move in phase with mirror M_2. Graph (b) shows the cavity length as a function of time around $t = 17\,s$ (recall that FWHM $= 10^{-8}\,m$). In graph (c), the relative velocity is plotted as a function of time. Notice how it is damped from the initial value of $1\,\mu m/s$ down to $0.1\,\mu m/s$.

the acceleration applied to the mirror is weak with respect to the seismic excitation and the cavity could fail to cross resonance again. As a consequence, the analysis procedure is not called and the train of pulses ends. The mirrors then begin to follow the motion caused by seismic noise.

Fig.(8.5) and fig.(8.6) show the results of the iterative application of the analysis and acting procedures (without enabling the linear feedback) as the relative motion is damped. It consists of a $t = 20\,s$ simulation run with $\varepsilon = 0.5$, Δt set to $10\,ms$ and the damping performed on mirror M_1. In fig.(8.5a), at $t = 0\,s$ the mirrors are at rest, and as time evolves they begin to acquire speed. The algorithm is triggered by the transmitted power at about $t = 17\,s$: the cavity is within the resonance FWHM. The window opens on the error signal, the relative velocity is reconstructed and a pulse is applied to M_1. The cavity is then forced to cross resonance again with half of its initial speed. Notice, from fig.(8.5a), how the algorithm forces the motion of M_1 to follow the motion of M_2, forcing it to be in-phase. Fig.(8.5b) shows both the spontaneous and forced resonance crossings: notice how the cavity remains within the FWHM $= 10^{-8}\,m$ of the optical resonance.

Fig.(8.5c) shows the initial and final velocity, where by final velocity we intend the last recon-

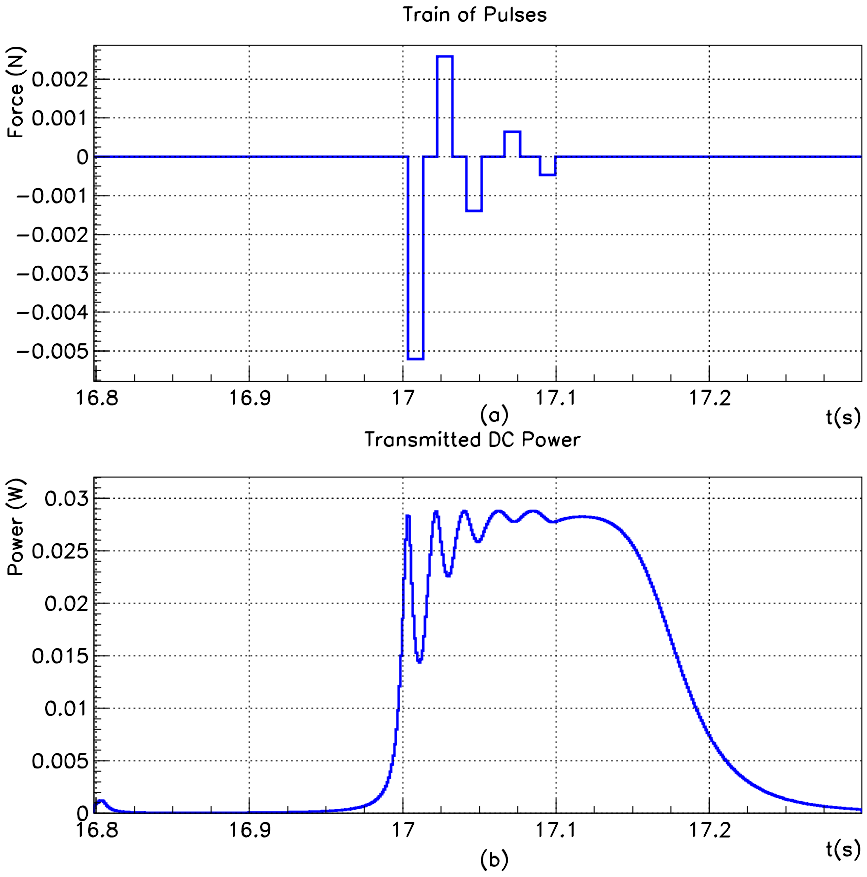

Figure 8.6: The train of pulses used by the non-linear locking algorithm and the resulting transmitted DC power.

structed velocity. In this case, the velocity attenuation is of a factor of ten, with the final velocity being below threshold: the linear feedback could be enabled. Fig.(8.6a) shows the pulses sent to mirror M_1. The forces used are of the order of $10\,mN$ and of duration $10\,ms$. Fig.(8.6b) shows the DC transmitted power as a function of time. The cavity is kept within the resonance FWHM, since the power is kept above the half-maximum value.

8.3 The CITF Locking Strategy

In this section we extend the algorithm presented for the VIRGO Fabry-Perot to the CITF[61]. Longer acquisition times, with respect to the Fabry-Perot, are expected and a means to guide the CITF into lock is necessary if a bandwidth of $20\,Hz$ for the linear control system is used. We first present the model used and then briefly recall the optical response of the CITF to longitudinal mirror motions already discussed in Ch.(5).

8.3.1 The Model for the CITF

Just as for the Fabry-Perot, the model shown in fig.(8.7a) is simulated in the time domain and it consists of three parts. The first generates the dynamical behavior of the mirrors caused by seismic noise and the possible presence of forces induced by the reference mass coils. The second deals with the optical response of the CITF, and the third treats the photodiode signals deriving from them, the error signals that are then filtered and applied, if necessary, to the reference mass coils.

The chosen displacement spectral density for the recycling mirror M_0, both end mirrors M_1 and M_2 as well as the beam-splitter M_{BS}, is shown in fig.(8.2), corresponding to an RMS displacement value, for each mirror, of $1.6\,\mu m$ at $200\,mHz$. Recalling that $\Delta l \equiv l_2 - l_1$ and $l_r \equiv l_0 + (1/2)(l_1 + l_2)$, we can define the velocity $v_{\Delta l}$ as

$$v_{\Delta l} \equiv \frac{d}{dt}\,\Delta l \tag{8.11}$$

and v_{l_r} as

$$v_{l_r} \equiv \frac{d}{dt}\,l_r \tag{8.12}$$

Fig.(8.8) shows the results of a free motion run. The distribution of the velocities $v_{\Delta l}$ and v_{l_r} is shown in fig.(8.8a) and fig.(8.8c). The velocity spectrum is wide, with speeds that range above $6\,\mu m/s$ with a mean velocity at about $1.8\,\mu m/s$. Fig.(8.8b) and fig.(8.8d) show the distribution of the time difference Δt between each dark fringe crossing and between each resonance crossing. About 75% of all crossings are found in a time Δt inferior to $0.5\,s$.

The parameters used in the model are slightly different from the one described in Ch.(5). In particular, the lengths used were set to $l_0 = 6.0\,m$, $l_1 = 6.2\,m$ and $l_2 = 5.8\,m$. The incoming laser power was $10\,W$, phase modulated at $\Omega/2\pi = c/2l_r$, with $J_1^2 \simeq 4\%$.

In order to apply the algorithm presented to the CITF, it is necessary to use signals for the control that depend mostly on either Δl or l_r. Sec.(5.6) showed that this is possible by taking the ratio of different photodiode signals. We here recall that the CITF can be seen as a Fabry-Perot cavity (see fig.(8.7)) of length l_r, whose end mirror transmittivity $\mathcal{T}(\Delta l)$ depends only on the dark fringe condition, regardless of the recycling resonance. It has been shown that this end mirror transmittivity can be obtained by taking the following ratio of signals:

$$\mid \mathcal{T}(\Delta l) \mid^2 = \frac{\mathrm{AR}}{2}\,\frac{d_1^{dc}}{d_5^{dc}} \tag{8.13}$$

where AR is the power reflectivity of the BS anti-reflective coating, d_5^{dc} is the DC power seen by photodiode 5 and d_1^{dc} is the DC power seen by photodiode 1. This ratio can be used to identify the interference condition regardless of the recycling power, as can be seen in fig.(5.9).

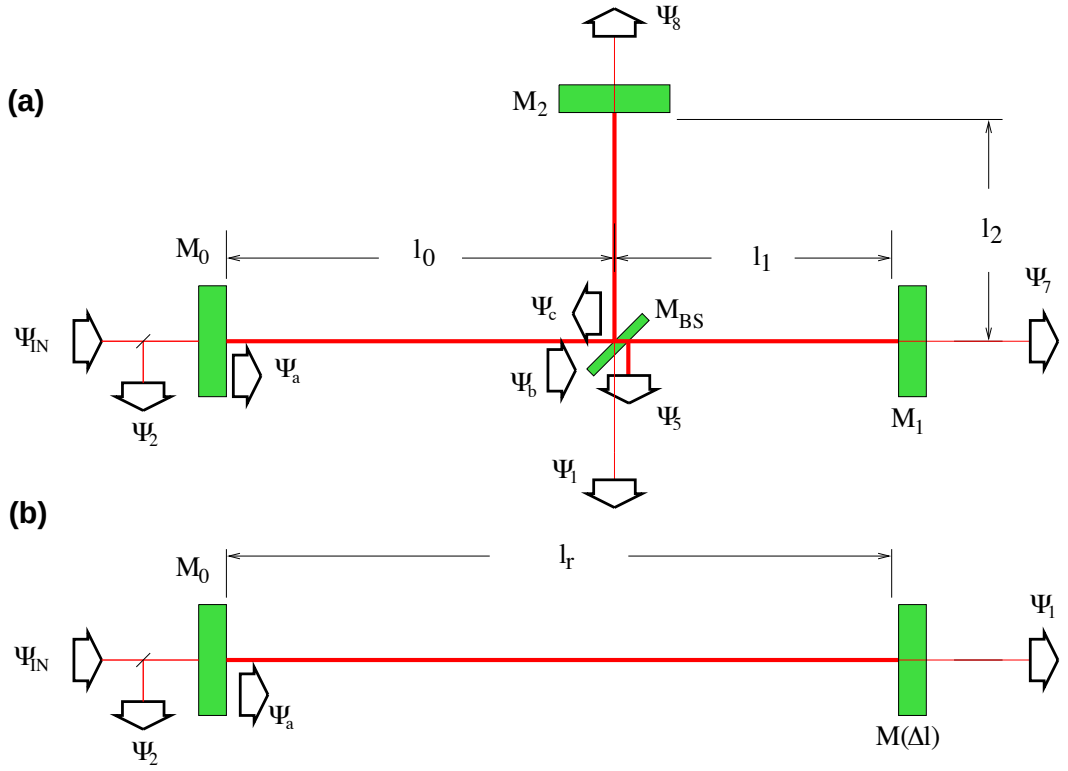

Figure 8.7: The CITF seen as a Fabry-Perot cavity.

Even though the ratio d_1^{dc}/d_5^{dc} can be used to identify dark fringe, it cannot be used for the control due to its quadratic dependence on Δl. On the other hand, the ratio d_1^{ph}/d_1^{dc}, shown in fig.(5.10), depends linearly on Δl and it can be used for its control regardless of the recycling condition.

Once dark fringe is controlled, we can estimate the acquisition times for the recycling cavity. Recall that the threshold relative velocity is $v_{\rm thr} = 2 \times 10^{-2}\,\mu m/s$. From the distribution of velocity, shown in fig.(8.8c), the threshold is well below the mean value of $\overline{v} = 1.8\,\mu m/s$. Only $0.07\,\%$ of all events have $v_{l_r} < 0.02\,\mu m/s$. Again, by considering all crossings separated by the mean time $\Delta t = 0.3\,s$, we can estimate the time required for lock acquisition as the average time between two events with velocity below threshold, or $0.3\,s/\,7 \times 10^{-4} \simeq 400\,s$.

8.3.2 Lock Acquisition Strategy

The overall strategy is simple and straightforward. By monitoring the two ratios $d_1^{dc}\,/\,d_5^{dc}$ and $d_1^{ph}\,/d_1^{dc}$, the analysis procedure reconstructs $v_{\Delta l}$. The acting procedure is then enabled, sending pulses to one end mirror so as to damp the relative motion of the two end mirrors and enable the linear feedback, when appropriate. Once acquisition of control for the dark fringe succeeds, locking of the recycling cavity is addressed by acting on the recycling mirror.

Dark Fringe analysis procedure

As already stated, the decoupling of signals makes it possible to find $v_{\Delta l}$. The first step consists in monitoring Δl and this is done by introducing a trigger on $d_1^{dc}\,/\,d_5^{dc}$, which for the simulations was set to 6×10^{-3} (here $AR = 1$ for simplicity). Once the trigger is satisfied, the system is about to go into dark fringe. The purpose of such a trigger is to enable a second one monitoring the error signal $d_1^{ph}\,/d_1^{dc}$. This second trigger, enabled for absolute values of $\mid d_1^{ph}\,/d_1^{dc}\mid \leq\ 1.0$,

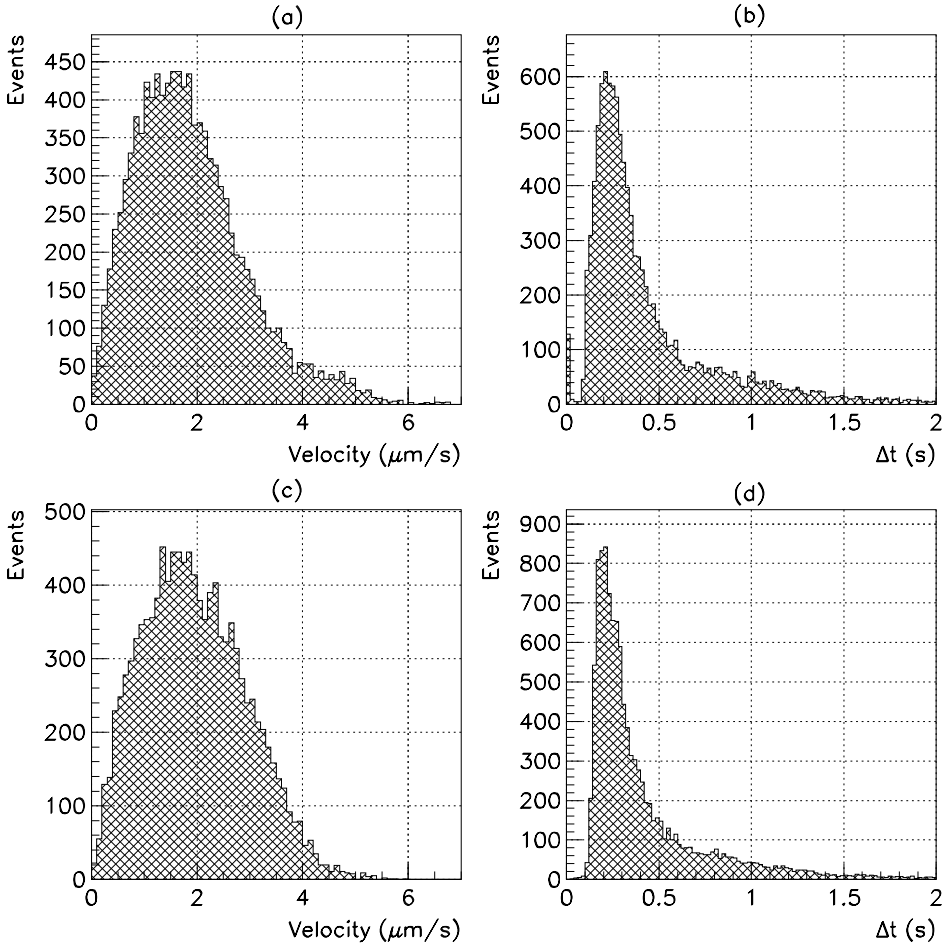

Figure 8.8: The velocities $v_{\Delta l}$ and v_{l_r} and the time distribution Δt for the CITF mirrors in free motion, as the system enters dark fringe and maximum recycling for the CITF. Graph (a) shows the $v_{\Delta l}$ distribution as the CITF enters dark fringe while graph (b) shows the time distribution Δt between dark fringe crossings. Graph (c) shows the v_{l_r} distribution as the CITF enters maximum power recycling while graph (d) shows the time distribution Δt between condition of maximum power recycling.

opens a window on the signal that now exhibits linearity. Sampled points are stored and a χ^2 minimization procedure reconstructs $v_{\Delta l}$.

Assuming that the mirror relative motion evolves at constant velocity, the analysis procedure reconstructs the relative speed correctly. This is a valid assumption due to the concentration of the motion in the sub Hertz region. The relative acceleration can often be considered insignificant for observation times inferior to the time scale of the accelerations, which is of the order of the second considering a dominant resonance at $200\,mHz$. Therefore, once the triggers are enabled, it is most likely that $v_{\Delta l}$ remains constant for time scales inferior to the second.

Fig.(8.9) shows the results of the reconstruction of $v_{\Delta l}$ as the four mirrors are left to move freely. During the simulation run, every time the two triggers are enabled, the algorithm reconstructs the velocity $v_{\rm recon}$ and compares it to the true value $\overline{v}_{\rm true}$. The top graph of fig.(8.9) plots the relative error

$$error = \frac{\overline{v}_{\rm true} - v_{\rm recon}}{\overline{v}_{\rm true}} \tag{8.14}$$

as a function of $\overline{v}_{\rm true}$, where $\overline{v}_{\rm true}$ is the mean value of $v_{\Delta l}$ taken over the time the window is kept open on the error signal. This procedure is able to make a reconstruction with errors below the 2% band. We can observe that as the relative mirror velocity increases, the number of sampled points in the window decreases, causing the reconstruction error to increase as well.

Another characteristic of the top graph of fig.(8.9) is the line structures present. The error signal is only to first approximation linear; a small non-linear component is also present. As a consequence, as the window on the error signal is opened, a fixed number of points can distribute themselves in different ways, giving rise to different results and generating these line structures.

The reader can also observe the presence of scattered events with errors well above 2%. These events correspond to a power build-up inside the recycling. As the power increases, the error signal changes as well: this can be seen from the plot shown in fig.(5.10). One way to improve the reconstruction is to consider events for which the value of the stored power is either above or below a certain value. Since the crossings of both dark fringe as well as recycling resonance are uncommon, we only considered events with d_5^{dc} below a threshold. For fig.(5.10), by considering only the dark fringe crossings with $d_5^{dc} < 5\,W$, 5% of all the events are discarded and the reconstructed procedure improves, as can be seen in the bottom graph of fig.(8.9).

Fig.(8.9) also shows how well the analysis procedure reconstructs the velocity by comparing the mean true velocity with the reconstructed value. It is also useful to compare the reconstructed value with the $v_{\rm true}$ value at the moment the χ^2 procedure ends. The acting procedure will use the reconstructed value to determine the pulse amplitude, and for this reason it is helpful to know by how much the reconstructed value is off the instantaneous value. Fig.(8.10) shows the result of the error

$$error = \frac{v_{\rm true} - v_{\rm recon}}{v_{\rm true}} \tag{8.15}$$

plotted as a function of $v_{\rm true}$, neglecting all the events with $d_5^{dc} < 5\,W$. As expected, for low velocities the reconstruction error is greater with respect to the case where $\overline{v}_{\rm true}$ was used. This can be explained by the fact that the χ^2 procedure gives an estimate of the mean velocity. The difference between the final velocity and the mean value increases as the velocity decreases.

Signal digitization

Both fig.(8.9) and fig.(8.10) show how the analysis procedure reconstructs the velocity. However, they do not take into account the signal digitization process performed by the ADCs. The phases of the acquisition of lock and the linear lock regime differ: in the linear regime, the photodiode signals do not change much from the values

$$\begin{aligned} d_1^{dc} &\simeq 1\,W \\ d_5^{dc} &\simeq 1300\,W \qquad (\mathrm{AR} = 1) \\ \mid d_1^{ph} \mid &\leq 7\,W \end{aligned} \tag{8.16}$$

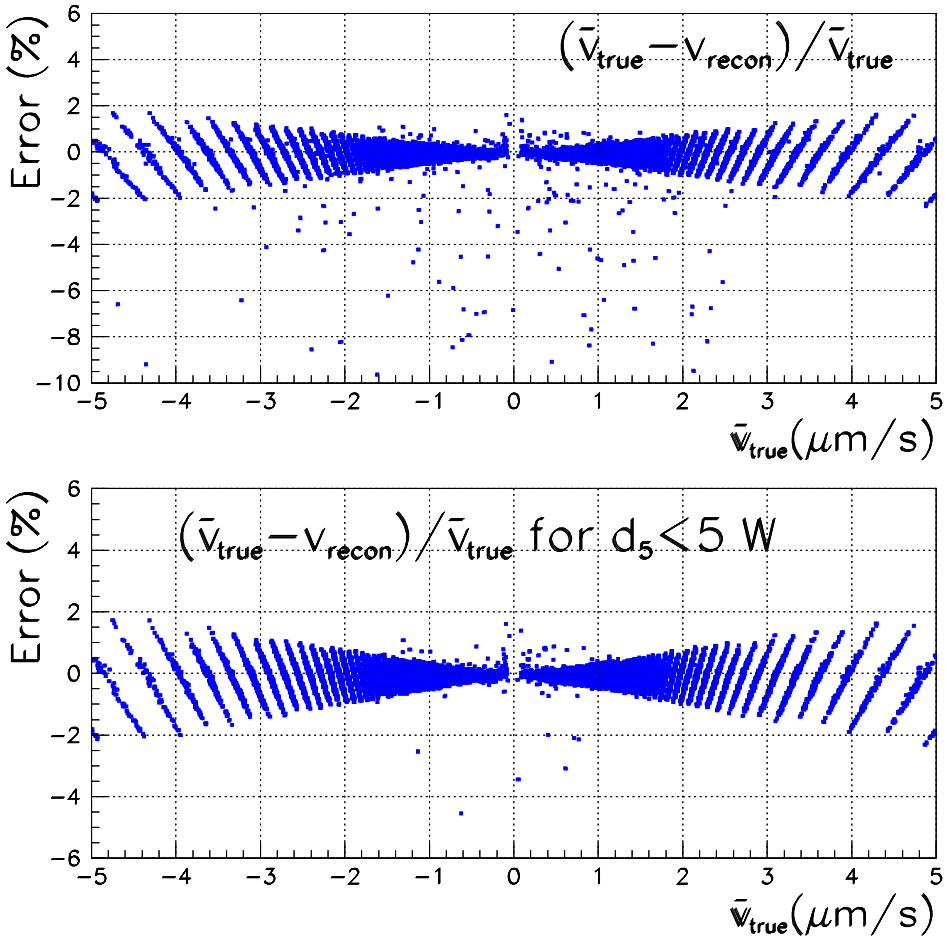

Figure 8.9: The error for the reconstruction of $v_{\Delta l}$. In top graph, $(\overline{v}_{\rm true} - v_{\rm recon})/\overline{v}_{\rm true}$ is plotted as a function of $v_{\rm true}$, where $\overline{v}_{\rm true}$ is the mean velocity value taken over the time the window on the error signal is open. The bottom graph shows again $(\overline{v}_{\rm true} - v_{\rm recon})/\overline{v}_{\rm true}$ as a function of $\overline{v}_{\rm true}$ but only the reconstructed events with $d_5^{dc} < 5\,W$ are considered.

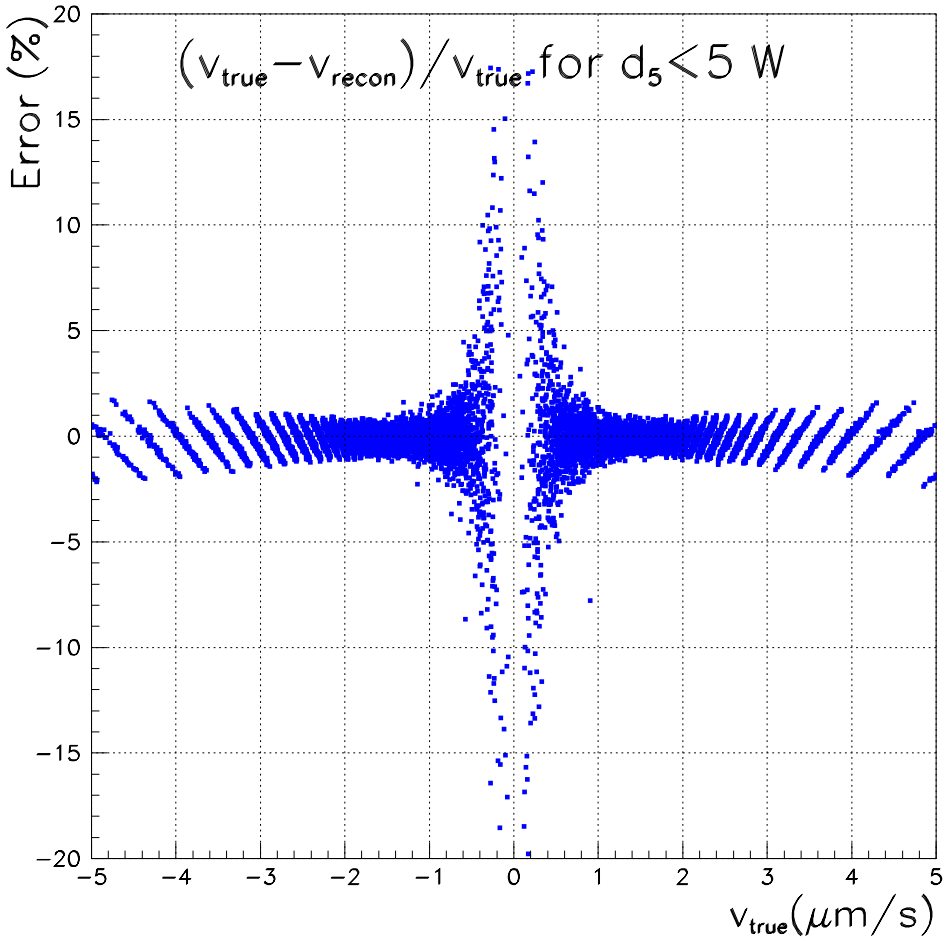

Figure 8.10: The error for the reconstruction of $v_{\Delta l}$. The error $(v_{\rm true} - v_{\rm recon})/v_{\rm true}$ is plotted as a function of $v_{\rm true}$, where $v_{\rm true}$ is the velocity at the time the χ^2 procedure ends. Only the reconstructed events with $d_5^{dc} < 5\,W$ are considered.

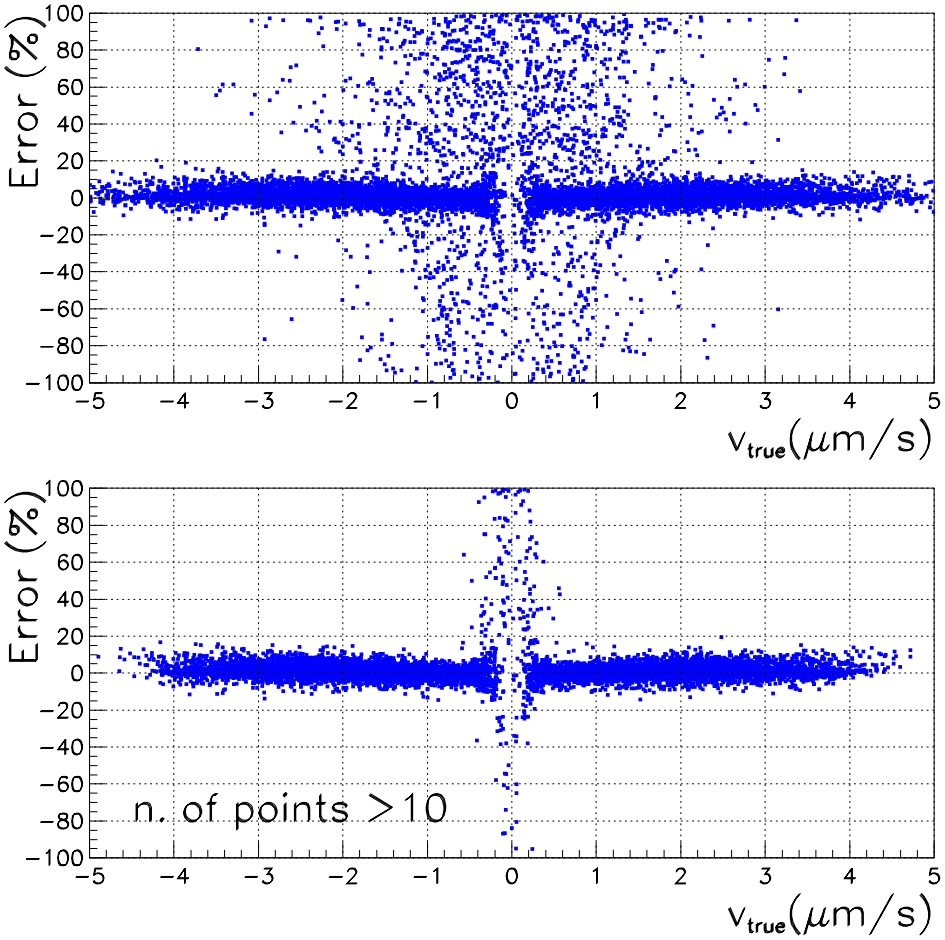

Figure 8.11: The error for the reconstruction of $v_{\Delta l}$ with the use of 16 bit ADCs. The error $(v_{\rm true} - v_{\rm recon})/v_{\rm true}$ is plotted as a function of $v_{\rm true}$. Only reconstructed events with a number of sampled points $N > 10$ are considered.

and the ADCs are adapted so as to operate for these values. On the other hand, in the lock acquisition phase, the value of the photodiode signals can change by as much as 5 orders of magnitude, as is shown in fig.(5.9) and fig.(5.10). In particular, we observe that these values are in the ranges

$$\begin{aligned} d_1^{dc} &\in [\,2\times 10^{-4} \div 10\,]\,W \\ d_5^{dc} &\in [\,2\times 10^{-2} \div 1300\,]\,W \quad (\mathrm{AR}=1) \\ |\,d_1^{ph}\,| &\in [\,10^{-3} \div 7\,]\,W \end{aligned} \tag{8.17}$$

In this case, the ADC *dynamic* may not be high enough to allow the observation, with precision, of the full excursion of signals, from their lowest to their highest value. In the acquisition of lock phase, d_1^{dc} and d_5^{dc} will often have low values, therefore by amplifying them we improve the precision in this phase.

Assuming a $n = 16$ bit ADC sampling photodiode signal d, then the digitized signal y can be

written as

$$y = A \cdot d \cdot \frac{2^n}{r} + x \tag{8.18}$$

where A is an amplification, r is the ADC range and x is a random variable simulating the ADC noise. By setting the range to $r = 10\,V$ and assuming a noise of $x = 1\,count$ RMS, then fig.(8.11) shows the reconstruction results with $A = 100$ for d_1^{dc}, $A = 1$ for d_5^{dc} and $A = 100$ for d_1^{ph}. From the top graph of the figure, we notice that there are many events with large reconstruction errors. By considering reconstructions with more than 10 sampling points, about 30% of all the events are discarded but the error is limited to within 20%, to be compared with the value of about $\pm 3\%$ relative to the case without ADCs (fig.(8.10)).

Dark Fringe acting procedure

Just as for the VIRGO Fabry-Perot, the procedure consists of an iteration between velocity reconstruction and pulse application. Once the reconstructed velocity is below threshold, the linear feedback is enabled.

Stored Power

The monitoring of the recycling resonance begins once dark fringe is locked. A trigger monitoring one of the two transmitted beams, set to $60\,mW$, enables the analysis procedure by using d_2^{qu}. Just as for dark fringe, the acting procedure sends pulses to M_0 so as to damp its motion with respect to the free end mirror and the linear feedback is enabled when appropriate.

8.3.3 Results

Fig.(8.12 - 8.14) show the results of one $150\,s$ simulation run with $\varepsilon_{\Delta l} = 0.5$, $\varepsilon_{l_r} = 0.5$ and a pulse width $\Delta t = 10\,ms$. The algorithm uses the ADC signals, described in the previous section, to reconstruct the velocities whereas the linear feedback reads the photodiode error signals directly. The algorithm was enabled at $t = 122\,s$ and stood by for the first dark fringe crossing. At $t \simeq 122.25\,s$, dark fringe was crossed and a train of pulses was sent to M_1 as shown in the top graph of fig.(8.12). The effect of these pulses is shown in the middle and bottom graph of the figure, where Δl and $v_{\Delta l}$ are plotted as a function of time. Once the velocity was damped, the dark fringe linear feedback was enabled on M_2. Less than a second was taken for the control.

Once the feedback of dark fringe was on, the monitoring of the recycling began. A resonance was crossed at $t \simeq 122.55\,s$, and from the top graph of fig.(8.13) the reader can observe that 4 pulses were sent to M_0 before the linear servo was enabled. The middle graph plots l_r as a function of time whereas the bottom graph its velocity v_{l_r}. Again, less than a second was taken to achieve control. The plots of d_1^{dc} and d_7^{dc} as a function of time are shown in the top and bottom graphs of fig.(8.14). In total, about $0.6\,s$ were necessary to guide the CITF into lock.

In a set of 6 simulation runs, where in each the algorithm was enabled at arbitrary times, the non-linear control system failed to guide the CITF into lock only once. In other words, the feedbacks were enabled but no lock was achieved. The remaining 5 runs gave a mean time of lock acquisition of the order of one second.

8.4 Conclusion

A simple method to guide the CITF into lock was here presented and simulated. By monitoring the digitized signals from photodiodes 1, 5 and 2, it was possible to reconstruct the time evolution of Δl and l_r. Once the reconstruction succeeded, an iterative application of reconstruction and pulse application damped the mirrors' relative motion, facilitating the acquisition of control by the linear feedback. An improvement of acquisition times of more than one order of magnitude was observed with respect to relying solely on the linear feedback.

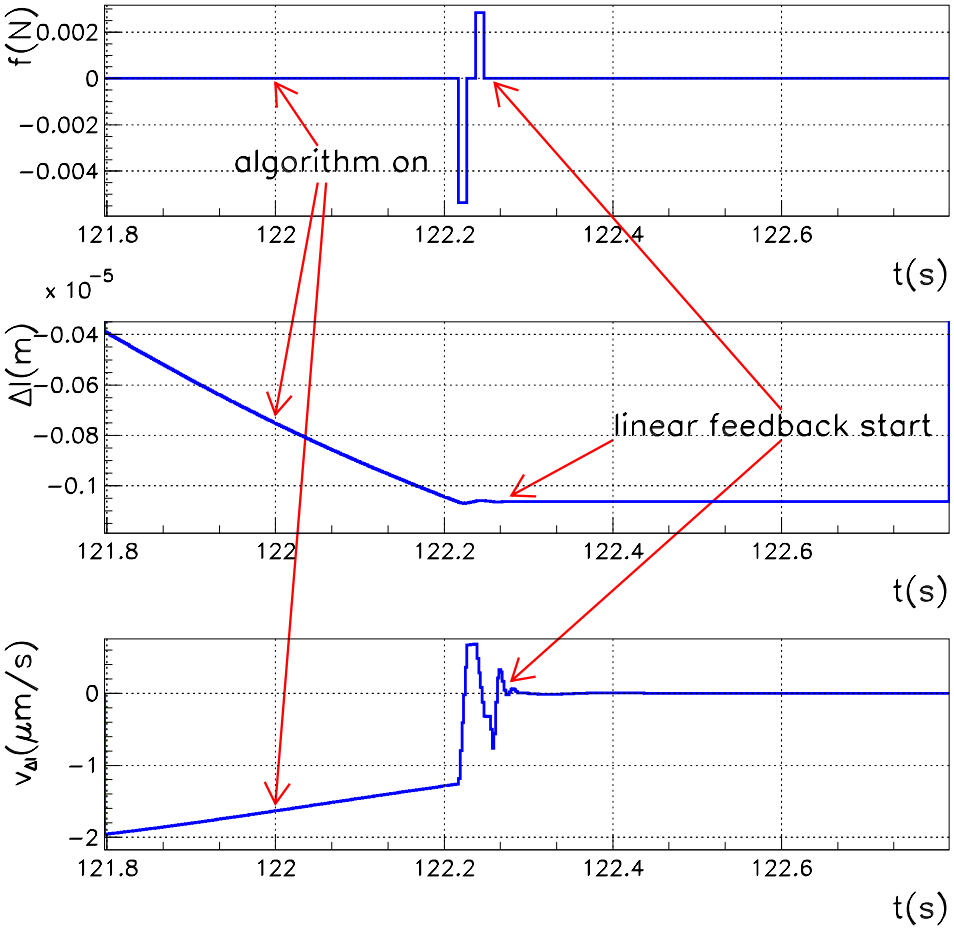

Figure 8.12: Results from a simulation run. The algorithm was enabled at $t = 122\,s$. Top graph: the forces sent to mirror M_1 as a function of time. Middle graph: Δl as a function of time. Bottom graph: $v_{\Delta l}$ as a function of time. In this case, about $0.3\,s$ were necessary for the control.

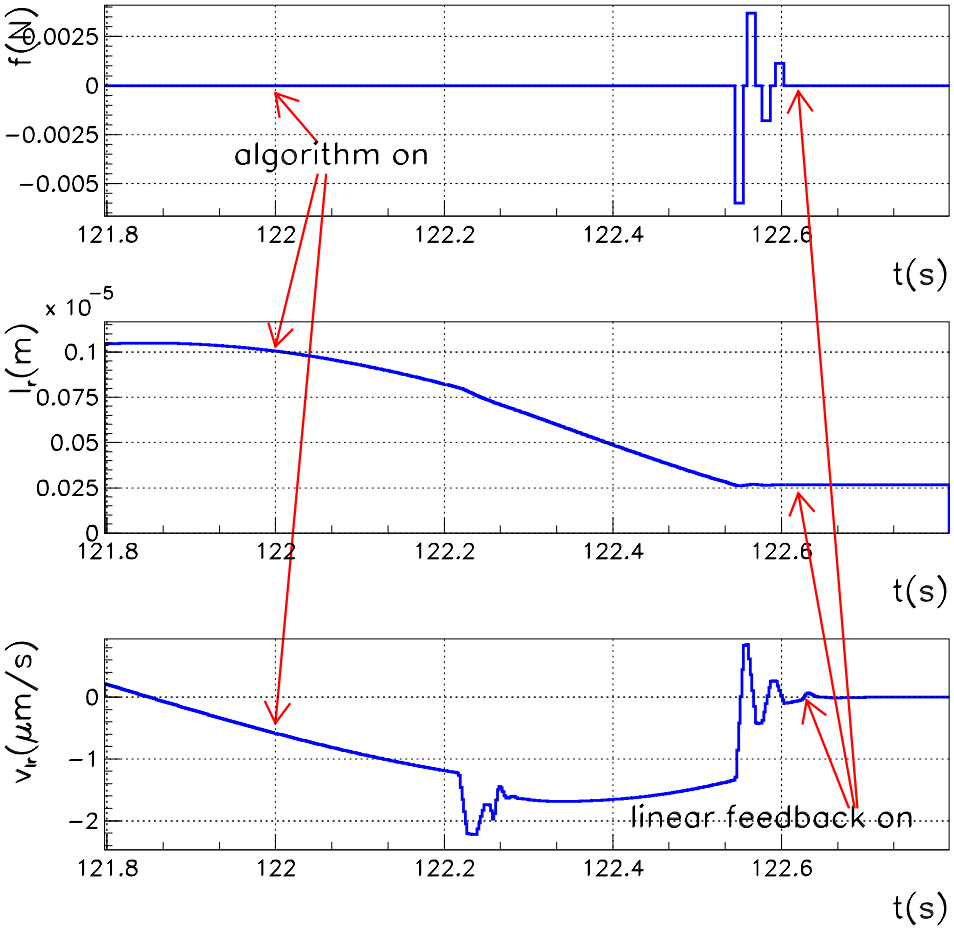

Figure 8.13: Results from a simulation run. The algorithm was enabled at $t = 122\,s$. Top graph: the forces sent to mirror M_0 as a function of time. Middle graph: l_r as a function of time. Bottom graph: v_{l_r} as a function of time. Less than one second was necessary for the algorithm to acquire complete control of the CITF.

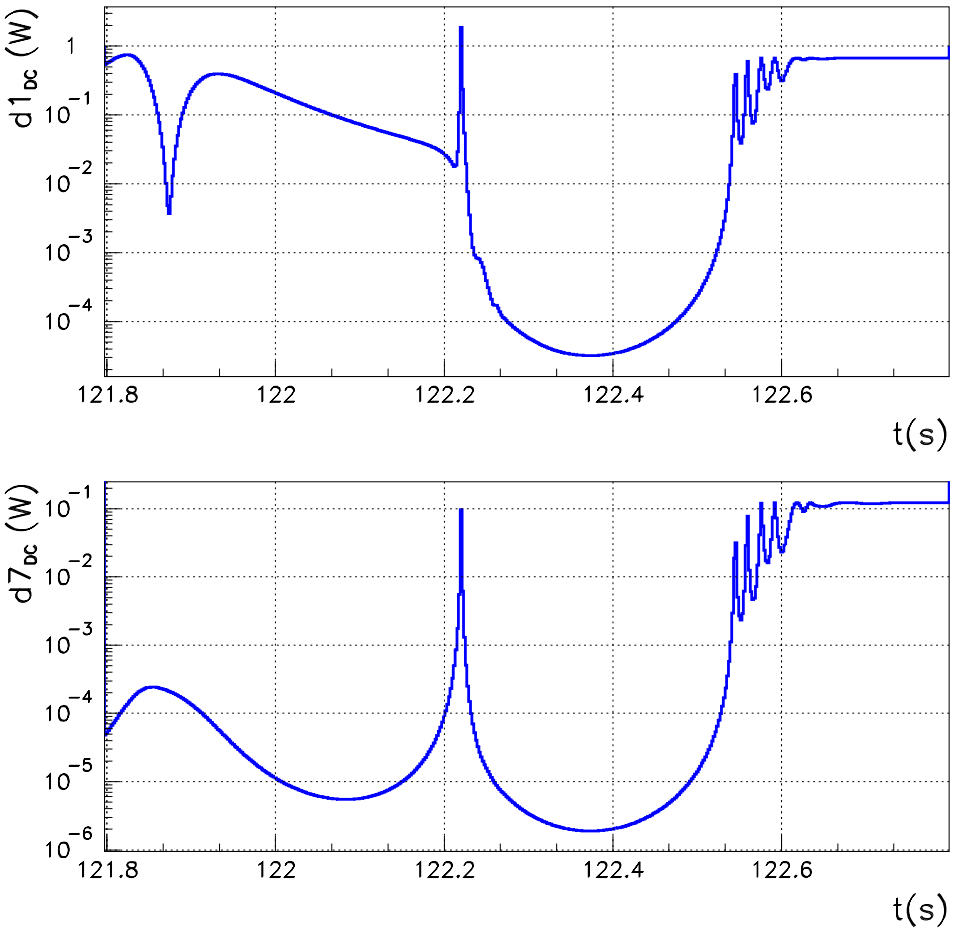

Figure 8.14: Results from a simulation run. The algorithm was enabled at $t = 122\,s$. Top graph: d_1^{dc} as a function of time. Bottom graph: d_7^{dc} as a function of time. Control of the CITF is achieved at about $122.6\,s$

Conclusion

This thesis presented a simulation study for the control of the CITF that focused on the problem of autoalignment and lock acquisition.

The first step in the problem-solving approach consisted in the study of the CITF optical response to

- longitudinal mirror displacements, with particular attention to the non-linear regime;
- angular mirror displacements once the CITF is in the locked regime.

It was shown, both analytically and numerically, how the ratio of photodiode signals can be used for the reconstruction of the microscopic arm length difference Δl and of its time derivative $v_{\Delta l}$ once all mirrors move freely. By numerically simulating the mirrors' free motion and the CITF optical response, we were able to observe the performance of the reconstruction procedure with and without the digitization process introduced by ADCs with errors within a few percent for the former, and below 20% for the latter.

The study on the optical response also showed that the longitudinal modulation frequency $\Omega/2\pi = c/2l_r$ can be used for the CITF alignment if an arm asymmetry is present. We were able to set up a routine, based on a χ^2 minimization procedure, capable of reading the error signals from quadrant photodiodes and reconstructing the mirrors' misalignments. By simulating the angular mirror motions and the CITF optical response, we were able to reconstruct each mirror misalignment using the error signals of 8 quadrant photodiodes.

The angular reconstruction scheme was then implemented in a control system for the CITF. It was shown that only the marionetta can be used. Furthermore, the piloting of the mirror from the steering filter requires a very good knowledge of the transfer function in question if the bandwidth of the system is to be limited to within some tens of Hz. By assuming a good knowledge of this transfer function, a filter has been designed for the autoalignment capable of attenuating the angular fluctuations down to the $10^{-9} rad$ RMS as required by the coupling laser jitter/misalignment.

The mode-cleaner prototype MC30 was introduced in order to comprehend the process of lock acquisition by a linear control system. The rotation of the laser beam polarization state allowed the study of this process for two different finesse values: $\mathcal{F} \simeq 100$ and $\mathcal{F} \simeq 1600$. We concluded that, for a given spectral amplitude displacement noise, the lock acquisition times depend on

- the finesse $\mathcal{F}$;
- the bandwidth of the linear control system.

In particular, it was shown how, for $\mathcal{F} \simeq 100$ and for a control bandwidth $B = 100\,Hz$, the non-linear components of the Pound-Drever error signal played a positive role in the process and short acquisition times were observed in both simulation and measurement. The case with $\mathcal{F} \simeq 1600$ and the same control bandwidth of $B = 100\,Hz$ was also studied. As expected, longer acquisition times were observed, both in simulation and in experiment, due to negligible non-linear components of the error signal. In this case, we defined a threshold velocity below which acquisition of lock is possible.

During the study of the MC30 prototype with $\mathcal{F} \simeq 1600$, a phenomenon was observed on the transmitted DC power, referred to as the ringing effect. This effect was here studied and simulated. The simulation outputs allowed us to fit measurements and estimate from them the cavity finesse as well as the mirrors' relative velocity during the resonance crossing. It was also observed how the position of the oscillations' minima and maxima depend, to first approximation, on the cavity expansion and not on the finesse value. An empirical formula was then presented capable of determining the relative velocity from the positions of the oscillations' minima and maxima. This chapter's results may be useful for a possible acquisition of lock algorithm relative to VIRGO's mode-cleaner prototype.

The study of the acquisition of lock was addressed again by extending it to the case of the CITF with a control system bandwidth set to $20\,Hz$. We argued that the expected acquisition times were of the order of $\sim 300\,s$ and an algorithm, using the ratio of photodiode signals, was presented in order to aid the control system to achieve lock. It consisted of an iterative procedure of velocity reconstruction and pulse application to damp the relative mirror motion to within the velocity threshold value. Once this was achieved, the linear feedback was enabled. These procedures were first applied to one end mirror for the control of dark fringe and then to the recycling mirror for the control of the in-cavity stored power. A numerical calculation simulated the algorithm, the mirrors' motion, the optical response and the ADCs' process. As a result, acquisition times of the order of one second were observed.

We would like to conclude that the alignment scheme, as well as the algorithm for lock acquisition, both described in this work, have been adopted as reference solutions for the VIRGO Central Area Interferometer.

Appendix A

Control Systems

This section outlines the basics of feedback control. The notions here presented are necessary for the understanding of Ch.(6) and Ch.(8). Both [53, 54] offer a good introduction to the subject.

In Ch.(2), the concept of *transfer function* was briefly introduced to describe the dynamical behaviour of a mechanical system such as a pendulum; it relates the input signal to the output signal of the system. In principle, any mechanical, electrical or even optical system can be described by a transfer function.

A control system may consist of a number of components, each of which can be described by a transfer function.

It is common to use *block diagrams* to show the functions of each component, how they are connected to each other and the flow of signals. For the case of a simple pendulum, shown in

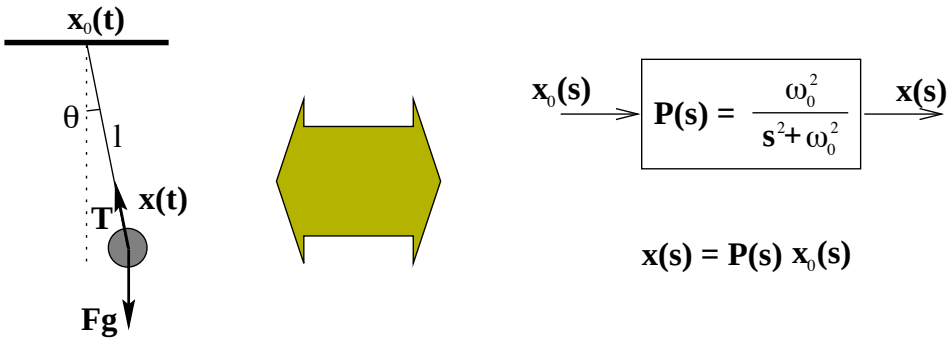

Figure A.1: The pendulum system and its block diagram representation.

fig.(A.1) together with its block diagram representation, the output signal $x(s)$, describing the mass position, is found by multiplying the input signal $x_0(s)$, describing the suspension point position, by the transfer function $P(s)$ of the mechanical system in question. The block diagram then gives a pictorial representation of the system. Such representation facilitates the study of the control system.

A system that maintains a prescribed relationship between the output and the input by comparing them and using the difference as a means of control is called a *feedback control system*, often referred to as *closed-loop control system*. Fig.(A.2) shows an example of a block diagram of a closed-loop system. The output $c(s)$, after being multiplied by $H(s)$ is fed back to the summing point, where it is compared to the reference input $r(s)$. The closed-loop nature of the system is clearly indicated by the figure. The output $c(s)$ is obtained by multiplying the transfer function $G(s)$ by its input $e(s)$. Any linear control system may be represented by a block diagram similar to the one shown in this figure, consisting of blocks, summing points and branch points.

The main properties of a control system, such as its stability, harmonic response and behaviour in any regime can be studied with the aid of (see fig.(A.2))

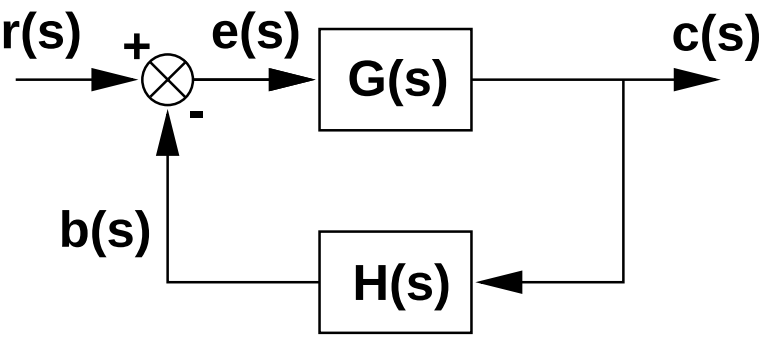

Figure A.2: The block diagram of a closed-loop system.

- the *open-loop* transfer function, defined as the ratio of the feedback signal $b(s)$ to the reference $r(s)$:

$$\text{Open-Loop Transfer Function} \equiv \frac{b(s)}{r(s)} = G(s)\,H(s) \tag{A.1}$$

  when $b(s)$ is disconnected from the summing point

- the *closed-loop* transfer function, relating the output $c(s)$ with the input $r(s)$ as

$$\text{Closed-Loop Transfer Function} \equiv \frac{c(s)}{r(s)} = \frac{G(s)}{1 + G(s)\,H(s)} \tag{A.2}$$

A.1 The Stability Criteria

The stability of a closed-loop system can be determined from the location of the poles[1] of the closed-loop transfer function in a plane where the axes are the real and imaginary parts respectively. If any of these poles lie in the right half-plane, then with increasing time they give rise to the dominant mode, and the time response increases or oscillates with increasing amplitude. This represents an unstable system. Therefore, closed-loop poles in the right half-plane are not permissible in the usual linear control system. If all closed-loop poles lie to the left half-plane, any transient response eventually reaches equilibrium.

The *Nyquist criterion* offers an effective aid to the study of the stability of a closed-loop system once the open-loop transfer function is known. It refers to the polar diagram of the function

$$G(s)\,H(s) \tag{A.3}$$

for values of $\mid s \mid$ ranging from $-\infty$ to ∞. According to [54], the Nyquist criterion is phrased as follows:

- Nyquist stability criterion: if the open-loop transfer function $G(s)\,H(s)$ has

  i. neither poles nor zeros on the imaginary axis;

  ii. k poles in the right half-plane;

  iii. and $\lim_{|s|\to\infty} G(s)\,H(s) =$ constant;

[1] By *poles* we mean the roots of the function's denominator while by *zeros* the roots of the numerator.

then for stability the $G(s)\,H(s)$ locus, as $\mid s \mid$ varies from $-\infty$ to ∞, must encircle the -1 point k times in the counterclockwise direction.

The polar diagram of the open-loop transfer function is of great help for the design of a closed-loop system.

A rule of thumb for loop stability is a 1/s behaviour for the amplitude of the open-loop transfer function at the unity gain frequency[2] (UGF).

A.2 Design Specifications

Not only must the control system be stable but it must also be conceived so as to fulfill specifications on the sensitivity to parameter variations and on the attenuation of noise sources present anywhere along the chain. Above all, the overall loop *gain* in closed-loop as well as the *bandwidth* of the control must be chosen accordingly.

The closed-loop transfer function, defined as

$$G_0(s) \equiv \frac{G(s)}{1 + G(s)\,H(s)} \tag{A.4}$$

must be such that, in a given bandwidth,

$$\mid G_0(s) \mid \sim 1 \tag{A.5}$$

where the bandwidth in question is defined as the angular frequency ω_f for which the amplitude of $\mid G_0(\omega_f) \mid$ is 3 db[3] less than $G_0(0)$. If the open-loop transfer function $G(s)\,H(s)$ is chosen so that

$$\mid G(s)\,H(s) \mid >> 1 \tag{A.6}$$

then eq.(A.4) can be approximated as

$$\begin{aligned} G_0(s) &\equiv \frac{G(s)}{1 + G(s)\,H(s)} \\ &\simeq \frac{1}{H(s)} \end{aligned} \tag{A.7}$$

independently of any variation in $G(s)$.

In conclusion, the choice on the open-loop transfer function must be such that in a chosen bandwidth, the control system is able to limit the excursion values of the error function $e(s)$ to the given specifications.

A.3 Amplitude and Phase Margin

Once the control system in question satisfies the stability criteria, it is also possible to quantify the margin of stability. It is clear that the farther the $G(s)\,H(s)$ locus is from the critical point -1, the less sensitive the system is to instabilities. Two parameters can quantify the *relative* stability of a feedback system:

1. *the Amplitude Margin* M_A:
   the inverse of the amplitude $\mid G(i\,\omega)\,H(i\,\omega) \mid$ at the angular frequency ω corresponding to the condition

$$\arg[G(i\,\omega)\,H(i\,\omega)] = -\,\pi \tag{A.8}$$

[2] The frequency for which the amplitude of the open-loop transfer function is 1.
[3] A gain of A can be expressed in B db with the formula B = 20 $\log_{10}$A.

2. *the Phase Margin* M_P:
   the angle difference between the phase $\arg[G(i\omega)\,H(i\omega)]$ for which

$$| G(i\omega)\,H(i\omega) | = 1 \tag{A.9}$$

   and the angle $-\pi$.

A general rule indicating the good behaviour of the control system is

$$\begin{aligned} 4 < \quad & M_A \quad < 6 \\ 45^o < \quad & M_P \quad < 60^o \end{aligned} \tag{A.10}$$

Bibliography

[1] R.A.Hulse and J.H.Taylor, *Astrophys.J.* **324** 355 (1975).

[2] B.F.Schutz, *Am.J.Phys.* **52**, 412 (1984)

[3] M.Tinto, *Am.J.Phys.* **56**, 1066 (1988)

[4] B.F.Schutz, *A First Course in General Relativity*, Cambridge University Press (1990).

[5] C.W.Misner, K.S.Thorne, J.Wheeler, *Gravitation*, ed. W.H.Freeman, S.Francisco (1973)

[6] S.Weinberg, *Gravitation and Cosmology: Principles and Applications of the General Theory of Relativity*, John Wiley & Sons, New York (1972).

[7] S.Bonazzola, J.A.Marck, *Annu.Nucl.Part.Sci.* 45:655 (1994)

[8] T.Zwerger, E.Müller, *Astron.Astrophys.*, **320**, 209 (1997)

[9] E.S. Phinney, *Astrophys.J.*, 380:L17, 1991

[10] I.H. Stairs et al., *Measurement of Relativistic Orbital Decay in the PSR B1534+12 Binary System*, (astro-ph/9712296)

[11] K.S.Thorne. Gravitational Radiation. In S.W.Hawking and W.Israel, editors, *300 Years of Gravitation*. Cambridge University Press, 1987

[12] P.S.Saulson, *Fundamentals of Interferometric Gravitational Wave Detectors*, World Scientific Publishing (1994)

[13] J-Y.Vinet, B.Meers, C.N.Man, A.Brillet, *Phys.Rev.D* **38** 433 (1988)

[14] F.Ricci, A.Brillet, *Ann.Rev.Nucl.Part.Sci* **47** 111 (1997)

[15] P.Hello, *Progress in Optics* **38** 85 (1998)

[16] B.J. Meers, *Phys. Rev. D* **38** 8 (1988).

[17] VIRGO *: Proposal for the construction of a large interferometric detector of Gravitational Waves*, The VIRGO Collaboration, Jan. 1990.

[18] VIRGO *Final Conceptual Design-Draft*, The VIRGO Collaboration, Jan. 1997.

[19] R. Barillet et al., *Rev.Sci.Instr*, **7** 162 (1996)

[20] P.R.Saulson, *Phys.Rev.D* **42** 2437 (1990)

[21] F.Bondu, PhD Thesis, Université Paris XI, Orsay, (1996)

[22] M.Beccaria et al., *Class.Quant.Grav.*, **15**, 1 (1998)

[23] G.Losurdo, PhD Thesis, Scuola Normale Superiore di Pisa, (Ottobre 1998)

[24] M.Barsuglia, PhD Thesis, Université Paris XI, Orsay, (May 1999)

[25] A. Dominjon, PhD Thesis, Université de Savoie (1996)

[26] R.Flaminio, PhD Thesis, Universitá degli Studi di Pisa, (1994)

[27] R.Flaminio, H.Heitmann, *Phys.Lett.A*, **214**, 112-122 (1996)

[28] F. Cavalier, M.Barsuglia, VIRGO internal note, VIR-NOT-LAL-1390-051

[29] D.Babusci, H.Fang, G.Giordano, G.Matone, L.Matone, V.Sannibale, VIRGO internal note

[30] D.Babusci, H.Fang, G.Giordano, G.Matone, L.Matone, V.Sannibale, *Phys.Lett.A*, **226**, 31-40 (1997)

[31] F.Cleva, M.Taubman, C.N.Man, A.Brillet, in *Gravitational Waves* eds. E.Coccia, G.Veneziano, G.Pizzella, World Scientific Publishing, Singapore (1-4 July 1997).

[32] C.N.Man, personal communication 1995-1996

[33] S.Braccini et al., *Rev.Sci.Instr.* **67**, 2899 (1996)

[34] J.Y.Vinet et al., *Phys.Rev.D*, **56**, 6085 (1997)

[35] G.Giordano, VIRGO internal note VIR-NOT-FRA-1390-131

[36] G.Giordano, M.Punturo, A.Viceré, VIRGO internal note VIR-NOT-FRA-1390-130

[37] D.Babusci, H.Fang, G.Giordano, G.Matone, F.Cavalier, P.Hello, L.Matone, F.Marion, VIRGO internal note VIR-NOT-FRA-1390-127

[38] G.Giordano, VIRGO Review (Pisa, 1-1999)

[39] G.Giordano, VIRGO Locking Meeting (Cascina, 27/10/98)

[40] L.Matone, Tesi di Laurea, Universitá degli Studi di Roma "Tor Vergata", (1996)

[41] M.Punturo et al., VIRGO internal note VIR-NOT-PER-1380-101

[42] H.Kogelnik and T.Li, *Appl.Opt.* **5**, 1550 (1966)

[43] M.Born, E.Wolf, *Principles of Optics*, Pergamon Press (1975)

[44] R.W.P.Drever et al., *Appl. Phys.* **B31**, 97 (1983)

[45] D.Z.Anderson, *Appl. Opt.* **23**, 2944 (1984)

[46] E.Morrison, B.J.Meers, D.J.Robertson and H.Ward, *Appl.Opt.* **33**, 8041 (1994)

[47] P.Hello, *Couplings in Interferometric Gravitational-Wave Detectors*, Mémoire d'habilitation à diriger des recherches, LAL 96-93

[48] F.Barone et al., *Phys.Lett.A*, **217**, 97 (1996)

[49] F. Marion et al., *SIESTA User's Guide*, VIR-MAN-LAP-5700-XXX

[50] J.Y.Vinet, VIRGO Note PJT94-12 (1994)

[51] A.G.Frodesen, O.Skjeggestad, H.Tofte, *Probability and Statistics in Particle Physics*, Universitetsforlaget (1979)

[52] H.Heitmann, C.Drezen, *Rev.Sci.Instr.*, **68** 3197 (1997)

[53] G. Marro, *Controlli Automatici*, Zanichelli (1997)

[54] K. Ogata, *Modern Control Engineering*, Prentice-Hall (1997)

[55] M.Barsuglia, private communication (1999)

[56] J.Pérôme et al., *J.Opt.Soc.Am.B*, **14** 2811 (1997)

[57] S. T'Jampens, *Rapport de Stage au LAL* (1996)

[58] F.Bondu, private communication (1999)

[59] J.Camp, L.Sievers, R.Bork, J.Heefner *Opt. Lett.* **20** 2463 (1995)

[60] F.Cavalier, L.Matone, VIRGO Note VIR-NOT-LAL-1390-93

[61] F.Cavalier, L.Matone, VIRGO Note VIR-NOT-LAL-1390-104

[62] B.Caron et al., *Astropart.Phys.* **6** 245 (1997)

[63] B.Caron et al., *Astropart.Phys.* **10** 369 (1999)

Remerciements

Je ne serais jamais arrivé jusqu'ici sans l'aide de ma famille, de mes amis et de mes collègues. Je voudrais consacrer cette page pour les remercier sincèrement.

D'abord, je voudrais remercier Jacques Lefrançois et François Richard pour m'avoir accueilli au Laboratoire de l'Accélérateur Linéaire.

J'ai eu beaucoup de chance d'avoir la possibilité de continuer mes études dans ce domaine en grand développement, et je voudrais remercier Michel Davier pour m'avoir offert cette opportunité. Je souhaite avoir acquis un peu de sa rigueur scientifique.

La plupart du travail qui apparaît dans cette thèse n'aurait pas été possible sans les discussions continues que j'ai eu avec Fabien Cavalier. Il est un collègue et un ami, et j'espère que l'on aura à nouveau la possibilité de travailler ensemble.

L'ambiance n'aurait pas été la même sans la bonne humeur de Patrice Hello. Je n'oublierai pas les conversations que l'on a eues: de celles sur le concept de "yo", jusqu'à celles sur le couplage entre l'alignement et le bruit de position du laser.

Je voudrais remercier Marie-Anne Bizouard, qui a récemment rejoint l'équipe VIRGO, dont l'amitié, l'encouragement, et les conseils ont été d'une grande aide pour moi.

Un merci particulier s'adresse à Matteo Barsuglia et Marumi Kado, compagni d'avventura. E' stata una bellissima avventura.

Non sarei mai arrivato qui senza la presenza di Gianfranco Giordano e Danilo Babusci. Per me saranno sempre un esempio e spero di avere ancora la fortuna di lavorare con loro.

Je voudrais remercier et souhaiter bonne chance aux "jeunes" de l'équipe, Nicolas Arnaud et Thierry Pradier, qui ont contribué à créer cet environnement si chaleureux.

Ronic Chiche a toujours été prêt à mettre de coté son travail quand j'avais besoin d'un conseil, je lui exprime ma gratitude.

Je remercie tous les membres du groupe VIRGO au Laboratoire de l'Accélérateur Linéaire pour leur accueil chaleureux et leur soutien.

Merci à Alain Brillet, Catherine Nary Man et tous les membres du groupe VIRGO-Laser-Optique pour m'avoir donné l'opportunité de travailler avec eux sur le prototype du mode-cleaner et pour les chaleureux déjeuners que l'on a eu ensemble.

Finalement, je remercie David Shoemaker et François Le Diberder, non seulement pour avoir accepté d'être rapporteurs de la thèse, mais aussi pour leurs commentaires constructifs. Je remercie François Richard pour avoir accepté d'être le président du Jury et Alain Brillet pour avoir accepté d'en faire partie.